Forschungsbericht
DLR-FB-2020-20

Design and Structural Optimization of a Flying Wing of Low Aspect Ratio Based on Flight Loads

Arne Voß

Deutsches Zentrum für Luft- und Raumfahrt
Institut für Aeroelastik
Göttingen

DLR Deutsches Zentrum für Luft- und Raumfahrt

Design and Structural Optimization of a Flying Wing of Low Aspect Ratio Based on Flight Loads

vorgelegt von
M.Sc.
Arne Voß

an der Faktultät V – Verkehrs- und Maschinensysteme
der Technischen Universität Berlin
zur Erlangung des akademischen Grads

Doktor der Ingenieurwissenschaften
- Dr. Ing. -

genehmigte Dissertation

Promotionsausschuss:

Vorsitzender:	Prof. Dr.-Ing. Flávio Silvestre
Gutachter:	Prof. Dr.-Ing. Andreas Bardenhagen
	Prof. Dr.-Ing. Wolf-Reiner Krüger
	Prof. Dr.-Ing. Hartmut Zingel

Tag der wissenschaftlichen Aussprache: 19. Februar 2020

Berlin 2020

Abstract

The design process for new aircraft configurations is complex, very costly and many disciplines are involved, like aerodynamics, structure, loads analysis, aeroelasticity, flight mechanics and weights. Their task is to substantiate the selected design, based on physically meaningful simulations and analyses. Modifications are much more costly at a later stage of the design process. Thus, the preliminary design should be as good as possible to avoid any "surprises" at a later stage. Therefore, it is very useful to include load requirements from the certification specifications already in the preliminary design. In addition, **flying wings** have some unique characteristics that need to be considered. These are a differentiating factor with respect to classical, wing-fuselage-empennage configurations. The aim of this thesis is to include these requirements as good and as early as possible. This is a trade-off, because the corresponding analyses require a detailed knowledge and models, which become available only later during the design process. New methodologies in the form of a comprehensive, algorithmic **design process** and a parametric **aeroelastic modeling** are developed.

The first aspect of this work concentrates on the **gust encounter** of flying wings. The **open loop gust encounter** is studied at the example of two flying wing configurations and both show a pronounced tendency of pitch up when encountering a positive gust. This has an increasing effect on section loads and should be included in every gust analysis. At the wing root for example, the peaks of the section loads are reduced by the unsteady aerodynamic influence but occur earlier in time, compared to quasi-steady aerodynamics. The **closed loop gust encounter** includes a controller for the pitching motion and significantly reduces the minimum and maximum pitch angles during a gust encounter. It was found the performance of the controller is limited by the maximal control surface rate, especially for short gust gradients. Concerning section load, two effects need to be considered. Because the controller

reduces the pitch up tendency, section loads are decreased. Then, from the deflection of the control surfaces, loads along the trailing edge are added. These two effects were found to balance out with respect to the shear force and the bending moment at the wing root but the torsional moment was increased. Obviously, actuation of the control surfaces causes much higher hinge moments and attachment loads. The operation range of the aircraft is extended to unstable conditions by allowing mass configurations where the payload is positioned further rearwards. The rigid body motion is increased compared to the naturally stable closed loop configuration. An increase in section load is observed for most monitoring stations as well.

The second focus is the comparison of low fidelity panel methods with higher fidelity aerodynamics. Similarities and differences between VLM and **CFD based maneuver loads** are shown. For a horizontal level flight at low speed, CFD and VLM converge and deliver similar results in terms of trim conditions with small difference in pressure distribution. Then, all maneuver load cases are calculated using high fidelity aerodynamics within the preliminary design process. Comparison of the CFD to the VLM based maneuver loads shows load envelopes at the wing root that are similar in size and shape but have an offset. At the outer wing and at the control surfaces, the envelopes take different shapes and new dimensioning load cases are identified. Application of parametric modeling and an algorithmic design process result in a final aeroelastic model, optimized for minimum structural weight. The new structural mass is approximately 200kg (~13%) heavier than the reference.

Acknowledgments

This work evolved during my employment as scientific employee at the German Aerospace Center (DLR) - Institute of Aeroelasticity in Göttingen, Germany. I would like to thank Prof. Dr.-Ing. Wolf Krüger for giving the possibility, the means, the necessary guidance and sufficient freedom for writing this thesis. I would also like to thank Prof. Dr.-Ing. Andreas Bardenhagen for supervising the thesis at the Technical University of Berlin and Prof. Dr.-Ing. Hartmut Zingel, University of Applied Sciences Hamburg, for agreeing to review the work.

My interest in flight physics was awakened by Dr.-Ing. Moritz Scharpenberg, who introduced me to the disciplines of loads and aeroelasticity during my Bachelor and Master thesis and my time as a working student at Airbus in Hamburg. It was also him who suggested to think about an academic career and initiated contact with Prof. Dr.-Ing. Wolf Krüger.

I would also like to thank my colleges at the institute who supported my work in various ways. Especially, I would like to thank Dr.-Ing. Thomas Klimmek for the guidance of my young and inexperienced self, coming as a novice directly from university. He also introduced me to the world of aeroelastic modeling, design and loads analysis with ModGen and Nastran. I would like to thank Guido Voß for many helpful discussions on CFD related topics and Dr.-Ing. Wolfgang Wegner, who is the Euler expert. Vega Handojo started his thesis in parallel and on a similar topic, motivating and driving my own progress and was a good partner for many technical discussions. I am also happy to have met “The” Jens Neumann, whom I would like to thank for his demonstrative examples, for always having a matching report/paper/article helping to solve my problem, and for having the current weather and snow forecast. Dr.-Ing. Jan Schwochow answered many questions to various aeroelastic topics and agreed to mentor this thesis. I am very grateful for the openness of the people at the Institute of Aeroelasticty and would like to thank everyone for the time and assistance whenever needed.

I would like to express that I enjoyed and still enjoy my time at the DLR in Göttingen very much and would like to thank my office neighbors Jannis, Jörn, David, Tobias and Yasser and everyone else who joined for an after-work beer or mojito. I think it is very exceptional to have colleges with who you go on skiing trips in the Alps, go hiking in the Smoky Mountains, or travel to Andalusia.

For Section 4.2, the author would like to thank the European Commission for funding the ACFA2020 (Active Control for Flexible 2020 Aircraft) project within the seventh Research Framework Program under grant agreement number 213321. The author would also like to thank his colleague, Thomas Klimmek, for providing the model data and to Andreas Wildschek for arranging the permission to exploit the ACFA2020 data for this work.

Finally, I would like to thank my parents, who always fostered my curiosity. With great enthusiasm, my mum spend much time proofreading this thesis. She found many (hopefully all) tpying und spellign errorrs I would never have spotted myself.

Thank You!

Table of Contents

Lists of Figures and Tables

List of Figures

List of Tables

Nomenclature

Abbreviations

ACFA	BWB configuration from the ACFA 2020 EU project within the seventh Research Framework Program
AIC	Matrix of aerodynamic influence coefficients
AR	Aspect ratio
BWB	Blended wing body
CFD	Computational fluid dynamics
CFL	Courant–Friedrichs–Lewy number
CFRP	Carbon fiber reinforced plastic
CS	Certification specification, control surface
DLM	Doublet lattice method
DLR	Deutsches Zentrum für Luft- und Raumfahrt
Euler	Euler equations
FE	Finite elements
FI	Failure index
FL	Flight level
FSI	Fluid structure interaction
FSM	Force summation method
GAF	Generalized aerodynamic forces
HALE	High altitude and long endurance configurations
LE	Leading edge
LK	Loads Kernel software package
LRA	Loads reference axis
M	Mass configuration
MAC	Modal assurance criterion, mean aerodynamic chord

MDM	Modal displacement method
MDO	Multidisciplinary optimization
MLW	Maximum landing weight
MTOW	Maximum take-off weight
MULDICON	Multi disciplinary configuration
NS	Navier-Stokes equations
RANS	Reynolds-Averaged-Navier-Stokes equations
RFA	Rational function approximation
TE	Trailing edge
VC / MC	Cruise speed / Mach number
VD / MD	Dive speed / Mach number
VLM	Vortex lattice method

Software

Centaur	CFD mesh generation software by CentaurSoft
Loads Kernel	Loads and aeroelastic analysis software developed in this thesis
MSC.Nastran	NASA structural analysis code, commercially distributed by MSC software
Python	High-level programming language for general-purpose programming
Scipy	Python library for scientific and technical computing
SOL103	Modal analysis sequence (MSC.Nastran)
SOL144	Static aeroelastic solution (MSC.Nastran)
SOL200	Structural optimization sequence (MSC.Nastran)
Tau	Computational fluid dynamics solver developed by DLR

Notation Conventions

$\mathbf{Q}$	Matrix
$\mathbf{q}$	Vector
q, Q	Scalars
$\dot{()}$	First derivative
$\ddot{()}$	Second derivative

Sub- and Superscripts

$()^{\mathrm{desc}}$	Descriptive superscript

$()_i$	Inertial coordinate system
$()_b$	Body-fixed coordinate system
$()_g$	g-set
$()_f$	f-set, flexible generalized coordinates
$()_a$	a-set
$()_o$	o-set
$()_k$	Center point of aerodynamic panel
$()_l$	One quarter point of aerodynamic panel
$()_j$	Three quarter point of aerodynamic panel
$()_{x,y,z}$	Quantity in the direction of or about the x, y and z axis
$()_{1,2}$	Quantity in fiber direction (1) and orthogonal to the fibers (2)
$()^{t,c}$	Quantity for tension, compression

Variables and Parameters

Latin:

$\mathbf{A}_{3...n+2}$	Unsteady aerodynamic terms	
AC	Aerodynamic center	
$\mathbf{AIC}$	Matrix of aerodynamic influence coefficients	
$\mathbf{B}_{jj}$	Matrix of wake downwash	
CG	Center of gravity	
CP	Center of pressure	
C_d, c_d	Drag coefficient	
C_l	Lift coefficient	
C_{my}	Pitch coefficient	
$\mathbf{D}$	Damping matrix, transformation matrix for velocities, direction cosine matrix	Kg/s, $Kg \cdot m/s$
$\mathbf{D}_{\mathrm{angular}}$	Transformation matrix for angular rates	
E	Elastic modulus	Pa
F	Design objective	
F_z	Shear force	N
G	Shear modulus	Pa
H	Gust gradient	m
$\mathbf{K}$	Stiffness matrix	N/m, Nm/rad
$K_{p,i,d}$	PID-Controller coefficients	

$\mathbf{M}$	Mass matrix	$Kg, Kg \cdot m$
Ma	Mach number	
MAC	Modal assurance criterion, mean aerodynamic chord	
M_x	Bending moment	Nm
M_y	Torsional moment	Nm
N_z	Load factor	
$\mathbf{Q}_k$	Stiffness matrix of fiber layer in global coordinate system	
$\mathbf{Q}'_k$	Stiffness matrix of fiber layer in local coordinate system	
R, S	Maximum allowable stress, shear	
$\mathbf{S}_{kj}$	Aerodynamic integration matrix	
$\mathbf{T}$	Spline matrix	
U	Gust velocity	m/s
V	Onflow velocity	m/s
b_{ref}	Reference span width	m
c_p	Pressure coefficient	
c_{ref}	Reference length	m
$\mathbf{d}$	Distance between two points	m
$\mathbf{g}$	Constraints	
i	Imaginary number	
$\mathbf{lag}_{1\ldots n}$	Unsteady lag states	
p, q, r	Angular rates in flight physical coordinate system	rad/s
$\mathbf{p}$	Nodal loads vector	N, Nm
$\mathbf{q}$	Onflow vector	m/s
q_∞	Dynamic pressure	Pa
s	Complex Laplace variable	
t	Time	s
t_k	Layer thickness	m
$\mathbf{u}$	Nodal displacement vector	m, rad
u, v, w	Velocities in flight physical coordinate system	m/s
$\mathbf{v}_b$	Velocities in body-fixed coordinate system	m/s
$\mathbf{w}_{j,\mathrm{cam}}$	Downwash due to camber and twist of the profiles	m/s
$\mathbf{w}_{j,\mathrm{cs}}$	Downwash due to control surface deflections	m/s
$\mathbf{w}_{j,uf}$	Downwash due to flexible structural deformation	m/s

$\mathbf{w}_{j,\dot{u}f}$	Downwash due to flexible structural motion	m/s
$\mathbf{w}_{j,\mathrm{rbm}}$	Downwash due to rigid body motion	m/s
$\mathbf{w}_j$	Downwash, induced at three quarter point	m/s
$\mathbf{x}$	Design variables	
x, y, z	Position in inertial coordinate system	m
z_k	Layer offset	m

Greek:

Γ	Circulation strength	m^2/s
$\mathbf{\Phi}$	Eigenvector	
Φ, Θ, Ψ	Euler angles in inertial coordinate system	$\circ$
α	Angle of attack	$\circ$
$\beta_{1\ldots n}$	Poles for rational function approximation	
δ	Local displacement	m
ϵ	Strain	-
ζ	Yaw command	$^\circ, rad$
η	Pitch command	$^\circ, rad$
$\boldsymbol{\lambda}$	Eigenvalues	
ν_{12}	Poisson's ratio	
ξ	Roll command	$^\circ, rad$
ρ	Density	Kg/m^3
σ	Stress	Pa
τ	Shear	Pa
ω	Angular rate	rad/s
$\boldsymbol{\omega}_b$	Angular rates in body-fixed coordinate system	rad/s

1 Introduction

1.1 Motivation of This Thesis

The design process for new aircraft configurations is complex, very costly and often takes several years until completion. Many disciplines are involved which define requirements, make a first concept, conduct analyses and do trade studies. All disciplines are equally important and have to interact. Thus, there is no clear beginning and dependencies are complex. According to Raymer [152], the design process can be broken into three phases:

- Conceptual Design
- Preliminary Design
- Detail Design

The aim of the conceptual design is to find a feasible configuration that satisfies all requirements. What does such an aircraft look like? Will it fly? Are there better aircraft configurations?

For the preliminary design, one configuration is selected and frozen. Major changes are no longer allowed. The aim is to substantiate the selected design, based on physically meaningful simulations and analyses. Depending on the configuration, important topics are aerodynamic performance, mass estimates, loads, aeroelastics, and other flight physical investigations. The more thorough the investigations and the better the methods, the more precise is the preliminary design. In the detail design, the actual pieces of the aircraft are designed and manufacturing is prepared. At this stage of the design process, changes become much more costly and might lead to a delay of the design process and even a delay of the entry into service. Thus, the preliminary design should be as good as possible to avoid any “surprises”

during a later stage. At the end of the detail design, the aircraft usually needs to be certified by an aviation authority, e.g. the Federal Aviation Administration (FAA) or the European Aviation Safety Agency (EASA). For the case of the EASA, it has to be shown that the aircraft withstands the loads that are specified in the Certification Specifications, e.g. CS-23 [47] for small aircraft or CS-25 [46] for large aircraft.

The aim is to include these requirements in the preliminary design as early as possible. This is a trade off, because the corresponding analyses require a detailed knowledge of the structure, the mass distribution, the structural dynamics as well as the steady and unsteady aerodynamics, which become available only later during the design process. During the last years, this conflict has driven the development of software packages that already allow the creation of aeroelastic simulation models at an earlier stage of the design process, compare with literature presented in Section 2.10.1. Parameterized aeroelastic models are state of the art and have been applied successfully to conventional configurations and to some extend also to unconventional configurations, as will be shown in Section 1.2. Mostly, finite element models are created which include primary structural components such as spars, ribs, outer skin and stringers. Masses are modeled as condensed or lumped masses and together with the structural mass calculated from the material density, this gives a first estimate of the aircraft mass. To a certain extend, parameterized models allow for a sizing of the structure with the calculated loads. This can be formulated as an iterative process, sketched in Figure 1.1, as the structural mass is primarily driven by the flight loads and the flight loads are influenced by the structural mass and stiffness. The process results in a final structural model once convergence is achieved.

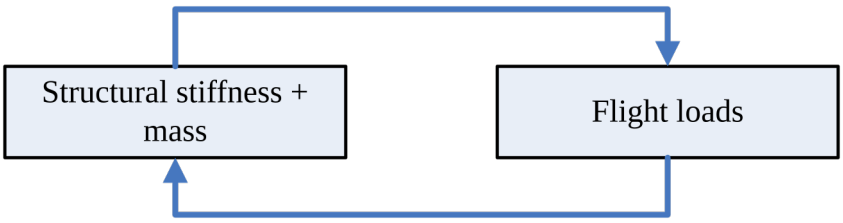

Figure 1.1: Interaction of flight loads and structural weight

For flying wings, some flight physical peculiarities can be expected, which are described briefly in the following. Conventional configurations with a wing, a fuselage and an empennage, shown in Figure 1.2, are naturally stable. The location in x-direction of the center of gravity (CG) in combination with the aerodynamic center (AC) determines the

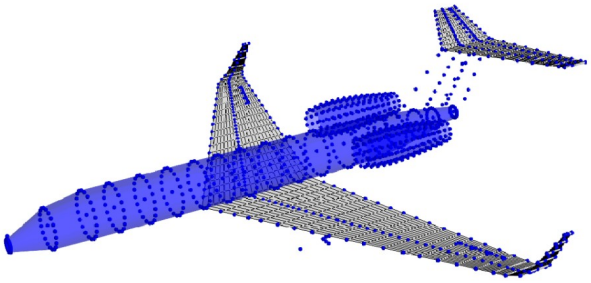

Figure 1.2: Example of an aeroelastic model of a conventional wing-fuselage-empennage aircraft (DLR HALO)

longitudinal stability. A CG in front of AC results in a stable aircraft. This is the case for most aircraft and natural stability is mandatory for all civil aircraft. Typically, there is a movement of CG due to passengers, payload or fuel tank levels while the shift of AC at increasing speed is small. During a gust encounter, the aircraft “dives” into the gust - assuming a positive (upwards) gust, the aircraft typically performs a heave motion in combination with a nose down recovery motion. Unsteady aerodynamic effects typically delay and reduce impact of the gust (compared to quasi-steady aerodynamics and without special effects that might come from aero-structural coupling).

Flying wings, shown in Figure 1.3, are rather sensitive about the pitch axis and large rigid body motions are expected. The MULDICON (compare Section 3.1) for example is only marginally stable, an empennage is missing, it has a rather large range of travel of the aerodynamic center compared to the aircraft length, and a low moment of inertia about pitch axis due to geometrical shape. Thus, a movement of CG is only allowed within a small margin and a good knowledge of AC is required. Considering this, it is very likely that a flying wing needs to operate under longitudinal unstable conditions over a large range of the flight envelope. Taking external disturbances such as a gust encounter into account, an active pitch control system is required.

When an aircraft enters a gust field, it experiences the induced gust velocities first at the aircraft nose. As the aircraft travels forward, the gust hits the aircraft body, then the wings and

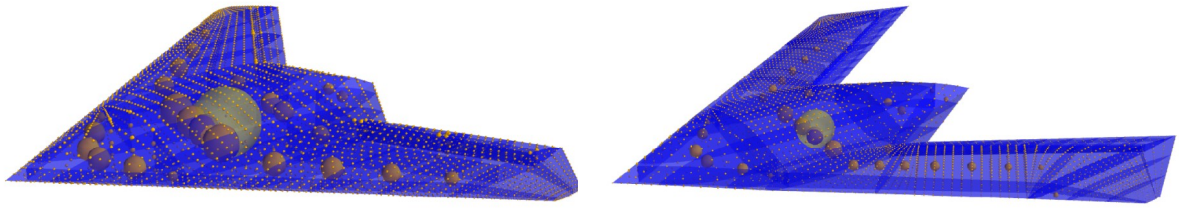

Figure 1.3: Examples of aeroelastic models of flying wings (MULDICON and DLR-F19)

eventually the tail. Depending on the aircraft length and flight speed, there is a delay in time of the gust impact along the longitudinal axis of the aircraft. Presumably, this so-called penetration effect is more pronounced with planar configurations as there are large areas of lifting surface in front of center of gravity, which might evoke a flight mechanical reaction and contributes to the aircraft loads.

As a means to increase stability, flying wings often have highly swept wings. Due to that geometrical shape, the three-dimensional flow and cross flow might be important and influence the spatial pressure distribution, especially in span-wise direction. In addition, transonic effects, such as compression shocks, alter the pressure distribution in chord direction and will change the pitching moment. Both effects alter the trim solution, especially if the aircraft is very sensitive about the pitch axis, which has an effect on loads.

Hypothesis: Due to these peculiarities of flying wings, the author expects the following **additional requirements** being important for the preliminary design:

I. Compared to wing-fuselage-empennage configurations, flying wings require unconventional structural layouts. No typical and well-proven layouts exist.

II. Strong three-dimensional flow characteristics and transonic effects have an influence on the structural design and should be included in the preliminary design of flying wings.

III. The gust encounter of flying wings requires a fully dynamic, unsteady simulation including penetration effect and flight mechanical aspects.

IV. A controller for the pitching motion of marginally stable/unstable flying wings interacts with gusts. The combination of both has a strong influence on the aircraft loads.

Conclusion: Additional new requirements are to be included in the preliminary design process for flying wings. Emphasis is put on a comprehensive loads process including a large number of load cases (>100) to cover the flight envelope to ensure a thorough preliminary design.

1.2 Overview of the State of the Art and Current Research

This section aims to provide an overview on scientific publications related to this work. It is divided into two sections. First, research on flying wing configurations is presented. The focus is not necessarily on flight loads but on flight physical topics generally relevant for such configurations. Second, research related to flight loads is presented. Here, the focus is on the state of the art of calculation principles. However, the methods are usually applied to conventional configurations.

1.2.1 Flight Physical Investigations on Flying Wings

While there is a considerable amount of knowledge about conventional configurations, there is little experience regarding flying wing configurations and data for comparison are rarely available. The aircraft considered in this overview may be divided in four groups:

- high altitude and long endurance configurations (HALE)
- blended wing body configurations (BWB)
- flying wings of low aspect ratio
- other flying wing configurations

Figure 1.4: The Helios Prototype flying wing over the Pacific Ocean during its first test flight [48]

A **HALE** configuration usually has the purpose to stay airborne for a very long time. Typical examples are the NASA Helios prototype [51] shown in Figure 1.4. Similar configurations but with tail are the Qinetiq Zephyr [148] or the Solar Impuls [180]. The aeroelastic behavior and

modeling of HALE configurations is well-studied and presented in the following. One important key event is probably the Helios mishap [121,122] in 2003, which got much public attention and has inspired people to start investigations. Is this way the mishap had a very positive effect and shows the need to include detailed and sophisticated methods as early as possible in the design process of an aircraft. HALE configurations feature wings of a very large aspect ratio at a very low structural weight. Thus, their wings are very flexible, can experience large deformations during flight and have low natural frequencies, possibly leading to an interaction with the aircraft's rigid body motion. In addition, structural geometrical non-linearities should be accounted for if the deformations are very large. Both effects have been studied by many authors, e.g. Patil et al. [136–139]. Raghavan [150] concentrated on the flight dynamical part only with a rigid structure. Su and Cesnik [186] added a spatially distributed, three dimensional gust. In another work, Su and Cesnik [187] studied the phenomena of body-freedom flutter for a very flexible configuration. Naser et al. [123] wrote a comprehensive report on the Alliance 1 Proof-of-Concept Airplane under gust loads with special focus on a spanwise variation of gust velocities. The aircraft is highly flexible but has an empennage. Analyses are conducted using MSC.Nastran. Dong [39] investigated a gust encounter of a HALE using CFD, coupled with a modal (thus linear) structural representation of the aircraft. Wang et al. [211] tried to capture stall areas at the wing tip. Ricciardi et al. [155–157] evaluated the applicability of a quasi-static gust analysis using Pratt's Formula. Kotikalpudi [89] performed body freedom flutter analyses using unsteady panel aerodynamics in the time domain and made the analysis code publicly available [88] to create a common platform for research. Leitner et al. [102] investigated both body freedom flutter and gust response, comparing linear and non-linear structural modeling. Ouellette [134] compared simulation results with flight test data of the X-56A MUTT.

A **BWB** is a fixed-wing aircraft whose classical fuselage is blended with the wing in an attempt to increase the aerodynamic lift while reducing the drag. To reduce the surface area further, an empennage is often omitted. The resulting planforms may look similar to flying wings of low aspect ratio at a first glance, but usually are much larger. The focus is on the efficient transport of a large number of passengers and payload. A typical example is the Boeing / NASA X-48B [231] shown in Figure 1.5. Like HALE confgurations, BWBs are well-studied. Comprehensive research on design concepts for large passenger BWB has been presented by Liebeck [104,105]. Wildschek [219,220] studied gust encounters and loads

Figure 1.5: The X-48B blended wing body prototype [84]

alleviation systems on a BWB within the EU projects NACRE and ACFA 2020. A substantial amount of work has been done within the Preliminary Aircraft Design and Optimization framework PrADO, primarily developed by Heinze [65] and maintained at TU Braunschweig. Österheld [131,132] added methods to include aeroelastic effects within the preliminary design. The framework was then used for the conceptual design of a BWB [133]. Hansen [58–60] added further details, especially for the modeling of the passenger cabin and studied various structural cabin layouts.

Flying wings of low aspect ratio are different to HALE and BWB configurations in several aspects. The missions have a varying focus and usually include flight and maneuverability in both high and low altitudes and at high speeds. In the case of a transport mission, flight speed and the ability to carry a payload is more important than long endurance and low drag, resulting in a more compact planform and in wings of lower aspect ratio. One example is the

Figure 1.6: The X-45 demonstrator [164]

NASA/DARPA/Boeing X-45 demonstrator shown in Figure 1.6. Only few such configurations can be found and the existing configurations tend to have a military focus. Therefore, on the civil side, few data and information is publicly available.

In medium to high ranges of angle of attack, a vortex dominated flow is expected [67,174,175]. The control of such complex and non-linear aerodynamics is one of the challenges and confronts the flight control system with great demands. In addition, due to the missing empennage, new approaches to maintain stability and control are required. Weisshaar and Ashley [216,217] investigated the static aeroelasticity of a flying wing configuration with special focus on divergence speeds at various control surface settings. Stenfelt and Ringertz [183,184] conducted wind tunnel tests to measure trailing edge control surface effectiveness. Lateral stability and yaw control is achieved using differential settings of the control surfaces. Chandrasekhara and McLain [24,25] analyzed the steady and unsteady flow of a maneuvering aircraft in a water tunnel. Forces and moments were studied at high angles of attack and for yawing motion. Nangia and Palmer [120] compared wing platforms regarding camber and twist to obtain a pitching moment coefficient in a certain range (stable, neutral and unstable) using numerical flow solvers. Woolvin [222,223] performed conceptual design studies, performance analyses and planform trade-offs. Tianyuan and Xiongqing [193] conducted a multidisciplinary optimization for low drag and low structural weight. Their work is interesting in respect to this work, because structural properties are considered and, at one stage, a finite element model is generated to estimate the structural weight. However, the authors don't provide any further information on e.g. the load cases, aerodynamic methods, etc.

An example for **other flying wing configurations** is the Northrop B-2, which is a very much larger stealth bomber not really fitting in any of the three categories above and was investigated in the 90s e.g. by Britt et al. [17,18], Crimaldi et al. [28] and Winther et al. [221]. On the civil side, with much higher aspect ratio and for lower speed, one example is Akaflieg Braunschweig's SB 13 on which Schweiger et al. [177] conducted flutter analyses. A second example is Akaflieg Karlsruhe's AK-X prototype on which Deck and Schwochow [33] assessed the flutter behavior based on a preliminary model. A comprehensive overview on flying wings, their design and flight characteristics is given by Nickel and Wohlfahrt [130].

Summary: Compared to HALE and BWB configurations, flying wings of low aspect ratio are studied very little on the civil side. Most of the aircraft are only prototypes, demonstrators or “paper planes”. No typical and well-proven structural layouts exist or models are not publicly accessible. Consequently, a parametric aeroelastic design and optimization process has yet to be applied to a flying wing of low aspect ratio, confirming requirement I from Section 1.1.

From the experience with HALE and BWB configurations, we learn that special attention need to be paid to the gust encounter of flying wings, which confirms requirement III from Section 1.1.

1.2.2 Load and Aeroelastic Investigations on Conventional Aircraft Configurations

The advent of computers introduced a new era in aircraft design. Aeroelastic engineers and scientists were among the pioneers to apply numerical methods to problems that were unsolvable before. One of the most known examples is the **Na**sa **Str**uctural **An**alysis System Nastran [160] by MSC Software Corporation, developed back in the 1960s and 70s by NASA [124]. Major additions to the aeroelastic solution sequences were contributed by Rodden et al. [159,160]. Another commercial computer program is ZAERO [225] by Zona Technoloy Inc. Most aircraft companies have developed their own methods and tools, but literature is rarely available. Lockheed developed the L-1011 TriStar using advanced computational methods for loads analysis, as reported by Stauffer et al. [181,182]. Next to Lockheed, work was also done at Boeing, e.g. by D'Vari and Baker [45] presenting an **a**eroelastic **i**ntegrated **l**oads **s**ubsystem (AILS). A framework used at Airbus and DLR is VarLoads, literature may be found by Kier et al. [79,81] or Scharpenberg et al. [167]. Scharpenberg and Voß [168] used the VarLoads framework to investigate non-linear geometrical effects and Scharpenberg [166] also quantified uncertainties with respect to a typical aircraft loads process. A comprehensive overview and in-depth description of the state of art (as of 2006) in aircraft loads modeling and simulation is presented by Reschke [154]. Marquard [117] used similar techniques but focused on an integral design of flight controllers. Teufel [188] studied the modeling of gusts and gust loads alleviation for a flexible aircraft. Handojo and Klimmek [57] compared loads obtained from quasi-static gust calculations employing Pratt's Formula with unsteady,

dynamic gust simulations using MSC Nastran for the ALLEGRA configuration with a forward-swept wing. Chudy [26] presented a similar study for a sailplane. Mauermann [118] conducted simulations for wake vortex encounters of a flexible aircraft using unsteady vortex lattice aerodynamics in the time domain. Silvestre [179] used slightly more simple but faster methods for the modeling of the motor glider Stemme S15. Although structural flexibility as well as unsteady aerodynamics are included, the focus lies on the aeroservoelastic design. An openly available and comprehensive framework (ASWING) is developed and maintained by Drela [42–44]. In ASWING, the focus is on integrated simulation models for preliminary aerodynamic, structural and control-law design. Because all components are modeled as beams and lifting lines, the approach is inherently limited to moderate or high aspect ratio wings. Some more general aspects and strategies for loads calculation can be found in academic textbooks, for example by Wright and Cooper [224] or Hoblit [66].

The preferred aerodynamic methods of the tools mentioned above are based on panel methods, making an adaptation for the transonic regime mandatory. Different possibilities and methodologies for correction have been developed and are still under investigation. An overview on correction methods is given by Brink-Spalink [16] and Palacio et al. [135]. Some examples in this field are works by Giesing et al. [52], Bruns and Brink-Spalink [16], Ganzert and Dirmeier [49], Thormann and Dimitrov [38,192] or Quero-Martin [149]. VarLoads has recently been extended by a 3D panel method and a reduced order aerodynamic model, based on proper orthogonal decomposition [82]. Palacios [135] discussed the weaknesses of different correction methods. Surprisingly, he already (2001) mentions linearized computational fluid dynamic (CFD) and a forced motion pulse method to compute matrices of generalized aerodynamic forces (GAFs) directly. Kaiser et al. [74] compared both methods and validated them against a fully non-linear solution using the DLR Tau code and the linear frequency domain solver DLR Tau LFD. Vidy [200] shows that the use of non-linear GAFs for steady aerodynamics already improves the final gust loads significantly due to the steady offset between DLM and CFD at the trim state. Dimitrov [38] comes to the same conclusion for the Aerostabil Wing using the quasi-steady iSKEM correction method. However, non-linearities occurring during a gust encounter at an angle off attack of 3° are not captured. This would require an unsteady correction. Hasselbrink [63] explains that the current industrial practice is a blending from k=0 with quasi-steady correction to pure DLM at higher reduced frequencies. To properly capture unsteady aerodynamics, the use of GAFs obtained from CFD

linearized about a non-linear steady solution appears to be the most promising strategy but is still under investigation. Unfortunately, application of such a correction scheme to gust loads in a preliminary design process is not yet feasible.

Other works at DLR by Ritter and Dillinger [158] or Reimer et al. [153] are in the field of high fidelity aerodynamics, using computational fluid dynamic (CFD) codes such as the DLR Tau code. The CFD solver is then coupled loosely to a structural solver. In combination with mesh deformation techniques, the structural flexibility is incorporated in the CFD solution. Neumann and Mai [129] applied this method to the simulation of an aeroelastic wind tunnel test for a gust response. A similar approach is developed at RWTH Aachen by Wellmer [218] using the CFD code FLOWer. Rampurawala [151] performed aeroelastic CFD investigations with respect to flutter and an emphasis on control surfaces.

To the author's best knowledge, there are few publications on the use of CFD within a comprehensive loads analysis and structural sizing process during preliminary design. Therefore, this is a field of research at the DLR Institute of Aeroelasticity and activities on both conventional and unconventional configurations are ongoing. Two recent publications are by Klimmek and Schulze [86] and Voß [201,202].

Conclusion: The closed loop gust encounter is studied for conventional configurations but not for flying wings. Another difference is the natural stability of conventional configurations and the focus on gust loads alleviation. This supports requirement IV from Section 1.1

CFD maneuver loads within a comprehensive loads analysis and structural sizing process during preliminary design are not state of the art, neither for flying wings nor for conventional configurations. However, the high number of publications on aerodynamic correction methods suggest that requirement II from Section 1.1 is very important.

1.3 Contributions and Overview of This Thesis

From the motivation and literature study in Sections 1.1 and 1.2, several important aspects are identified to fulfill the demand for a thorough preliminary design of flying wings. The focus of this thesis lies on **two major contributions**:

- The first aspect concentrates on the gust encounter of flying wings. Next to external disturbance, a controller for the pitching motion of marginally stable/unstable flying wings has an influence on loads. The combination of both presumably increases loads and has not been considered in the preliminary design of flying wings. In this work, the gust encounter of flying wings is studied first for the open loop, then for the closed loop system. The requirements on the preliminary design of flying wings number III and IV from Section 1.1 are addressed here.
- The second focus is the improvement or replacement of low fidelity panel methods with higher fidelity aerodynamics from computational fluid dynamics (CFD) for maneuver loads. This is important for flying wings because strong three-dimensional flow characteristics and transonic effects are expected (requirement number II from Section 1.1). Similarities and differences between CFD and VLM based maneuver loads will be demonstrated. Then, all maneuver load cases will be calculated using high fidelity aerodynamics within the preliminary design process.

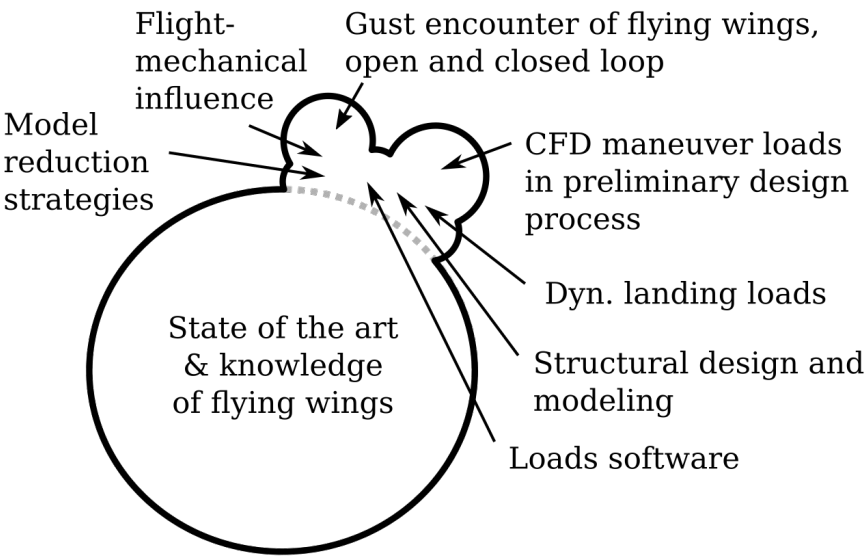

Figure 1.7: Contributions of this thesis

Several minor topics are touched during these studies. They are important as they enable and/or contribute to the investigations of the two major topics:

- During the preliminary design process, a structural design for a flying wing of low aspect ratio is developed and aeroelastic simulation models are created which enable the following numerical analyses.
- During the structural design, time was spent to develop a new model reduction strategy to reflect the characteristics of compact, planar configurations with wings of low aspect ratio. The classical concept for a loads reference axis (LRA) is unsuitable because of the few number of ribs in span direction and the fuselage bending characteristics would be neglected. Including leading and trailing edges as well as control surfaces is an improvement compared to modeling the wing box only.
- From the literature study on HALE and BWB configurations, it is apparent that flight mechanical characteristics are likely to be important for aircraft loads and aeroelastics. Therefore, the methods are selected carefully to include these effects. They partially exist for the design of conventional configurations and can be adopted for the design of flying wings. The result is a fully dynamic, unsteady time simulation of gust encounters including flight mechanics.
- Next to maneuver and gust loads, loads from the landing impact are suspected to be important. A generic landing gear module is developed to enable the fast analysis of landing loads during the preliminary design. This contributes to the goal of a thorough design.
- To enable the use of new methods, the Loads Kernel software is developed. It allows for greater flexibility and deviation from standard procedures offered in commercial products. In addition, both the user and developer gain a much deeper insight into the loads process and detailed, custom analyses are possible.

To reflect its focus, this thesis is **structured as follows**:

In Section 2, the theoretical foundation for flight loads calculation is presented. The technical studies are performed at the example of the MULDICON (presented in Section 3.1), which is a very suitable example for a flying wing of low aspect ratio. The configuration is the result of a multi disciplinary optimization and many disciples were involved. Thus, the design is rather

sophisticated and advanced and much data is available and has been published. The parametric aeroelastic models that are developed for this thesis are presented in Section 3. A structural optimization is conducted to create a baseline configuration. The resulting model presents an answer to requirement number I from Section 1.1.

The physical effects of an open loop gust encounter are studied at the example of the MULDICON in Section 4.1. General validity is demonstrated with the help of a (much larger) BWB configuration in Section 4.2. The closed loop gust encounter is investigated in a two-step approach. First, the design and application of a controller for marginally stable configurations is described in Section 5.1 and the influence on the design is investigated in Section 5.2. In a second step, the exercise is repeated for a naturally unstable configuration in Section 5.3. The influence on the design in terms of structural weight and loading is evaluated in Section 5.4.

The influence of CFD based maneuver loads are studied in Section 6. The technical details of various methods are discussed in Section 6.1 and a CFD solution scheme is selected. Differences and similarities between the VLM and CFD based are discussed at the example of a horizontal level flight, first at low speed (Section 6.2), then at high speed (Section 6.3). In a next step in Section 6.4, all maneuver load cases are considered. The influence on the design in terms of structural weight and loading is evaluated in Section 6.5.

A summary and an outlook is given in Section 7.

2 Theoretical Foundation for Flight Loads

2.1 Coordinate Systems

In this section, a brief description of the coordinate systems and coordinate transformation is given. Only the principal coordinate systems that are important for the understanding of this work are shown. More detailed information is given in most books on flight dynamics such as by Cook [27], Chapter 2 or by Brockhaus et al. [18], also Chapter 2.

Most information related to mass and structure is exported from an external program, in this case MSC.Nastran, and is usually given in a global, structural coordinate system 'g'. In most cases, the origin is in front of the aircraft and axes orientation is “rear-right-up” as sketched in Figure 2.1. In addition, a body fixed coordinate system 'b' with the same orientation is placed with its origin at the center of gravity CG. That system will be used for example in Section

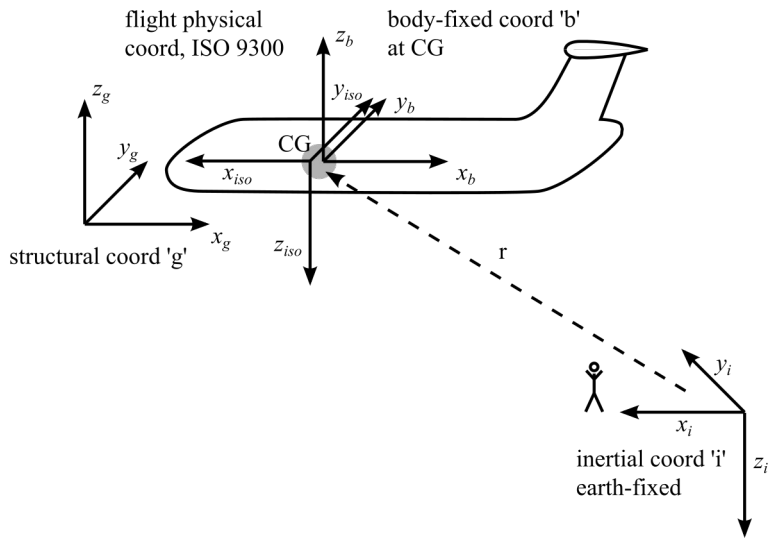

Figure 2.1: Overview of principal coordinate systems for a free-flying aircraft

2.5 for the equations of motion. The transformation between sets, such as 'g' and 'b', can be accomplished using splining methods as described in Section 2.3. The flight physical coordinate system is also placed at CG but with a “front-right-down” orientation. Finally, an earth-fixed coordinate system 'i' is used as a reference frame for the free-flying aircraft. To a certain extend and for small angles, splining methods might be used for these coordinate transformations as well. However, for the free-flying aircraft, angles can be large, and non-linear transformations need to be applied.

A transformation of velocities $[\dot{x}, \dot{y}, \dot{z}]^T$ from the earth fixed inertial coordinate system 'i' into the flight physical coordinate system according to ISO 9300 (see Brockhaus et al. [19]) is achieved by successive rotation of the Euler angles Φ, Θ and Ψ about the axis x, y, and z respectively

$$\begin{bmatrix} u \\ v \\ w \end{bmatrix} = \mathbf{D} \cdot \begin{bmatrix} \dot{x} \\ \dot{y} \\ \dot{z} \end{bmatrix} \tag{2.1}$$

using the direction cosine matrix $\mathbf{D}$

$$\mathbf{D} = \begin{bmatrix} 1 & 0 & 0 \\ 0 & cos(\Phi), & sin(\Phi) \\ 0 & -sin(\Phi) & cos(\Phi) \end{bmatrix} \cdot \begin{bmatrix} cos(\Theta) & 0 & -sin(\Theta) \\ 0 & 1 & 0 \\ sin(\Theta) & 0 & cos(\Theta) \end{bmatrix} \cdot \begin{bmatrix} cos(\Psi) & sin(\Psi) & 0 \\ -sin(\Psi) & cos(\Psi) & 0 \\ 0 & 0 & 1 \end{bmatrix} . \tag{2.2}$$

A transformation of angular rates $[\dot{\Phi}, \dot{\Theta}, \dot{\Psi}]^T$ from the earth fixed inertial coordinate system 'i' into the flight physical coordinate system

$$\begin{bmatrix} p \\ q \\ r \end{bmatrix} = \mathbf{D}_{\text{angular}} \cdot \begin{bmatrix} \dot{\Phi} \\ \dot{\Theta} \\ \dot{\Psi} \end{bmatrix} \tag{2.3}$$

is achieved using matrix

$$\mathbf{D}_{\text{angular}} = \begin{bmatrix} 1 & 0 & -sin(\theta) \\ 0 & cos(\Phi) & sin(\Phi)cos(\Theta) \\ 0 & -sin(\Phi) & cos(\Phi)cos(\Theta) \end{bmatrix} . \tag{2.4}$$

For a transformation in opposite direction, the inverse of $\mathbf{D}$ is given by

$$\mathbf{D}^{-1} = \mathbf{D}^T \tag{2.5}$$

and the inverse of $\mathbf{D}_{\text{angular}}$ is given by

$$\mathbf{D}_{\text{angular}}^{-1} = \begin{bmatrix} 1 & sin(\Phi)tan(\Theta) & cos(\Phi)tan(\theta) \\ 0 & cos(\Phi) & -sin(\Phi) \\ 0 & sin(\Phi)/cos(\Theta) & cos(\Phi)/cos(\Theta) \end{bmatrix} . \tag{2.6}$$

Note that due to the trigonometric functions singularities may occur, for example if Φ or Θ approach $\pm 90°$. However, this is not the case for most flight maneuvers relevant for loads simulation. These singularities could be avoided by using quaternions instead of Euler angles for the rotations in three dimensional space.

2.2 Steady and Unsteady Aerodynamics

The classical aerodynamic approach using a steady Vortex Lattice Method (VLM) and an unsteady Doublet Lattice Method (DLM) is chosen in this work. The formulation of the VLM used and described herein follows closely the derivation given by Katz and Plotkin [77] using horse shoe vortices. The DLM is formulated as presented by Albano and Rodden [2]. It should be mentioned that the origins of compressible, unsteady aerodynamic theories date back to the early 1940s when for example Küssner published his General Airfoil Theory [97], referring again to Prandtl [145] who introduced the theory of a lifting surface based on potential accelerations instead of velocity fields in 1936. The translation of Küssners work into English language by NACA [98], shows that the development of the DLM was an international effort with contributions of scientists from multiple nations. At the time of formulation, its solution was only possible for some special cases and it took three decades until, in the late 1960s, Albano and Rodden had the computational power available for a general, numerical solution applicable to arbitrary three-dimensional wings. Therefore, Albano and Rodden didn't actually invent the DLM but were those bright minds who properly implemented the DLM for the first time. For further reading, a historical overview is given by R. Voss [210] and a very comprehensive work on the mathematical background is published by Blair [11].

An implementation of the DLM in Matlab is publicly available from Kotikalpudi [88,89]. That version is translated into the python language for performance and independence from commercial licenses. In a next step, it is slightly adapted to respect the dihedral of the wings, and the Prandtl-Glauert transformation with $\beta = \sqrt{(1 - Ma^2)}$ is applied to the VLM as

suggested by Hedman [64]. In addition, the computational process is split into more sub-functions to allow for the extraction of matrices at different stages, e.g. to obtain the circulation matrix $\mathbf{\Gamma}$ and the $\mathbf{AIC}$ matrices for both lift and drag.

Both the VLM and the DLM are based on a matrix of aerodynamic influence coefficients $\mathbf{AIC}$, which depends on the Mach number Ma, the reduced frequency k defined by

$$k = \frac{c_{ref}}{2V} \cdot \omega \tag{2.7}$$

and the geometry of the aircraft. The geometry is discretized using an aerodynamic panel mesh as sketched in Figure 2.2. The $\mathbf{AIC}$ matrix then relates an induced downwash $\mathbf{w}_j$ on each aerodynamic panel to a circulation strength Γ_j, which is translated to a complex pressure coefficient c_p.

$$\mathbf{\Delta c_p} = \mathbf{AIC}(Ma, k) \cdot \mathbf{w}_j \tag{2.8}$$

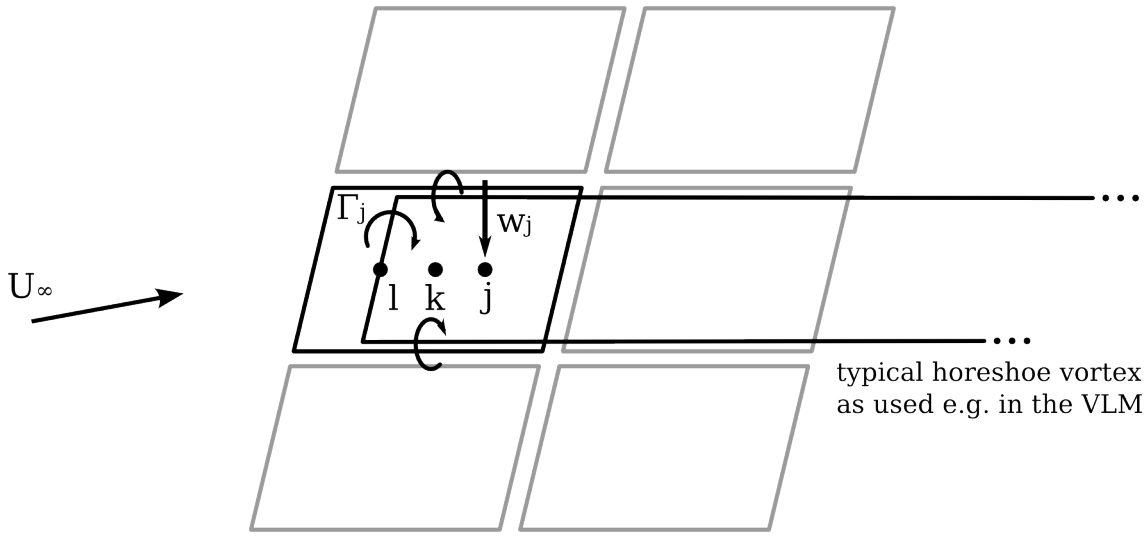

Figure 2.2: The geometrical mesh for aerodynamic panel methods

With $k = 0$ for the quasi static case, the solution of the DLM is equivalent to the VLM [161]. The calculation of the steady aerodynamic forces is given by

$$\begin{aligned}\mathbf{p}_k^{\text{aero,steady}} = q_\infty \cdot \mathbf{S}_{kj} \cdot \mathbf{AIC}^{\text{steady}} \cdot \big(&\mathbf{w}_{j,\text{rbm}} + \mathbf{w}_{j,\text{cs}} \\ &+ \mathbf{w}_{j,uf} + \mathbf{w}_{j,\dot{u}f} + \mathbf{w}_{j,\text{cam}} \big)\end{aligned} \tag{2.9}$$

q_∞	dynamic pressure
$\mathbf{S}_{kj}$	aerodynamic integration matrix
$\mathbf{AIC}$	AIC-matrix
$\mathbf{w}_{j,\mathrm{rbm}}$	downwash due to rigid body motion
$\mathbf{w}_{j,\mathrm{cs}}$	downwash due to control surface deflections
$\mathbf{w}_{j,uf}$	downwash due to flexible structural deformation
$\mathbf{w}_{j,\dot{u}f}$	downwash due to flexible structural motion
$\mathbf{w}_{j,\mathrm{cam}}$	downwash due to camber and twist of the profiles

containing several sources of aerodynamic forces. For the steady aerodynamics, the downwash due to rigid body motion $\mathbf{w}_{j,\mathrm{rbm}}$, due to control surface deflections $\mathbf{w}_{j,\mathrm{cs}}$, due to flexible structural deformation $\mathbf{w}_{j,uf}$ and due to flexible structural motion $\mathbf{w}_{j,\dot{u}f}$ is calculated from the onflow and the aircraft motions. Camber and twist of the profiles create an additional offset in downwash which is accounted for by the term $\mathbf{w}_{j,\mathrm{cam}}$. Note that the aerodynamic grid remains undeformed and the aerodynamic forces are modeled by changing the induced downwash for every panel. Using an AIC-matrix approach leads to a local pressure distribution which is integrated using matrix $\mathbf{S}_{kj}$. As the AIC-matrix is normalized with the dynamic pressure q_∞, the resulting loads need to be multiplied with q_∞ to obtain forces and moments. In this implementation, forces from the different sources given in equation (2.9) are calculated independently and superimposed

$$\mathbf{p}_k^{\mathrm{aero,steady}} = \mathbf{p}_k^{\mathrm{aero,rbm}} + \mathbf{p}_k^{\mathrm{aero,cs}} + \mathbf{p}_k^{\mathrm{aero,flex}} + \mathbf{p}_k^{\mathrm{aero,cam}} \quad , \tag{2.10}$$

which is possible due to linearity.

For dynamic gust analyses, two additional components $\mathbf{p}_k^{\mathrm{aero,gust}}$ and $\mathbf{p}_k^{\mathrm{aero,unsteady}}$ are added to the steady aerodynamic forces

$$\mathbf{p}_k^{\mathrm{aero}} = \mathbf{p}_k^{\mathrm{aero,steady}} + \mathbf{p}_k^{\mathrm{aero,gust}} + \mathbf{p}_k^{\mathrm{aero,unsteady}}. \tag{2.11}$$

Term $\mathbf{p}_k^{\mathrm{aero,gust}}$ represents the aerodynamic forces due to the gust acting on the aircraft. Because the gust induced downwash is applied to every panel individually, penetration effects are taken into account. Note that this is a very generic approach and allows for arbitrary gust fields. In this work, the gust velocity

$$U = \frac{U_{ds}}{2}\left[1 - cos\left(\frac{\pi s}{H}\right)\right] \quad for \quad 0 \leq s \leq 2H \tag{2.12}$$

is defined by the certification specifications CS 25.341 [46] in dependence of the distance s penetrated into the gust and the design gust velocity U_{ds}. The so-called gust gradient H determines the length (parallel to the aircraft's flight path) for the gust to reach its peak velocity.

Because the gust encounter is a very short and sudden event, the certification specifications explicitly ask to account for unsteady aerodynamic characteristics. In this work, unsteady aerodynamic forces in the time domain are obtained by a rational function approximation (RFA) as suggested by Roger [163]. Similar implementations are shown by various authors. From all authors, Gupta [55] gives the most detailed description. The work by Kier and Looye [80] points out the features of the “physical RFA”. Karpel and Strul [76] have a slightly different focus (minimizing the number of states of the RFA) but give an overview on possible constraints. Other publications making use of the RFA are by Goggin [53], Abel [1] and Vepa [199]. A difference of this work with respect to other authors is the approximation on panel level using physical coordinates. This leads to a large number of lag states but the implementation is more generic and leads to physical, nodal forces. This is required in order to use the force summation method, which will be explained in Section 2.5. In other works, so-called gust-modes are used that include all panels in one row. This is more difficult with highly swept flying wing configurations. In addition, these gust-modes have shown difficulties in the approximation due to a spiraling nature of the transfer function in the complex plane, see for example Figure 9 in [213]. Finding a good approximation of the gust-modes is still a field of research [213].

In the RFA, the $\mathbf{AIC}$ matrix is approximated for each reduced frequency k with the following rational function:

$$\mathbf{AIC}(k_{\mathrm{red}}) = \mathbf{A}_0 + \mathbf{A}_1 \cdot ik + \mathbf{A}_2 \cdot (ik)^2 + \sum_{n=1}^{n_{\mathrm{poles}}} \mathbf{A}_{n+2} \cdot \frac{ik}{ik + \beta_n} \ . \tag{2.13}$$

The approximation is done by solving the equation (2.13) in a least squares sense. Matrix $\mathbf{A}_2$ is omitted during the approximation, as suggested by Kier and Looye [80]. In addition, it is necessary to separate into real and imaginary parts. This is possible with

$$\frac{ik}{ik + \beta_n} = \frac{k^2}{k^2 + \beta_n^2} + \frac{ik\beta_n}{k^2 + \beta_n^2} \ . \tag{2.14}$$

In this work, the poles $\boldsymbol{\beta}_n$ used for the approximation are determined by

$$\boldsymbol{\beta}_n = \frac{\mathbf{k}_{\max}}{n} \tag{2.15}$$

as given by Roger [163]. A slightly different proposal is given by ZONA [225]. Both methods were tested and showed comparable results. In addition to the number of poles n_{poles}, the frequency range and frequency distribution is important. It is recommended to provide many samples close to zero with an increasing step size up to the highest reduced frequency $k_{\max}$. Typical value for the reduced frequency are $k_{\max} = 2.0$ with $n_{\text{poles}} = 6 \ldots 9$, but the actual values strongly depend on the aircraft configuration.

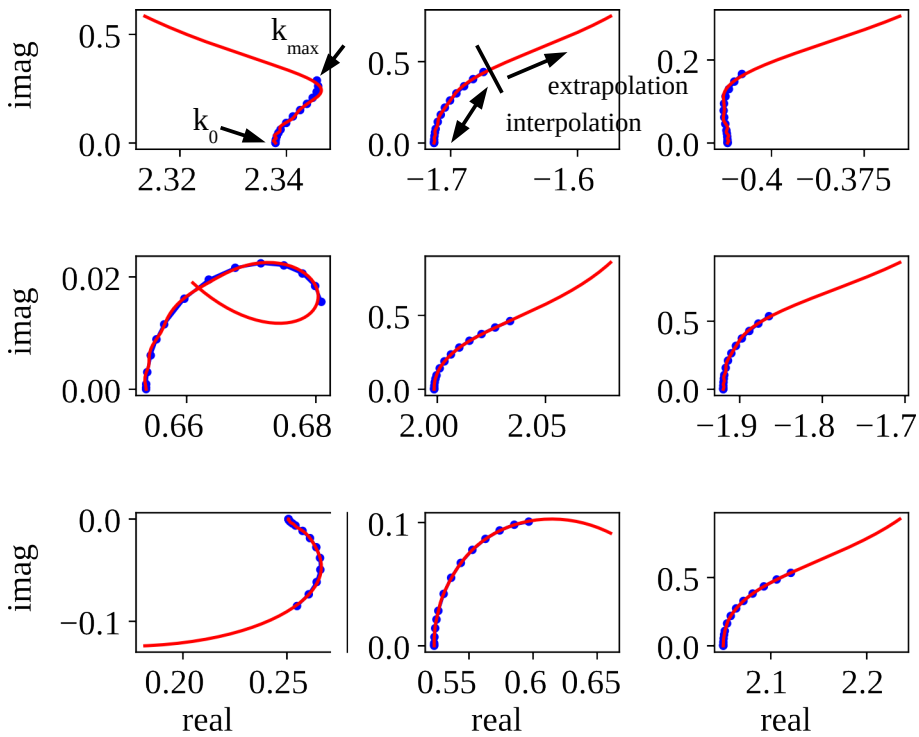

Figure 2.3: Real and imaginary parts of the first 3x3 entries of an AIC matrix (blue dots) and approximation (red line)

However, there is no general rule and the quality of the approximation has to be checked carefully, because too few poles result in a bad approximation, leading to nonphysical results. Figure 2.3 shows the real and imaginary parts of the first 3x3 entries of the $\mathbf{AIC}$ matrices and allows for a qualitative assessment of the approximation. Every blue dot marks the values of one given reduced frequency k. The red line is calculated from the approximation. In this case, the approximation looks good by visual judgment in the area covered by the given reduced frequencies. In addition, an extrapolation is shown. Here, the results are questionable in some cases. As a consequence, the given reduced frequencies should cover the complete

range of application and an extrapolation should be avoided. A quantitative assessment is possible by calculating the root mean squared error E_{RMS} of the given and the approximated matrices at the given frequencies

$$E_{\mathrm{RMS}}(k) = \sqrt{\frac{1}{n_j^2} \sum_{j=1}^{n_j^2} \left(\mathbf{AIC}(k)_{jj,\mathrm{approx}} - \mathbf{AIC}(k)_{jj,\mathrm{given}}\right)^2} \ . \tag{2.16}$$

For typical configurations, the root mean squared error E_{RMS} should drop below $10^{-2} \ldots 10^{-4}$ for all reduced frequencies.

With $s = i \cdot \omega$ and k defined in equation (2.7), ik may be written as

$$ik = i \cdot \frac{c_{\mathrm{ref}}}{2V} \cdot \omega = \left(\frac{c_{\mathrm{ref}}}{2V}\right) s \ . \tag{2.17}$$

Equation (2.13) is expanded to

$$\begin{aligned} \mathbf{p}_k^{\mathrm{aero}}(s) = q_\infty \cdot \mathbf{S}_{kj} \cdot w_j \cdot \Big[\mathbf{A}_0 + \mathbf{A}_1 \cdot \left(\frac{c_{\mathrm{ref}}}{2V}\right) s + \mathbf{A}_2 \cdot \left(\left(\frac{c_{\mathrm{ref}}}{2V}\right) s\right)^2 \\ + \sum_{n=1}^{n_{\mathrm{poles}}} \mathbf{A}_{n+2} \cdot \frac{\left(\frac{c_{\mathrm{ref}}}{2V}\right) s}{\left(\frac{c_{\mathrm{ref}}}{2V}\right) s + \beta_n} \Bigg] \ . \end{aligned} \tag{2.18}$$

Transformation from the Laplace domain into the time domain leads to

$$\begin{aligned} \mathbf{p}_k^{\mathrm{aero}}(t) = q_\infty \cdot \mathbf{S}_{kj} \cdot \Big[\mathbf{A}_0 \mathbf{w}_j + \mathbf{A}_1 \left(\frac{c_{\mathrm{ref}}}{2V}\right) \dot{\mathbf{w}}_j + \mathbf{A}_2 \left(\frac{c_{\mathrm{ref}}}{2V}\right)^2 \ddot{\mathbf{w}}_j \\ + \sum_{n=1}^{n_{\mathrm{poles}}} \mathbf{A}_{n+2} \cdot \mathbf{lag}_n \Bigg] \ . \end{aligned} \tag{2.19}$$

The lag states $\mathbf{lag}_n$ are defined as

$$\mathbf{lag}_n = \frac{s}{s + \frac{2V}{c_{\mathrm{ref}}} \beta_n} \cdot \mathbf{w}_j \tag{2.20}$$

or

$$\mathbf{lag}_n \cdot s = \mathbf{w}_j \cdot s - \left(\frac{2V}{c_{\mathrm{ref}}}\right) \boldsymbol{\beta}_n \cdot \mathbf{lag} \tag{2.21}$$

in the Laplace domain. Transformation into the time domain yields

$$\dot{\mathbf{lag}}_n = \dot{\mathbf{w}}_j - \left(\frac{2V}{c_{\mathrm{ref}}}\right) \cdot \boldsymbol{\beta}_n \cdot \mathbf{lag}_n \ . \tag{2.22}$$

It can be seen that the evolution of the lag states is described by a differential equation, which can be solved independently or simply appended to the system of equations which will be described in Section 2.5.

From equation (2.19) it can the seen that a rational function approximation allows for a decomposition of the aerodynamic forces into a steady term $\mathbf{A}_0$ depending on the downwash $\mathbf{w}_j$, corresponding to equation (2.10), a damping term $\mathbf{A}_1$ depending on the rate of change of the downwash $\dot{\mathbf{w}}_j$ and a term $\mathbf{A}_2$ depending on the acceleration of the downwash $\ddot{\mathbf{w}}_j$. Because $\ddot{\mathbf{w}}_j$ is difficult to calculate, it is omitted in the approximation step. The unsteady terms $\mathbf{A}_3, \mathbf{A}_4, \ldots, \mathbf{A}_{n+2}$ depend on the lag states $\mathbf{lag}_1, \mathbf{lag}_2, \ldots, \mathbf{lag}_n$. As the time simulation usually starts from an initial steady level flight, the lag states are assumed to be zero at the beginning.

Drag is neglected by most commercial software packages and has little direct influence on the loads. In addition, wing structures are typically sized by the shear force F_z, bending moment M_x or torsional moment M_y. However, the local induced drag is important to capture the roll-yaw-coupling of the aircraft. (Note that there are also other contributors to the roll-yaw-coupling, e.g. profile drag, which is not considered at this point.) Thus, the induced drag might have an indirect influence on the loads. Therefore, the VLM is extended. The standard procedure described above involves a linearization about an angle of attack $\alpha = 0°$, resulting in a lift vector orthogonal to the body frame but not orthogonal to the onflow for angles of attack $\alpha \neq 0°$. This would result in an artificial drag component depending on the angle of attack α, which is not desired. This can be avoided by selecting a slightly different formulation of the VLM

$$\mathbf{p}_k^{\mathrm{aero,steady,nonlin}} = \mathbf{\Phi}_{lk} \cdot \rho \cdot \mathbf{\Gamma} \cdot \mathbf{w}_j \cdot (\mathbf{q} \times \mathbf{r}) \ . \tag{2.23}$$

The induced downwash w_j on each aerodynamic panel is multiplied with the circulation matrix $\mathbf{\Gamma}$ obtained from the VLM. The cross product of the onflow vector $\mathbf{q}$ and the panel span vector $\mathbf{r}$ at quarter chord yield a lift vector orthogonal to the onflow condition. Multiplication with the air density ρ and translation matrix $\mathbf{\Phi}_{lk}$ gives the aerodynamic forces $\mathbf{p}_k^{\mathrm{aero,steady,nonlin}}$. The induced downwash $\mathbf{w}_j$ is calculated in the same way as before, allowing for a smooth integration into the existing code.

In a flow field, the Trefftz plane located at an infinite distance downstream of the aircraft may be used to analyze the wake in order to obtain the total induced drag C_d^{ind}. In a similar manner, the wake $\mathbf{w}_j^{\mathrm{wake}}$ of every panel, defined by the trailing vortices of the horseshoe, may be used to calculate the local induced drag $\mathbf{c}_{dj}^{\mathrm{ind}}$ at every panel. Formally, this can be expressed with matrix $\mathbf{B}_{jj}$ (similar to the $\mathbf{AIC}$ matrix but only for the trailing vortices) and $\mathbf{c}_{pj}$ from equation (2.8), which gives the downwash of the wake

$$\mathbf{w}_j^{\mathrm{wake}} = -\mathbf{B}_{jj} \cdot \mathbf{c}_{pj}, \tag{2.24}$$

and the downwash leads to the induced drag

$$\mathbf{c}_{dj}^{\mathrm{ind}} = \mathbf{w}_j^{\mathrm{wake}} \cdot \mathbf{c}_{pj}. \tag{2.25}$$

The calculated induced drag can be compared to the theoretically lowest induced drag for planar wings based on an elliptical lift distribution. Division of theoretical and calculated induced drag yields the span efficiency value e

$$e = \frac{C_l^2}{\pi \Lambda C_d^{\mathrm{ind}}}\,, \tag{2.26}$$

which should be close to $e = 1.0$.

To maintain compatibility of the formulation of the the VLM with the DLM, in this work the linearization about an angle of attack $\alpha = 0°$ is used. Also, the formulation of the induced drag is not compatible to the DLM. An application where both effects are important is shown in [207,208] at the example of a sailplane. That work was prepared using the same methods and tools but is not part of this thesis.

2.3 Aero-Structural Coupling

In a next step step, the aerodynamic forces need to be applied to the structure. Formally, the coupling can be handled using a transformation matrix $\mathbf{T}_{kf}$ which relates displacements of the structural grid $\mathbf{u}_f$ to displacements of the aerodynamic grid $\mathbf{u}_k$ with

$$\mathbf{u}_k = \mathbf{T}_{kf} \cdot \mathbf{u}_f. \tag{2.27}$$

In addition, the transposed matrix $\mathbf{T}_{kf}^T$ transfers forces and moments from the aerodynamic grid $\mathbf{p}_k$ to the structural grid $\mathbf{p}_f$ with

$$\mathbf{p}_f = \mathbf{T}_{kf}^T \cdot \mathbf{p}_k. \tag{2.28}$$

Note that the structural displacements and loads (index 'f') are not given in physical but in modal coordinates, which will be explained in more detail in Section 2.4. The size of the problem depends on the degrees of freedom of both the aerodynamic and structural grid. In this case, the structural grid has a much finer discretization with 34482 degrees of freedom. Therefore, a projection into modal coordinates in combination with a truncation of higher frequency modes implies a significant reduction.

In general, a transformation matrix $\mathbf{T}_{di}$ may be defined by various methods [206]. One commonly used approach for loads calculation is the **rigid body spline**. Each grid point of the dependent grid is mapped to exactly one point on the independent grid. The distance $\mathbf{d} = [d_x, d_y, d_z]^T$ between these two grid points is assumed as a rigid body that transfers forces and moments. In addition, forces $\mathbf{f}$ create moments $\mathbf{m}$ due to their lever arm

$$\mathbf{m} = \mathbf{d} \times \mathbf{f}. \tag{2.29}$$

In reverse, translations and rotations are directly transferred and rotations create additional translations. For one set of two points, this can be expressed by matrix $\mathbf{T}_{di}^\star$ with

$$\mathbf{T}_{di}^\star = \begin{bmatrix} 1 & & & & d_z & d_y \\ & 1 & & -d_z & & d_x \\ & & 1 & -d_y & d_x & \\ & & & 1 & & \\ & & & & 1 & \\ & & & & & 1 \end{bmatrix}. \tag{2.30}$$

The mapping of the points may be defined manually or automatically, e.g. with a nearest neighbor search. This concept is quite versatile and can be used for many application other than the aero-structural coupling, e.g. to gather all external forces $\mathbf{p}_g^{\text{ext}}$ at the center of gravity $\mathbf{p}_b^{\text{ext}}$

$$\mathbf{p}_b^{\text{ext}} = \mathbf{T}_{bg}^T \cdot \mathbf{p}_g^{\text{ext}}. \tag{2.31}$$

Another widely used method are **radial basis functions**. A very good example is given by Neumann and Krüger [128] who show the application to large, industrial scale models. The method is best visualized by a curve running through a number of supporting points. At the supporting points, the results are exact. For the values in-between, the results are approximated. The approximation is influenced by the neighboring supporting points which

are weighted according to their distance to the approximation point. Although the influence reduces over the distance, every supporting point has an influence on all other points. This influence is calculated with the help of radial basis functions. A popular example is the Infinite Plate Spline (IPS) by Harder and Desmarais [61] which uses

$$\phi(\|d\|) = \|d\|^2 \cdot log(\|d\|) \tag{2.32}$$

as a function for the influence ϕ. Beckert and Wendland [8] have compared and investigated various radial basis functions as an alternative to equation (2.32). Some radial basis functions provide a compact support radius, limiting the influence to a local area. However, Neumann [127] showed that local radial basis functions are likely to results in crinkled surfaces, which is not beneficial. Therefore, in this work only globally supported radial basis functions will be applied. Finally, the spline can be constructed as a surface spline where only two dimensions are considered. An extension by the third dimension leads to a volume spline.

Advantages and disadvantages with respect to flying wing configurations have been discussed by Voß and Klimmek [206] and are summarized in Tables 2.1 and 2.2. The rigid body spline allows for a clear and comprehensible mapping of the aerodynamic grid to the structure. Due to the direct mapping of the rigid body spline, matrix $\mathbf{T}_{di}$ is sparse while $\mathbf{T}_{di}$ is dense when using a global surface or volume spline. To construct a surface or volume spline, a system of equations needs to be solved. This results in longer computational time in comparison to the rigid body spline. Although globally correct, a surface or volume spline may locally result in very large, opposing forces, which are not physical. This behavior has been observed when the number of structural grid points is much larger than the number of aerodynamic grid points. These large, local forces may change the magnitude of section loads significantly while the integral forces of the entire aircraft are correct. Therefore, the rigid body spline is more suitable for the transfer of forces and moments. In contrast, a surface spline is more suitable for smooth surface deformation whereas a rigid body spline usually results in bad and bumpy surface deformations. This is acceptable when using aerodynamic panel methods such as VLM or DLM, but may have a fatal impact on CFD simulations.

advantages	disadvantages
• clear and comprehensible mapping • forces and moments are conserved • forces and moments normally act on the proper structural element (e.g. intersection between wing and control surface, intersection between fuselage and wing) • use of different coordinate systems possible • fast	• possibly high nodal forces • possibly uneven/bumpy surface deformation (fatal impact on CFD simulation)

Table 2.1: Advantages and disadvantages of rigid body splines

advantages	disadvantages
• high quality surface deformation • forces are distributed evenly on the structure	• slow for large problems • splining should be conducted separately for each structural part • locally unphysical, possible problems in section forces

Table 2.2: Advantages and disadvantages of surface and volume splines

2.4 Full FEM for Loads: Modal Analysis, Structural Degrees of Freedom and Masses

The degrees of freedom for a grid point of a finite element model (FEM) include the six components of displacement: translation in x, y, and z direction and rotation about the x, y, and z axis. In MSC.Nastran, these degrees of freedom are organized in so-called sets [228]. The relation of the most relevant sets for this work is shown in Figure 2.4. The global set, or

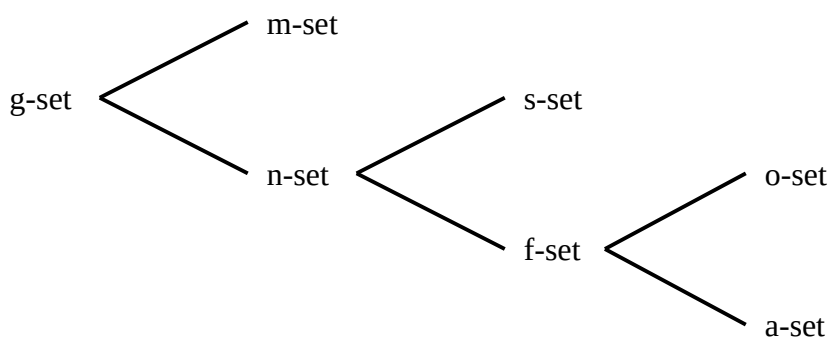

Figure 2.4: Schematic overview of structural sets

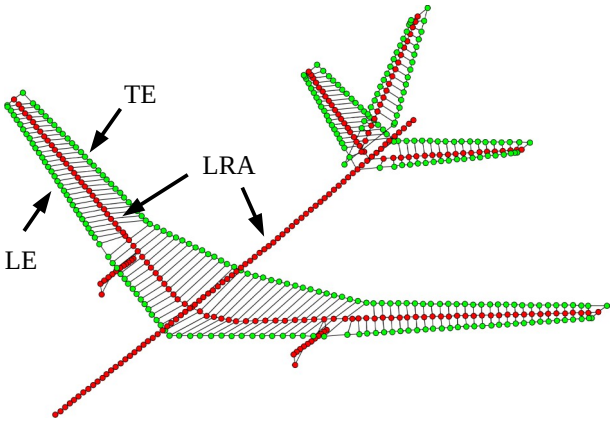

Figure 2.5: Condensed finite element model of the FERMAT configuration [84]

g-set, contains all degrees of freedom and is the top-level set. Usually, the g-set contains linear relationships, which are for example constructed with rigid body elements and multipoint constraints. These dependent degrees of freedom are moved into the m-set. The remaining, independent degrees of freedom form the n-set. Sometimes, a structural model contains single point constraints, for example to realize a clamping. These degrees of freedom are moved into the s-set. The remaining degrees of freedom are organized in the f-set. Therefore, the f-set contains all “free” degrees of freedom, the corresponding mass and stiffness matrices $\mathbf{K}$ and $\mathbf{M}$ are no longer singular and suitable for a solution if arranged in a set of equations.

Finally, the f-set may be partitioned into the a-set and the o-set. This process can be achieved by a static condensation or Guyan reduction [56]. In aeroelastic applications, the wing and fuselage structure is often condensed to a loads reference axis (LRA). The loads reference axis is placed e.g. along the quarter chord line of the wing. A typical example is shown in Figure 2.5. Note that the points of the leading and trailing edge (LE and TE, green points) are connected with rigid body elements to the loads reference axis. The concept of a loads reference axis has several advantages. First, the model is simplified significantly, making physical interpretations easier. Second, mass estimates are often done by a different department than the structural analysis. The loads reference axis is a suitable basis for communication and data exchange, as condensed masses can be easily attached to the condensed structural grid points. Third, computational time is reduced for all following calculations. However, considering the available computational power of today, this argument is no longer relevant. Finally, local modes are avoided during the modal analysis. Such local

modes appear if for example a thin shell element vibrates at a low frequency. Using a condensation, the model is “cleaned” from such local modes.

Remark: Technically, there is no such thing as a “cleaning” procedure. The spatial resolution of the structural model is reduced so much that local modes are not resolved by a sufficient number of points. Only global mode shapes can be represented.

The partitioning of the f-set into the a-set and the o-set is achieved in the following way. The equation for static deflection

$$\mathbf{K} \cdot \mathbf{u} = \mathbf{p} \tag{2.33}$$

relating forces $\mathbf{p}$ to stiffness matrix $\mathbf{K}$ times deflections $\mathbf{u}$ can be rearranged to

$$\begin{bmatrix} \mathbf{K}_{aa} & \mathbf{K}_{ao} \\ \mathbf{K}_{oa} & \mathbf{K}_{oo} \end{bmatrix} \cdot \begin{pmatrix} \mathbf{u}_a \\ \mathbf{u}_o \end{pmatrix} = \begin{pmatrix} \mathbf{p}_a \\ \mathbf{p}_o \end{pmatrix} \tag{2.34}$$

according to Guyan [56]. Here, the degrees of freedom with index 'o' are those to which no force is applied to and which can be eliminated. With $\mathbf{p}_0 = 0$, the equations are solved to

$$\left[\mathbf{K}_{aa} - \mathbf{K}_{ao} \cdot \mathbf{K}_{oo}^{-}1 \cdot \mathbf{K}_{oa}\right] \cdot (\mathbf{u}_a) = (\mathbf{p}_a). \tag{2.35}$$

From this, the reduced stiffness matrix $\mathbf{K}_{aa,\text{reduced}}$ is identified as

$$\mathbf{K}_{aa,\text{reduced}} = \mathbf{K}_{aa} - \mathbf{K}_{ao} \cdot \mathbf{K}_{oo}^{-1} \cdot \mathbf{K}_{oa}. \tag{2.36}$$

Due to the analytical solution of the problem, the Guyan reduction of the stiffness matrix is exact.

The same procedure could be applied to the mass matrix $\mathbf{M}$, although the term $\mathbf{M}_{ao}$ is usually zero as mass matrices are usually diagonal. However, multiplication with $\mathbf{M}_{ao}$ would eliminate all masses of the o-set and only the masses on the a-set would remain. This problem is solved by Guyan by combining mass and stiffness matrices

$$\begin{aligned} \mathbf{M}_{aa,\text{reduced}} =& \mathbf{M}_{aa} - \mathbf{M}_{ao} \cdot \mathbf{K}_{oo}^{-1} \cdot \mathbf{K}_{oa} \\ & - (\mathbf{K}_{oo}^{-1} \cdot \mathbf{K}_{oa})^T \cdot (\mathbf{M}_{oa} - \mathbf{M}_{oo} \cdot \mathbf{K}_{oo}^{-1} \cdot \mathbf{K}_{oa}) \end{aligned} \tag{2.37}$$

to obtain a reduced mass matrix, too. The influence of the masses on the o-set is weighted with the stiffness. Guyan states that “the eigenvalue-eigenvector problem is closely but not exactly preserved” [56]. Comparison studies show that this is true for low frequencies. The

higher the frequency, the greater the deviation. Therefore, the Guyan reduction is suitable for typical aircraft configurations where mainly the first eigenvalues are of interest.

For convenience and to significantly improve computational performance, $\mathbf{K}_{oo}^{-1} \cdot \mathbf{K}_{oa}$ is written as

$$\mathbf{K}_{oo} \cdot \mathbf{G}_{oa} = \mathbf{K}_{oa} \tag{2.38}$$

and solved for $\mathbf{G}_{oa}$. This step has to be done only once, and, in addition, the solution of a sparse linear system $\mathbf{A} \cdot \mathbf{x} = \mathbf{b}$ is much faster than a matrix inversion.

A modal analysis comprises the characterization of the dynamic behavior of an elastic, vibrating system. The oscillating behavior of that system about an idle state is described by modal parameters such as natural frequency, mode shapes, modal mass and modal damping. The behavior of the undamped, unexcited system of mass $\mathbf{M}$ and stiffness $\mathbf{K}$ is governed by

$$\mathbf{M} \cdot \ddot{\mathbf{x}} + \mathbf{K} \cdot \mathbf{x} = 0, \tag{2.39}$$

which corresponds to

$$\omega^2 \cdot \mathbf{M} \cdot \hat{\mathbf{x}} + \mathbf{K} \cdot \hat{\mathbf{x}} = 0 \tag{2.40}$$

in the frequency domain. Damping is omitted at this step and added later in equation (2.47). The problem can be rearranged to the form of the generalized eigenvalue problem

$$-\mathbf{K} \cdot \hat{\mathbf{x}} = \omega^2 \cdot \mathbf{M} \cdot \hat{\mathbf{x}} \quad \text{or} \quad \mathbf{A} \cdot \mathbf{\Phi} = \boldsymbol{\lambda} \cdot \mathbf{B} \cdot \mathbf{\Phi}, \tag{2.41}$$

with $\mathbf{\Phi}$ being the matrix of generalized eigenvectors and $\boldsymbol{\lambda}$ the generalized eigenvalues of $\mathbf{A}$ and $\mathbf{B}$. For large matrices $\mathbf{A}$ and $\mathbf{B}$, which is usually the case in structural dynamics, the system is solved iteratively for the first n_f eigenvalues. In MSC.Nastran, the calculation of the real eigenvalues typically uses the Lanczos method, in Scipy an Arnoldi method is available [101,191]. Because matrices $\mathbf{M}$ and $\mathbf{K}$ are sparse, using the sparse eigenvalue analysis capability significantly increases performance. Both methods have been tested and return numerically equivalent eigenvalues $\boldsymbol{\lambda}$ for typical aircraft configurations. The eigenvectors $\mathbf{\Phi}$ are more difficult to compare. Here, the modal assurance criterion (MAC) [3] is a suitable means for comparison. Assuming two eigenvectors $\phi_a$and ϕ_b, the MAC value is calculated with

$$MAC = \frac{\left|\phi_a^T \phi_b\right|^2}{\left(\phi_a^T \phi_a\right)\left(\phi_b^T \phi_b\right)} \ , \tag{2.42}$$

resulting in a scalar value $MAC = 0.0 \ldots 1.0$ where a value of 1.0 indicates a perfect agreement of both eigenvectors. Applied to all combinations of eigenvectors, a matrix of MAC values is constructed.

The Auto-MAC with $\mathbf{\Phi}_a = \mathbf{\Phi}_b$ is shown in Figure 2.6. As expected, all values along the diagonal are very close to 1.0. The off-diagonal terms show very small values close to 0.0. The areas of weak correlation are due to the discretization of the numerical model. Figure 2.7 shows the MAC matrix comparing the eigenvectors obtained from MSC.Nastran SOL103 and Scipy for a typical aircraft configuration. It can be seen that the eigenvectors are numerically equal.

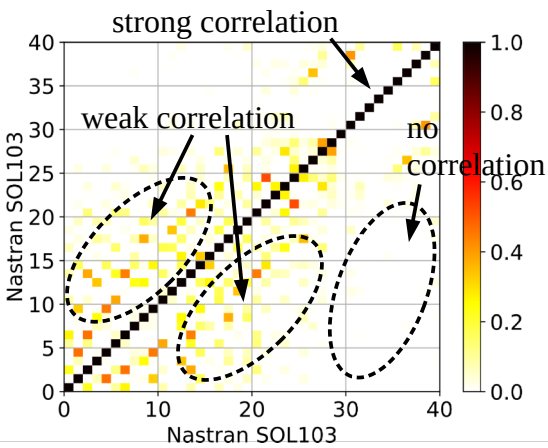

Figure 2.6: Auto MAC for the first 40 modes

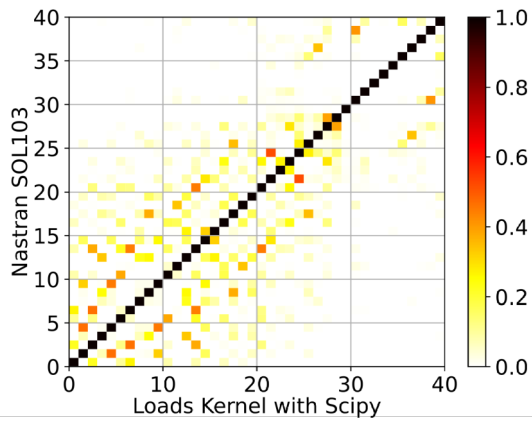

Figure 2.7: MAC matrix comparing MSC.Nastran SOL103 and Scipy

Assuming the modal analysis is conducted on the reduced a-set, the corresponding displacements of the remaining degrees of freedom $\mathbf{u}_o$, $\mathbf{u}_s$ and $\mathbf{u}_m$ need to be reconstructed from the eigenvectors. The displacements $\mathbf{u}_o$ of the o-set, see equation (2.34), may be reconstructed from the a-set with

$$\mathbf{u}_o = -\mathbf{K}_{oa} \cdot \mathbf{u}_a \cdot \mathbf{K}_{oo}^{-1}. \tag{2.43}$$

The s-set displacements $\mathbf{u}_s$ are set to zero. With this information, the displacements $\mathbf{u}_n$ of the n-set can be assembled. As mentioned at the beginning, the m-set is linearly dependent on the

n-set. Therefore, the displacements $\mathbf{u}_m$ of the m-set can be derived from $\mathbf{u}_n$ by applying matrix $\mathbf{GM}$ [124]

$$\mathbf{u}_m = \mathbf{GM} \cdot \mathbf{u}_n. \tag{2.44}$$

Following that procedure, the eigenvector $\mathbf{\Phi}_{gf}$ for all degrees of freedom of the g-set is assembled.

The benefit and the physical interpretation is the following. An eigenvalue analysis of a finite element model projects the dynamic deformation into a set of flexible modes. Because the resulting mode shapes are uncoupled, a superposition of several modes is possible. With $\omega^2 = \lambda$, the eigenvalue λ defines the angular frequency of the mode. The eigenvector $\mathbf{\Phi}$ contains the corresponding deflection in physical coordinates. In addition, eigenvector $\mathbf{\Phi}$ allows for the calculation of the modal stiffness and modal mass matrices $\mathbf{K}_{ff}$ and $\mathbf{M}_{ff}$ from the original matrices $\mathbf{K}_{aa}$ and $\mathbf{M}_{aa}$ in physical coordinates:

$$\mathbf{K}_{ff} = \mathbf{\Phi}^T \mathbf{K}_{aa} \mathbf{\Phi} \tag{2.45}$$

$$\mathbf{M}_{ff} = \mathbf{\Phi}^T \mathbf{M}_{aa} \mathbf{\Phi} \tag{2.46}$$

In absence of a more rational analysis, uniform modal damping [9]

$$\mathbf{D}_{ff} = \mathbf{I} \cdot \boldsymbol{\lambda}^2 \cdot 2.0 \cdot d \tag{2.47}$$

may be assumed with typical damping values ranging from $d = 0 \ldots 3.0\%$. For simplicity, in most academic works no damping is assumed.

Note that at this step, index 'f' refers to the flexible mode set obtained from modal analysis and not the f-set including the “free” degrees of freedom. This inconsistency exists because if no reduction is made and no degrees of freedom are omitted, the f-set is equivalent to the a-set. Therefore, the a-set is favored for calculation purposes and the f-set is rarely used.

The final challenge of the Guyan reduction lies in the determination of the degrees of freedom for the a-set. The LRA concept mentioned at the beginning of this section is a very good choice for classical wing-fuselage-empennage configurations but has its limits with planar flying wings of low aspect ration. Because of the low number of ribs, only very few points would be selected for the a-set. In addition, the resolution in chord direction is questionable and not representative, especially in the fuselage region. Therefore, a new selection scheme

for the a-set is required. The use of sub section corner points is a suitable answer to the above problem. One sub segment is the area between two ribs and two spars, as visualized in Figure 2.8. The identification of the corner points of every sub section leads to a satisfactory number of points distributed over the whole aircraft. For the MULDICON, see Section 3, 178 points or 1068 degrees of freedom are identified. In addition, only structurally significant points are selected. The o-set then consists of the remaining degrees of freedom.

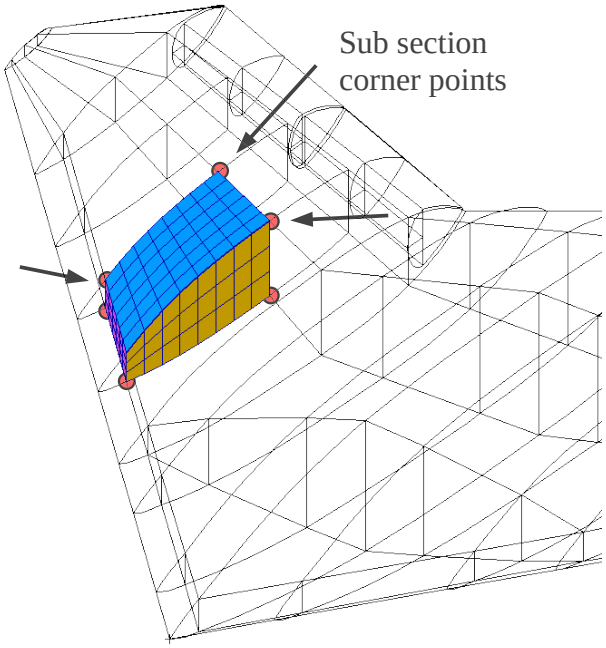

Figure 2.8: Selection of degrees of freedom of the a-set based of sub section corner points

With the assumption that low frequency modes are more important than higher frequency modes, a truncation is possible. The number of modes n_f to be kept should be selected in relation with the highest desired frequency $k_{\max}$. That frequency should be selected again in relation to the capabilities of the unsteady aerodynamics. If the system is analyzed in free-free conditions, the first six eigenvalues are characterized by $\lambda \approx 0.0$ and correspond to the rigid body motion of the system. They are discarded if only the flexible modes are required.

With the knowledge of the set definitions and a mass matrix M_{gg}, the total mass properties of the rigid body can be calculated. This is done in a two step approach. In the first step, all masses are gathered at a reference point 0 by applying Φ_{0g} and Φ_{0g}^T

$$\mathbf{M}_0 = \mathbf{\Phi}_{0g}^T \mathbf{M}_{gg} \mathbf{\Phi}_{0g} \ . \tag{2.48}$$

The resulting matrix M_0 has the shape 6x6 with the following entries of interest:

$$\mathbf{M}_0 = \begin{bmatrix} M_{xx} & & & & r_z M_{xx} & -r_y M_{xx} \\ & M_{yy} & & -r_z M_{yy} & & r_x M_{yy} \\ & & M_{zz} & r_y M_{zz} & -r_x M_{zz} & \\ & & & & \dots & \\ & & & & & \end{bmatrix} . \tag{2.49}$$

The finite element method theoretically allows for different mass properties in the directions x , y and z. Practically, this is usually not the case and leads to the assumption

$$M = M_{xx} = M_{yy} = M_{zz} \tag{2.50}$$

Therefore, the total aircraft mass M can be derived from the upper left corner of M_0. The upper right corner contains a coupling between translational and rotational mass terms in the form of rM. At the center of gravity, they should become zero. With this information, these terms can be used to establish the offset r_b of the center of gravity.

$$\mathbf{r}_b = [r_x Myy, r_y M_{zz}, r_z M_{xx}]^T / M \tag{2.51}$$

In the second step, the final rigid body mass matrix $\hat{\mathbf{M}}_b$ is calculated with respect to the body coordinate system 'b' located at the CG.

$$\hat{\mathbf{M}}_b = \begin{bmatrix} \mathbf{M}_b & \\ & \mathbf{I}_b \end{bmatrix} = \begin{bmatrix} M_{xx} & & & & & \\ & M_{yy} & & & & \\ & & M_{zz} & & & \\ & & & I_{xx} & I_{xy} & I_{xz} \\ & & & & I_{yy} & I_{yz} \\ & & & & & I_{zz} \end{bmatrix} \tag{2.52}$$

In the upper left corner, mass matrix $\mathbf{M}_b$ is given. In the lower right corner, the inertia matrix $\mathbf{I}_b$ is located, including moments of inertia I_{xx}, I_{yy} and I_{zz} about the the x, y and z axis of the body coordinate system 'b', plus some additional coupling terms I_{xy}, I_{xz} and I_{yz}. All remaining entries should become zero. Matrices $\mathbf{M}_b$ and $\mathbf{I}_b$ are important to calculate the rigid body motion of the aircraft, which is presented in the next section.

2.5 Equations of Motion

The motion of the aircraft is divided into a rigid and a flexible part. For the rigid body motion, the aircraft is considered as a point mass with inertia matrices $\mathbf{M}_b$ and $\mathbf{I}_b$, where the components of the inertia tensor $\mathbf{I}_b$ are calculated with respect to the body axes 'b'. Its origin is

positioned at the center of gravity. All external forces and moments $\mathbf{p}_g^{ext}$ are gathered at the same point. The non-linear equations of motion are given by

$$\dot{\mathbf{v}}_b = \mathbf{M}_b^{-1} \cdot \mathbf{p}_b^{\text{ext, forces}} + \mathbf{v}_b \times \boldsymbol{\omega}_b + \dot{\mathbf{v}}_b^{\text{grav}} \tag{2.53}$$

and

$$\dot{\boldsymbol{\omega}}_b = \mathbf{I}_b^{-1} \cdot \left(\mathbf{p}_b^{\text{ext, moments}} - \boldsymbol{\omega}_b \times (\mathbf{I}_b \cdot \boldsymbol{\omega}_b)\right) \tag{2.54}$$

yield the translational and rotational accelerations $\dot{\mathbf{v}}_b$ and $\dot{\boldsymbol{\omega}}_b$ of the aircraft body frame. The coupling terms between translation and rotation $\mathbf{v}_b \times \boldsymbol{\omega}_b$ and $\boldsymbol{\omega}_b \times (\mathbf{I}_b \cdot \boldsymbol{\omega}_b)$ are derived by Waszak, Schmidt and Buttrill [21,214,215]. Gravitational acceleration is accounted for by $\dot{\mathbf{v}}_b^{\text{grav}}$ in equation (2.53).

In addition to the rigid body motion of the aircraft, linear structural dynamics are incorporated by

$$\mathbf{M}_{ff}\ddot{\mathbf{u}}_f + \mathbf{D}_{ff}\dot{\mathbf{u}}_f + \mathbf{K}_{ff}\mathbf{u}_f = \mathbf{p}_f^{ext} \tag{2.55}$$

Here, generalized external forces $\mathbf{p}_f^{ext}$ interact with linear elastic deflections $\mathbf{u}_f$, velocities $\dot{\mathbf{u}}_f$ and accelerations $\ddot{\mathbf{u}}_f$. The matrices $\mathbf{M}_{ff}$, $\mathbf{D}_{ff}$ and $\mathbf{K}_{ff}$ refer to the generalized mass, damping, and stiffness matrices from equations (2.45) to (2.47) from Section 2.4.

2.6 System of Equations and Solution Schemes

The calculation of aerodynamic forces and the evaluation of the equation of motion described in the previous sections are transformed into a single set of coupled equations. For the solution of this system, it is convenient to convert the equations into a first order system:

$$\begin{pmatrix} \dot{\mathbf{u}}_i \\ \ddot{\mathbf{u}}_b \\ \dot{\mathbf{u}}_f \\ \ddot{\mathbf{u}}_f \\ \dot{\mathbf{u}}_{cs} \end{pmatrix} = \mathrm{f} \begin{pmatrix} \mathbf{u}_i \\ \dot{\mathbf{u}}_b \\ \mathbf{u}_f \\ \dot{\mathbf{u}}_f \\ \mathbf{u}_{cs} \end{pmatrix} . \tag{2.56}$$

The vector $\mathbf{u}_i$ contains the aircraft position and Euler angles $(x, y, z, \Phi, \Theta, \Psi)^T$ with respect to the earth-fixed frame 'i', vector $\dot{\mathbf{u}}_i$ describes the aircraft velocities and rates $(\dot{x}, \dot{y}, \dot{z}, \dot{\Phi}, \dot{\Theta}, \dot{\Psi})^T$. The vector $\dot{\mathbf{u}}_b$ contains the aircraft velocities and rates $(u, v, w, p, q, r)^T$ in

the body-fixed frame 'b', vector $\ddot{\mathbf{u}}_b$ the aircraft translational and rotational accelerations $(\dot{u}, \dot{v}, \dot{w}, \dot{p}, \dot{q}, \dot{r})^T$. Vector $\mathbf{u}_{cs}$ contains the control commands about x, y and z axis $(\xi, \eta, \zeta)^T$.

To find the trimmed state of the aircraft, trim conditions need to be defined in such a way that the system is not over- or under-determined in order to calculate one unique solution of the equations. One example of such a trim condition is a horizontal level flight at a given velocity u. This requires the roll and pitch rates $\dot{p}, \dot{q}$ to be zero while the control surface deflections ξ, η are flagged as free. Yaw is omitted due to the lack of a dedicated control about the z axis. Equation (2.56) is then solved with Powell's non-linear root-finding algorithm [50,144,190]. This procedure is validated numerically [206] against MSC.Nastran SOL144. Once the initial flight condition is found, a time simulation may be started. The time simulation is performed by an integration of equation (2.56) over a period of time. Two different integration schemes have been tested. The explicit Runge-Kutta method of 4th/5th order [41] and an implicit Adams-Bashforth method [20], both implemented in Scipy [189], have shown numerically equivalent results. Because of the fewer function evaluations, the Adams-Bashforth method is selected.

The above description of the solution of the trim problem uses a direct approach based on partial derivatives to construct the jacobian matrix. Note that the structural deformation is already included by terms $\mathbf{u}_f$, $\dot{\mathbf{u}}_f$ and $\ddot{\mathbf{u}}_f$. Using a different aerodynamic method such as CFD, the calculation of partial derivatives is no longer feasible, especially if many mode shapes are considered for structural deformation. Therefore, an iterative approach is selected as sketched in Figure 2.9. Based on a CFD solution for the undeformed geometry, the structural deformation is calculated and applied to the CFD mesh. The fluid structure interaction (FSI) loop is repeated until convergence is achieved. The FSI solution is then subject to an outer loop to determine the trim condition. The solution of the trim problem is found (as before) using Powell's non-linear root-finding algorithm. The difference is that the trim problem is more non-linear. Compared to the direct trim solution using potential aerodynamics, the tolerances for convergence need to be modified as both the CFD and the FSI solutions are solved iteratively, too. The challenge is the selection of an appropriate set of convergence criteria. Convergence of the CFD solution is determined using Cauchy convergence of the lift, drag, rolling and pitching moment coefficients. Convergence of the

FSI loop is determined by an inspection of the maximal relative translational deformation between the current and the last loop. The following set of parameters is selected in this work:

- Convergence of the trim solution: $1.0 \cdot 10^{-3}$
- Convergence of fluid structure interaction: $|\Delta \mathbf{u}^{f}_{g,xyz}| \leq 1.0 \cdot 10^{-6}$
- Convergence of the CFD solution: Cauchy convergence with $\Delta C_l \leq 1.0 \cdot 10^{-4}$, $\Delta C_d \leq 1.0 \cdot 10^{-5}$, $\Delta C_{mx} \leq 1.0 \cdot 10^{-4}$ and $\Delta C_{my} \leq 1.0 \cdot 10^{-4}$ using 30 samples

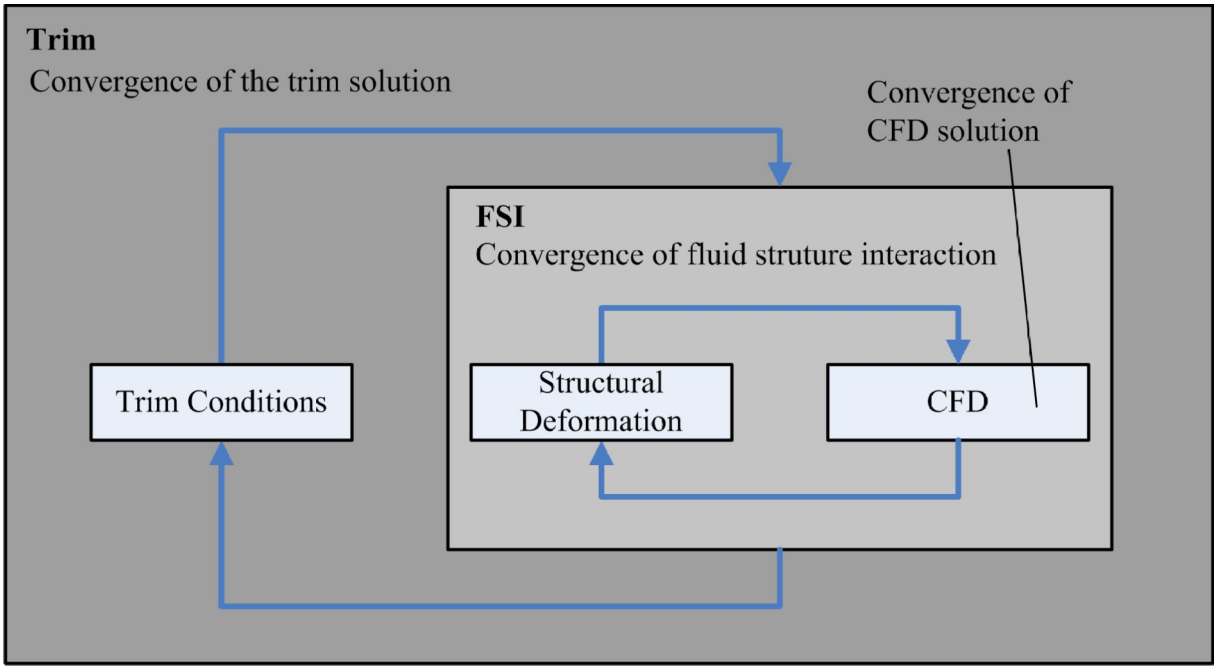

Figure 2.9: Sketch of iterative trim solution scheme

2.7 Landing Impact

The landing gear of an aircraft has to fulfill several purposes. An overview is given by Krüger et al. [94]. State of the art aircraft landing simulations are normally carried out using multi body simulation techniques, e.g. as described by Krüger [93] and Cumnuantip [31], and include a detailed model of the landing gear and tires. However, the aircraft is often assumed as a rigid body, neglecting the dynamic response of the aircraft's flexible structure. There are several possibilities to address this shortcoming. One approach is to incorporate the aircraft's structural properties in the multi body simulation environment. This can be achieved by a modal representation of the aircraft as Lemmens [103] demonstrates for a business jet.

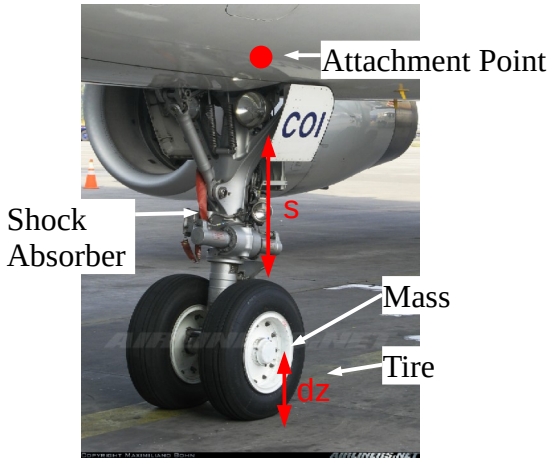

Figure 2.10: Key feature of a typical nose landing gear, photograph from [12]

Castrichini et al. [22] even include unsteady aerodynamics for the calculation of both gust and ground loads. An alternative to the modal representation is the discretisation of the elastic structure by means of rigid bodies, which are connected by rotational springs to account for wing bending and rotational stiffness, as shown by Krüger [92]. A different approach by Jaques and Garrigues [72] uses a dynamic, transient finite elements (FE) analysis. Special nonlinear elements, joints and hinges are added to the FE code to describe the behavior of the landing gear.

For aircraft loads analyses, the primary task is to analyze the effect of the landing impact on the aircraft structure and to include the resulting loads in the sizing process. Therefore, the selected approach in this work includes the landing gear directly within the transient, dynamic loads simulation. For a sizing procedure in the preliminary design phase, some simplifications may be made while maintaining the key elements, which are explained in the following. The emphasis lies on the absorption of the vertical kinetic energy occurring during the landing impact. Therefore, the landing gear module considers the vertical components of all accelerations, velocities, translations and forces. The following equations are derived from [31,93].

A typical landing gear of a large aircraft is shown in Figure 2.10. One key feature is a hydropneumatic air and oil shock absorber. The gas spring force F_f

$$F_f = F_0 \left(\frac{1-s}{s_m} \right)^{-n \cdot c_k} \tag{2.57}$$

is calculated based on a pre-stress force F_0, a stroke length s, a maximal stroke s_m and a polytropic coefficient n with $1 \leq n \leq \kappa$. The damping force F_d

$$F_d = sign(\dot{s}) \cdot d \cdot \dot{s}^2 \tag{2.58}$$

depends on the stroke velocity $\dot{s}$ and damping coefficient d.

For the tires, a linear behavior is assumed, forces act in z-direction and only when the tire makes contact with ground. Its deflection d_z is determined by subtracting its rolling radius r from its nominal radius r_{nom}. This leads to

$$F_{\mathrm{tire}} = c \cdot d_z + d \cdot \dot{d}_z \tag{2.59}$$

with a tire stiffness c and damping coefficient d. In addition, the tire may have a mass m_{tire}, causing a force F_{acc}

$$F_{\mathrm{acc}} = m_{\mathrm{tire}} \cdot \ddot{d}_z \tag{2.60}$$

In a next step, the landing gear model is incorporated into the time simulation. The positions, velocities and accelerations of the landing gear attachment point, indicated in Figure 2.10, are extracted at every time step and fed into the landing gear module. The landing gear reaction forces are then applied as external forces $\mathbf{p}_g^{\mathrm{ext}}$ on the aircraft at the landing gear attachment point. As the landing gear model is evaluated “on-the-fly”, the interaction between aircraft and landing gear is captured. In this way, the landing gear forces are counteracted by the aircraft's inertia, leading to a balanced set of loads.

2.8 Loads Recovery and Identification of Dimensioning Loads

The resulting nodal loads acting on the aircraft structure may be calculated by two different methods, the mode displacement method [10] and the force summation method [154]. The convergence of the mode displacement method (MDM), given by

$$\mathbf{p}_g = \mathbf{K}_g \cdot \mathbf{u}_g = \mathbf{K}_g \cdot \mathbf{\Phi}_{fg} \cdot \mathbf{u}_f \,, \tag{2.61}$$

strongly depends on the number of modes considered for the modal deformation vector $\mathbf{u}_f$. The more modes are used, the more precise is the result. Using all modes, both methods should lead to identical results.

With the force summation method (FSM), given by

$$\mathbf{p}_g = \mathbf{p}_g^{ext} + \mathbf{p}_g^{iner} \,, \tag{2.62}$$

the calculation is done using physical coordinates and the sum of inertia and external forces leads to the loads that are carried by the structure. Because of the more precise results, the force summation method is selected. Note that this only possible because the approximation of the unsteady aerodynamics (RFA) is performed in physical coordinates, see Section 2.2, and is thereby harmonized with the FSM. For most other applications, such as stability, flutter or aeroservoelasticity, there is no need to recover nodal forces and the approximation in generalized coordinates is sufficient.

In a typical loads analysis campaign for aircraft certification, several thousand load cases need to be computed. This is because structural strength has to be demonstrated for all maneuvers at all operational points. Thus, the maneuver cases need to be combined with all mass configurations, flight speeds, altitudes, Mach numbers, etc. The difficulty is to determine the load cases that yield the dimensioning loads in advance. To reduce the amount of guesswork and uncertainties already during the preliminary design, emphasis is put on a comprehensive loads process including a large number of load cases to ensure a thorough design.

From the nodal loads $\mathbf{p}_g$ obtained from equation (2.62), so-called interesting quantities are calculated. Interesting quantities usually include section forces and moments at various stations (e.g. along the wing) and attachment loads (e.g. from control surfaces, payload, landing gear, etc.). These quantities are calculated at monitoring stations. The calculation of section loads at the monitoring stations $\mathbf{p}_{\mathrm{mon}}$ involves an integration of the nodal loads $\mathbf{p}_g$, which can be expressed as a matrix multiplication.

$$\mathbf{p}_{\mathrm{mon}} = \mathbf{\Phi}_{g,\mathrm{mon}} \cdot \mathbf{p}_g \tag{2.63}$$

The section loads can be plotted as one-dimensional envelopes that show the section loads at one aircraft component, e.g. along the wing. The minimum and maximum values determine the highest loads, compare Wright and Cooper [224], Chapter 18.9.1, Figure 18.17. With this procedure, only one quantity can be examined. A more sophisticated approach can be realized with two-dimensional loads envelopes that show a combination of two quantities, for a wing typically the shear force F_z, bending moment M_x or torsional moment M_y. These plots, sometimes referred to as SMT-Plots, are very important for the dimensioning of an aircraft structure. Typical examples are shown in Figure 2.11. Every dot corresponds to one load case.

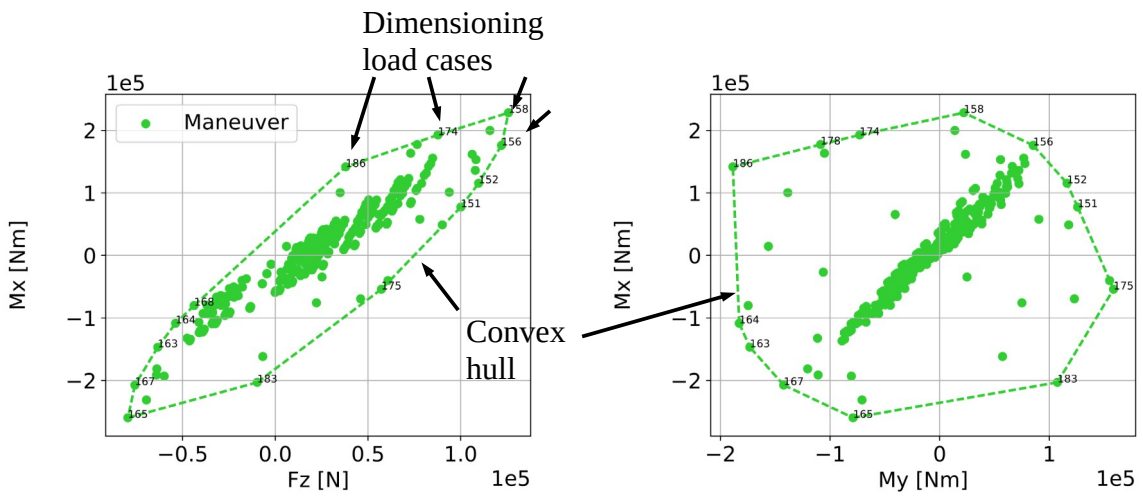

Figure 2.11: Identification of dimensioning load cases using loads envelopes constructed with the convex hull

In a next step, the convex hull is drawn to identify not only the minimum and maximum values of one quantity but also the minimum and maximum of two combined quantities. This approach is very useful for maneuver loads, but not directly applicable to gust or landing loads.

In contrast to maneuver loads, 1-cos gust or landing loads are the result of a time simulation. Therefore, they can no longer be represented by one single dot as shown previously in Figure 2.11. The approach selected in this work involves an extraction of several snapshots from the time simulation. In this way, dynamic loads are transferred into quasi-static loads and are usable for a dimensioning process. The snapshots are selected by identifying the minimum and maximum values at every monitoring station for every interesting quantity. An example is

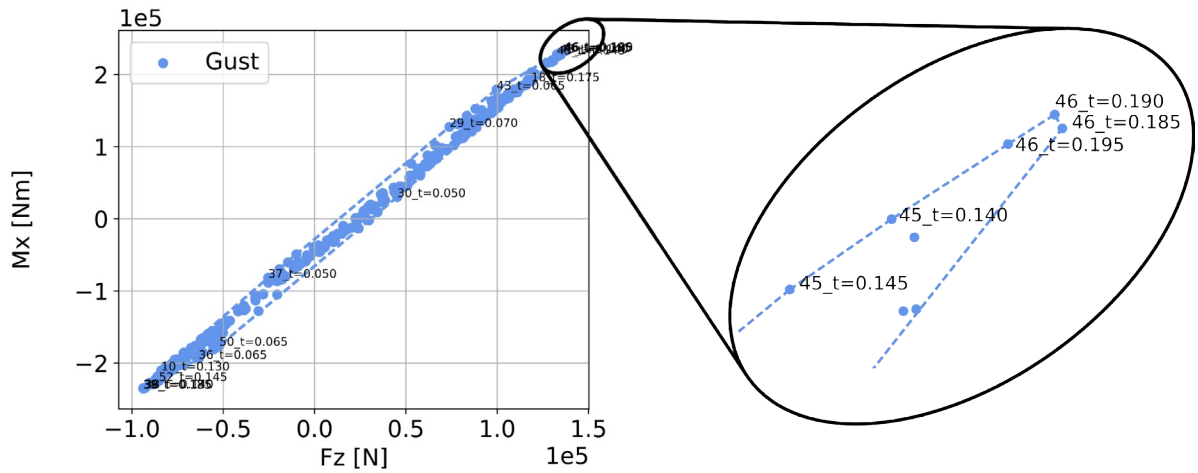

Figure 2.12: Identification of dimensioning dynamic load cases using time snapshots

shown in Figure 2.12. Every dot corresponds to one snapshot, which has been identified from the time simulation, and one gust simulation produces several dots. A closer look reveals that the right upper corner of the convex hull is formed by three snapshots from gust load case number 46 at the time steps t=0.185s, 0.190s and 0.195s.

One can also see that the three selected snapshots are very close to each other. In general, the number of dimensioning load cases could be reduced further by using a more conservative shape than the convex hull.

2.9 Assembly of the Methods for Flight Loads Analysis

The methods and theories presented in the Sections 2.1 through 2.8 are prepared and tested in simple scripts, first using academic examples, then with more complex aircraft configurations. Whenever possible, comparisons are made to other software. The individual scripts are integrated into functions and modules to be assembled to the Loads Kernel (LK) software package. Therefore, the development can be considered as a major contribution to this thesis and is inseparably connected to this work. From a technical perspective, the following points are improved with respect to the standard solution by MSC.Nastran:

- VLM and DLM Code, translated to python
  - Linear and nonlinear version, induced drag
- Aero-structural coupling (not new, but required e.g. for CFD surface mesh deformation)
  - Rigid body spline (with nearest neighbor search)
  - Surface and volume spline (radial basis functions)
- Trim conditions for different types of maneuver
  - Pitch-, roll-, yaw-maneuver, landing at constant sink rate, gliding with loss of altitude at constant speed, ...
  - EFCS for control surface scheduling
- Linear and non-linear equation for rigid body motion
  - Free flying, flexible aircraft in time domain

  - Flight mechanics included → good for comparisons with flight test
  - Rigid body motion captured correctly (aperiodic motion difficult in frequency domain)
  - Non-linear control possible (not possible in frequency domain)
  - Non-linear external forces, e.g. from landing gear
- CFD (DLR Tau Code) for maneuver loads
  - Structural flexibility and control surfaces via mesh deformation
  - CFD surface mesh deformation by LK → volume deformation by Tau
  - Directly comparable to VLM-based solution: same trim conditions, matrices, ...
  - Benefits form LK's integration in our loads process

The Loads Kernel is split into three processing steps:

- pre
- main
- post

These three steps need to be performed sequentially, but can also be performed individually. The process flow is sketched in Figures 2.13 and 2.14. The data is stored to the file system after every step. This is an advantage if for example only the load case definitions are changed while the model itself remains unchanged. In that case, only the main- and post-processing have to be repeated. This is also beneficial if the main-processing is to be run on a different computer or a high performance cluster. The resulting model data from the pre-processing can be copied to any location, where the main-processing is started. The resulting response may be copied back to the local file system for the post-processing step. Indeed, the main-processing is parallelized in the sense that $n-1$ load cases are calculated in parallel where n is the number of local CPUs. This is achieved by a worker / listener concept with a pool of $n-1$ workers and one listener which collects the results. The worker and the listener communicate via a queuing system available in the Python multiprocessing module.

During the pre-processing, all required model data is read, processed and assembled to one model. Input to the pre-processing are the mass and stiffness matrices, the FE geometry and the aerodynamic panel mesh. The pre-processing is designed in such a way that it directly interfaces with the data and files prepared by ModGen. The mass and stiffness matrices are exported from MSC.Nastran in the op4 file format, which is achieved with a DMAP alter. Technically, MSC.Nastran is only used in the role of a pre-processor and the use of any other FE processor is thinkable. From the mass matrix, the center of gravity, the mass and the corresponding moments of inertia are calculated as described in Section 2.4. Optionally, a Guyan reduction is applied. Next, a modal analysis is conducted to determine the eigenvalues and the eigenvector. Finally, the generalized mass and stiffness matrices are calculated. This procedure is repeated for all mass cases. For the definition of the aerodynamic panel mesh, CAERO4, CAERO7 or CQUAD4 cards are parsed. CAERO4 are used in MSC.Nastran while CAERO7 are used in ZAERO. With the aerodynamic panel mesh, the VLM and the DLM routines are started, according to the requirement of steady or unsteady aerodynamics. In the case of unsteady aerodynamics, the rational function approximation as described in Section 2.2 is performed automatically. This procedure is repeated for all Mach numbers defined in the operation parameters by the user. In addition, the AESURF and AELIST cards defining the control surfaces are parsed. With the help of a rigid body spline, deflection matrices are constructed that allow the calculation of the induced downwash on a control surface due to a given rotation angle about a hinge line. The aero-structural coupling depends on the FE geometry and the aerodynamic panel mesh. As described in Section 2.3, either a rigid body spline or a surface or volume spline based on radial basis functions may be used. The resulting coupling matrix is stored in the model as a sparse matrix to save memory and computational time during the main-processing. In a next step, the parameters of the international standard atmosphere (ISA) are calculated with respect to the altitudes requested in the operation parameters. Finally, a matrix for the integration of section loads is built based on the monitoring stations defined by the user. The resulting model data is stored to disk.

Remark: Because the ISA documents are not publicly available, the US standard atmosphere [230], which is equivalent up to 32 km altitude, may be taken as a convenient alternative reference.

The run time of the pre-processing can be very rapid for small, condensed models and rather lengthy if large FE models are involved or unsteady AIC matrices need to be calculated for many reduced frequencies and Mach numbers. As mentioned at the beginning, it is beneficial that the pre-processing has to be done only once if no changes are made to the model, which is an advantage with respect to commercial software.

The main-processing depends on the model data prepared in the pre-processing. In addition, a load case definition is needed as input. The load case definition contains parameters for every load case that shall be calculated and typically comprises parameters such as the type of maneuver, the mass configuration, flight speed, altitude, load factor, rates, accelerations, sub case identification number etc. In addition to the sub case identification number, the user may assign a descriptive string, preferably according to the nomenclature defined by Chiozzotto [142]. With this input, the first step of the main-processing is to establish a set of so-called trim conditions. The aircraft states are set as free or fixed according to the selected maneuver and in such a way that the system is neither over- nor under-determined. Next, the solution of this system is computed, yielding a trimmed aircraft as described in Section 2.5. For gust and landing loads, a time simulation is started, using the trimmed aircraft as an initial solution. Nodal loads are recovered from the aircraft states using the force summation method (FSM). In a next step, these nodal loads are integrated to section loads. In case of a time simulation, the dynamic section loads need to be transferred into single snapshots as described in Section 2.8. In addition, the nodal loads are translated into a global coordinate system. The results of the main-processing are stored to disk in a response file.

The calculation time for one maneuver load case is below one second for all models that have ever been used with the Loads Kernel. Therefore, even several hundreds of load cases are calculated within some minutes. Time domain simulations are a little more time consuming as they usually involve structural dynamics and unsteady aerodynamics. In most cases, the corresponding states change rapidly during the time simulation, resulting in very small time steps of the integration scheme, selected in Section 2.5. This is desirable in order to achieve good results but comes at the cost of many function evaluations. Changes of the maximum allowable time step size were tested and finally increased slightly to $\Delta t_{\max} = 5 \cdot 10^{-4} s$. The relative tolerance is set to $tol_r = 10^{-6}$. Using these parameters, no degradation of the results could be observed.

The post-processing is dedicated to the evaluation, visualization and export of the results. The dimensioning load cases are identified as described in Section 2.8. The automated plotting allows for a fast control of the results and a quick detection of erroneous data by the user. For maximum compatibility, currently four different formats are supported for the export of the corresponding nodal loads:

- MSC.Nastran format using FORCE and MOMENT cards
- Internal, hierarchical format using the pickle module in Python
- DLR CPACS format using the Tixi XML interface library [178]
- Matlab format using the scipy.io module in Python

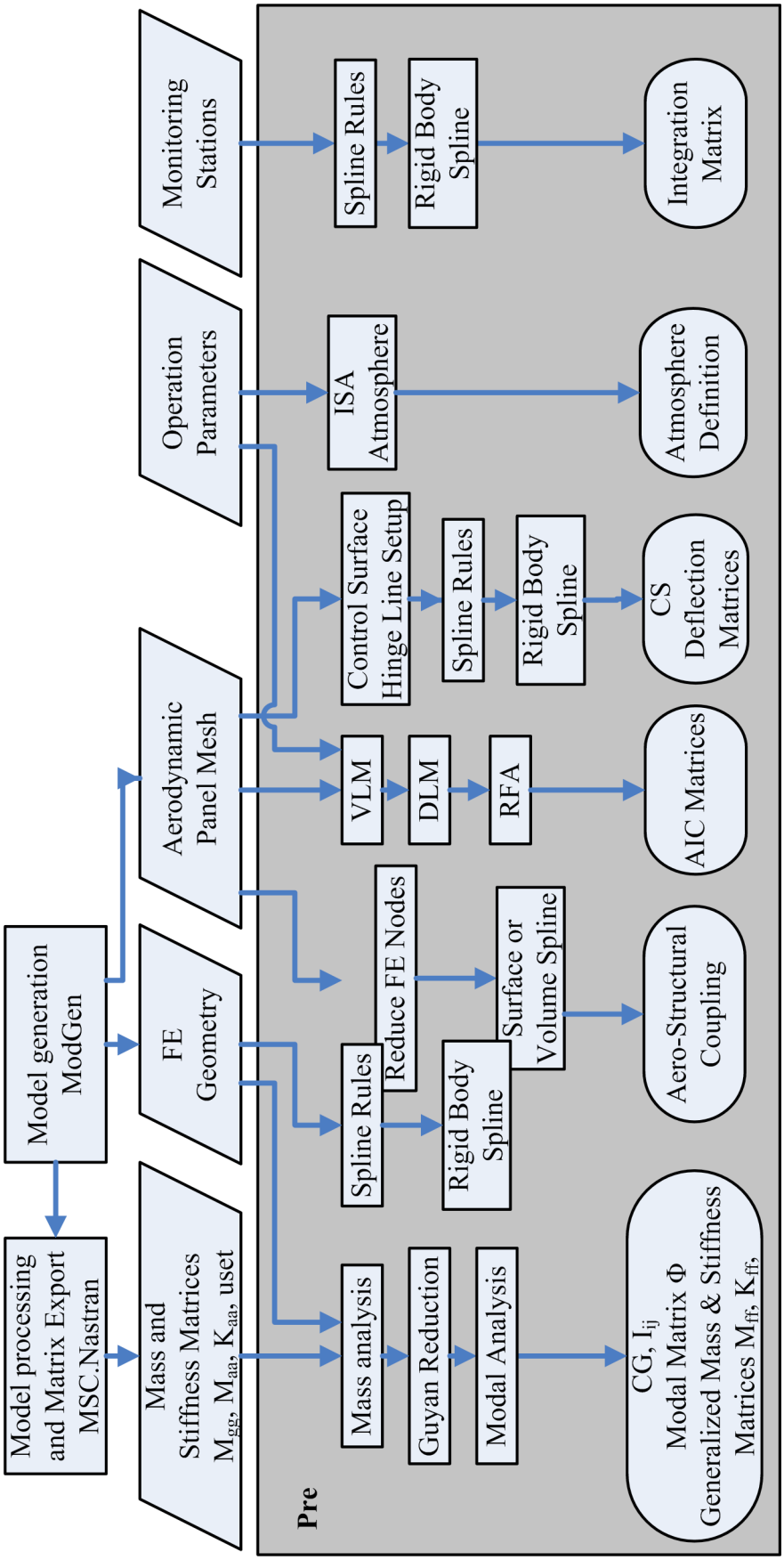

Figure 2.13: Schematic process flow of the Loads Kernel pre-processing

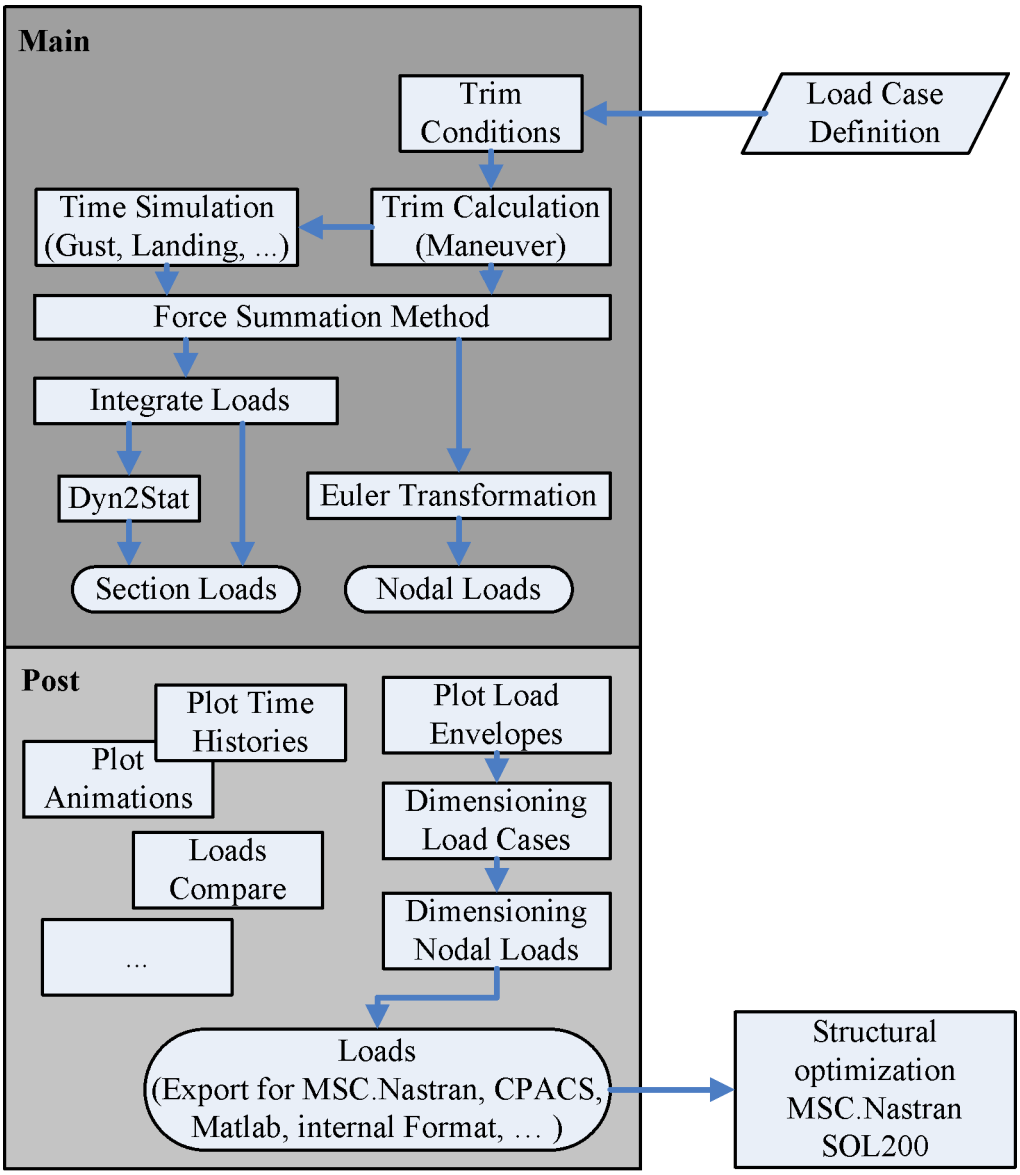

Figure 2.14: Schematic process flow of the Loads Kernel main and post-processing

2.10 Optimization of Aircraft Structures for Aeroelastic Application

Aeroelastic analyses are only as good as the underlying theories and the data that is included in the models. Therefore, mature and sophisticated data is required in order to build the corresponding models for the structure, masses and aerodynamics as described in the previous Sections 2.2 to 2.9. The data and models need to be as detailed as possible. The level of detail is not only determined by the number of points used for the discretization but by the number and types of structural and mass components that are included. The aim is to capture all effects that have an influence on the global structural behavior and local effects such as small holes, peaks in the stress distribution at sharp corners, etc., are not resolved. Therefore, a structural model for aeroelastic application is not suitable for a prove of strength and the stress office will use different models of higher resolution.

As mentioned in the introduction in Section 1.1, the aim is to include as many details as possible in the preliminary design as early as possible. This is a general conflict, because a detailed knowledge of the structure, the mass distribution, the structural dynamics as well as the steady and unsteady aerodynamics become available only later during the design process. Multiple people and companies have addressed this challenge in the past. In Section 2.10.1, a short overview on the field of parameterized modeling with a focus on aeroelastic applications is given and in Section 2.10.2 the solution selected in this work is presented.

2.10.1 Principles of Parameterized Modeling for Application of Structural Optimization with Aeroelastic Constraints

One approach is to use simple methods, which often rely on empirical data and formulas. A comprehensive compilation is given by Torenbeek [196]. Empirical formulas, however, may not be applicable to new, unconventional configurations. In addition, the investigation of aeroelastic effects is difficult. Chiozzotto [140,141,143] tries to find simple formulations of physical effects based on beam models and lifting line theories. With this, new concepts such as strut-braced wings can be analyzed for a wide range of possible configuration parameters. Haryanto [62] uses equivalent plate models to represent the structural dynamics of a wing structure. In combination with a lifting line theory, the structure is optimized for minimum weight and a high flutter speed. The “NeoCASS” Next generation Conceptual Aero Structural Sizing Framework developed by FOI and Politecnico di Milano also serves the purpose of

finding an optimized aircraft design, including aeroelastic analyses. Similar to the work of Haryanto, equivalent plate or beam models are used to represent structural aspects. A good overview of the project is given by Cavagna et al. [23].

Another approach is to use higher fidelity finite elements models based on shell elements, which are set-up using a parametric processor. Generally, these frameworks are less flexible and require a larger amount of work before first results are available, but the transition is fuzzy. In most cases, the structure is optimized for minimum weight under a given loading. The resulting FE model is then ready for any other kind of aeroelastic investigation. In some cases, a flutter or divergence analysis is included in the optimization as a constraint. Schumacher et al. [171] present an optimization of the Fairchild Dornier 728. The involved FE model of the wing is very detailed and consists of approximately 93,000 degrees of freedom. The center of the optimization is MSC.Nastran SOL200 and various external tools are integrated for evaluation of the results, e.g. for buckling and strength analysis. A similar work is performed by Schuhmacher et al. [172] for the optimization of the A400M rear fuselage. This time, Schuhmacher makes use of the LAGRANGE framework, extended by a post-buckling analysis. The FE model that is created has a very high level of detail as can be seen from Figure 5 in [172]. A similar approach is followed in the Preliminary Aircraft Design and Optimization framework PrADO, primarily developed by Heinze [65] and maintained at TU Braunschweig. Österheld [131,132] added methods to include aeroelastic effects within the preliminary design. Dorbath [40] sets up a framework for wing mass estimation based on a parametrization and the DLR CPACS format. Recent developments at Airbus Defense and Space aim to generate FE models for optimization purpose from a CPACS data sets, too. Some examples and first results are presented by Maierl et al. [114–116]. At Lockheed Martin, the PreCEPT tool chain is developed to generate FE Models from CATIA data. An overview of the recent developments is given by De La Garza [32]. At Airbus, the FAME-W tool for wing mass estimation, presented by Kelm et al. [78], also uses an automatically generated FE model. Hürlimann [68–70] from ETH combined CATIA and Matlab in his work to generate FE models for wing box mass estimation. Another major optimization framework is the Automated Structural Optimization System ASTROS by Lockheed Martin. ASTROS was already developed during the 90s with the aim to add enhancements relevant for design tasks to Nastran. A summary is given by Neill et al. [126]. Finally, the STARS [54]

framework developed by NASA and the ARGON framework by TsAGI should be mentioned. Kuzmina [99] shows an application of ARGON on a generic wide body airplane.

A very interesting activity of the Garteur group on Structures and Materials (AG 21) is summarized by Arendsen [4]. The report shows a comparison of different structural optimization codes for a multidisciplinary wing design when aeroelastic constraints are involved. The analyses include loads, aileron efficiency, static divergence and flutter. Optimization codes such as MCS.Nastran SOL200, LAGRANGE and STARS are used. These tools are all FEM based and produce comparable results with minor differences. Again, the FE models involved are rather detailed as can be seen from Figure B.6 in [4].

In general, every design optimization has a design objective. For structural optimization, this is usually the minimum structural weight of the finite elements model. To achieve this goal, the optimizer is allowed to make changes to the model, which are defined as design variables by the user. In addition, design variables can be linked in such a way that a certain area of elements is changed simultaneously. This reduces the number of effective design variables and might be reasonable with respect to manufacturing and production costs. At the same time, the optimizer has to respect design constraints. For structural optimization tasks, the typical constraint is that a structural response quantity (e.g. stress, strain, failure index, …) stays within a range defined by an upper and a lower boundary. The response quantity is calculated from the the finite element model under given loading conditions. In addition to these constraints, side constraints can be imposed. An example is the definition of lower and upper boundaries of the design variables, representing for example minimum or maximum shell thicknesses.

In mathematical terms, the optimizer has the task to find the design variables $\mathbf{x}$

$$\mathbf{x} = [x_1, x_2, \ldots, x_n]^T \tag{2.64}$$

that minimize the design objective F

$$min\,\{F(\mathbf{x})\} \tag{2.65}$$

such that constraints $\mathbf{g}$ are satisfied

$$\mathbf{g}(\mathbf{x}) \leq 0 \tag{2.66}$$

and the side constraints imposed on $\mathbf{x}$

$$\mathbf{x}_{lower} \leq \mathbf{x} \leq \mathbf{x}_{upper} \tag{2.67}$$

are not violated.

The solution to the problem described above is found by using an optimization algorithm. In the case of MSC.Nastran SOL200, a gradient based optimizer is employed. In a design sensitivity analysis, the rates of change of structural responses with respect to changes in design variables are computed. The use of these partial derivatives enables the optimization of problems with a large number of design variables. In SOL200, the default optimization scheme is a modified version of the Automated Design Synthesis (ADS) algorithm developed by Vanderplaats [176] with a focus on problems with a large number of design variables.

Finally, it should be mentioned that every optimization task has its limits and should be formulated carefully. This is phrased very metaphorically in the introductory section of the Nastran Design Sensitivity and Optimization User's Guide as follows:

"Suppose you asked a friend to find you a nice apartment on his street. Your friend, the optimizer, may have a somewhat different definition of "nice" than you do. His income might be higher than yours, so that the optimal design he proposes may be infeasible in terms of your bank account. Even though he is searching just on his street, the next block may turn out to have an apartment that you consider a better value. The optimizer is not able to go beyond your specifications to search out other possible configurations." [229]

2.10.2 Setup of the MONA-L(o)K Process

In this section, the general set up of the selected process for parametric aeroelastic modeling and structural optimization is presented. The resulting models are presented in Section 3. Three principal steps need to be considered:

- Model generation
- Loads calculation
- Structural optimization

The models are created with the in-house software ModGen developed by Klimmek [83,85]. ModGen is a parametrized processor to set up finite element (FE) models as well as aerodynamic models, optimization models for structural sizing, and other simulation models

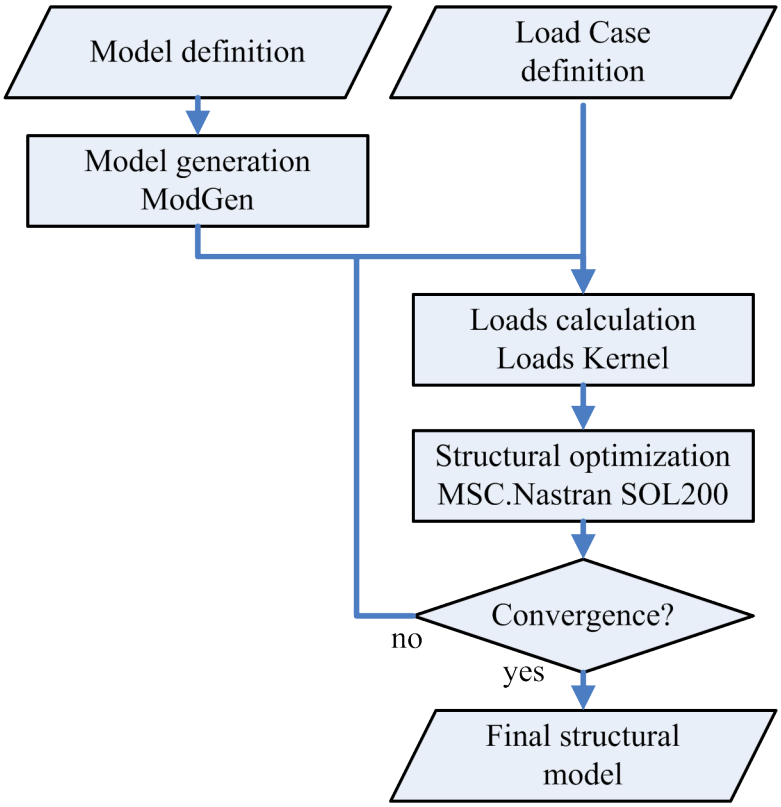

Figure 2.15: Model generation, loads calculation and structural optimization using the MONA-L(o)K process

(e.g. for mass modeling). The input for this process consists of basic information such as profile data, geometrical dimensions and design parameters of the wing box (e.g. number, position and orientation of spars, ribs and stringer). The ModGen has various modules that take care of the individual aircraft components and creates nearly all data required for the succeeding loads calculation and structural optimization.

The calculation of the aircraft loads is done using the Loads Kernel as described in detail in Section 2.9. The resulting loads are exported and the structure is optimized. The selected structural optimization scheme is implemented in MSC.Nastran SOL200.

The three steps of model generation, loads calculation and structural optimization are arranged in a process as shown in Figure 2.15. The resulting, improved design after the structural optimization has different stiffness and mass properties than the initial design. Accordingly, the resulting loads of the improved design are different with respect to the initial loads. As a consequence, both loads calculation and structural optimization form an outer optimization loop that is repeated until convergence is achieved. A suitable criterion to determine convergence of the outer loop is the resulting aircraft mass. Once convergence of

the outer loop is achieved, the optimization process is finished and the final structural model is ready for aeroelastic applications and further analyses.

The process, described formally in the previous sections, is referred to as **MONA** process according to the involved software packages **Mo**dGen and **Na**stran. Examples of application are the development of a structural model for the FERMAT configuration presented by Klimmek [84] or the ALLEGRA configuration with forward-swept wings presented by Krüger et al. [91]. Liepelt et al. [106] show the development of a long range aircraft within an MDO environment based on a CPACS dataset. Note that the process is not fixed and comes in different arrangements, depending on the requirements and intentions of the user. In this work, the loads calculation step is accomplished using the **L**oads **K**ernel software, causing an extension of the process name to **MONA-L(o)K**.

Summary: The **MONA** process is a means to further exploit, to evaluate and to interpret the loads established with the new methodologies of the **L**oads **K**ernel software with respect to structural dimensioning and in terms of structural weight. It allows the engineer to judge the results from a more global perspective and to understand the “big picture”.

3 Simulation Models of a Flying Wing of Low Aspect Ratio

3.1 Background and Conceptual Design

First aeroelastic models for flying wings of low aspect ratio have been developed based on the Saccon and DLR-F17 geometries [29,30,67,73,112,175] and already use parametric aeroelastic modeling techniques to set-up finite elements models. Those models are embedded in a multidisciplinary conceptual design process presented by Krüger et al. [95]. In a first approach, the geometry is assumed to be similar to the wing box of a classical aircraft. From that starting point, the structural layout evolved towards a structure more suitable for flying wings of low aspect ratio wings as shown in Figure 7 in [95]. The resulting models are used by G. Voss et al. [209] for studies of steady aeroelastic effects. The development of the DLR-F19 marks the step from geometries developed with a focus on wind tunnel experiments (Saccon, DLR-F17) towards a geometry for a feasible aircraft design (DLR-F19). The conceptual design is refined by Liersch et al. [108,109], who performed multidisciplinary studies for the conceptual design of the DLR-F19. The authors try to include the experts of various disciplines, their tools and knowledge even in the very beginning of the design. This concept is based on the common data format CPACS [34] and the remote control environment RCE [35], both developed and maintained by DLR. In a subsequent work, Voß and Klimmek [205] developed a parametric structural model of the DLR-F19-S configuration for loads and aeroelastic analysis. Schäfer et al. [165] then assessed the phenomena of body-freedom flutter for that configuration.

Using a similar, multidisciplinary approach, Liersch [111] developed a conceptual design for the MULDICON. The conceptual design comprises the planform and a structural layout with respect to the space required for fuel tanks, payload, landing gear, engine, etc. The data is then

provided as a project internal conceptual design sheet [107]. The underlying design requirements are summarized in a design specifications sheet [110]. An overview of the key aircraft parameters is given in Appendix A.1.

It can be concluded that the models of the MULDICON have a rather sophisticated foundation concerning the underlying data, which has matured over the years, and the MULDICON is an evolution of the DLR-F19. The modeling work is partially performed within the scope of a master thesis by Bramsiepe, documented in [13] and published by Bramsiepe et al. in [15]. The dynamic aeroelastic stability of that configuration is evaluated by Schreiber et al. [170]. The developed models serve as a baseline for in this work, except for some minor changes. In the following sections, the structural, mass, aerodynamic and coupling models are described briefly.

3.2 Structural Modeling

The parametric, structural modeling with ModGen requires a basic information input. For the MULDICON, the profiles and the planform are already defined by the conceptual design. From that information, three dimensional segments are constructed, one between each of the profiles, as shown in Figure 3.1 a) and b). In a next step, the positions and number of spars and ribs are defined in such a way that they don't interfere with other aircraft systems, resulting in an internal, geometrical layout shown in Figure 3.1 c). That geometrical layout is meshed using finite elements, resulting in a structural model shown in Figure 3.1 d). In the

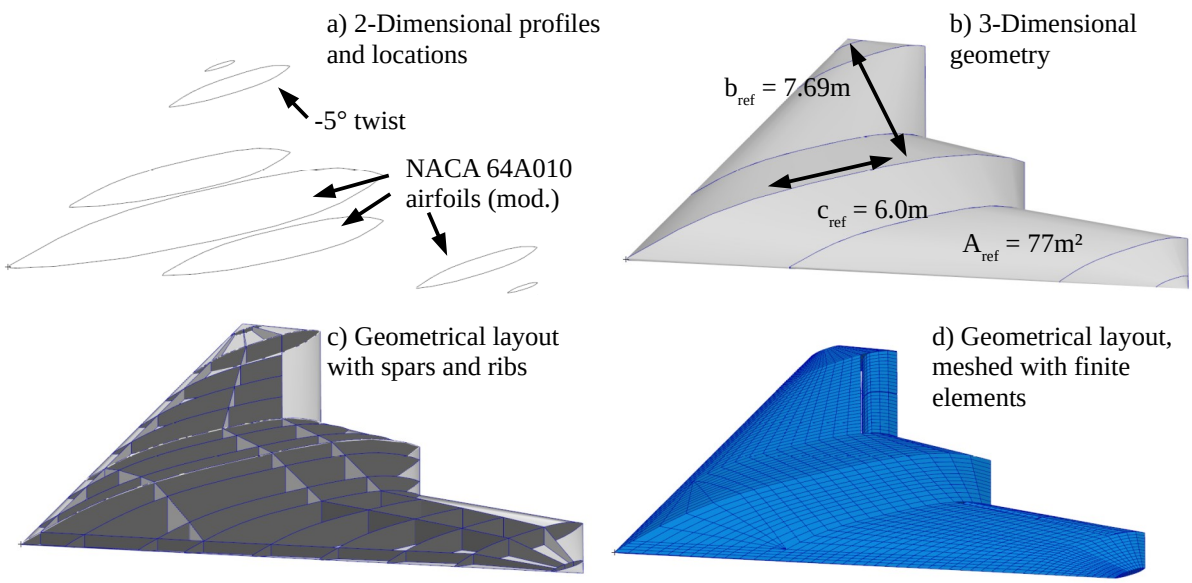

Figure 3.1: From 2-dimensional model information to FE model

case of the MULDICON, mainly shell elements are used. Beam elements are added as stiffening elements for the spars and ribs. For the upper and lower skin, stringers with hat profiles support the shell elements. Note that typical structural models for MDO application often only include the wing box (between front and rear spar). The MULDICON is modeled from the leading to the trailing edge and control surfaces are included as well. Therefore, the model is much more detailed, closer to a real aircraft and allows for more thorough investigations. Figure 3.2 shows the inner layout with sufficient space for the engine (red), the payload bay (yellow) as well as the nose and main landing gear bays (green). Comparing Figure 3.1 c) with Figure 3.2, note that not all elements defined in the geometrical layout are actually meshed and modeled with FE elements. The symmetrical left and right side of the MULDICON are modeled in individual runs of ModGen and connected to each other at the center line using rigid body elements. In a similar way, the four control surfaces are modeled individually and attached to the main wing with a hinge construction and spring elements.

The material of the shell elements is carbon fiber reinforced plastic (CFRP). Several layers of unidirectional (UD) fibers are combined to a laminate. The behavior of the laminate can be tracked back to the properties of the individual layers. The calculation principles are based on the classical laminate theory (CLT). A useful summary of the state of the art and practical advice on the development and analysis of CFRP components is published by the Verein Deutscher Ingenieure in guideline VDI 2014, Part 3 [198] (available in English and German).

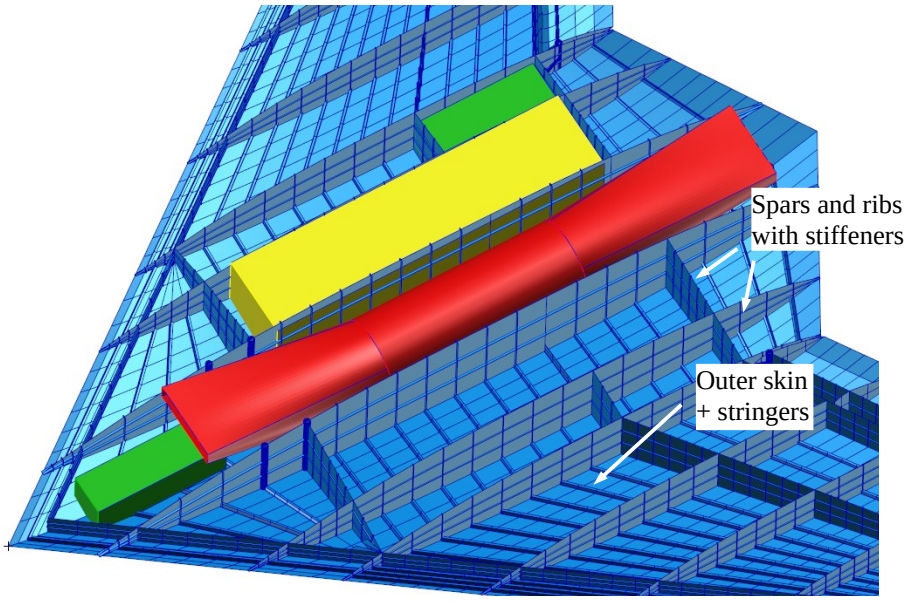

Figure 3.2: Inner, structural layout and FE modeling with spaces for engine (red), payload (yellow) and landing gears (green)

A very comprehensive and detailed reference is Schürmann [173]. The CLT is based on the description of the orthotropic material properties of the individual layers: the elastic modulus E_1, E_2, poisson's ratio ν_{12} and shear modulus G_{12} in the material directions 1 and 2. Direction 1 denotes the fiber direction and 2 the direction orthogonal to the fibers. Using that information, a local stiffness matrix $\mathbf{Q}'_k$ is constructed for every layer k.

$$\mathbf{Q}'_k = \begin{bmatrix} \frac{E_1}{1-\nu_{12}^2 \frac{E_2}{E_1}} & \frac{\nu_{12} \cdot E_1}{1-\nu_{12}^2 \frac{E_2}{E_1}} & 0 \\ \frac{\nu_{12} \cdot E_2}{1-\nu_{12}^2 \frac{E_2}{E_1}} & \frac{E_2}{1-\nu_{12}^2 \frac{E_2}{E_1}} & 0 \\ 0 & 0 & G_{12} \end{bmatrix} \tag{3.1}$$

The fibers of a unidirectional layer may be placed at an angle ϕ with respect to the global coordinate system, typically with $\phi = 0°$, $\pm 45°$ or $90°$. Transformation of $\mathbf{Q}'_k$ from local to global coordinates yields the global stiffness matrix $\mathbf{Q}_k$ of the individual layer. The layers may be arranged with a given stacking sequence, leading to a complete laminate set-up. The stiffness matrix of the laminate is divided into the in-plane stiffness matrix $\mathbf{A}$, the coupling matrix $\mathbf{B}$ and the bending stiffness matrix $\mathbf{D}$. The linear elastic law

$$\begin{pmatrix} \mathbf{f}_{xyz} \\ \mathbf{m}_{xyz} \end{pmatrix} = \begin{bmatrix} \mathbf{A} & \mathbf{B} \\ \mathbf{B} & \mathbf{D} \end{bmatrix} \cdot \begin{pmatrix} \delta_{xyz} \\ \delta_{rxyz} \end{pmatrix} \tag{3.2}$$

relates deformations δ with forces and moments $\mathbf{f}$ and $\mathbf{m}$, compare equation (15.10) in [173]. Matrices $\mathbf{A}$, $\mathbf{B}$ and $\mathbf{D}$ are calculated from the stiffness matrices $\mathbf{Q}_k$ of all layers, the layer thickness t_k and offset z_k in laminate normal direction with respect to the reference plane.

$$\mathbf{A} = \sum_{k=1}^{n} \mathbf{Q}_k \cdot t_k \tag{3.3}$$

$$\mathbf{B} = -\sum_{k=1}^{n} \mathbf{Q}_k \cdot t_k \cdot \frac{z_{k+1} + z_k}{2} \tag{3.4}$$

$$\mathbf{D} = \sum_{k=1}^{n} \mathbf{Q}_k \cdot t_k \cdot \left[\frac{t_k^2}{12} + \left(\frac{z_{k+1} + z_k}{2} \right)^2 \right] \tag{3.5}$$

For the properties of the CFRP material, typical values are assumed and given in Table 3.1.

E_1	E_2	ν_{12}	G_{12}
155000 MPa	8000 MPa	0.3	3700 MPa

Table 3.1: Single layer material properties

For the damping characteristics of the material, 2.0% modal damping (compare Section 2.4) are assumed. This dampens higher frequency modes, which are excited for example by the landing impact, which will be discussed in Section 2.7.

Theoretically, arbitrary angles ϕ are thinkable. Within the aviation industry, laminates with layers in $0°$, $\pm 45°$ and $90°$ direction are established, as they correspond to the dominant stress conditions in light weight constructions, compare section 11.4.5 in [173]. The mixture is given in percent of the volume using the following notation: $[0°/\pm 45°/90°]$. For the spars of the MULDICON, mainly $\pm 45°$ layer are used to take the shear forces. For the rips, also $90°$ layers are important to maintain the shape of the aerodynamic profile. The skin contains both $0°$ and $\pm 45°$ layers to take the bending and torsion moments. A summary is given in Table 3.2.

Component	Spars	Ribs	Skin
Selected laminate $[0°/\pm 45°/90°]$	$[10/80/10]$	$[10/40/50]$	$[40/40/20]$

Table 3.2: Laminate definitions for different components

The stacking sequences are given in Table 3.3. Assuming a constant layer thickness t_k for all layers, the stacking sequences correspond to the laminate definitions of Table 3.2. In this work, all 20 layers are modeled individually. This means a rather high computational effort in comparison to the modeling of an isotropic material (just one layer per shell element).

An alternative approach is the representation of the composite material with just four layers of $0°$, $+45°$, $-45°$ and $90°$ fiber orientation and a layer thickness t_k corresponding to the volumetric laminate definitions. In this case, the $\mathbf{D}$ matrix is unknown.

Another methodology uses a set of so-called lamination parameters. The 12 lamination parameters describe the $\mathbf{A}$, $\mathbf{B}$ and $\mathbf{D}$ matrices as functions of the fiber orientation ϕ. The number of lamination parameters is reduced to 8 for symmetric laminates and can be reduced to 4 for symmetric and balanced laminate set-ups. Because the fiber orientation is unknown, the sizing of the laminate is based on allowable strains. The approach appears very promising and is currently a field of extensive research, examples are the works by Dillinger [36,37] and IJsselmuiden [71]. In both cases, the actual stacking sequence needs to be reconstructed in a post-processing step, shown for example by Meddaikar [119].

Spars	Rips	Skin
45°	90°	0°
−45°	90°	0°
45°	45°	45°
−45°	0°	90°
0°	−45°	−45°
45°	90°	0°
45°	45°	0°
90°	90°	45°
−45°	−45°	90°
−45°	90°	−45°
Symmetry Plane	Symmetry Plane	Symmetry Plane
−45°	90°	−45°
−45°	−45°	90°
90°	90°	45°
45°	45°	0°
45°	90°	0°
0°	−45°	−45°
−45°	0°	90°
45°	45°	45°
−45°	90°	0°
45°	90°	0°

Table 3.3: Laminate stacking sequence for spars, rips and skin components

For the stiffening elements of the spars and ribs and for the stringers, bar elements are used. The carbon fibre material is implemented using a quasi-isotropic approach. Their shape and the dimensions have been approximated using conceptual design methods and engineering judgement. For the stringers, for example a hat profile with two different sizes is used, one for areas with little space and one for the rest of the aircraft.

The resulting structural model allows for the computation of flexible deformations under load. The loads are applied to the structure as forces and moments in x, y and z direction on every grid point. The procedure of a finite elements analysis is straight forward and is implemented

in a large variety of finite element processors. In the following, the general procedure is outlined and the modifications required for flight physical investigations are explained. The procedure can be summarized with the following seven steps (compare flow chart for linear elastic analysis in Figure 1-5, Chapter 1 in [227]):

1. Represent a continuous structure as a collection of discrete elements connected at grid points.
2. Formulate element stiffness matrices from element properties, geometry, and material properties.
3. Assemble all element stiffness matrices into a global stiffness matrix $\mathbf{K}$.
4. Apply boundary conditions to constrain model.
5. Apply loads $\mathbf{p}$ to the model (forces, moments, pressure, etc.)
6. Solve the matrix equation $\mathbf{p} = \mathbf{K} \cdot \mathbf{u}$ for displacements $\mathbf{u}$.
7. Calculate element strains, stresses and reaction forces from the displacement results.

Step 1 is typically accomplished by using a pre-processor, in this case the ModGen software. Based on the structural elements geometry, material and properties defined by the pre-processor, local element stiffness matrices are formulated in Step 2. For simple elements such as a single rod element, this may even be accomplished by hand. For many and more complex elements such as shells with composite materials, a software such as MSC.Nastran is advisable. In Step 3, the local matrices are assembled into global matrices. The transition from a ModGen and MSC.Nastran based finite elements model towards a flight physical model to be used within the Loads Kernel software is achieved in two steps. First, the coordinates of the structural grid points are parsed from the GRID cards created in Step 1. After this, the structural model exists only as a cloud of structural grid points as visualized in Figure 3.3. The shell elements are now for visualization purpose only and have no physical properties. In a second step, the stiffness properties connecting each of the grid points are transferred by reading stiffness matrix K_{aa} and the u-set, yielding the set definitions as described in Section 2.4. Both become available with Step 3, and, technically, the finite elements analysis process can be stopped.

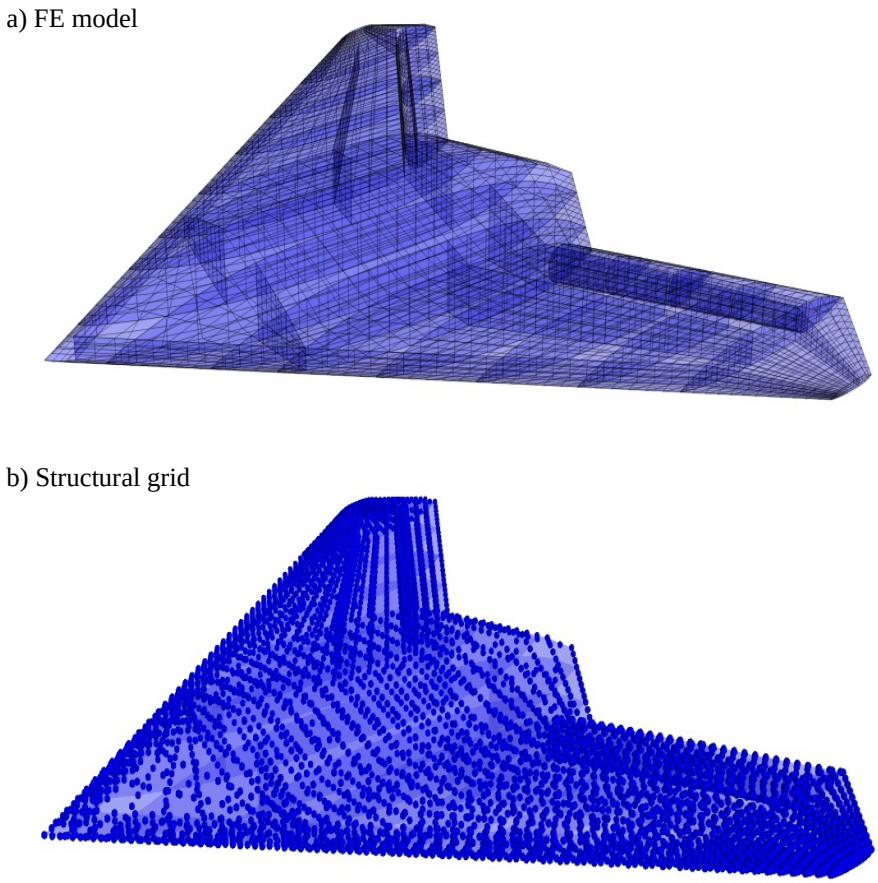

Figure 3.3: From a) FE model to b) structural grid representation for loads

Once the flight physical nodal loads $\mathbf{p}$ are calculated, they may be applied to the structure in Step 5. Similar to equation (2.55), the displacements $\mathbf{u}$ are determined by evaluating $\mathbf{p} = \mathbf{K} \cdot \mathbf{u}$ in Step 6. The solution requires a determined system (at least), which is realized by application of the boundary conditions defined in Step 4. For aircraft, typically the rigid body degrees of freedom need to be supported. Note that for a linear static analysis, damping and mass are not considered and the loads are assumed to be applied slowly. This is sufficient as mass and damping have been considered in equation (2.55) already. Thus, they are part of the nodal loads $\mathbf{p}$. A very important calculation is done in Step 7. Here, the displacements $\mathbf{u}$ are translated into element strains by calculating the strain ϵ for every element based on the local displacement δ. For a simple rod of length l, the strain ϵ is given by

$$\epsilon = \frac{\delta}{l}. \tag{3.6}$$

The modulus of elasticity E relates the element strain ϵ to element stress σ

$$\sigma = E \cdot \epsilon. \tag{3.7}$$

Again, for the example of a simple rod, this could be accomplished by hand. For a more complex model, many coordinate transformations are involved and the use of a software such as MSC.Nastran is advisable. Next to the element strain ϵ and stress σ, many other parameters, for example the failure indices FI for composite materials, are calculated as well. Note that a linear static analysis is restricted to small displacements and a linear elastic behavior is assumed.

3.3 Mass Modeling

The mass of the structure is determined from the element thickness and cross sections in combination with the material density. Because neither the structural nor the mass model is reduced, the structural mass is distributed over all grid points as shown in Figure 3.5 a). In a next step, system masses are added, shown in Figure 3.5 b). Examples of these masses are landing gear masses, engine mass and masses of other aircraft systems such as avionics, hydraulics, flight control system, electronics, wiring, radar, engine installation, intake and nozzle, data link, etc. The engine mass is derived from a related design task by Becker et al. [7] and Nauroz [125]. Masses for the landing gears are estimated using the in-house software LG Design [31]. In a next step, the fuel tanks are modeled geometrically using ModGen as shown in Figure 3.4. A fuel tank is modeled using several bays and each bay is bounded by ribs and spars, compare Figure 8 in reference [83]. The resulting fuel tank bays are filled with volumetric finite elements with a density of kerosene to a required filling level. Note that the filling level and the actual fuel mass have a nonlinear relationship due to the geometry of the tank. With this procedure, the mass, inertia and the center of gravity is evaluated for each bay. Fuel tank 2 for example consists of four bays, resulting in four condensed masses along the wing. The corresponding condensed masses are shown in the mass model in Figure 3.5 c). Finally, a payload is positioned in both the left and right side payload bays with 1000kg each, visible in the mass model in Figure 3.5 d).

Different combinations of payload and fuel lead to nine different mass configurations, listed in Table 3.4. The structure is listed as reference only. Looking at the position in x direction of the center of gravity CG_x, the values are very close to each other and barely move. Assuming

a mean aerodynamic center $MAC_x = 6.0m$, the center of gravity is always slightly in front of the mean aerodynamic center, expressed by

$$CG[\%MAC] = \frac{CG_x - MAC_x}{c_{\text{ref}}} \cdot 100 \tag{3.8}$$

in the last column. The negative sign indicates a stable configuration.

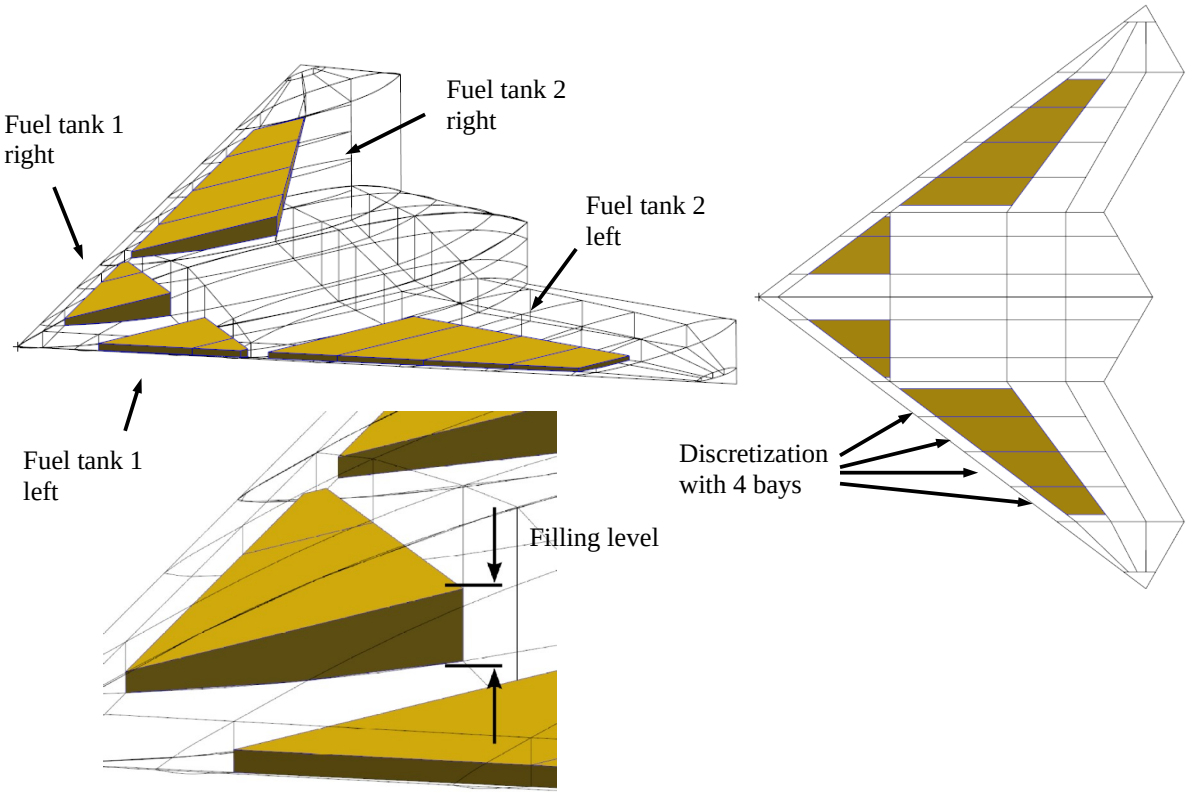

Figure 3.4: Geometrical modeling of fuel masses

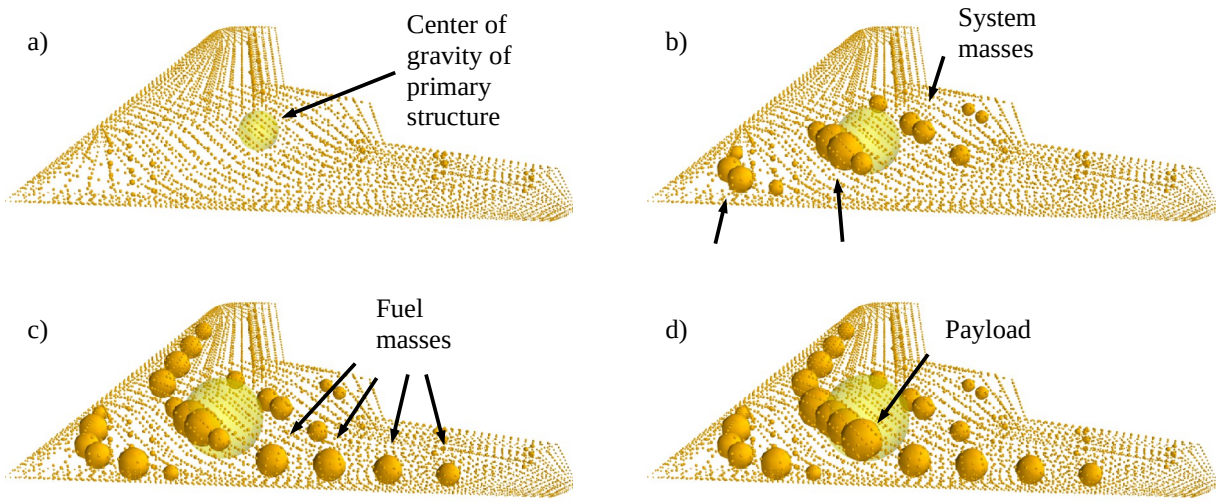

Figure 3.5: Mass configurations of the MULDICON: a) structure only, b) plus system masses, c) plus fuel masses, d) plus payload

#	Mass config.	System masses	Payload	Fuel	Mass $[kg]$	$CG_x[m]$	$CG_x[\%MAC]$
	Structure only	no	no	empty	1383	6.81	13.68
1	M1	yes	no	empty	5921	5.81	-3.18
2	M2	yes	no	half	8279	5.75	-4.12
3	M3 / MLW	yes	no	full	10635	5.76	-4.07
4	M11	yes	both	empty	8422	5.84	-2.73
5	M12 / BFDM	yes	both	half	10779	5.79	-3.55
6	M13 / MTOW	yes	both	full	13136	5.78	-3.60
7	M21	yes	left only	empty	7172	5.82	-2.92
8	M22	yes	left only	half	9529	5.77	-3.78
9	M23	yes	left only	full	11885	5.77	-3.82

Table 3.4: Mass configurations of the MULDICON-F

3.4 Aerodynamic Modeling

The aerodynamic theories used in this work, the VLM and DLM, require an aerodynamic grid as explained in Section 2.2. The modeling of the aerodynamic grid of the MULDICON bears some difficulties, which are discussed briefly in the following. The first consideration concerns the number of panels in chord direction, as the mesh should model unsteady aerodynamics appropriately. The unsteady pressure solutions are calculated for harmonic motion in the frequency domain by the DLM as described in Section 2.2. The number of cycles in chord direction increase with the reduced frequency k_{red}, but the number of panels is limited. Convergence of the unsteady solution depends on the number of panels in chord direction. The theoretical background is discussed in [226] in Section 5.4.1, page 5-12 ff. Finally, an equation is found (compare equation (3.9) with equation on page 5-13 in [226]) that calculates the minimum panel length Δx from the reference chord length $c_{\text{ref}} = 6.0m$, the Mach number $M = 0.9$ and the highest reduced frequency $k_{\max} = 2.0$, assuming a discretization with 12 sampling points per wave.

$$\Delta x < \frac{c_{\text{ref}}}{12} \cdot \frac{\pi}{k_{\max}\left(\frac{M}{\sqrt{1-M^2}}\right)^2} \tag{3.9}$$

Based on this considerations, 24 panels in chord directions are selected. A second, important consideration concerns the aspect ratio of the panels. The aspect ratio of a panel is limited

because of the numerical approximation of integral I_2 during the solution of the DLM that has been selected in [2], page 3, from 1968. Some 30 years later, a refinement is published by Rodden et al. [162] that replaces the original parabolic approximation with a quadratic approximation, relaxing the limitations of the aspect ratio. This refinement, however, is not implemented in the version of the DLM used in this work, leading to a maximum aspect ratio $AR < 3 \ldots 4$ as recommended for example in [160] in Section 3.1, page 88. At the wing tip of the MULDICON, this would lead to a great number of tiny panels. In addition, the panels of the last strip would need to be triangles to model the pointed shape of the wing tip. In order to avoid numerical problems, the outer wing tip is not modeled. This is a reasonable solution as the area is small and the aerodynamic contributions are considered to be negligible. For the modeling of the control surfaces, the panels have to be placed in such a way that the panel boundaries coincide with the control surfaces boundaries. In this case, they are located along the trailing edge and the inner and outer control surfaces are discretized using 5x5 and 5x7 panels respectively.

In general, the discretization of such a highly swept geometry needs to be a compromise between the long wing root and the short wing tip. Jumps in the discretization are to be avoided. The resulting mesh is shown in Figure 3.6 and has 1248 panels. It includes four control surfaces along the trailing edge, which are highlighted in the top view in Figure 3.6.

As can be seen from Figure 3.6, the aerodynamic panel mesh is planar. Still, it is possible to account for camber and twist of the profile geometry by a modification of the aerodynamic

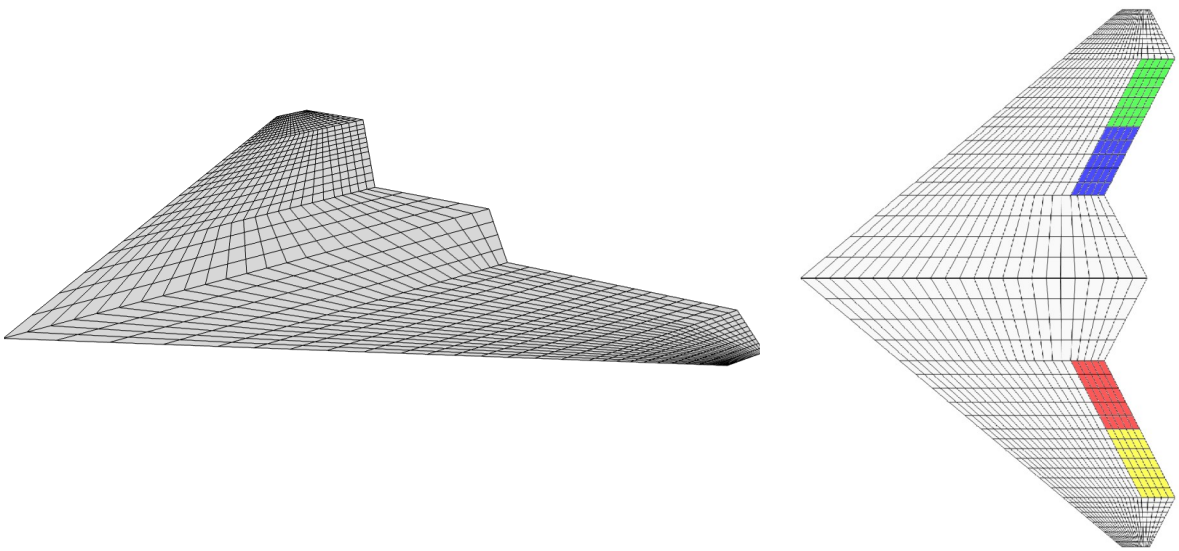

Figure 3.6: Aerodynamic panel mesh of the MULDICON

onflow condition as sketched in Figure 3.7. For every panel, an additional downwash $\mathbf{w}_{j,cam}$ is added in equation (2.9), resulting in an offset of the lift polar and a modified zero-lift coefficient. In MSC.Nastran, such correction factors are implemented as well, given in a matrix named W2GJ.

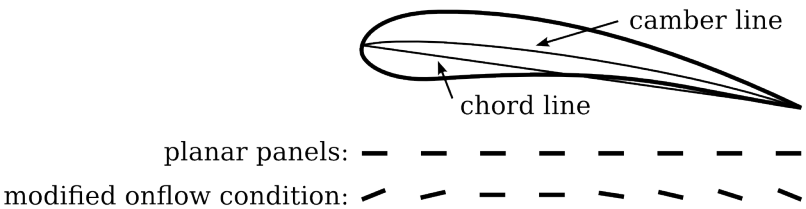

Figure 3.7: Modeling of camber and twist

In addition to the classical, aerodynamic panel methods, investigations comprising CFD calculations are conducted in Section 6. Therefore, an additional aerodynamic mesh is required. The creation process is of manual nature, requires some experience and is rather time-consuming. In a first step, a clean surface geometry is needed. In this work, the surface geometry generated during the model set-up using the ModGen software is taken, compare Figure 3.1 b). This ensures the aerodynamic mesh matches exactly the remaining parts of the model in terms of size and shape. Both left and right hand side of the MULDICON are imported into the meshing software Centaur as IGES files. The ModGen surface geometries are usually of good quality and in this case, the cleaning and repair routines resolved most issues automatically. The resulting CFD surface geometry is shown in Figure 3.8.

In a second step, the surface is discretized. Generally, an unstructured discretization using triangles and a structured discretization using quadrilaterals are possible. Compared to triangles, the use of quadrilaterals could reduce the number of cells on the surface if cells of a high aspect ratio in span-wise direction are used. This is especially helpful for the modeling of

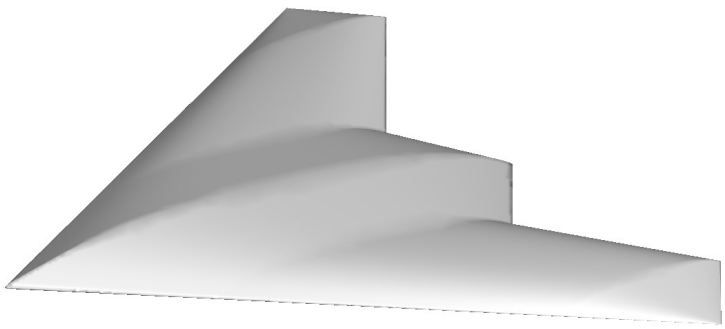

Figure 3.8: Step one, a clean surface geometry

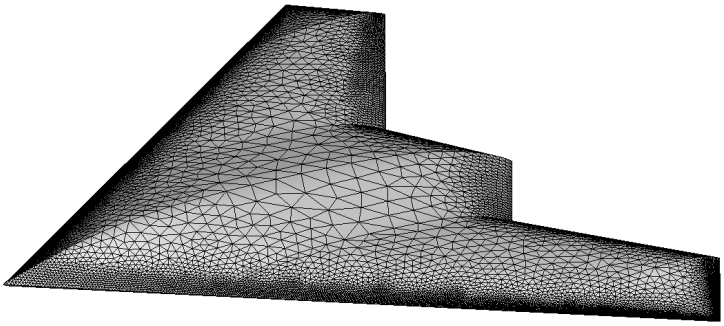

Figure 3.9: Step two, unstructured surface discretization with triangles

a boundary layer. The indented CFD calculations are of inviscid nature, thus require no modeling of a boundary layer. The DLR Tau code [176] is an unstructured CFD code and does not benefit from a structured mesh in terms of calculation time. In the case of the MULDICON, a structured mesh is difficult to realize due to the highly swept geometry, as already pointed out above concerning the VLM/DLM modeling. The advantage of surface triangles over quadrilaterals is the simple meshing procedure and the volume mesh can be filled with tetrahedrons directly. Considering the above arguments, the decision of discretization is in favor an unstructured mesh. The resulting surface mesh is shown in Figure 3.9 and comprises 54,476 surface elements.

The control volume is constructed using a spherical farfield with a diameter of 200 m and the MULDICON at the center. That volume is filled using 818,352 tetrahedrons and 153,109 nodes. For CFD meshes, the meshing quality in terms of cell aspect ratio, skew and sliver is an important indicator to achieve a good numerical convergence of the solution. After the theoretical inspection, a practical test calculation showed an excellent convergence behavior, see Figure 6.2 in Section 6.2.

3.5 Coupling Strategies

Structural models of classical wing-fuselage-empennage configurations are often reduced to a loads reference axis (LRA) as explained in Section 2.4. The coupling of the planar, two-dimensional aerodynamic distribution to the one-dimensional structural model is accomplished using additional points positioned along the leading and trailing edge that are connected to the LRA with rigid body elements. For a structural optimization, nodal forces are

required. This is accomplished by re-distributing the loads from the LRA onto the full structural model.

Because the structural model of the MULDICON already contains both leading and trailing edge, the above steps are no longer necessary. The planar, two-dimensional aerodynamic distributions can be coupled directly to the three-dimensional structural model. Because aerodynamic panel methods calculate the pressure difference $\mathbf{\Delta c_p}$ between upper and lower surface as explained in Section 2.2, the engineer is forced to choose one side only for coupling. In this case, the lower side is selected.

For the VLM / DLM based solutions, the aero-structural coupling uses the rigid body spline in combination with a nearest neighbor search visualized in Figure 3.10. The small black lines visualize the mapping of the aerodynamic grids onto the structural grids.

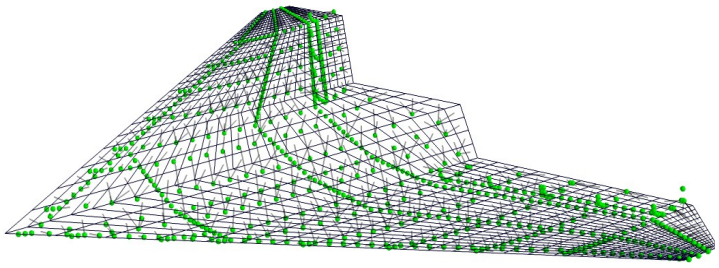

Figure 3.10: Aero-structural coupling of the MULDICON using a rigid body spline

As there are more structural nodes than aerodynamic nodes, the application of a rigid body spline leads to moderately high nodal forces at individual structural nodes. This leads to local stress peaks, especially with nodal forces located in the middle of a skin field. During the structural optimization of the baseline configuration, this effect was good-natured and thus tolerated. With higher loads from the closed loop analysis, higher local stress peaks occurred, causing a significant increase of the material thickness of the affected skin fields. The coupling was modified in such a way that the forces are distributed to all spars and ribs on the lower side. This avoids numerical problems and preserves the global characteristics of the aircraft structure.

With a three dimensional CFD solution available, the above restrictions could be removed and the aerodynamic forces could be distributed more evenly on both the upper and lower surface. In addition, local peaks of the nodal forces are more unlikely to occur because there are more CFD nodes than structural nodes. However, to allow for a good comparison between VLM

and CFD in Section 6, the CFD forces are first transferred to the VLM grid. They are then processed in the same way and using the same matrices as if they would be from VLM. The mesh deformation of the CFD surface is performed using a volume spline to achieve smooth, high quality surface deformation.

3.6 Structural Optimization

3.6.1 Optimization Model

The design variables $\mathbf{x}$, see equation (2.64), of the MULDICON are the material thicknesses of the shell elements of the skin, spars and ribs. Note that other parameters, such as stringer size or spacing, remain fixed. As mentioned in Section 2.10.2, a relationship may be defined in such a way that a certain area of elements is changed simultaneously. This area is called design field. For the MULDICON, the shell elements of one skin, spar or rib sub segment are linked. One sub segment is the area between two ribs and two spars as visualized in Figure 3.11.

The MULDICON comprises 115 of these design fields, resulting in 115 design variables $\mathbf{x}$. For the upper and lower skin, there are eight design fields in span direction, three design fields in chord direction on the wing and five design fields in chord direction in the fuselage region. This division applies to the corresponding spar and rips as well. The objective $F(x)$ is

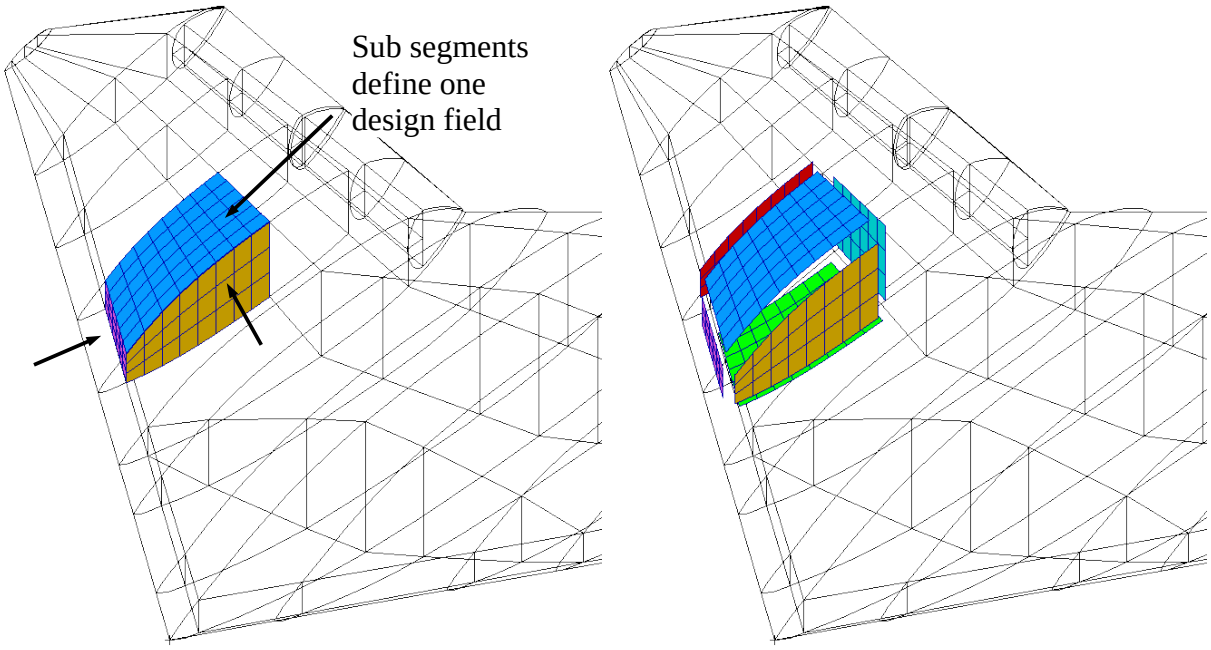

Figure 3.11: Design fields are defined for every skin, spar and rib sub segments

to minimize the structural weight, see equation (2.65), while the constraints $\mathbf{g}$ are satisfied, see equation (2.66). As constraints $\mathbf{g}$, the failure index (FI) of the CFRP material is evaluated. For the MULDICON, the Tsai-Hill criterion by Azzi and Tsai [5] is selected. This choice is the result of a study on different failure criteria where the Tsai-Hill criterion turned out as the most conservative, see Figure 8 in [15] or Section 3.3 and 4.3 in [13] for more details. The Tsai-Hill criterion

$$FI_{\text{Tsai-Hill}} = \left(\frac{\sigma_1}{R_1}\right)^2 + \left(\frac{\sigma_2}{R_2}\right)^2 + \left(\frac{\tau_{12}}{S}\right)^2 - \frac{\sigma_1\sigma_2}{R_1^2} \tag{3.10}$$

relates the stresses σ_1 and σ_2 and shear τ_{12} in material coordinates to the maximum allowable stresses R_1 and R_2 and maximum allowable shear S of the CFRP material. The failure condition is given by

$$FI \geq 1.0. \tag{3.11}$$

Because of the an-isotropic characteristics, one needs to distinguish tensile and compression strength. The strength properties of the CFRP material are selected as given in Table 3.5.

R_1^t	R_1^c	R_2^t	R_2^c	S
833 MPa	250 MPa	16.67 MPa	66.67 MPa	25 MPa

Table 3.5: Strength properties of the CFRP material

The 115 design fields comprise 5358 shell elements. As shown in Table 3.3, every element consists of a stack of 20 individual layers. For the MULDICON, all 20 layers are modeled individually as described in Section 3.2, resulting in 20 FI per element. This leads to 107160 structural responses and constraints $\mathbf{g}$ for every load case. The side constraints imposed on $\mathbf{x}$ are the minimum and maximum allowable layer thickness $t_{k,min} = 0.125mm$ and $t_{k,max} = 1.0mm$. However, only $t_{k,min}$ is of practical importance as $t_{k,max}$ is virtually never reached. All layers are scaled linearly to ensure the desired volumetric laminate definitions given in Table 3.2 are not corrupted. With 20 layers, this leads to a minimum skin thickness $t_{min} = 2.5mm$.

Other, additional failure criteria could be matrix failure or buckling. Next to the material thickness of the shell elements, the blending of the fiber layers could be considered and the dimensions of the stifferens and stringers could be adjusted. That would lead to additional modelling work and to additional constraints $\mathbf{g}$, which would decrease the performance of the

optimization. This is still an active field of research, a good overview of the current state of the art is given e.g. by Bramsiepe et al. [14]. For simplicity, only fibre failure is considered in this work.

3.6.2 Applied Load Cases

The maneuver load cases consist of two groups. Vertical maneuvers following CS 25.337 include pull up with $N_z = 2.5$, horizontal level flight with $N_z = 1.0$ and push down with $N_z = -1.0$. The load factor for push down at VD/MD is reduced to $N_z = 0.0$. They are calculated for all mass configurations, altitudes and flight speeds, resulting in 270 maneuver load cases. The vertical maneuvers are completed by a number of so-called design maneuvers that are performed at sea level, with VD and for the basic flight design mass (BFDM) only. For the MULDICON, mass configuration M12 corresponds to BFDM. These design maneuvers include high pull up and push down load factors, roll rates p and roll accelerations $\dot{p}$ and various combination of them.

	Number	Description
Mass configurations	9	All (M1, M2, M3, …) → see Table 3.4
Altitudes	5	FL000, FL055 / FL075, FL200, FL300 and FL450
Speeds	2	VC/MC, VD/MD
Vertical maneuvers	3	Pull up, horizontal level flight, push down For all masses, altitudes, speeds
Sub-total	270	
Design maneuvers	36	At FL000, VD and M12 only
Total	306	

Table 3.6: Overview of maneuver load cases

The gust load cases are calculated following CS 25.341. They include positive (from below) and negative 1-cos gusts (from above) with gust gradients $H = 9.0 \ldots 107.0m$. The reference gust velocity $U_{\mathrm{ref}} = 17.07[m/s]$, given at sea level, is reduced with increasing altitude and is reduced further at dive velocity VD. In addition, a flight profile alleviation factor $F_g \approx 0.78$ at sea level is established based on aircraft specific parameters such as maximum landing weight, maximum take off weight, etc., and linearly increased to $F_g = 1.0$ at the maximum operating altitude. The design gust velocity U_{ds} is then given by

$$U_{\mathrm{ds}} = U_{\mathrm{ref}} \cdot F_g \cdot \left[\frac{H}{107.0}\right]^{1/6}, \tag{3.12}$$

leading to the 1-cos shaped gust

$$U = \frac{U_{ds}}{2}\left[1 - cos\left(\frac{\pi s}{H}\right)\right] \quad for \quad 0 \leq s \leq 2H \tag{3.13}$$

in dependence of the distance s penetrated into the gust. For example, the design gust velocities U_{ds} to be considered for the MULDICON at VC/MC and at sea level range from 8.76 to 13.23 m/s. To reduce the number of gust load cases, only four mass configurations and only three altitudes are considered, leading to 336 gust load cases.

	Number	Description
Mass configurations	4	M1, M3, M11 and M13
Altitudes	3	FL000, FL200, FL450
Speeds	2	$VC/MC, VD/MD$
1-cos gusts	14	H = 9.0, 15.0, 30.0, 46.0, 61.0, 76.0, 107.0 m positive and negative
Total	336	

Table 3.7: Overview of gust load cases

The landing load cases are selected following CS 25.473 ff. Three main types of landing conditions are considered: one-wheel, two-wheel and three-wheel landings. For maximum landing weight (MLW), the sink speed is specified with 3.05 m/s and for maximum take-off weight (MTOW) only with 1.83 m/s. Note that there are many more landing and ground load conditions such as drift landings, tail-down landings, breaking, turning, etc. that are not considered at this point. Combination of all parameters leads to 12 landing load cases.

	Number	Description
Mass configurations	2	MLW = M3 and MTOW = M13
Altitude	1	Start at 2.0 m above ground
Speeds	2	VL_1, VL_2
Sink rates	2	3.05 m/s (10 ft/s) and 1.83 m/s (6 ft/s)
Landing cases	3	One-wheel, two-wheel, three-wheel landings
Total	12	

Table 3.8: Overview of landing load cases

3.6.3 Overview of Material and Optimization Parameters

This section is intended to gather the material properties and give an overview on the most important optimization parameters.

Optimization parameters

Design objective:
- Minimum weight (see Section 2.10.2)

Design variables:
- Skin thickness of 115 design fields (see Section 3.6.1)

Constraints:
- Material failure determined by the Tsai-Hill failure index of every uni-directional fiber layer (see Section 3.6.1)
- $FI \leq 1.0$
- 20 layers per element, 5358 shell elements (see Section 3.2), 107160 responses per load case

Side constraints:
- Minimum and maximum skin thickness
- $\mathbf{x}_{lower} \leq \mathbf{x} \leq \mathbf{x}_{upper}$

Load cases:
- 306 maneuvers
- 336 gusts
- 12 landing cases
- Selection of dimensioning load cases via time snapshots and envelopes (typically F_z, M_x, M_y) at monitoring stations (see Section 2.8)
- Typically 50 to 65 dimensioning load cases

Material properties

Laminate definitions for different components (see Section 3.2):

Component	Spars	Ribs	Skin
Selected Laminate $[0°/\pm 45°/90°]$	$[10/80/10]$	$[10/40/50]$	$[40/40/20]$

Material properties of the uni-directional fiber layer (see Section 3.2):

E_1	E_2	ν_{12}	G_{12}
155000 MPa	8000 MPa	0.3	3700 MPa

Strength properties of the CFRP material (see Section 3.6.1):

R_1^t	R_1^c	R_2^t	R_2^c	S
833 MPa	250 MPa	16.67 MPa	66.67 MPa	25 MPa

3.6.4 Optimization Results

For the structural optimization, the MONA-L(o)K process, as outlined in Section 2.10.2, is executed. The outer optimization loop, see Figure 2.15, is repeated until convergence is achieved. The convergence is judged from the structural net mass, plotted in Figure 3.12. In the first loop, an initial material thickness is set. For the MULDICON, the initial material thickness is set at the lower boundary of $t_{min} = 2.5mm$, resulting in an initial mass of

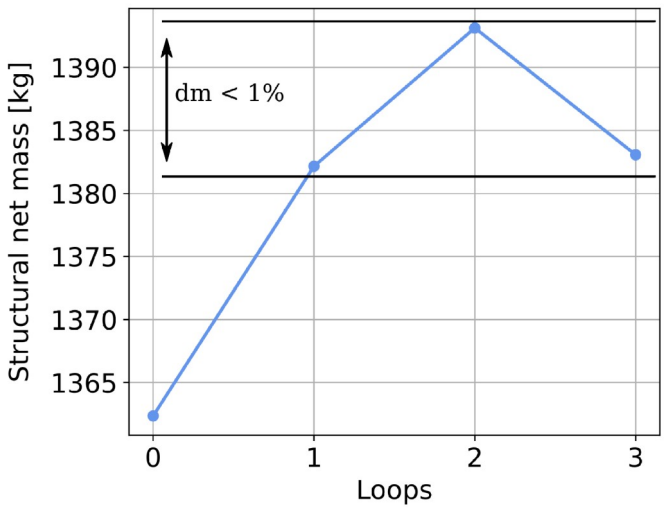

Figure 3.12: Convergence history of structural net mass of the MULDICON-F

g

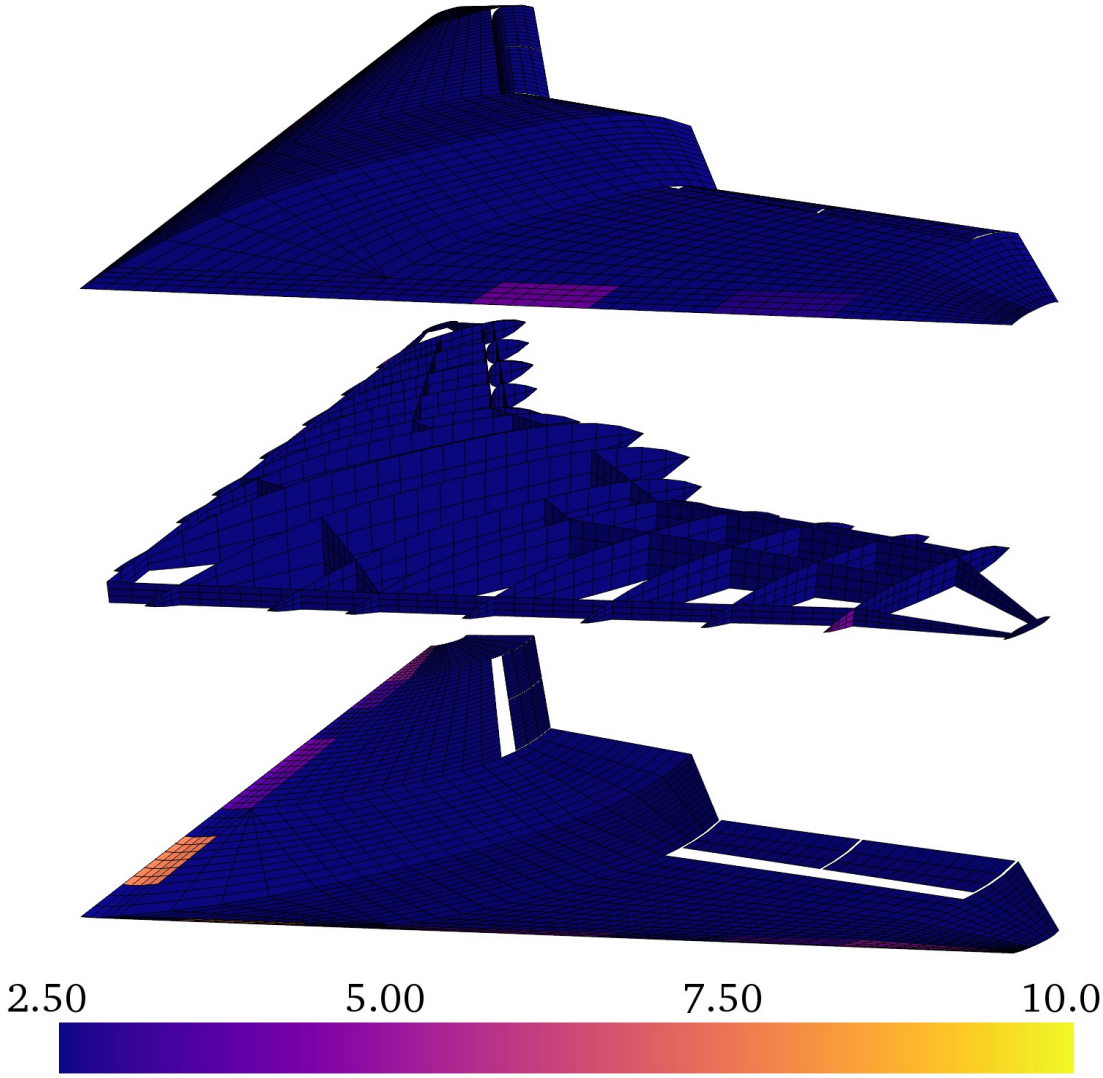

Figure 3.13: Resulting material thickness distribution of skin, spars and ribs in [mm]

1362kg. The optimizer is then expected to increase the material thickness until all constraints $\mathbf{g}$ are satisfied. A different strategy is to start with a high material thickness so that the optimizer has to reduce the material thickness and moves towards a minimum weight. Theoretically, both strategies should work equally. Practically, the second strategy seems to be more robust in some cases and should be used if the first strategy fails due to numerical reasons. One common issue is for example that too many constraints $\mathbf{g}$ might be violated simultaneously.

It can be seen that the structural net mass only changes slightly over the loops. After four loops, the structural net mass is considered as converged as the changes are below 1%. The final structural net mass is 1383kg. As the final structural net mass is only slightly higher than

the initial mass, it can be concluded that only minor changes needed to be done to the structural model. Although the dimensioning criterion of the CFRP material is selected conservatively, the material thickness is in most areas the minimum thickness of $t_{min} = 2.5mm$ and only some regions along the leading edge and at the wing tip are reinforced as can be seen from the material thickness distribution in Figure 3.13. This can be explained by the geometrical shape, which is rather thick in the center region to accommodate the engine and to provide space for payload, fuel and other aircraft systems. At the same time, the wing is very short and thus produces comparatively low bending moments. Although payload and landing gear bays are planned, the outer skin is closed in the structural model. Additional cutouts for payload and landing gear doors might weaken the structure, leading to a different result. Investigations on this topic are not subject of this work.

Next to the structural mass, the dynamic characteristics of the aircraft structure is important. A modal analysis is performed in combination with a Guyan reduction as described in Section 2.4. The first ten eigenmodes of mass configuration M12 are plotted in Figures 3.14 to 3.23. The first mode has an eigenfrequency of ~14 Hz, already indicating a very stiff aircraft structure. The eigenfrequency increases rapidly up to ~57 Hz for the tenth mode. In all cases, there is a strong coupling of wing bending and wing twist. This is different from classical wing-fuselage-empennage configurations where there are typically modes of pure wing bending and pure wing twist. In most cases, there is also an interaction between the wing and the fuselage region. Looking at the example of the second mode in Figure 3.15, both wings bend upward. In addition, the aircraft nose moves upward and the rear downward. Modes 5 and 8 in Figures 3.18 and 3.21 show further combinations of wing, nose and rear deflections plus torsion. Another important observation is that the eigenmodes have global characteristics and are free from local modes, indicating a successful application of the Guyan reduction.

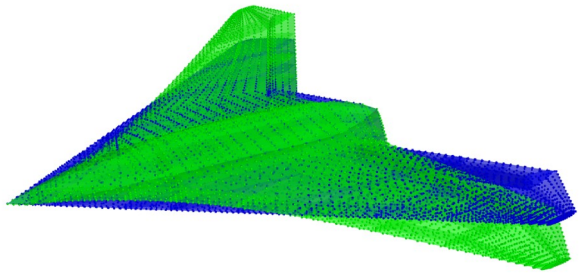

Mode 1, 14.2402 Hz
1st antisymmetric wing bending

Figure 3.14: MULDICON-F M12, Mode 1

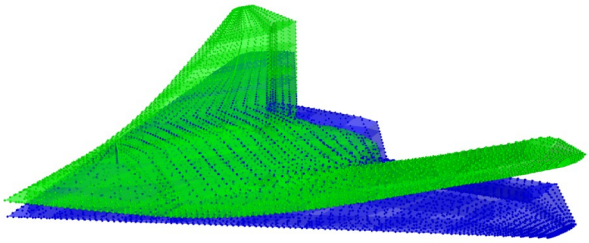

Mode 2, 18.5003 Hz
1st symmetric wing bending

Figure 3.15: MULDICON-F M12, Mode 2

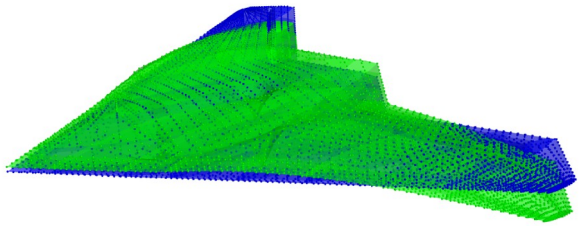

Mode 3, 26.6575 Hz
2nd symmetric wing bending

Figure 3.16: MULDICON-F M12, Mode 3

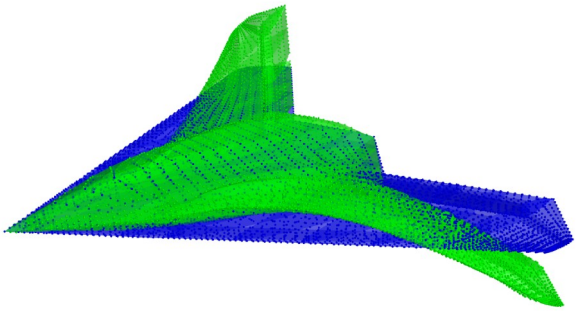

Mode 4, 28.2264 Hz
2nd antisymmetric wing bending

Figure 3.17: MULDICON-F M12, Mode 4

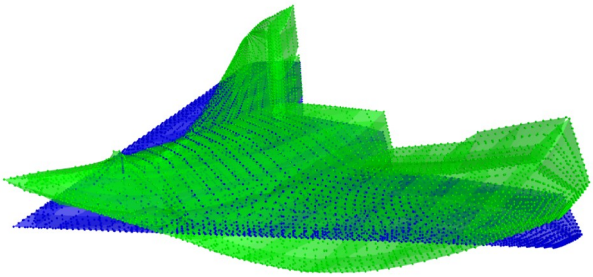

Mode 5, 30.7719 Hz
3rd symmetric wing bending plus torsion

Figure 3.18: MULDICON-F M12, Mode 5

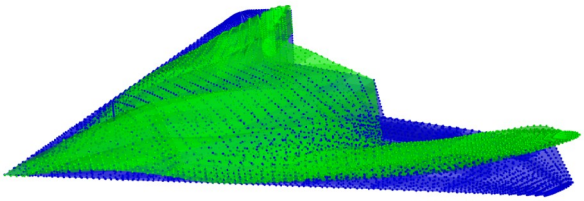

Mode 6, 42.1920 Hz
3rd antisymmetric wing bending

Figure 3.19: MULDICON-F M12, Mode 6

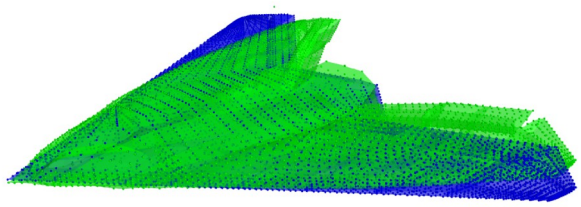

Mode 7, 42.6304 Hz
1st lateral symmetric wing bending

Figure 3.20: MULDICON-F M12, Mode 7

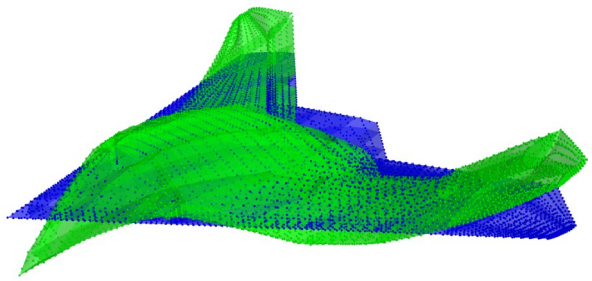

Mode 8, 48.5697 Hz
4th symmetric wing bending plus torsion

Figure 3.21: MULDICON-F M12, Mode 8

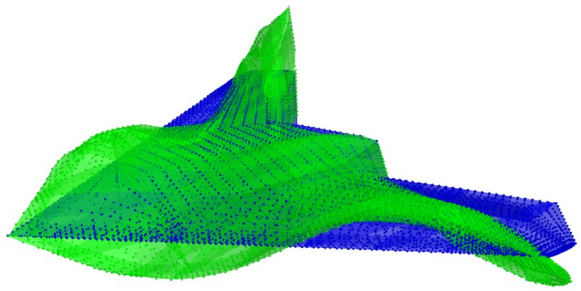

Mode 9, 50.9687 Hz
4th antisymmetric wing bending

Figure 3.22: MULDICON-F M12, Mode 9

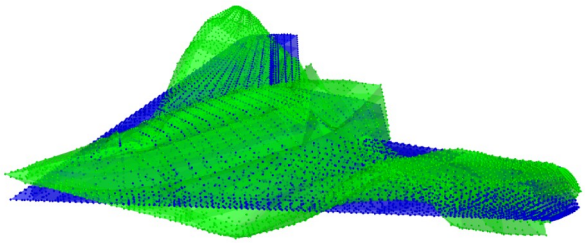

Mode 10, 57.9827 Hz
5th antisymmetric wing bending

Figure 3.23: MULDICON-F M12, Mode 10

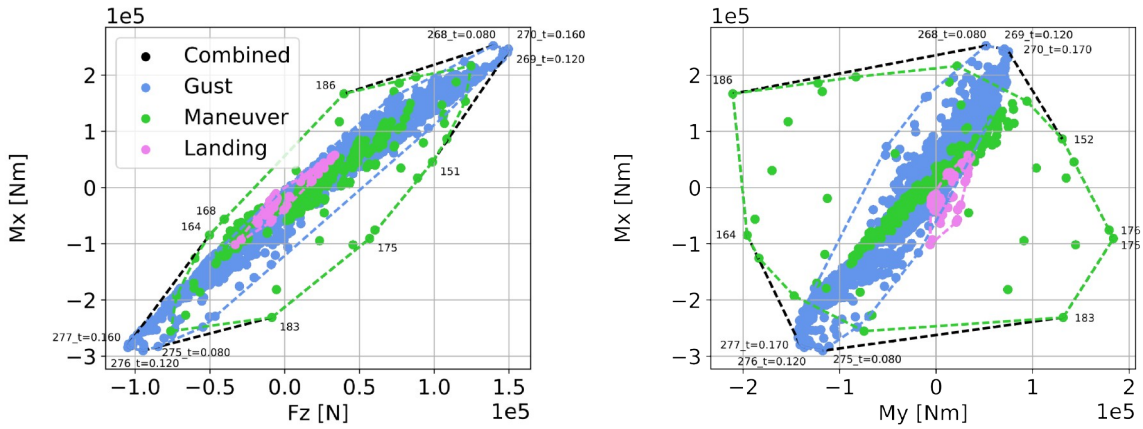

Figure 3.24: Loads envelope of shear force F_z, bending moment M_x and torsion moment M_y at the right wing root

In a last step, the dimensioning load cases and the corresponding section loads are determined, following the procedure described in Section 2.8. In Figure 3.24, the loads envelopes of shear force F_z, bending moment M_x and torsion moment M_y are shown for the right wing root. The loads envelopes of maneuver, gust and landing are shown in green, blue and violet color respectively. One dot represents one load case or one snapshot identified from a time simulation. In Figure 3.24 on the left, the envelopes of shear force F_z and bending moment M_x have a slender shape and extend from the bottom left (both F_z and M_x negative) to the top right corner (both F_z and M_x positive). For the MULDICON, the shear force F_z and bending moment M_x are roughly of the same order of magnitude, indicating a rather low bending moment M_x. This is as expected but in contrast to wings of higher aspect ratios. In Figure 3.24 on the right, the envelopes of torsion moment M_y and bending moment M_x have a more round bodied shape. This is especially true for the maneuver loads. The control surface deflections, required for high roll rates p and roll accelerations $\dot{p}$ during pull-up or push-down, add additional forces along the trailing edge. These control surface forces have a rather

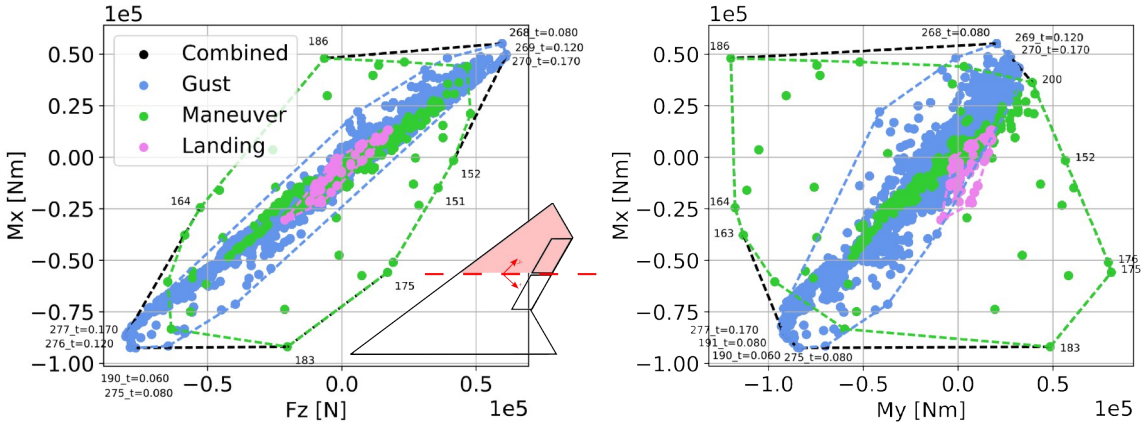

Figure 3.25: Loads envelope of shear force F_z, bending moment M_x and torsion moment M_y at the outer wing

long lever arm with respect to the y-axis of the monitoring station sketched in Figure 3.24, causing a higher torsion moments M_y than for example a gust encounter. The gust loads show higher shear forces F_z and bending moments M_x than the maneuver loads. The landing loads are well within the envelopes of maneuver and gust loads. Finally, the combination of maneuver, gust and landing loads is plotted in black color. The load cases identified by this combined envelope are the dimensioning load cases for the MULDICON.

In Figure 3.25, the loads envelopes for the outer wing are shown. Comparing the envelopes of the wing root (Figure 3.24) and the outer wing (Figure 3.25), the shapes of the envelopes are comparable but the loads are of smaller magnitude. The dimensioning load cases identified by the combined envelope are nearly the same, too.

These plots contain much information and highlight the importance of a sophisticated load case selection. To reduce the amount to data, many studies tend to use small numbers of load cases, often even less than 10 different cases. Such a reduction affects the meaning of the results. Therefore it is better to calculate many different load cases and to identify the dimensioning cases afterwards. This reduces the chances of missing an important load case.

Note: The aeroelastic models presented in this section are released as MULDICON-F. Due to the continuous evolution and updates to the models and methods, the aeroelastic models used in Sections 4, 5 and 6 show slight differences which are due to the modified coupling procedure as explained in section 3.5.

4 Physical Effects of an Open Loop Gust Encounter

The investigations on the physical effects of the open loop gust encounter address the first major topic of this thesis. As mentioned in the introduction, a flying wing has a very distinct, physical behavior during a gust encounter, deviating from classical wing-fuselage-empennage configurations. The effects of the open loop gust encounter will be examined at the example of two different flying wing configurations. A summary of the results from Sections 4.1 and 5 has been published on a conference [203] and as a journal article [204].

4.1 Example One: Flying Wing of Low Aspect Ratio

A first effect is the penetration of the MULDICON into the gust field, visualized in Figure 4.1. The aerodynamic force vectors due to the gust are shown in red color and the unsteady aerodynamic contributions are shown in cyan color. Note that the magnitude of the vectors is scaled non-linearly to highlight small forces. The qualitative meaning is enhanced while the quantitative meaning is lost. The selected gust is the shortest according to certification specifications, has a gradient $H = 9m$ (total length = 18m), a positive orientation (gust from

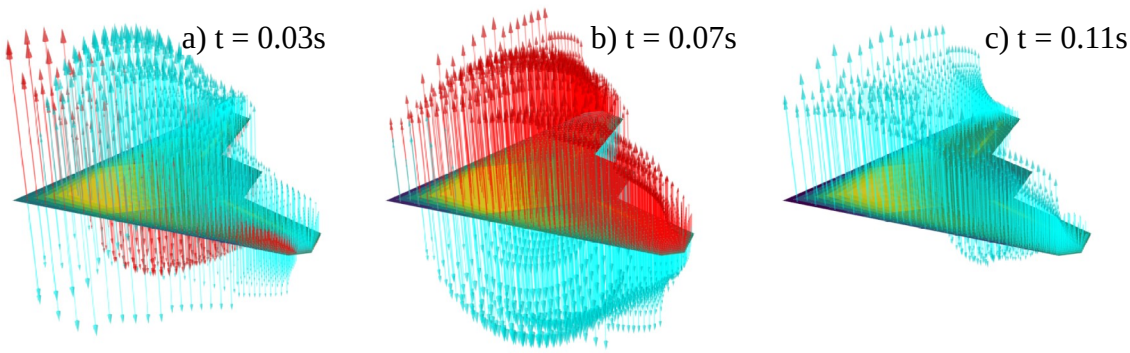

Figure 4.1: Temporal evolution of aerodynamic gust forces (red) and unsteady forces (cyan) on the MULDICON

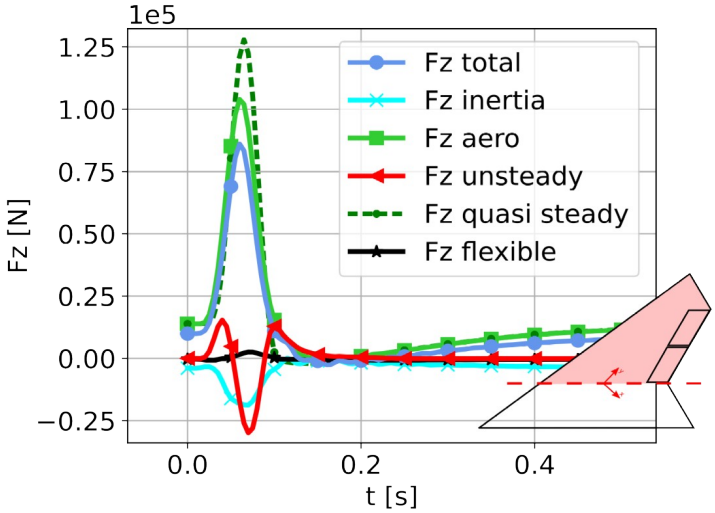

Figure 4.2: Composition of the right wing root shear force F_z of the MULDICON in detail

below) and a gust velocity of 8.76 m/s. The selected mass configuration is M11 at cruise Mach number $MC = 0.8$ and at sea level. In Figure 4.1 a), the gust has just reached the aircraft nose, resulting in gust forces (red) pointing upwards. The additional lift at the nose immediately induces velocities on the other areas of the aircraft, for example on the rear fuselage and the wing tips. Due to the sudden change in downwash, unsteady aerodynamic forces (cyan) occur, counteracting the impact of the gust and thus introducing the lagging behavior. The delay in time due to the propagation of disturbances within the fluid is captured by the DLM. In Figure 4.1 b), the aircraft is approximately in the center of the gust field. The gust shape is clearly visible when looking at the gust force vectors (red). In Figure 4.1 c), the aircraft has just left the gust field and there are no more aerodynamic gust forces (red) visible. However, the gust has still an indirect impact on the aircraft as the unsteady aerodynamic forces (cyan) are still active while the flow condition returns to a normal state. In contrast to Figure 4.1 b), they point upwards. Their magnitude will decrease quickly within the next time steps. Note that in this implementation, unsteady effects are also calculated for flexible and rigid body motion. As the aircraft is still in motion, these unsteady forces remain and fade out slowly.

This physical behavior is also reflected in the section loads. Here, a quantitative assessment is possible. Figure 4.2 shows the contributions of different forces to the shear force F_z at the right wing root. The quasi-steady aerodynamics are plotted with the green dashed line whereas the red triangles refer to the unsteady ones. As expected from Figure 4.1, the

unsteady aerodynamic forces first act in the same direction as the quasi-steady aerodynamics (positive sign) and then start to counteract (negative sign) and have a negative peak at ~0.07s when the aircraft is completely immersed in the gust field, compare with Figure 4.1. Therefore, they not only reduce the peak of the quasi-steady aerodynamics but also cause the peak to occur earlier in time. The sum of both lead to the aerodynamic forces plotted with green squares. The inertia force is plotted with cyan crosses. The sum of both leads to the total force, plotted with blue dots. Finally, the aerodynamic force due to structural flexibility are plotted with black stars. One can see that they only have a minor contribution.

Figure 4.3: A traditional weathercock [87]

Reminder: The weathercock effect

On many churches and older building in the countryside, a weather vane with the shape of a cock is installed on the roof top. The weathercock rotates about a vertical axis and the head always turns in the direction of the wind, because the tail area behind the rotational axis is slightly larger than the rest of the bird. The free-flying aircraft rotates about its center of gravity. Like the weathercock, the naturally stable aircraft is expected to turn in the direction of the gust.

Another physically interesting effect is the rigid body motion of the aircraft in the gust field. The MULDICON is designed with only a small stability margin of $\approx 3.0\% MAC$ to achieve high maneuverability. Therefore, the aerodynamic center is close to the center of gravity. In a gust encounter, this should result in a comparatively large heave motion and only a small pitching motion because the pitching moment about CG is small. However, due to the lack of an empennage, the MULDICON is very sensitive to the pitching motion. The flight characteristics are studied more closely by examining the pitch angle Θ and the pitch rate q. Figure 4.4 shows the results for a series of positive gust encounters (gust from below) of one mass configuration (M11) and gust gradients ranging from $H = 9m$ to $107m$. In all cases, the aircraft experiences a positive, nose up pitching motion. This is contrary to the behavior observed with classical configurations which typically dive into the gust (weathercock effect, nose down). The pitch up presumably increases the aircraft loads.

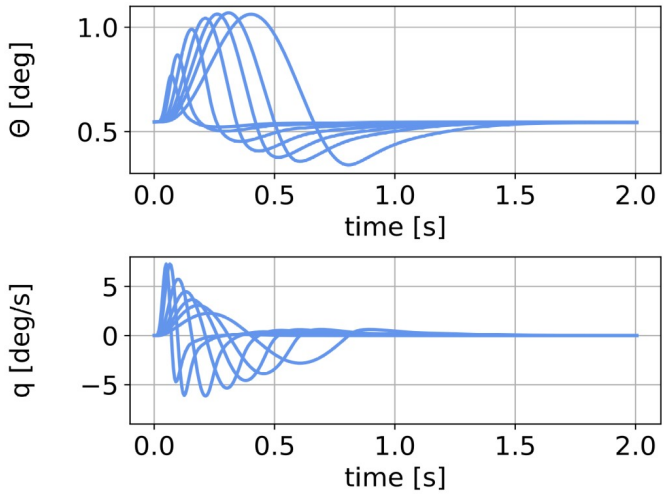

Figure 4.4: Pitch angle Θ and pitch rate q for a series of gust encounters of the MULDICON

A quantification of the loads due to the pitching motion is achieved by comparing a free-free gust encounter with a gust encounter with supported pitching motion q. Only the heave motion is allowed. The results for the shear force F_z, bending moment M_x and torsion moment M_y at the right wing root are shown in Figure 4.5. The difference between the free-free and supported loads in blue and green can only be attributed to the pitching motion.

As an alternative to the dynamic, unsteady 1-cos gust simulation, the Pratt formula can be used. Following Pratt, gusts are converted to an equivalent load factor N_z. More detailed information can be found in CS 23.341 [47], in NACA Technical Note 2964 [146] and Report 1206 [147]. The loads are then calculated as quasi-static maneuvers for both positive and negative gusts. Handojo [57] showed that the Pratt formula agrees well with the results from

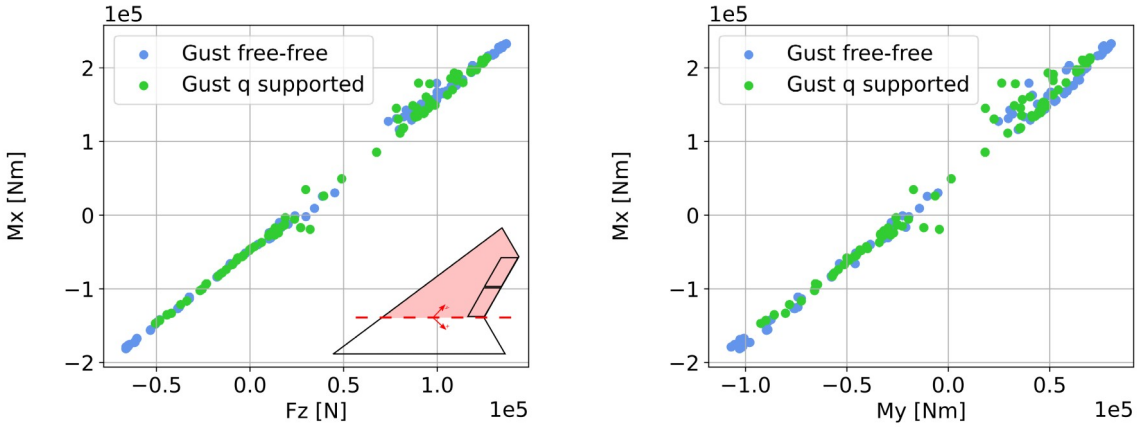

Figure 4.5: Comparison of free-free and supported loads envelopes of shear force F_z, bending moment M_x and torsion moment M_y at the right wing root

the dynamic, unsteady 1-cos gust simulation for transport type aircraft. The applicability of the Pratt formula on flying wings has been studied by Voß and Klimmek [205] and shall be evaluated for the MULDICON as well.

The shear force F_z, bending moment M_x and torsion moment M_y are shown again in Figure 4.6 for the right wing root. In addition to the section loads extracted from the dynamic, unsteady 1-cos gust simulations, gust loads obtained from the Pratt formula are calculated. These loads need to be superposed with a horizontal level flight, resulting in the combined quasi-steady gust loads plotted in green color. One can see that the section loads extracted from the dynamic 1-cos gust simulations don't agree with the Pratt loads. One reason for this could be the complex unsteady aerodynamic behavior in combination with the penetration effect presented in the previous paragraphs. Another explanation for the disagreement could be the rigid body motion of the aircraft, which includes a strong pitching motion. The Pratt formula, however, assumes pure heave motion. Surprisingly, the findings concerning the magnitude of the loads contradict previous findings by Voß and Klimmek [205], although the configuration is very similar. It can be concluded that a general rule on the magnitude of the Pratt loads can't be found and the reaction of a flying wing to a gust encounter strongly depends on the actual configuration.

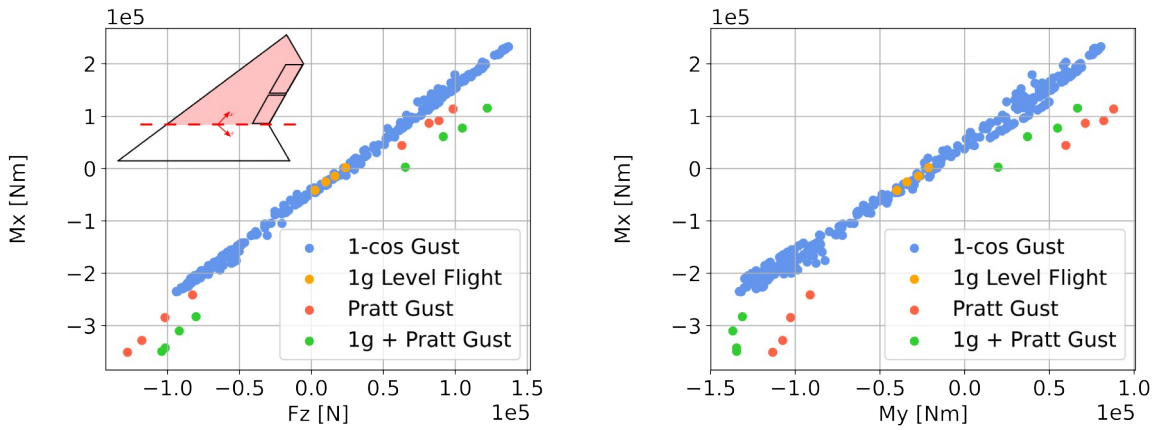

Figure 4.6: Loads envelopes of shear force F_z, bending moment M_x and torsion moment M_y at the right wing root

Summary: The MULDICON shows a strong penetration effect due to its compact, non-slender and highly swept geometry. This causes the unsteady aerodynamics to behave differently than with classical configurations. The MULDICON also shows a pronounced

tendency to pitch up when entering a gust field. It can be shown that the use of the Pratt formula for quasi-steady gust loads is unsuitable.

Remark: The results obtained from a standard approach in the frequency domain are questionable and require additional attention. This is because a harmonic motion is assumed but the rigid body motion, especially the translation in z-direction (gain of altitude), is an aperiodic motion.

4.2 Example Two: Flying Wing for Passenger Transport

Because blended wing body configurations (BWB) are widely studied in literature, see Section 1.2.1, the above study is repeated for a typical BWB configuration. It will be demonstrated that the physical effects observed during a gust encounter exist for BWB configurations as well.

A comprehensive overview on the modeling and control of blended wing body aircraft is given by Kozek and Schirrer [90]. In their book, Chapter 2 is dedicated to the conceptual design [6] and Chapter 3 to the corresponding numerical models [185]. The studies were performed within the related ACFA 2020 project. The ACFA configuration is a very good example of a flying wing and because of the extensive studies performed by the international consortium of engineers and scientists, it has a high degree of maturity.

The main difference of the ACFA configuration with respect to the MULDICON is the size and mass of the aircraft. Designed for the transport of up to 460 passengers over a distance of 7200 nm, the aircraft has a half wing span of $b_{\mathrm{ref}} = 39.9m$ and a maximum take-off mass of $MTOM = 401.6t$. With a cruise Mach number $MC = 0.85$, the flying speed is well within the transonic regime and comparable to the MULDICON.

The properties of the MULDICON and the ACFA configuration concerning their longitudinal characteristics are compared in Table 4.1. While the reference length of the ACFA configuration is “only” 8 times longer than for the MULDICON, the selected mass configuration is approximately 38 times heavier. And due to the quadratic influence of the length and size, the inertia I_{yy} about the body axis in y-direction is approximately 1200 times larger.

	MULDICON (M11, Table 3.4)	ACFA	ACFA / MULDICON
Mass configuration	$8421kg$	$2 \cdot 159304kg$	37.8
Inertia I_{yy}	$2.208 \cdot 10^4 kgm^2$	$2 \cdot 1.316 \cdot 10^7 kgm^2$	1186.6
Reference length	$6.0m$	$48.92m$	8.15

Table 4.1: Comparison of selected parameters of the MULDICON and the ACFA configuration

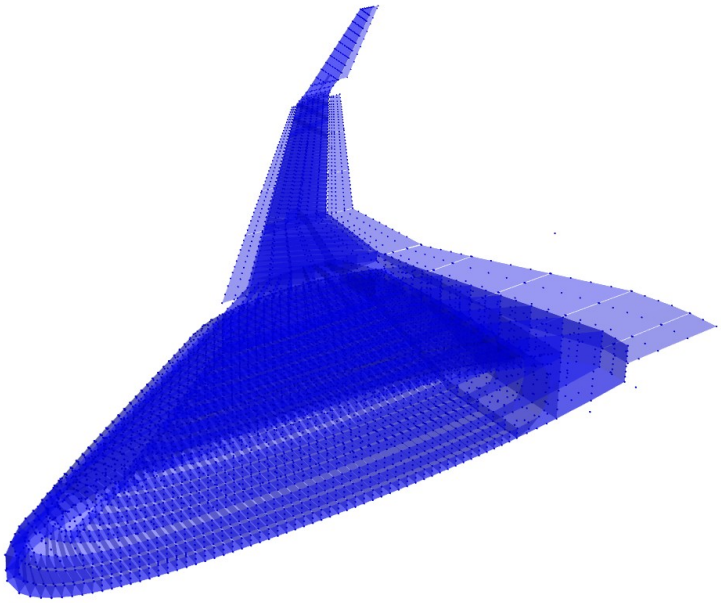

Figure 4.7: Structural grid of the ACFA configuration

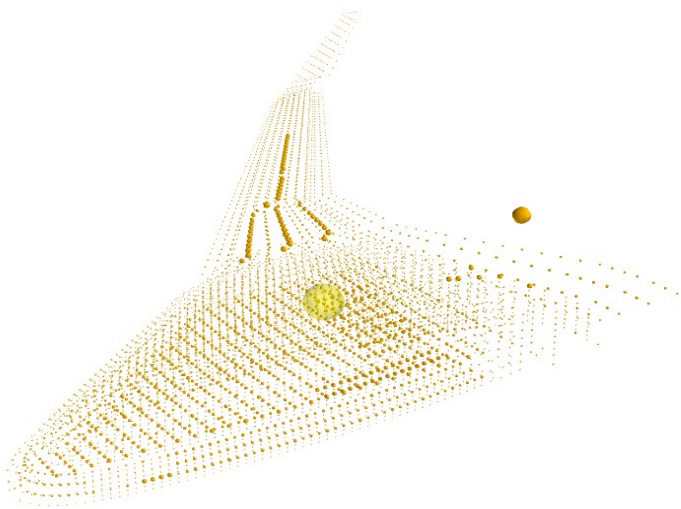

Figure 4.8: Mass discretization of the ACFA configuration

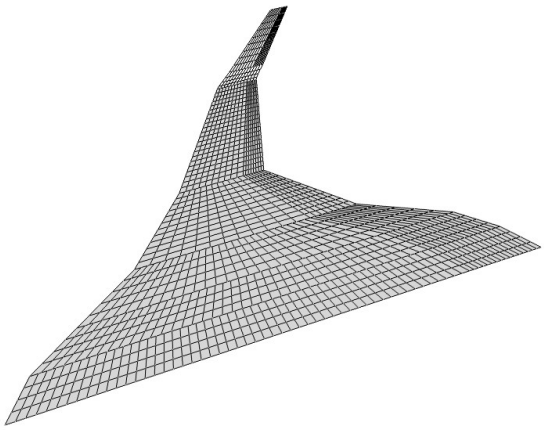

Figure 4.9: Aerodynamic panel mesh of the ACFA configuration

The aeroelastic models of the ACFA configuration are reused with permission in this work and are presented briefly in the following. The structural model shown in Figure 4.7 is a finite elements model with 41784 degrees of freedom and a rather high level of details for the application in structural dynamics. Because only the right half of the aircraft is modeled, care has to be taken during the modal analysis. Constraining the translation in z-direction as well as the roll and yaw motion at the center line allows for the calculation of the symmetrical mode shapes. Assuming a symmetrical aircraft and a symmetrical disturbance by the gust, the antisymmetrical mode shapes are not required.

The aircraft is naturally stable. To allow a good comparison with the MULDICON, the mass configuration is chosen in such a way that the center of gravity is located in its most backward position. The aircraft mass of the half model is $159t$ with the center of gravity located at $CG_x = 24.28m$, corresponding to $CG_x[\%MAC] = -4.55\%$. The corresponding mass discretization is shown in Figure 4.8.

The aerodynamic panel mesh of the ACFA configuration is shown in Figure 4.9. Effects of camber and twist are not considered. The Vortex Lattice Method and the Doublet Lattice Methods used in this work are extended to allow for the calculation of the aerodynamic force of the half model. Therefore, a symmetry option is implemented that calculates the influence of the missing left half on the right half.

The penetration of the ACFA configuration into the gust field is visualized in Figure 4.10. As in the previous section, the aerodynamic force vectors due to the gust are shown in red color and the unsteady aerodynamic reactions are shown in cyan color. Also, the magnitude of the vectors is scaled non-linearly to highlight small forces. As the ACFA configuration is significantly larger than the MULDICON and allowing for a more meaningful comparison with Figure 4.1, the selected gust has a longer gradient of $H = 15m$ (total length = 30m) with a gust velocity of 10.22 m/s. The selected Mach number is 0.61 at flight level FL100. In Figure 4.10 a), the aircraft has just entered the gust field. Similar to Figure 4.1, the gust forces at the aircraft nose cause a change in circulation downstream, along with an unsteady reaction. This concerns not only the fuselage region but also large parts of the wing. Figure 4.10 b) shows the aircraft approximately in the center of the gust field. Although a longer gust is selected, one can see the aircraft length is longer than the gust and the aircraft is not fully submerged in the gust field. The aircraft requires approximately 0.38s to travel the gust field. As soon as the aircraft has left the gust field, the flow conditions return to normal, which is also accompanied by an unsteady reaction that can be seen Figure 4.10 c). Because of a higher degree of structural flexibility of the ACFA configuration, the wing, which has been excited by the gust, is still in motion and causes additional unsteady aerodynamic forces. These motions take a longer time to settle than the motions of the MULDICON, which are dominated by rigid body motion.

The physical behavior observed in Figure 4.10 is quantified in terms of section loads in Figure 4.11. The monitoring station is placed at the right wing root and shows the contributions of different forces to shear force F_z. For comparison, the color scheme is identical to Figure 4.2.

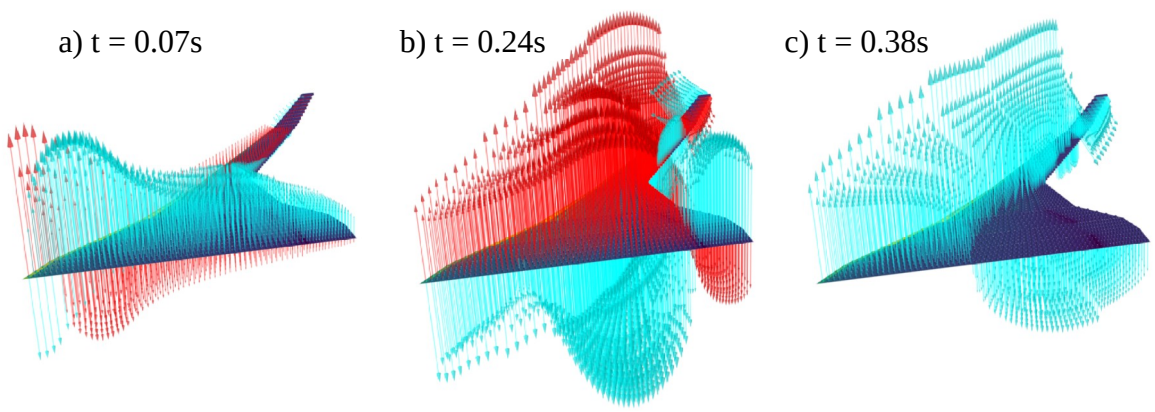

Figure 4.10: Temporal evolution of aerodynamic gust forces (red) and unsteady forces (cyan) on the ACFA configuration

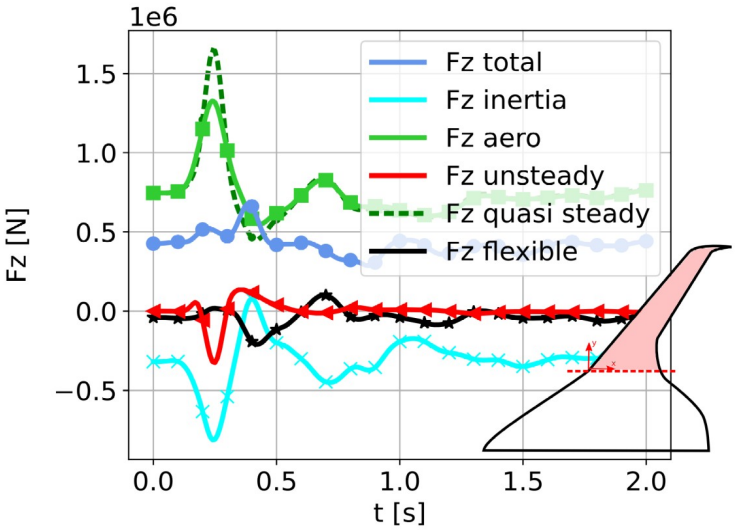

Figure 4.11: Composition of the right wing root shear force F_z of the ACFA configuration in detail

Note that the scale of the x-axis is different and shows the time history from 0.0 to 2.0s. Similar to the MULDICON, the unsteady forces plotted in red reduce the peak of the quasi-steady aerodynamics significantly. It can be seen that the unsteady forces at ~0.2s act in the same direction as the gust force, then start to counteract at ~0.3s. However, this effect is not as pronounced as in Figure 4.2, which can be explained by the different geometry and a lower sweep angle of the ACFA configuration. One significant difference is seen for the forces due to structural flexibility plotted in black. The elastic deformation and oscillation of the wing is much stronger compared to the MULDICON, causing higher aerodynamic forces. This is also reflected in the inertia forces plotted in cyan, which show a much more dynamic behavior. The sum of aerodynamic and inertia forces lead to the total shear force plotted in blue. Compared to the MULDICON, it can be seen that the total shear force of the ACFA configuration is much less effected by the gust.

The ACFA configuration is very sensitive to the pitching motion and lacks an empennage, too. The flight characteristics are studied more closely by examining the pitch angle Θ and the pitch rate q. Figure 4.12 shows the results for a series of positive gust encounters (gust from below) of one mass configuration and gust gradients ranging from $H = 9m$ to $107m$. In all cases, the aircraft experiences a positive, nose up pitching motion. The ACFA configuration shows the same behavior as observed previously with the MULDICON.

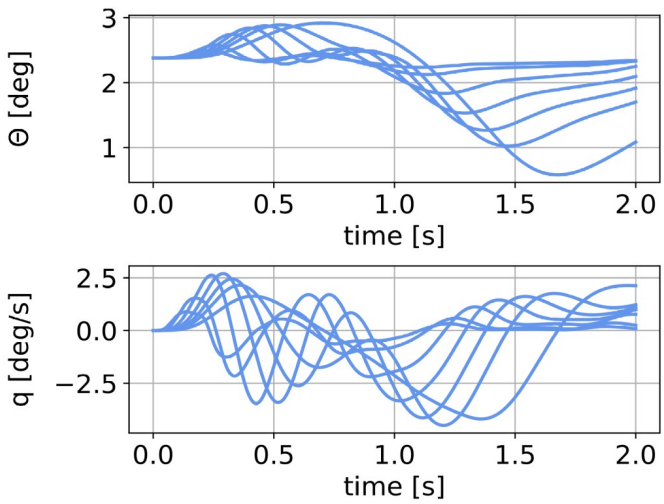

Figure 4.12: Pitch angle Θ and pitch rate q for a series of gust encounters of the ACFA configuration

Summary: The observations with respect to penetration effects and rigid body reaction of a flying wing during a gust encounter are confirmed by the example of a much larger blended wing body configuration.

Remark: Next to the physical effects, this section highlights the flexibility and the generic approach of the Loads Kernel software, which allows to process aeroelastic models that were prepared by completely different organization using different modeling strategies and tools.

5 Physical Effects of a Closed Loop Gust Encounter

In this section, the aim is to investigate the flight characteristics of a naturally unstable configuration while the aircraft is subject to external disturbances such a gust encounter. Then, the aim is to quantify the influence on loads. Aircraft companies typically seek to alleviate the loads [75] due to maneuver and gust encounter to reduce structural loading, save weight and/or increase aircraft life. As the MULDICON structural design is rather robust in terms of mass and material thickness, an increase in loads is acceptable and potentially necessary to achieve a flight under naturally unstable conditions. The effects of a flight controller are first studied on the naturally stable aircraft in Section 5.2, the unstable case is investigated in Section 5.3.

5.1 Active Pitch Control

The flight controller for the MULDICON considered in this work is restricted to the control of the pitching motion only. A commanded pitch angle $\Theta_{\text{com.}}$ must be maintained and the deviations should be small. As the pitch angle Θ is an integral value, the control of the pitch rate $q_{\text{com.}}$ is better suitable to achieve quick reaction times. The proposed pitch controller is shown in Figure 5.1 and consists of two cascaded feedback loops. The commanded pitch rate $q_{\text{com.}}$ may stem from the pilot's stick command or a flight path control system shown in gray

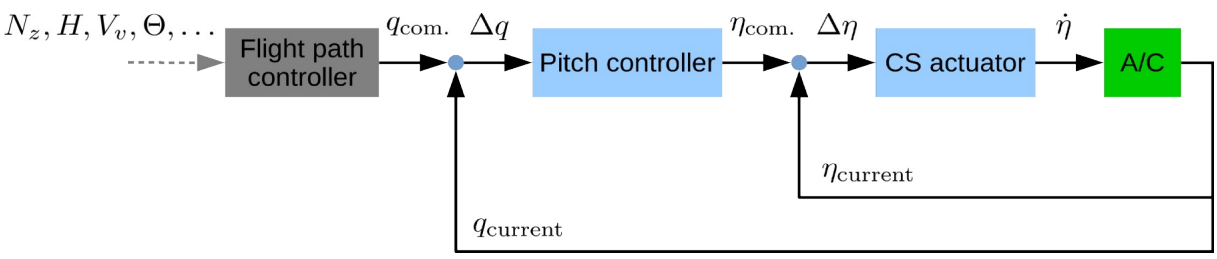

Figure 5.1: Layout of a flight controller for pitching motion

color. For simplicity, the commanded pitch rate $q_{\text{com.}}$ is assumed to be given. The flight path control system can be excluded because it is expected to be of much lower frequency. The pitch controller consists of a proportional and an integral control element with coefficients K_p and K_i. The output of the pitch controller is the commanded control surface deflection $\eta_{\text{com.}}$. The control surface actuator consists of a proportional element and returns the control surface rate $\dot{\eta}$. The MULDICON has four control surfaces, as described in Section 3.4. For pitch control, all four control surfaces are desired to behave identically, requiring only one actuator model in the simulation. The actuator becomes non-linear by enforcing a maximal actuator rate $\dot{\eta} = \pm 40°/s$, which is selected in such a way to reflect the abilities of a typical hydraulic actuation system. The two control loops of the pitch controller and the actuator are closed by the feedback of the actual pitch rate q_{current} and the actual control surface deflection η_{current} of the aircraft.

For the design of the controller and the selection of the coefficients K_p and K_i, the aircraft system is linearized at a selected operational point using finite differences and cast into the form of a state space system. The system is then subject to a unit step input and optimized for minimum rise time, settling time and overshoot. For quantification, the Integral of Absolute Error Criterion A_{IAE} is selected as suggested in [113]. The A_{IAE} criterion is based on the absolute difference e of command signal and system reaction. The coefficients are then determined in an iterative procedure.

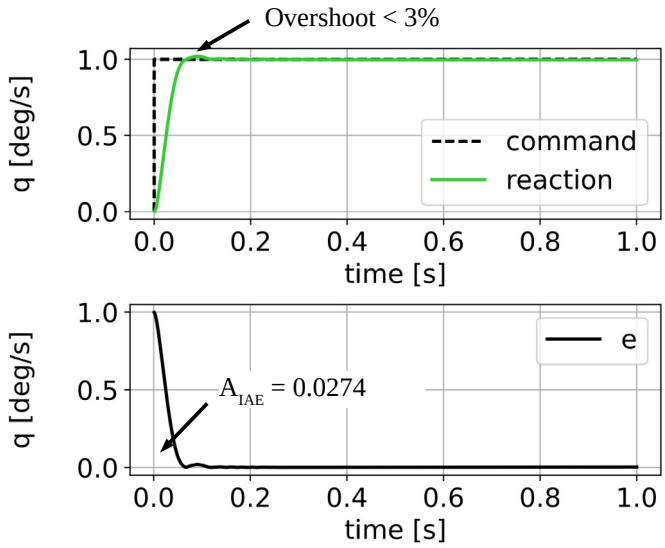

Figure 5.2: Quantification of controller performance

The functionality of the controller is then demonstrated for a series of larger step inputs of the commanded pitch rate $q_{\text{com.}} = \pm 10° s^{-1}$. The dashed line in Figure 5.3 shows the commanded pitch rate $q_{\text{com.}}$ and the continuous line represents the aircraft reaction q_{current}. The closed-loop system follows the desired commands quickly with a slight, quickly decreasing overshoot.

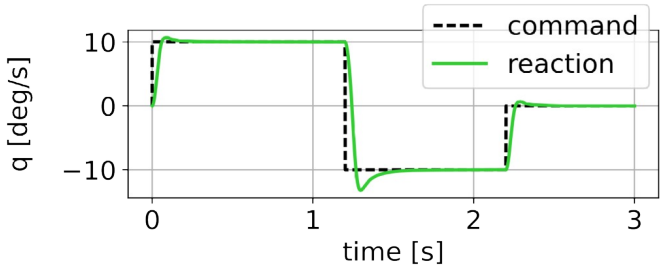

Figure 5.3: Commanded pitch rate $q_{\text{com.}}$ and the aircraft reaction q_{current} for a series of step inputs

The corresponding states of the control surface are shown in Figure 5.4. In the top graph, the commanded control surface deflection $\eta_{\text{com.}}$ of the pitch controller is plotted as a dashed line. The reaction is delayed by the rate limit of the control surface actuator. The bottom graph shows the actual deflection rate $\dot{\eta}$ controlled by the actuator. As mentioned before, a rate limit of $\pm 40° s^{-1}$ is enforced. In this case, that limit is hit three times as indicated by the arrows in the plot.

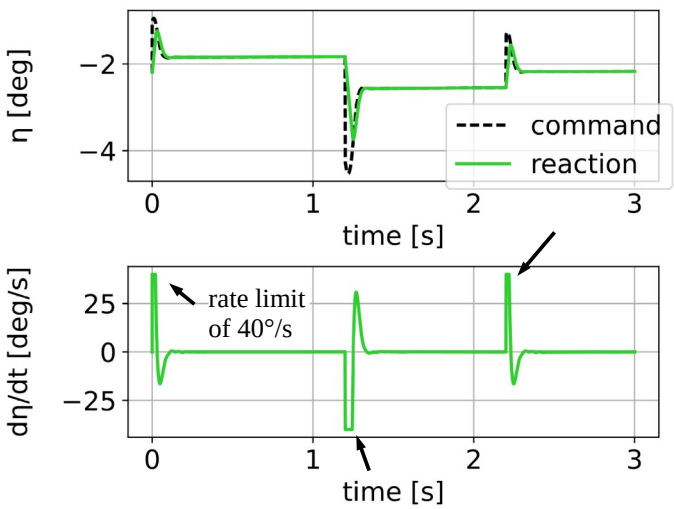

Figure 5.4: Commanded control surface deflection $\eta_{\text{com.}}$ and η_{current} and control surface rate $\dot{\eta}$

Summing up, the controller works as expected. The performance could be improved further by allowing higher deflection rates $\dot{\eta}$ and by increasing the coefficients K_p of the actuator,

which would speed up the control surface deflection as well. From a theoretical point of view, this could result in hitting the rate limit more often and would reduce the capability of the control surface to fulfill other tasks. From the practical point of view, the actuator mechanism might wear out faster.

Sign conventions: Because some authors use different sign conventions, the definitions for the longitudinal motion are given below. See also Figure 2.1, Section 2.1 Coordinate Systems.

Euler angle Θ and pitch rate q positive $\rightarrow$ nose up

Pitch command η and command rate $\dot{\eta}$ positive $\rightarrow$ pilot pulls the stick $\rightarrow$ nose up

5.2 Step One: Naturally Stable Configurations

The gust encounter poses a similar challenge to the controller as demonstrated above, but with a different set-up: the pitch rate $q_{\text{com.}} = 0.0 = const.$ remains constant while the gust diverts the aircraft. The dashed lines in Figure 5.5 show the pitch angle Θ and the pitch rate q of the open loop aircraft. The blue lines show the results of the closed loop system. Comparing the open and closed loop system, the maximum pitch angle is reduced by $\approx 60\%$ and the minimum pitch angle is reduced by $\approx 30\%$ with respect to the initial value. For the open loop system, the minimum and maximum values are reached by the longer gusts while in the closed loop system, the minimum and maximum values are caused by the short gusts. In addition, the short gusts show a more pronounced overshoot, which is also reflected in the pitch rate q. Summing up, it is observed the controller of the closed loop system performs excellently for longer gusts while having troubles with the shorter gusts. This behavior is as expected and caused by physical limitations such as the control surface rate $\dot{\eta}$. Figure 5.6 shows the control surface deflection η and the control surface rate $\dot{\eta}$. Although only small deflections are required, the control surface is moved at high rates, hitting the limit of $\pm 40° s^{-1}$ for the two shortest gusts of $H = 9$ and $15m$. The performance for short gusts can only be improved with higher rates, as discussed before, or by adding prior knowledge of the gust. For classical wing-fuselage-empennage configurations, such information could be obtained by a sensor at the aircraft nose. Depending on the length of the fuselage and the flight speed, this gives some additional time before the gust hits the wing. For flying wings

such as the MULDICON, a future alternative could be LIDAR techniques, measuring the flow field several meters in front of the aircraft, see for example Wang et al. [212].

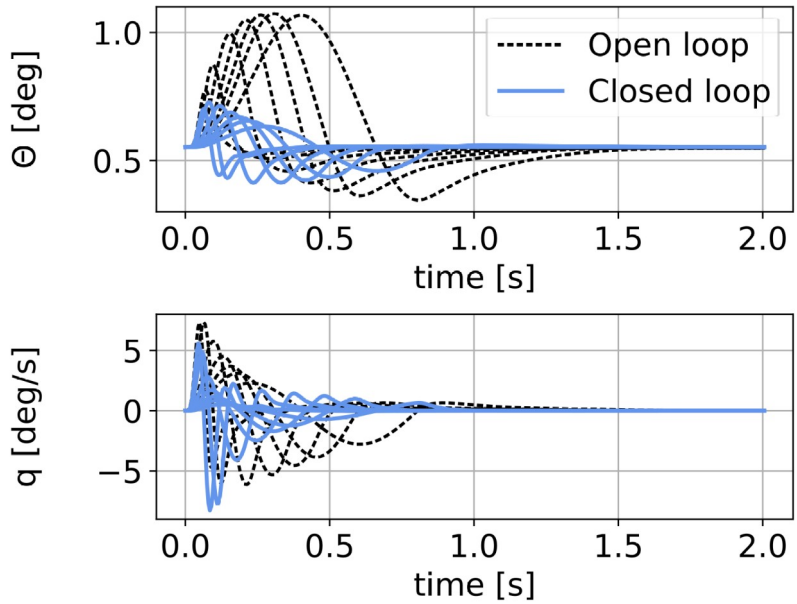

Figure 5.5: Pitch angle Θ and pitch rate q for the closed loop system

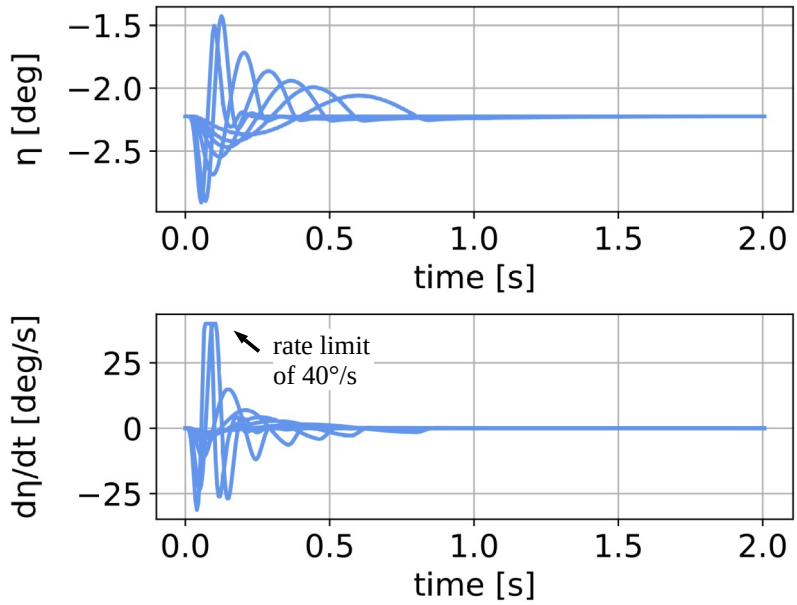

Figure 5.6: Commanded control surface deflection η and control surface rate $\dot{\eta}$

To obtain a first glance on the effect on loads, the load factor N_z shown in Figure 5.7 can be consulted. Because the positive, nose up pitching motion is reduced in the closed loop system, the load factor N_z is reduced as well, suggesting a reduction in loads. The vertical displacement of the aircraft is shown in Figure 5.8. Note that the z-coordinate points downwards and a negative value indicates a higher altitude. For example, the longest gust lifts the aircraft by more than five meters within less than two seconds. Both open and closed loop aircraft reach the same final displacement. The vertical velocity component of the gust is unchanged and induces the same aerodynamic forces acting on the aircraft. Also, the gust length and aircraft speed is unchanged, resulting in the same amount of time the aircraft spends within the gust field. Thus, the energy coming from gust is the same, adding the same (potential) energy in terms of vertical displacement to the aircraft.

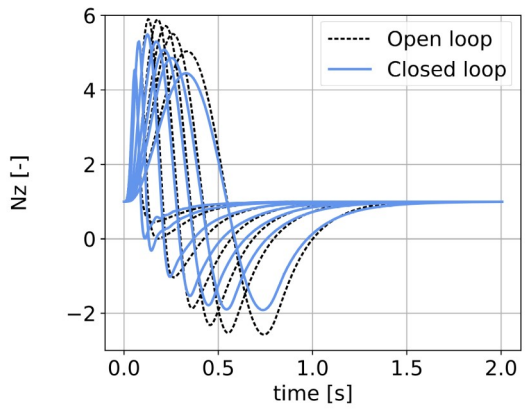

Figure 5.7: Load factor N_z for the closed loop system

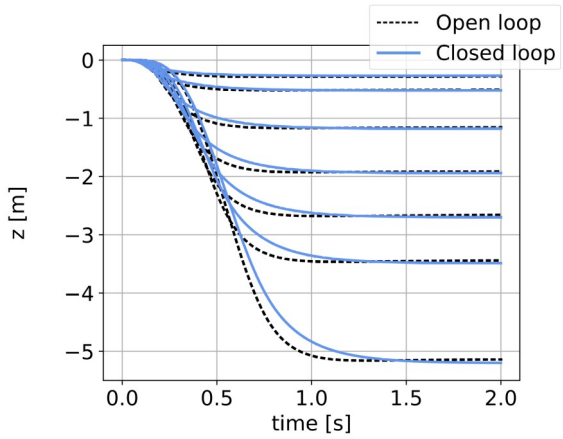

Figure 5.8: Vertical displacement in z-direction

In Figure 5.9, the loads envelopes of shear force F_z, bending moment M_x and torsion moment M_y are shown for the right wing root and in Figure 5.10 for the outer wing. For reference, the gust loads of the open loop simulation are shown as well. It can be seen that while the controller reduced the load factor N_z, this is not generally the case for the section loads. On the one hand, the reduction of the pitching motion reduces loads. On the other hand, the control surfaces add attachment loads along the trailing edge. The envelopes of shear force F_z and bending moment M_x have a similar shape and the closed loop system leads to a slightly lower shear forces F_z and slightly higher bending moments M_x. The two effects more or less balance out. This is not the case for the torsional moment M_y. While bending and shear are more or less balanced, the envelopes of bending moment M_x and torsion moment M_y of the closed loop system appear larger.

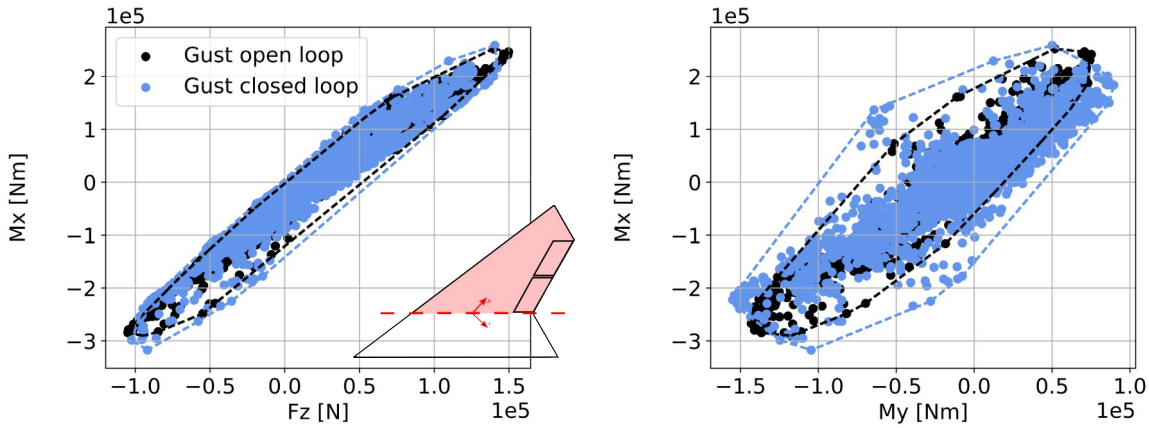

Figure 5.9: Loads envelope of shear force F_z, bending moment M_x and torsion moment M_y at the right wing root

In Figure 5.11, the control surface attachment loads in terms of shear force F_z and hinge moment M_y are shown for the inner and outer control surface. Obviously, the actuator of the closed loop system and the corresponding deflections causes much higher loads compared to the open loop system. These attachment loads are the reason for the increased torsion moment M_y observed in Figure 5.9.

A closer examination of the control surface attachment loads is shown in Figure 5.12. Here, the time histories of the shear force F_z and hinge moment M_y are shown for both the open and closed loop system. For clarity, only one exemplary operating point and seven gust encounters of different gust length from $H = 9m$ to $107m$ are shown. The starting point is the same for all simulations and the direction of time progression is indicated by an arrow.

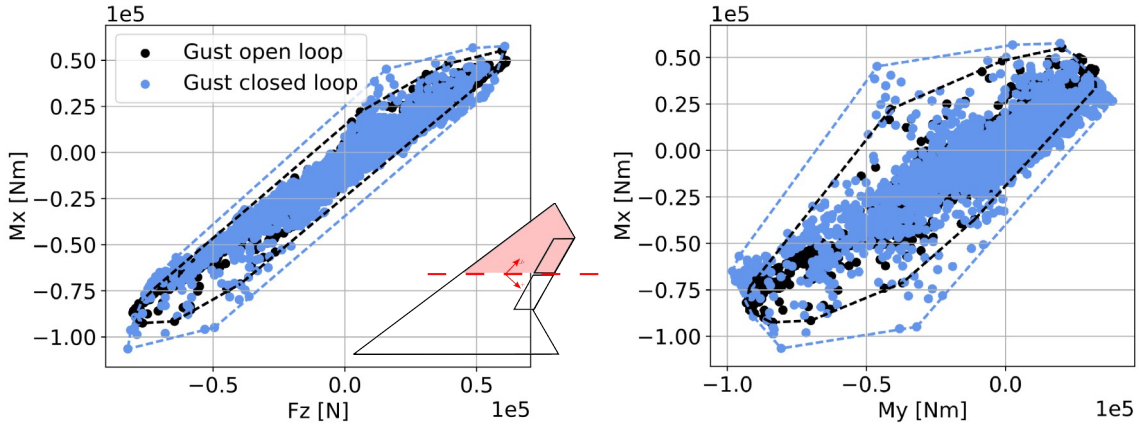

Figure 5.10: Loads envelope of shear force F_z, bending moment M_x and torsion moment M_y at the outer wing

Remark: Not included in the simulation are the inertia forces and moments which might arise due to the acceleration of the control surfaces by the actuator. These are difficult to obtain as in the underlying finite elements model, the control surfaces are not rotated. All other accelerations, e.g. from rigid body motion and structural flexibility, are included.

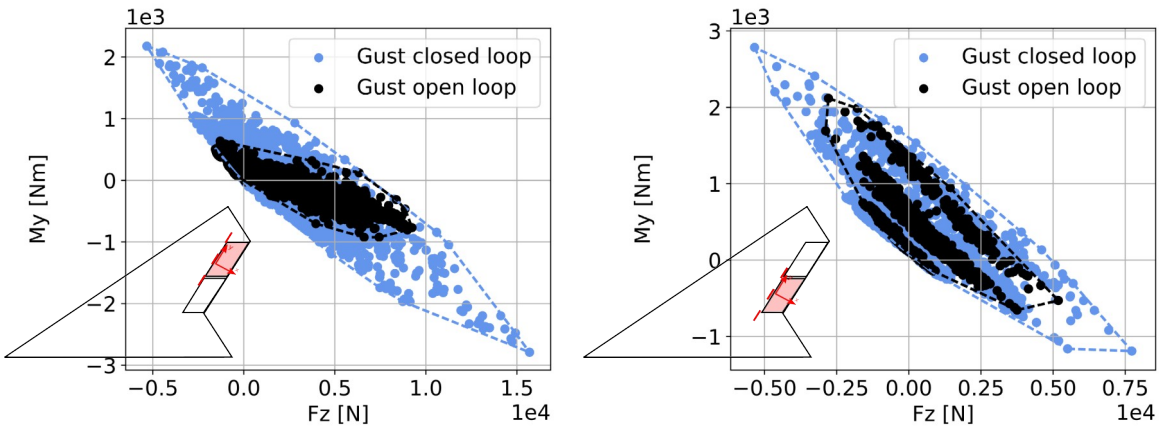

Figure 5.11: Envelope of control surface attachment loads

Comparing with Figure 5.6, the control surface deflections are the largest for short gusts. Correspondingly, the section loads of short gusts should be higher than for the longer gusts. This is confirmed by Figure 5.12. It can be noted there is a large difference between the $H = 30m$ and $H = 15m$ gust. However, there is only little change comparing the $15m$ and $9m$ gusts. One explanation is that the control surface deflections η are of similar magnitude because the control surface rate $\dot{\eta}$ is limited and the limit is hit in both cases, which can be seen from Figure 5.6.

Summary: The MULDICON is exposed to a series of gust encounters with flight control switched on. The longitudinal stability is increased successfully by means of a flight controller at the cost of moderately higher structural loads.

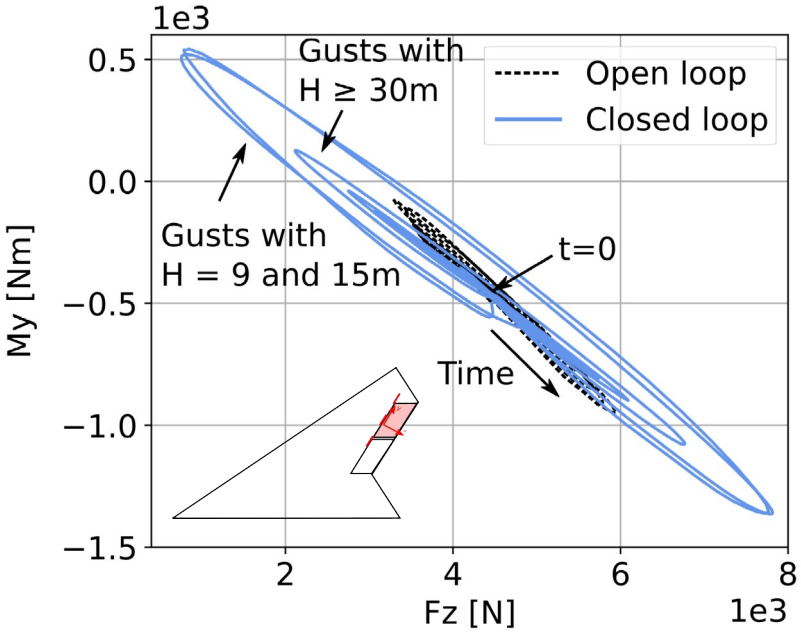

Figure 5.12: Time histories of control surface attachment loads

5.3 Step Two: Naturally Unstable Configurations

The MULDICON has been designed with a positive longitudinal stability and a desired center of gravity approximately at $CG_x \approx -3.0\% MAC$ with the exact value depending on the mass configuration. In this section, the design restriction will be lifted and a rearward shift of CG_x will be allowed, resulting in a naturally unstable configuration. The influence on gust loads is expected to be high as the demand on the flight controller is even higher than in the previous section: no disturbances and gusts are possible for naturally unstable configurations without control.

A naturally unstable configuration might occur due to several reasons. In the current model, two fuel tanks are positioned in front of CG and two fuel tanks behind CG, compare Figure

Figure 5.13: A rearward shift of payload creates a unstable configuration. Left: M11, Right: M11b

in Section 3.3. The fuel tanks could be drained unbalanced, either on purpose or due to a system failure, resulting in a shift of CG. The payload of 2 x 1000 kg is assumed to be in the center of the payload bays. This is probably true for a payload of uniform shape and density. To create an unstable configuration, the payload is shifted from its design position at $x = 5.9m$ slightly rearwards to $x = 7.0m$ as indicated in Figure 5.13. The payload is still located within the bounds of the payload bay and the location of CG_x is changed from -2.9 to $+2.4\% \, MAC$. In the gust analysis, two out of four mass configurations are with payload. The detailed values are given in Table 5.1. Note that the mass case M11 is without fuel and thus the payload shift has a larger impact than for case M13 with fuel. The reason for the selection of both cases is that the fuel level changes during flight but the position of the payload is fixed. (Also note that the values given in Table 5.1 are calculated after the optimization loop and thus differ slightly from the baseline configuration.) For a real aircraft, it might be beneficial to adapt the control laws for each mass configuration. For better comparison, in this work the controller coefficients K_p and K_i are the same for all mass configurations.

Mass config.	System masses	Payload	Fuel	Mass $[kg]$	$CG_x[m]$	$CG_x[\%MAC]$
M11	yes	centered	empty	8543	5.82	-2.9
M11b	yes	rearward	empty	8543	6.14	+2.4
M13	yes	centered	full	13258	5.78	-3.6
M13b	yes	rearward	full	13258	5.98	-0.2

Table 5.1: Stable and unstable mass configurations of the MULDICON

In a first step, the rigid body motion is re-evaluated for the naturally unstable configuration and compared to the naturally stable closed loop configuration (M11 from the previous Section 5.2 and M11b). Figure 5.14 shows the pitch angle Θ and the pitch rate q. It can be seen that the controller performs reasonably well for short gusts but worse for longer gusts. The maximum pitch angle Θ is approximately $+1.1°$ and comparable to the results for the open loop system, see the dashed line in Figure 5.5 in Section 5.2. The dynamic overshoot is much larger, leading to a the minimum pitch angle Θ of about $-0.05°$. The long gusts are more difficult to control than the short gusts. This is also reflected in the pitch rates q. Still, the proposed controller of the closed loop system manages to maintain stability and leads the aircraft safely back into a horizontal flight condition. Note that there is a small offset between the naturally stable and unstable configuration already at $t = 0.0s$. This can be explained by

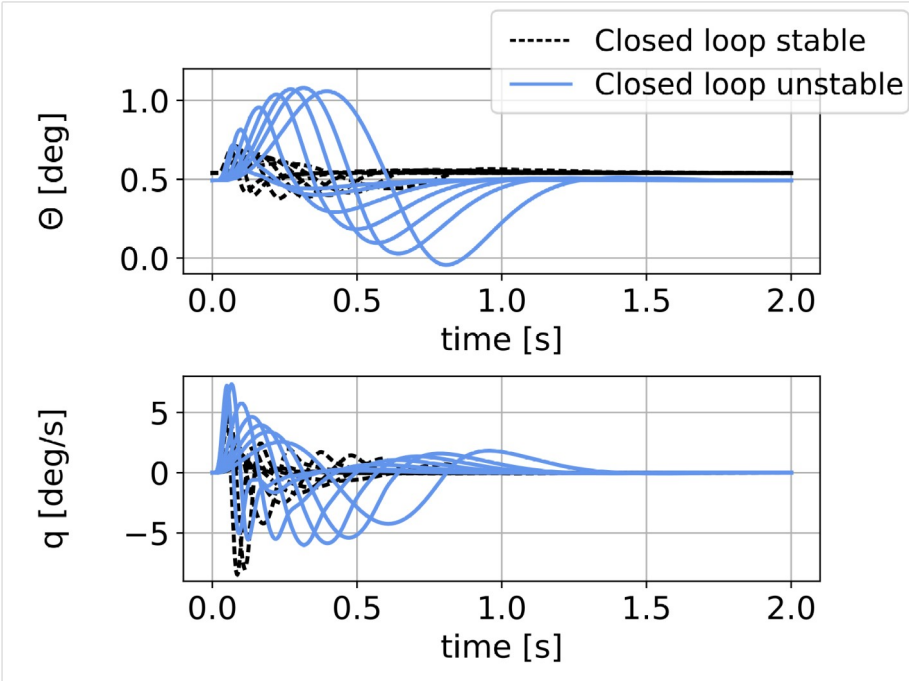

Figure 5.14: Pitch angle Θ and pitch rate q for the naturally unstable system

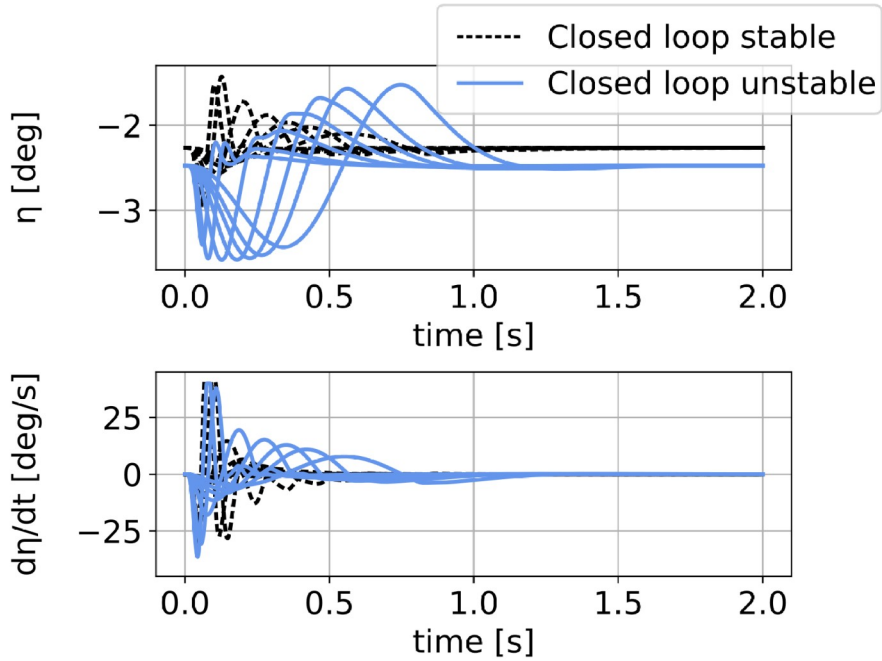

Figure 5.15: Commanded control surface deflection η and control surface rate $\dot{\eta}$

the initial trim condition. Due to the modified mass configuration, the control surfaces are employed to balance the aircraft, leading to a new pitch angle Θ. The corresponding offset of the control surface deflection is visible in Figure 5.15. From Figure 5.15 it can be seen that for the short gusts, the allowable control surface rate $\dot{\eta}$ is again the limiting factor. The longer

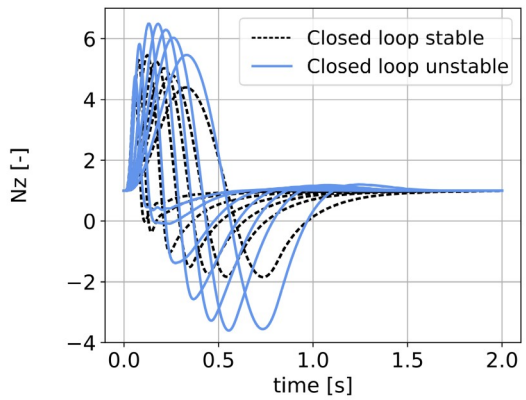

Figure 5.16: Load factor N_z for the naturally unstable system

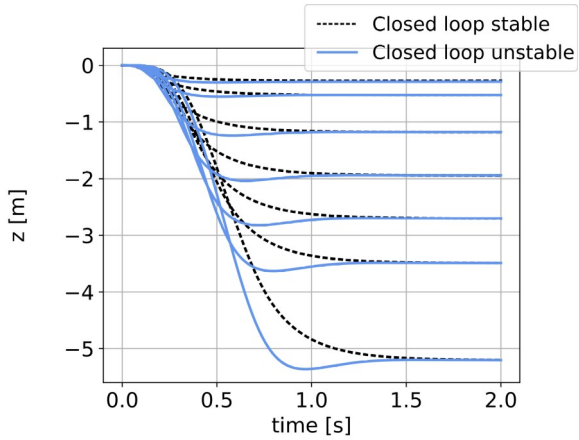

Figure 5.17: Vertical displacement in z-direction

gusts require larger control surface deflections η compared to the naturally stable configuration but a lower rate $\dot{\eta}$ is sufficient.

The final vertical displacement shown in Figure 5.17 reaches the same altitude as before (see Figure 5.8 in Section 5.2). However, the gradients are much steeper, indicating a higher acceleration of the aircraft. This is confirmed by the load factor N_z shown in Figure 5.16. The maximum load factors N_z are approximately $+6.6$ and -3.6. With the horizontal level flight condition $N_z = 1.0$ as reference, this is an increase by 22% and 58% respectively compared to the naturally stable closed loop configuration.

In Figure 5.18, the loads envelopes of shear force F_z, bending moment M_x and torsion moment M_y are shown for the right wing root. The envelope of shear force F_z and the bending moment M_x is significantly larger compared to the naturally stable configuration but

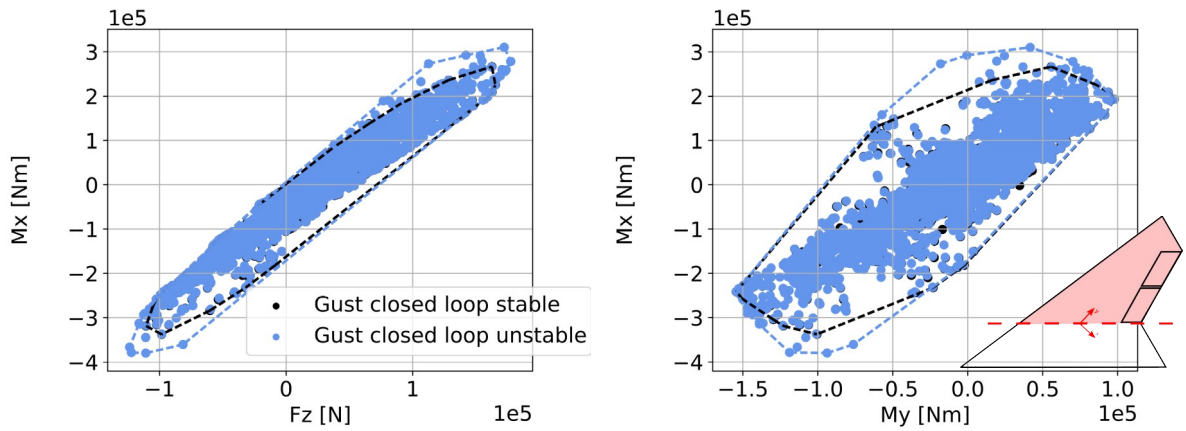

Figure 5.18: Loads envelope of shear force F_z, bending moment M_x and torsion moment M_y at the right wing root

the increase is not as large as for the load factor N_z. Surprisingly, the torsional moment M_y has the same minimum and maximum amplitude compared to the naturally stable closed loop configuration. Due to the combination with the bending moment M_x, the envelope is still larger. In the previous section, the increase of torsional moment M_y could be traced back to the control surface attachment loads, adding higher forces and moments along the trailing edge compared to the open loop system. In the case of the naturally unstable system, it can be concluded that the control surface attachment loads have approximately the same amplitudes as for the naturally stable system, leading to a similar torsional moment M_y along the wing. This can be confirmed by consulting Figure 5.19. The envelopes of the control surface attachment loads F_z and M_y haven't changed much. Only for the inner control surface, a slight increase is visible.

This in turn can be explained by identifying the dimensioning load cases that form the envelope. The required information is given in Figure 5.20. For the naturally stable closed loop envelope, the two extreme points are marked by load cases 184 and 191. Both load cases correspond to mass configuration M11 and a gust with $H = 15m$ of positive and negative orientation respectively. The extreme points of the naturally unstable envelope are marked by load cases 184 and 191, too. Load case 275 is very interesting and just next to load case 191. That load case corresponds to mass configuration M11b and a negative gust with $H = 15m$. All parameters, except for the mass configuration, are identical to load case 191. Due to the mass case, the attachment loads should be higher, but this is not the case. As discussed before, the flight controller is limited by the maximal allowable control surface rate $\dot{\eta}$ and that limit is touched for the shorter gusts with $H = 9m$ and $15m$ for both the naturally stable and unstable configuration. Therefore, the control surfaces move in a similar manner and experience a similar loading.

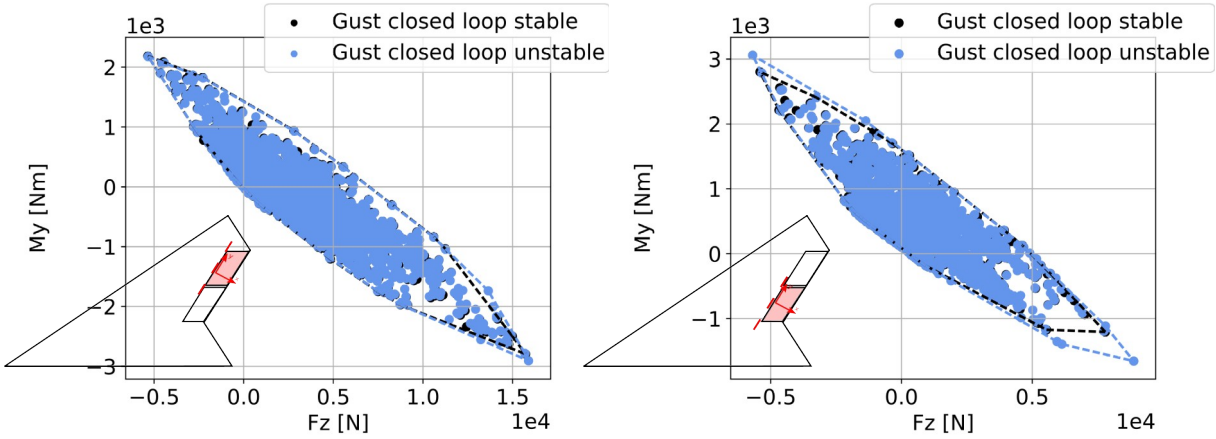

Figure 5.19: Envelope of control surface attachment loads

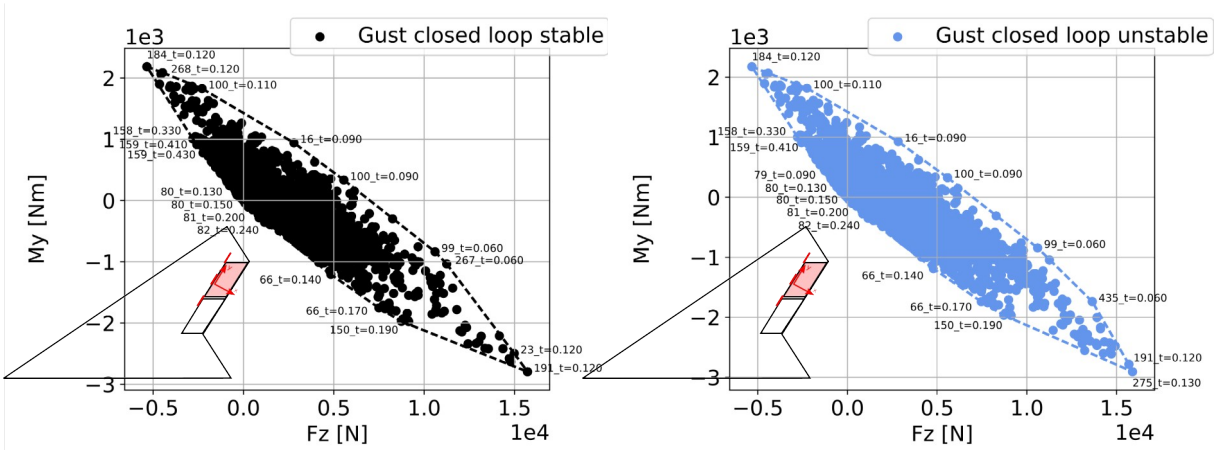

Figure 5.20: Identification of dimensioning load cases for control surface attachment loads

Summary: The operation range of the aircraft is extended to unstable conditions by allowing mass configurations where the payload is positioned further rearwards. A load increase is observed for most monitoring stations. The attachment loads of the control surfaces are barely affected as they are limited by the maximal allowable control surface rate $\dot{\eta}$.

5.4 Influence in Terms of Structural Weight and Loading

From these observations, the next step is a reassessment of the structural optimization of the MULDICON, including gust loads of the closed loop systems.

As for the baseline configuration (compare Figure 3.12), the convergence behavior is good as shown in Figure 5.21 and Table 5.2. A difference with respect to Figure 3.12 is the initial material thickness, which is now set to a higher value to increase the robustness of the optimizer, as discussed in Section 3.6.4. Three outer loops lead to converged results in all cases. The use of three loops also has a physical meaning which can be interpreted as follows. The first loop gives a first estimate. If necessary, the second loop adjusts the estimate slightly and the third loops confirms the results. For the MULDICON, the first estimate is confirmed twice. The convergence can be considered as very trustable if no general trend is visible and the first loop shows for example a slight underestimate, the second loop an overestimate and the third loop again a slight underestimate or vice versa. For the MULDICON, this applies to all cases.

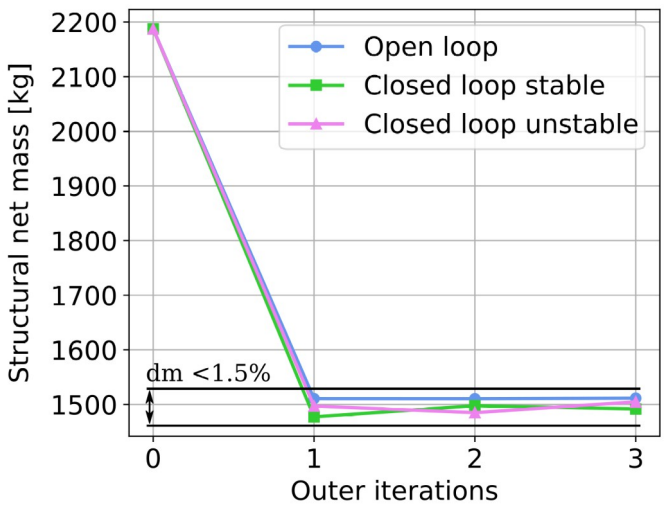

Figure 5.21: Convergence history of structural net mass

Mass after outer iteration	Initial	1	2	3
Open loop	2187.4 kg	1510.6 kg	1510.5 kg	1511.5 kg
Closed loop stable	2187.4 kg	1477.3 kg	1497.7 kg	1491.7 kg
Closed loop unstable	2187.4 kg	1497.0 kg	1485.0 kg	1504.8 kg

Table 5.2: Convergence history of structural net mass

In all cases, the final structural weight is approximately 1500 kg. The difference of approximately 20 kg is well within the precision of the optimization. Reasons for this could be the extremely high stiffness of the structure and high strength capacity. For a stress

engineer, this is a very preferable situation. Although Figure 5.11 showed higher control surface attachment loads, no increase of material thickness of the rear spar, where the control surfaces are attached, is observed. An inspection of the failure index of the carbon fiber material, see Figure 5.22, shows that the rear spar experiences a loading higher than for example the middle spar. The magnitude is well below 1.0 so that the minimum material thickness is still sufficient.

During later phases of the aircraft design, for example during the detail design, the global structural stiffness might be reduced by holes and cut-outs in the outer skin. This might lead to different results. Also, a more detailed attachment of large non-structural system masses, such as the engine, might influence the structural characteristics, mode shapes and frequencies of the aircraft and change its global stiffness.

Looking at the material thickness distribution, see Figures 5.23, 5.24 and 5.25, mainly the leading edge and the front spar are affected. Apparently, a modification of these design variables has the largest impact on the overall design objective of minimum weight. This can be explained by the nature of the flight controller to steer the aircraft into the gust. This increases the effective angle of attack, resulting in a higher lift, which acts on the aircraft just behind the front spar (approximately at a local chord length of 25%). To further improve the

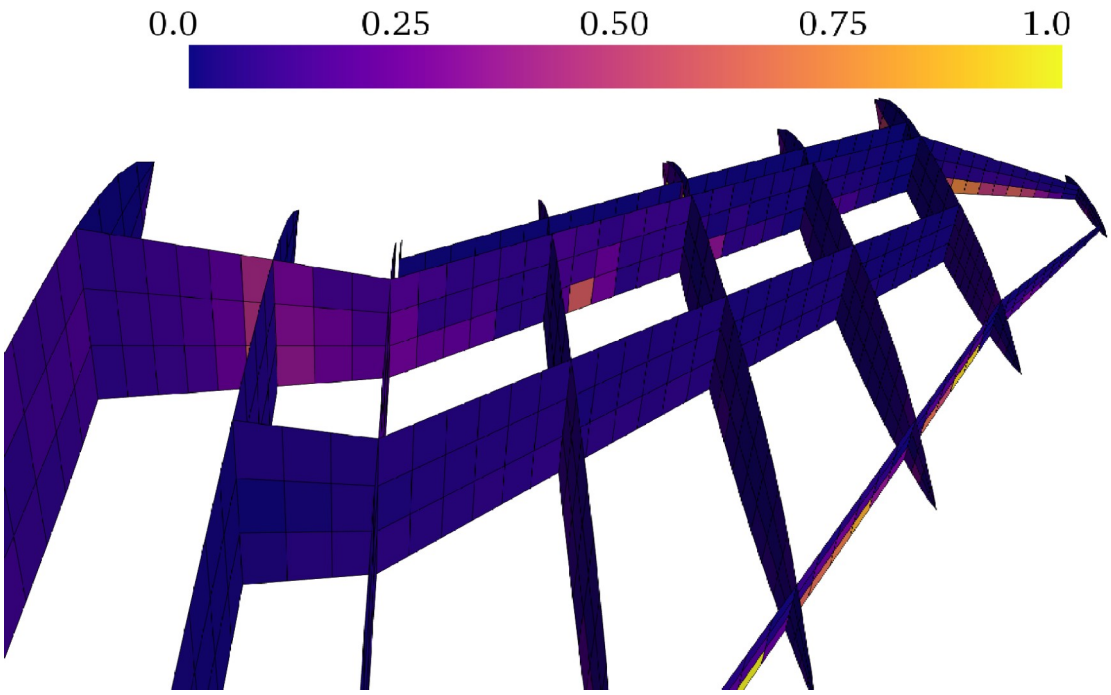

Figure 5.22: Failure index of rear spar over all plies and load cases

structural layout in terms of geometry, the front spar could be shifted rearwards, which would increase its height and second area moment.

Summary: In general, it can be concluded that such a compact flying wing configuration of low aspect ratio is sized mainly by local nodal loads. This is contrary to the experience with high aspect ratio wing-fuselage-empennage configurations, where the structural sizing is dominated for example by large bending moments at the wing root.

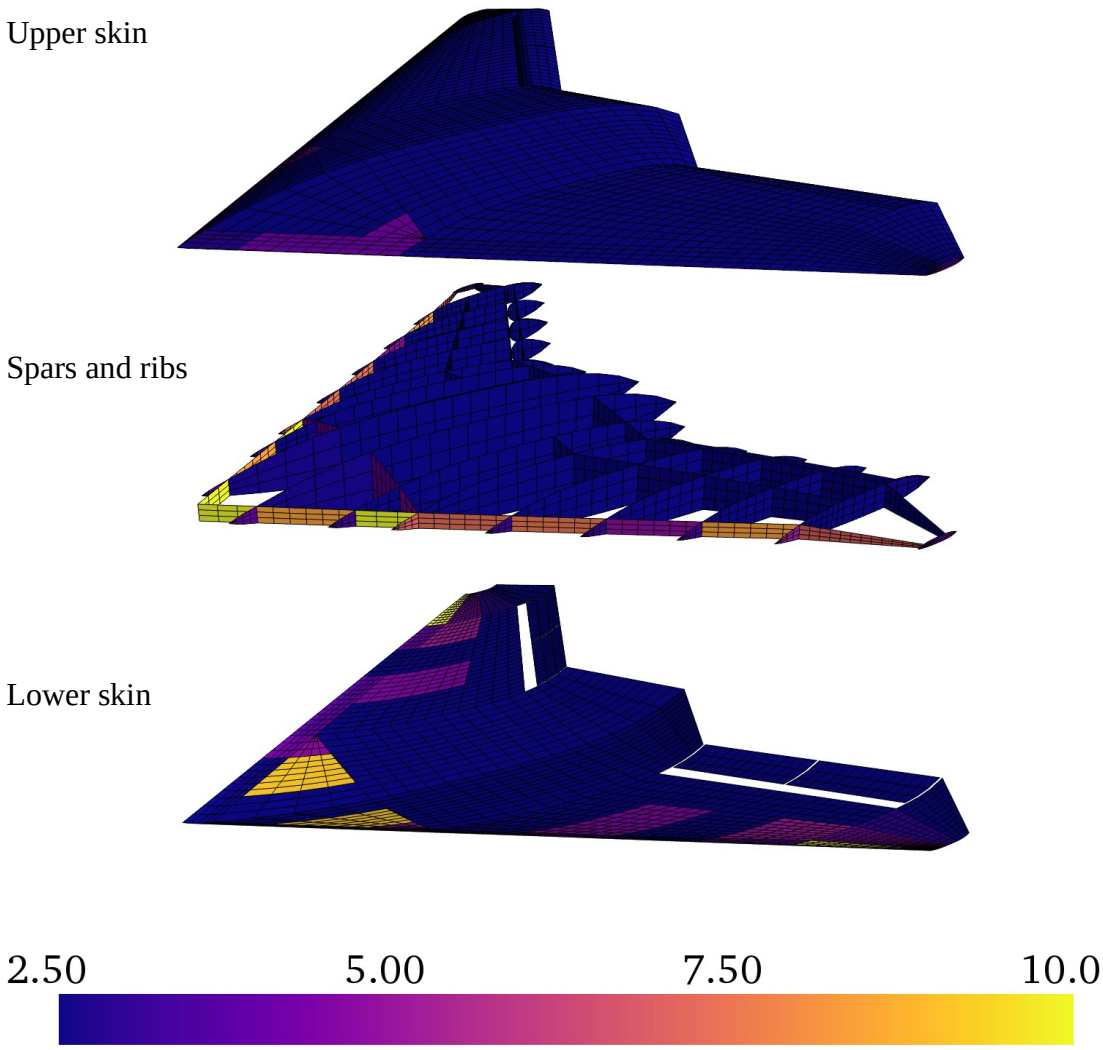

Figure 5.23: Open loop: material thickness distribution of skin, spars and ribs in [mm]

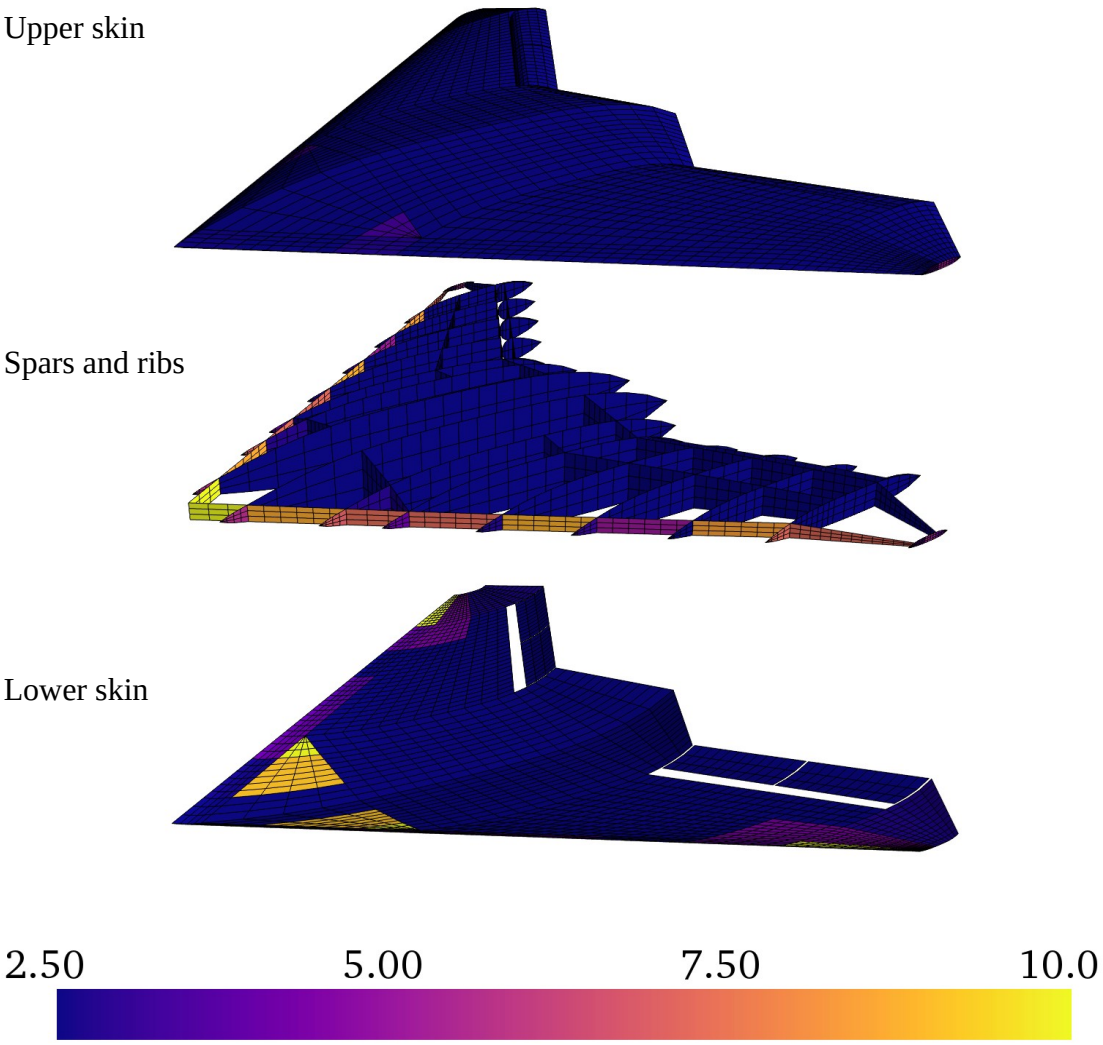

Figure 5.24: Naturally stable closed loop: material thickness distribution of skin, spars and ribs in [mm]

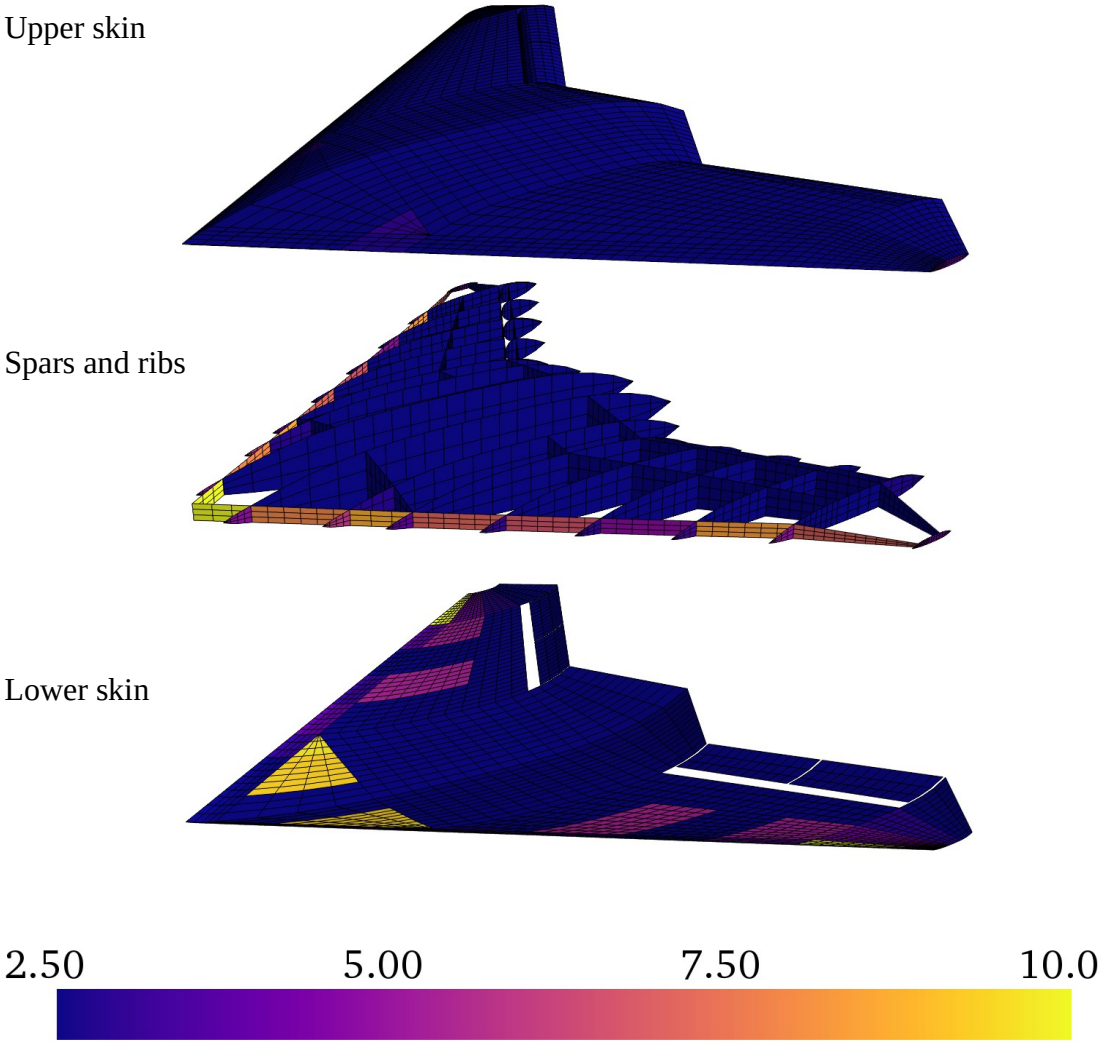

Figure 5.25: Naturally unstable closed loop: material thickness distribution of skin, spars and ribs in [mm]

6 Physical Effects of CFD Maneuver Loads and Comparison to VLM

This section takes the challenge to bring together disciplines in which the respective experts often have very different interests. Probably, many amazing and incredibly interesting aerodynamic effects will occur, such as compression shocks in the transonic regime, vortex build-up and break-down at the sharp leading edge or the interaction with and efficiency of control surface deflection. Unfortunately, the focus of this work is on aircraft loads. The aerodynamic CFD solutions are prepared with care and due diligence but are not the center of attention.

In Section 6.1, the selection of the CFD solution scheme is discussed. With this basis, two examples at low and high speed are studied in Sections 6.2 and 6.3. The low speed examples demonstrate the application of the numerical CFD solutions. For a horizontal level flight at low speed, CFD and VLM should converge and deliver similar results in terms of trim condition and pressure distribution. For high speed case, different physical effects occur and their influence is discussed. Section 6.4 shows the results of all 306 maneuver load cases in terms of section loads. Finally, in Section 6.5, the influence on the structural mass is evaluated. A summary of the results of this section has been published on a conference [201] and as a journal article [202].

6.1 Thoughts on the Selection of a CFD Solution Scheme

Classical panel methods such as the VLM are designed for the calculation of the inviscid, subsonic flow. For low speeds and moderate Reynolds numbers, the results are acceptable and the agreement with higher order aerodynamic methods is usually (surprisingly) good with respect to loads and aeroelastic analysis.

For a better description of the aerodynamic properties of an aircraft, the Navier-Stokes equations (NS), describing the viscous, compressible fluid in terms of mass, impulse and energy, need to be solved. As of today, the solution of the full Navier-Stokes equations is possible for small problems but not feasible for entire aircraft due to high calculation costs. Instead, the Reynolds-Averaged-Navier-Stokes equations (RANS) are a suitable choice, approximating small turbulences with the help of turbulence models [100]. Depending on the application, the RANS equations are often a good choice and various implementations and turbulence models are available. The solution time for a single three dimensional flow problem ranges from several hours up to days. The next step of simplification leads to the Euler equations, neglecting viscosity and assuming an attached flow. Still, compression shocks are captured. The main drawback is the missing boundary layer due to the assumption of an inviscid flow. A thick boundary layer changes the effective shape of an airfoil, which may have an influence on a compression shock with respect to its position in chord direction. The higher the Mach number, the thinner the boundary layer and the better the Euler solution. The solution time for a single three dimensional flow problem ranges from several minutes up to some hours. All sets of equations are solved iteratively using a finite differences or finite volume approach. For a more detailed description of the differences between the flow solutions, Chapter 2.4. in reference [100] could be consulted.

An attempt to arrange the available flow solution schemes in terms of cost and benefit is shown in Figure 6.1. The diagram shows that an increase in precision always comes at the cost of higher computational times and modeling effort. Current industrial approaches are usually based on 3D panel methods such as the VLM and DLM, which are used in this work as well, in combination with an AIC correction. In some cases, higher order panel methods are used. As of today, a RANS solution is the best available option but still only feasible for a few number of load cases. Considering this and the literature presented in Section 1.2.2, this section presents a significant progress of the aerodynamic methodologies applied within a comprehensive loads analysis and structural sizing process during preliminary design.

In addition to the selection of the flow solution scheme, considerations should be made concerning the modeling of the problem. A good resolution of the boundary layer in a RANS calculation requires a high spatial discretization, resulting not only in higher calculation times but also in an increased modeling effort. In contrast, meshes for Euler calculations have lower

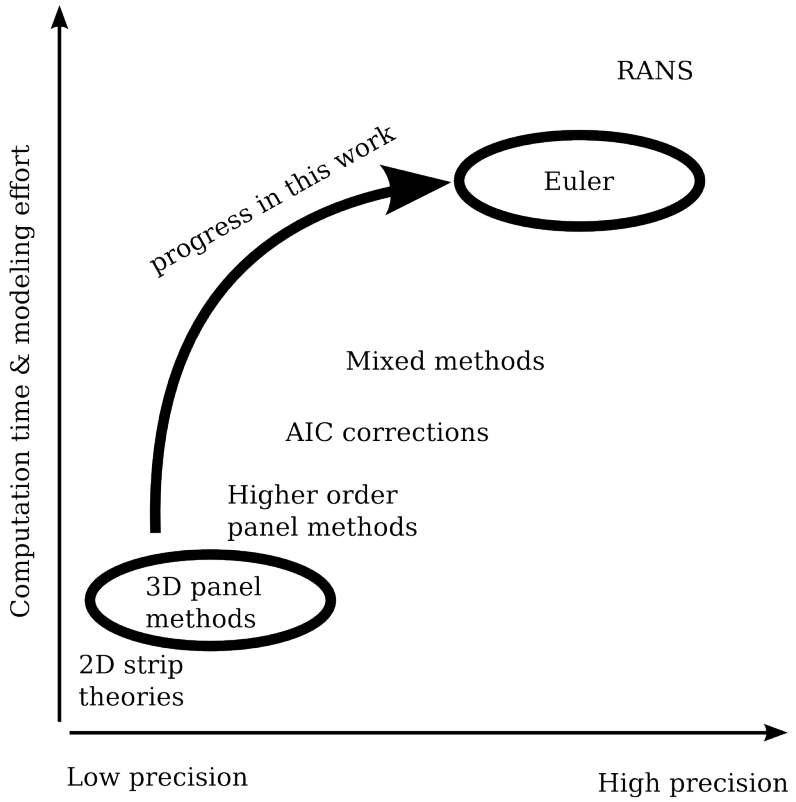

Figure 6.1: Comparison of aerodynamic methods in terms of precision and computation time for comprehensive loads analysis and sizing

requirements and the model set-up is much easier. Comparing the convergence behavior of the iterative solution of Euler and RANS equations, Euler equations are usually faster and more stable than RANS equations. This results in little to no adjustments of parameters and "maintenance" during the solution process, which is an important consideration when thinking about an automated work flow for many load cases. Finally, the CFD code used in this work, the DLR Tau code [176], offers both RANS and Euler solutions. This makes a swapping at a later stage relatively easy.

In general, the engineer needs to evaluate the requirements for the solution of his problem carefully and select the appropriate tool. The Euler equations seem to be an appropriate choice for this work and signify a huge improvement in terms of physical accuracy in comparison to the VLM.

Summary of principal physical effects that are captured by Euler:

- Three-dimensional flow and cross flow in span-wise direction: influences flow about control surfaces → changes the trim conditions → has an effect on loads
- Surface pressure distribution: influences the pitching moment M_y → changes the trim conditions → has an effect on loads
- Geometrical control surface deflections: influences the control surface efficiency →changes the trim conditions → has an effect on loads
- Thickness of profile: more physical representation of flow (e.g. $dC_l/d\alpha$, $C_{l,\max}$,...) → has an effect on loads
- Thickness of large bodies: important e.g. for a classical fuselage (doesn't occur in this work)
- Vortices and separated flow (geometry based): could occur at discontinuities and sharp edges of the geometry → has an effect on loads

Summary of physical effects that are <u>not</u> captured by Euler:

- Viscosity: boundary layer not included → position and strength of compression shock subject to uncertainties
- Viscosity: influence on amplitude and phase of unsteady aerodynamics → important for flutter and high frequencies (doesn't occur in this work)
- Viscosity: flow separation subject to uncertainties (pressure based) → complex vortex systems, detaching and reattaching flow → start at $\alpha = 10 \ldots 15°$ → is not anticipated
- Mesh deformation: no gaps along control surface trailing edges and sides → sliding boundaries / chimera techniques / … not yet feasible, subject to current research
- Mesh deformation: smooth transitions between wing and control surface

6.2 Step One: Low Speed Horizontal Level Flight

The aircraft is trimmed in a horizontal level flight at a subsonic Mach number of $Ma = 0.4$ at sea level, which corresponds to a true air speed $V = 136.12m/s$ and a dynamic pressure of $q_\infty = 11348.4Pa$. The mass configuration is M12, the load factor is $N_z = 1.0$ and results in a required lift coefficient in z direction $C_z = 0.1197$. The required pitching moment coefficient is $C_{my} = 0.004258$ and the rolling moment coefficient is to be $C_{mx} = 0.0$. The trim variables are the angle of attack α and the pilot commands ξ and η for roll and pitch.

Remark: Note that the angle of attack α is actually not a trim variable but the result of the aircraft velocities u and w. The velocities are selected by the trim algorithm in such a way that sufficient lift is created and that the true air speed V_{tas} is matched.

During the trim calculation, the CFD code, in combination with the aerodynamic mesh presented in Section 3.4, shows an excellent convergence behavior as shown in Figure 6.2. The outer trim loop requires 8 evaluations of the inner FSI loop, leading to 21 inner iterations plus one final iteration. Looking at the lift, the rolling and the pitching coefficients, the data in

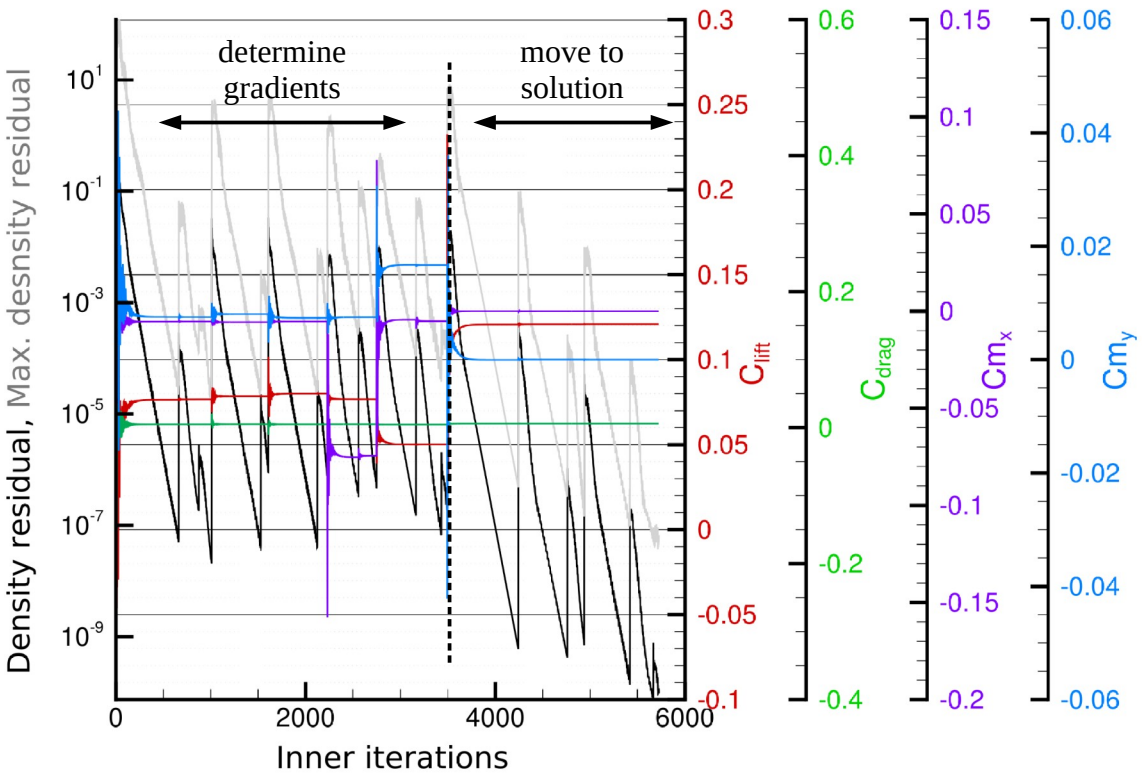

Figure 6.2: CFD convergence history for trim of low speed level flight

Figure 6.2 reflects the steps of the trim algorithm. The trim algorithm requires the first ~3500 inner iterations of the CFD solver to determine the gradients of the trim parameters, then moves towards the trim solution. From that point on, large changes are not any longer visible and the next ~2500 steps are spent on closing in on the final solution.

The trim results are given in Table 6.1. The angle of attack α is very similar for both the CFD and the VLM solution. The CFD trim requires a small rolling command ξ. The aerodynamic mesh of the VLM solution, the structural and the mass model are all three perfectly symmetrical in a numerical sense. This is no longer the case for the unstructured CFD mesh where the surface is discretized with triangles. The pitching command η has a negative sign in both cases, indicating a downward deflection of the control surfaces to compensate a nose up pitching moment (the pilot pushes the stick). The pitching command η is slightly smaller for the CFD solution. Assuming similar control surface efficiency, it can be concluded that the pressure distribution of the CFD solution leads to a slightly lower pitching moment M_y than the VLM solution. Note that the VLM is corrected for both camber and twist (see Section 3.4). However, it is only a correction and probably not perfect. In addition, the thickness of the airfoils is modeled in CFD but not in VLM. All three effects influence the pitching moment M_y, so this is where the largest differences can be expected.

Trim Solution	VLM	CFD, small grid	CFD, large grid
α	2.45°	2.49°	2.50°
ξ	0.0°	-0.16°	0.19°
η	-2.49°	-1.24°	-0.90

Table 6.1: Trim solution for low speed level flight

In a second step, the CFD mesh of Section 3.4 is refined to demonstrate mesh convergence. The number of surface elements is increased from 54,476 to 331,588. In the control volume, the number of tetrahedrons is increased from 818,352 to 3,895,199 and the number of nodes is increased from 153,109 to 744,503. This is a substantial increase by a factor of ~6 for the surface and a factor of ~4.8 for the volume discretization. The corresponding trim results are listed in Table 6.1 in the last column. The computation time using the small mesh is ~20 minutes and ~105 minutes for the large mesh. Because the differences between the two meshes are small in terms of trim results, the small mesh appears sufficient.

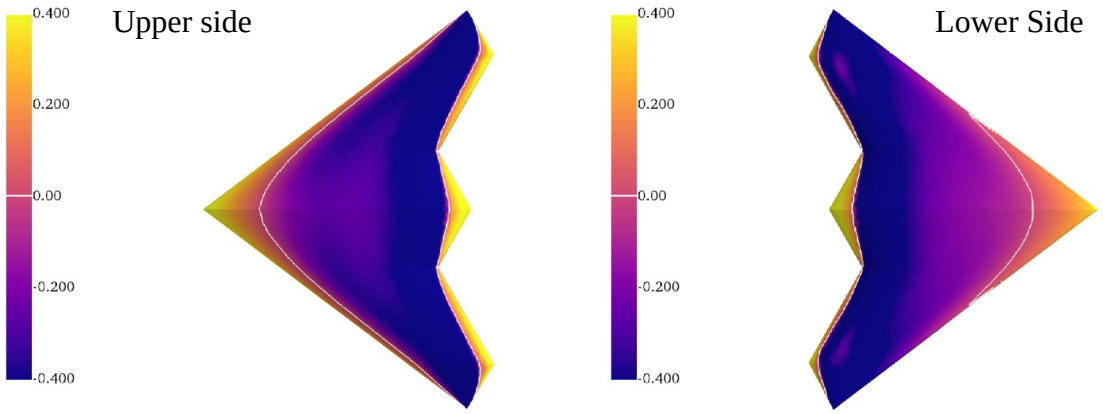

Figure 6.3: CFD pressure coefficient distribution $\mathbf{c}_p^{\mathrm{CFD}}$ on upper (left) and lower (right) side, low speed ($Ma = 0.4$)

With the trimmed solutions, the pressure distribution on the lifting surface may be inspected for any differences. For the CFD solution, the corresponding pressure coefficient distribution is shown in Figure 6.3. Because the CFD solution is based on a modeling of the volumetric aircraft body and the VLM solution on a planar panel mesh, a direct comparison is not straight forward and needs an intermediate step. The CFD solution needs to be split into an upper and a lower part and is projected onto the xy-plane of the VLM grid. Then, a linear interpolation is used to determine the CFD pressure coefficients $\mathbf{c}_p^{\mathrm{CFD,interp}}$ at the center of every VLM panel. Finally, the upper side is subtracted from the lower side

$$\boldsymbol{\Delta}\mathbf{c}_p^{\mathrm{CFD,\ interp}} = \mathbf{c}_{p,\mathrm{lower}}^{\mathrm{CFD,\ interp}} - \mathbf{c}_{p,\mathrm{upper}}^{\mathrm{CFD,\ interp}} \tag{6.1}$$

allowing a comparison of the pressure distributions $\boldsymbol{\Delta}\mathbf{c}_p^{\mathrm{CFD,interp}}$ and $\boldsymbol{\Delta}\mathbf{c}_p^{\mathrm{VLM}}$ plotted in Figure 6.4. As expected from the similar trim results, the pressure distributions look similar in

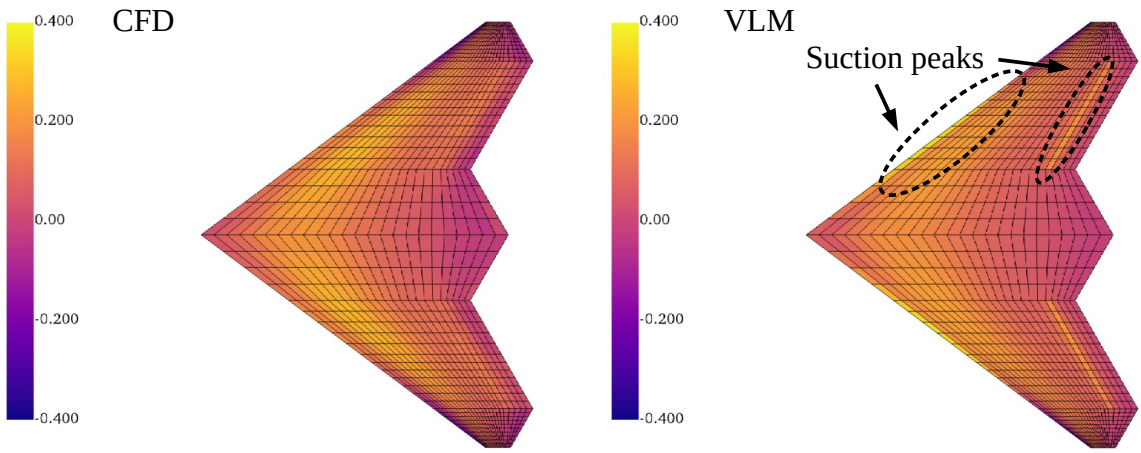

Figure 6.4: Pressure coefficient distributions from CFD $\boldsymbol{\Delta}\mathbf{c}_p^{\mathrm{CFD,interp}}$ (left) compared to VLM $\boldsymbol{\Delta}\mathbf{c}_p^{\mathrm{VLM}}$ (right), low speed ($Ma = 0.4$)

both magnitude and spatial distribution. Compared to CFD, the VLM solutions shows a slightly more pronounced suction peak along the leading edge and along the leading edges of the control surfaces. This can be explained by the aerodynamic approach based on the potential theory and the assumption of a flat plate.

Figure 6.5 shows the difference of CFD and VLM ($\mathbf{\Delta c}_p^{\mathrm{CFD,interp}} - \mathbf{\Delta c}_p^{\mathrm{VLM}}$) in a more direct manner and on a smaller scale ranging from -0.1 to 0.1. Blue areas indicate that VLM is producing more lift, red areas indicate that CFD is stronger. Next to the suction peaks, one can see that the pressure distributions of VLM varies from the CFD solution mainly in chord-wise direction. This can be explained by the modeling of airfoil camber described in Section 3.4 (see Figure 3.7), which is imperfect in VLM. There are also some differences in span-wise direction, which can be observed especially along the trailing edge. A possible explanation is given in the next section at the example of the high speed case, where the effect is more pronounced (see stream lines in Figures 6.8 and 6.9). Unfortunately, along the trailing edge the control surfaces are located. As mentioned before, the pitching command η has a negative sign in both cases, indicating a downward deflection of the control surfaces, generating lift (positive $\mathbf{\Delta c}_p$). Because the pitching command η is slightly smaller for the CFD solution, the lift at the control surface is smaller, which agrees well with the blue area on the inner control surfaces. This is contrary in the area of the outer control surfaces, where there is more red

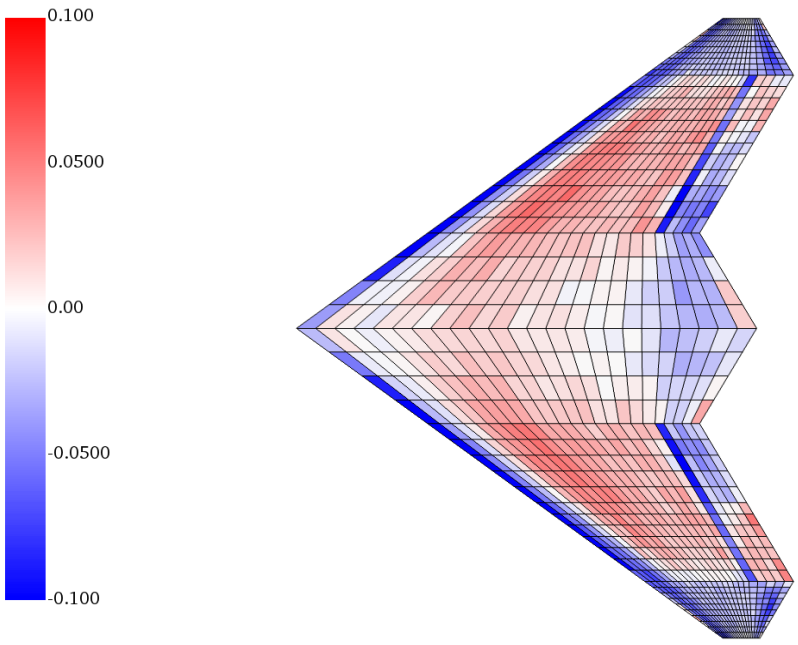

Figure 6.5: Difference of pressure coefficient distributions of CFD and VLM $\mathbf{\Delta c}_p^{\mathrm{CFD,interp}} - \mathbf{\Delta c}_p^{\mathrm{VLM}}$, low speed ($Ma = 0.4$)

color. If the outer control surfaces are more efficient in CFD and in combination with a longer lever arm with respect to CG, this could be an another explanation for the smaller pitching command η required by CFD.

Summary: Good convergence is demonstrated for the numerical CFD solutions. For a horizontal level flight at low speed, CFD and VLM converge and deliver similar results in terms of trim condition with small difference in pressure distribution. This is as expected and serves as a baseline for the following investigations.

6.3 Step Two: High Speed Horizontal Level Flight

For the second example, the aircraft speed is successively increased up to $Ma = 0.9$. All other parameters of the operation point remain unchanged. A summary of the trim solutions is given in Table 6.2. As the dynamic pressure increases with the Mach number, the required angle of attack α for horizontal level flight reduces compared to the low speed case. At a Mach number of $Ma = 0.8$, the CFD solution is still comparable to the VLM solution. The angle of attack α and pitching command η are slightly lower than the VLM solution. For Mach numbers $Ma = 0.85$ and $Ma = 0.9$, the differences get larger. While the pitching command η has been lower for the CFD solution, its magnitude increases significantly up to $\eta = -7.27°$ for the CFD solution compared to $\eta = -2.03°$ for the VLM solution.

Trim solution / Ma		0.4	...	0.8	0.85	0.9
VLM	α	2.45°	...	0.68°	0.60°	0.54°
	ξ	0.0°	...	0.0°	0.0°	0.0°
	η	-2.49°	...	-2.16°	-2.03°	-2.03°
CFD	α	2.49°	...	0.61°	0.54°	0.37°
	ξ	-0.16°	...	-0.05°	-0.07°	-0.13
	η	-1.24°	...	-1.43°	-2.77°	-7.27°

Table 6.2: Trim solutions for low and high speed level flight

The answer for the behavior of the trim solution is found in the surface pressure distribution of the $Ma = 0.9$ flight condition shown in Figure 6.6. Two shock systems can be identified. The first compression shock system is visible in the fuselage region. Because of the low angle of attack and the symmetrical airfoil, the shock is both visible on the upper and lower surface

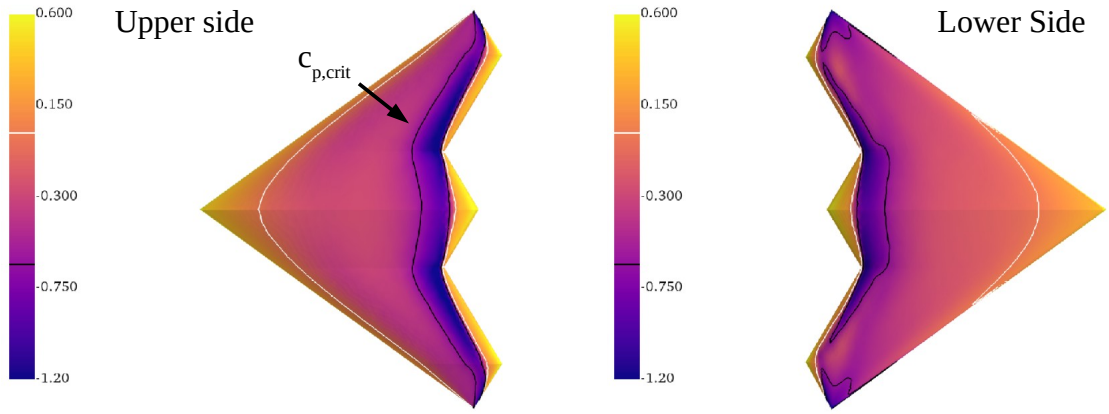

Figure 6.6: CFD pressure coefficient distribution $\mathbf{c}_p^{\mathrm{CFD}}$ *on upper (left) and lower (right) side, high speed*

and approximately at the same chord position. Looking at the pressure difference between upper and lower side $\mathbf{\Delta c}_p^{CFD,interp}$ given in Figure 6.7, the two shocks compensate each other. The result actually looks very similar to the VLM solution. However, this is more or less by coincidence and only true for this flight condition. Higher altitudes or higher load factors might lead to higher angles of attack, resulting in different flow solutions and compression shocks at different chord positions. This could change the pitching moment significantly.

A second compression shock system is visible at the wing trailing edge, where unfortunately the control surfaces are located. As the control surfaces are deflected downwards, this weakens the shock on the lower side and strengthens the shock on the upper side. This interaction has an impact on the difference in pressure $\mathbf{\Delta c}_p^{CFD,interp}$, see marked areas in

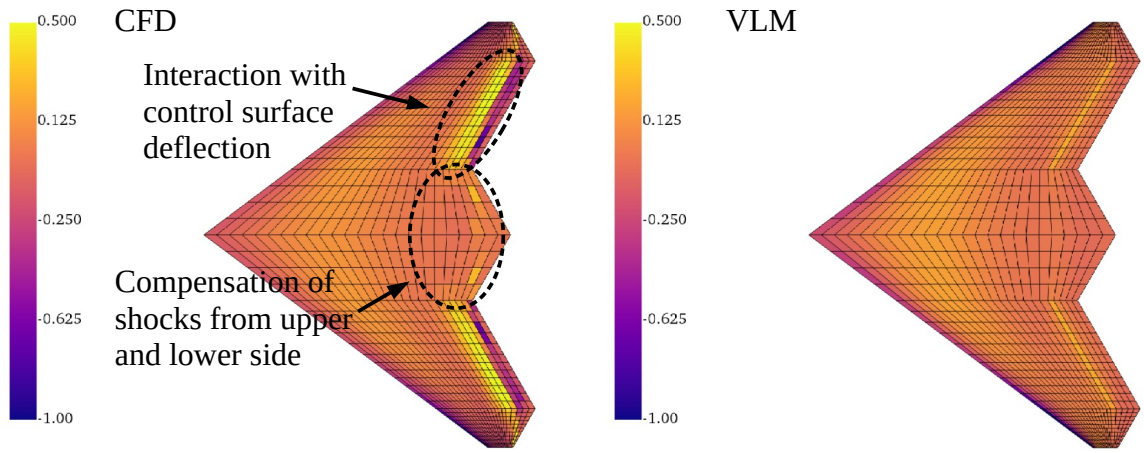

Figure 6.7: Pressure coefficient distributions from CFD $\mathbf{\Delta c}_p^{\mathrm{CFD,interp}}$ *(left) compared to VLM* $\mathbf{\Delta c}_p^{\mathrm{VLM}}$ *(right), high speed*

Figure 6.7. In addition, there is a strong interaction of the location of the compression shock and the control surface deflection. This leads to strong non-linearities during the process of the trim solution. A comprehensive discussion of transonic flow patterns on flapped airfoils and different types of shocks is given in literature, see Chapter 3 in Tijdeman [194]. In the numerical analysis, these non-linearities are reflected in an increase of the number of function evaluations from 8 to 11 and an increase of inner FSI iterations from 21 to 33.

Following Schlichting and Truckenbrodt [169] (page 179, eq. 8.85), the shock-free design condition can be determined by calculating the critical pressure coefficient of the swept wing

$$\mathrm{c}_{p,\mathrm{crit}} = -\frac{2}{\kappa+1} \cdot \frac{1-Ma^2 \cdot cos^2(\phi)}{Ma^2} \quad . \tag{6.2}$$

With $Ma = 0.9$, $\kappa = 1.4$ and a representative sweep angle $\phi = 45°$, the above equation yields $c_{p,\mathrm{crit}} = -0.61$. A pressure coefficient below the critical pressure coefficient indicates the occurrence of a compression shock. Looking at the pressure coefficient distribution in Figure 6.6, this condition is clearly not met. Probably, the aircraft will never be shock-free at high speed conditions. However, it might be beneficial to modify the airfoil in such a way that the shock occurs more towards the nose of the airfoil and far ahead of the control surfaces. Also, the airfoil might be designed with a flat upper side in such a way that the compression shock is weaker by accelerating and then slowly decelerating the flow along the airfoil. A cambered center line could be used to add a rear loading to the airfoil and to avoid compression shocks on the lower side, such that the lower side of the control surfaces remains fully functional. Unfortunately, for a flying wing, a different airfoil comes with a complete re-design of the whole aircraft because as the pitching moments change, masses need to be shifted to adjust CG, requiring a different structural layout, etc. This would be a very interesting task for further work.

Looking at the stream lines visualized in Figures 6.8 and 6.9, one can see a pronounced flow in span-wise direction on both the upper and lower side of the wing. Starting at the leading edge, the flow first travels outwards, then inwards and again outwards along the trailing edge, resulting in a S-shape of the stream lines (compare with the dashed, vertical line for reference). The velocities in y-direction (over $\pm 60 m/s$) are very high and make up to $\pm 20\%$ of the on-flow velocity. This physical phenomenon is not captured by the VLM and could be an explanation for the difference in pressure distribution between CFD and VLM in span-wise

direction, observed especially along the trailing edge in the previous section. Although a flying wing configuration seems to be more simple to analyze aerodynamically because of the smaller number of components (no large engine nacelles, no tail), in fact detailed investigations are necessary to capture and understand complex flow characteristics for the wing-like fuselage and the highly swept wing. This will be in particular interesting if e.g. engine inlets and nozzles are taken into account.

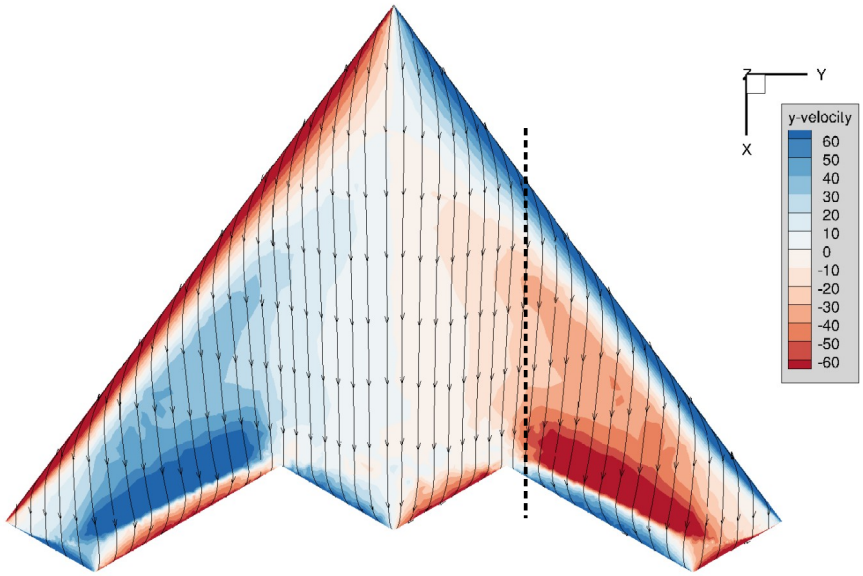

Figure 6.8: Visualization of stream lines obtained from CFD on the upper side and y-velocity [m/s]

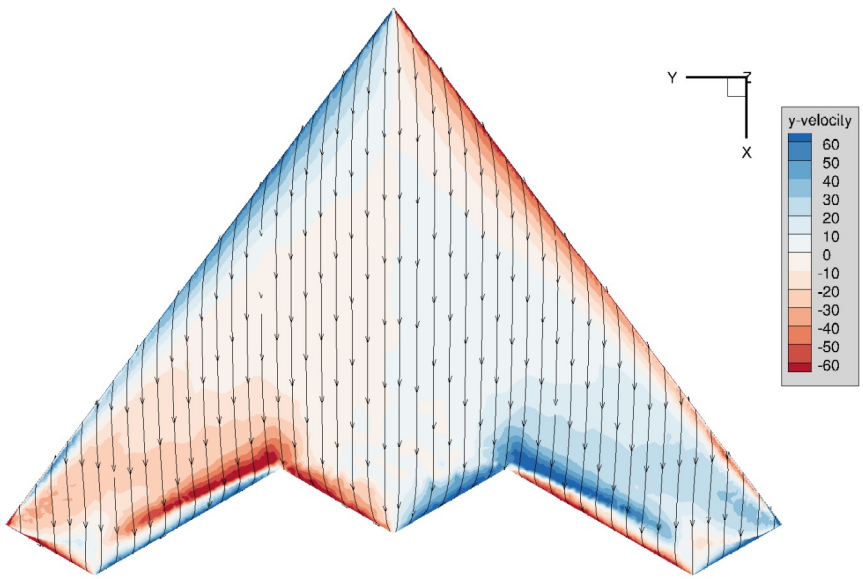

Figure 6.9: Visualization of stream lines obtained from CFD on the lower side and y-velocity [m/s]

Summary: Strong transonic effects are visible at high speed conditions. They could change the pitching moment significantly, leading to different trim conditions. In addition, a compression shock just in front of / on the control surfaces substantially reduces the control efficiency. The pronounced flow in span-wise direction observed on the upper and lower side of the wing is not captured by VLM.

6.4 Step Three: All Maneuver Load Cases

Due to the observations of the previous section, the maneuver load cases specified in Section 3.6.2 going up to $Ma = 0.97$ are unrealistic, as the compression shocks would be too strong and prohibit the use of the control surfaces along the trailing edge. For the following work, the speed been set to $MC = 0.8$ and $MD = 0.9$. In addition, a preliminary assessment showed that the intended maneuvers are unrealistic at very high altitudes as the low dynamic pressure does not allow for high load factors. Therefore, the altitudes are reduced slightly from FL200, FL300 and FL450 to FL150, FL250 and FL350 respectively. The total number of 306 maneuver load cases remains unchanged and the selected operation points are still representative. Another limitation of CFD are the control surface deflection based on mesh deformation techniques. High deflections (e.g. $> 15 \ldots 20°$) often result in cells of bad quality, leading to numerical instabilities, while VLM always gives a solution. However, it is unlikely that high deflections will occur on the real aircraft during high speed flight, giving a physical justification to limit the deflections, in this case at $\pm 15°$.

Although care has been taken, some maneuver load cases are expected to fail. Generally, three modes of failure are considered.

- The first failure mode is divergence of the numerical procedure of the CFD solution. In this case, the trim algorithm detects the error of the CFD solution and skips the load case. The affected cases are collected and repeated with different parameter settings that lead to a more stable but slower numerical solution. Typical parameters are the Courant–Friedrichs–Lewy (CFL) number, which is reduced to a lower value, and the multi grid scheme (faster convergence), with is switched to single grid (slower, more robust convergence) [100]. Failures of this type are desired to be reduced to a minimum, but considering a high degree on automation, they won't be prevented

completely. If the solution still diverges, this is an indicator for a very unsteady flow. The pragmatic decision is that a flight under such conditions is unrealistic and the maneuver load case can be omitted.

- The second failure mode is missing convergence of the structural deformation. This failure typically occurs if there is an unsteady, oscillating flow solution, leading to a different structural deformation in each aero-structural iteration step. Missing convergence is determined after ten aero-structural iterations, compare Figure 1.3 in Section 2.6. Another accompanying indicator is the missing Cauchy convergence of the flow solution. As before, the pragmatic assumption is that such a flight condition is unrealistic and the maneuver load case is omitted.
- The third failure mode is missing convergence of the trim solution. In this case the trim algorithm can't find a suitable set of parameters to solve the system of equations. The requested maneuver is without the physically possible bounds or the solution lies without the bounds of e.g. the allowed control commands. Therefore, the aircraft will never reach that condition and the maneuver load case can be safely omitted.

A first finding is that there are load cases which are impossible to calculate using CFD while VLM always gives a solution. This might sound rather obvious, but it is a crucial finding. It is a very good argument in favor of comprehensive maneuver loads analyses and only the engineer who includes many maneuver load cases at different altitudes, speeds, etc. will encounter and realize these boundaries. In addition, most CFD codes have difficulties and show convergence issues for operation points in areas far away from the aircraft design point and according to Tinoco [195] most CFD calculations are done near the cruise point, compare Figure 1 in [195]. Krumbein [96] identifies turbulence and transition models are the weakest link in simulation chain. Reliable models are a key technology to allow for the step from Euler to RANS and still a field of research as of today. To allow for a reasonable comparison of CFD to VLM results, of course only those maneuvers that were successful in CFD should be compared.

With this strategy, the loads loops could be performed without further problems. The CFD-based calculations failed only for some maneuver load cases, mainly with failure mode three. All of them were pull-up maneuvers with $N_z = 2.5$, and mainly at combination of high altitudes, high speeds and high mass. The total number of failed load cases was less than 2%.

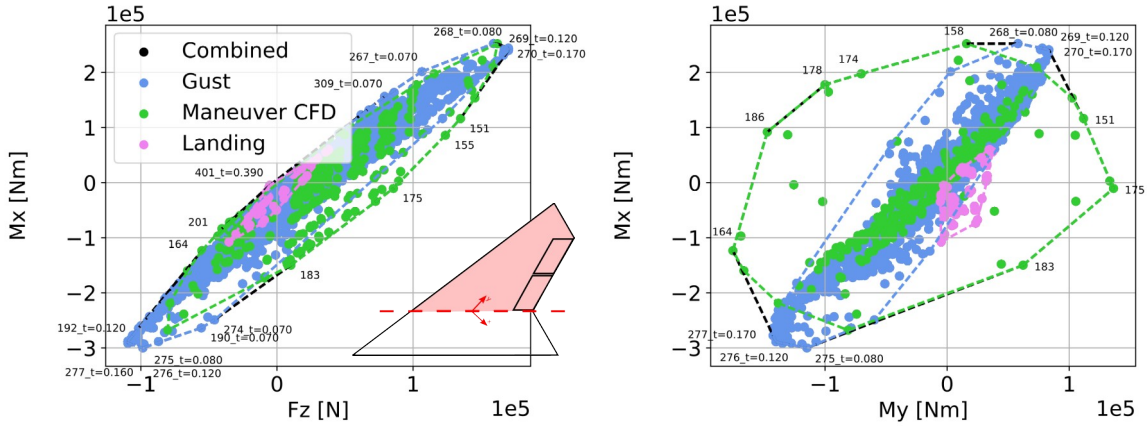

Figure 6.10: Loads envelope of shear force F_z, bending moment M_x and torsion moment M_y at the right wing root

A VLM-based solution revealed the affected cases to be well within the bounds of the loads envelope.

Because of the large number of maneuver load cases, an individual inspection of every case with trim conditions, pressure plots, etc., is no longer feasible. Loads envelopes are an appropriate means and will be used in the following. Looking at the resulting loads envelopes of shear force F_z, bending moment M_x and torsion moment M_y shown in Figure 6.10 for the right wing root, both the shape and magnitude are comparable to the envelopes of the baseline configuration, see Figure 3.24, Section 3.6.4, page 81. Because of the smaller flight envelope for the maneuver loads, the resulting envelope has a more slender shape. The top right and bottom left corner are still formed by the same gust load cases. On the left and right side of the envelope, more load cases are identified as dimensioning load cases and even include one landing load case (number 401).

A direct comparison of the maneuver load envelopes from CFD and VLM is shown in Figure 6.11 for the right wing root. One can clearly see a shift and stretching of the loads envelopes while the shape is nearly unchanged. The minimum shear force F_z is decreased by 2.4% while the maximum value is increased by 9.4%. The minimum bending moment M_x is increased by 7.1% while the maximum value is decreased by 1.0%. The minimum torsional moment M_y is increased by 8.4% and the maximum value is decreased by 13.0%. Looking at the labels that identify the dimensioning load case, one can see the same cases for VLM and CFD.

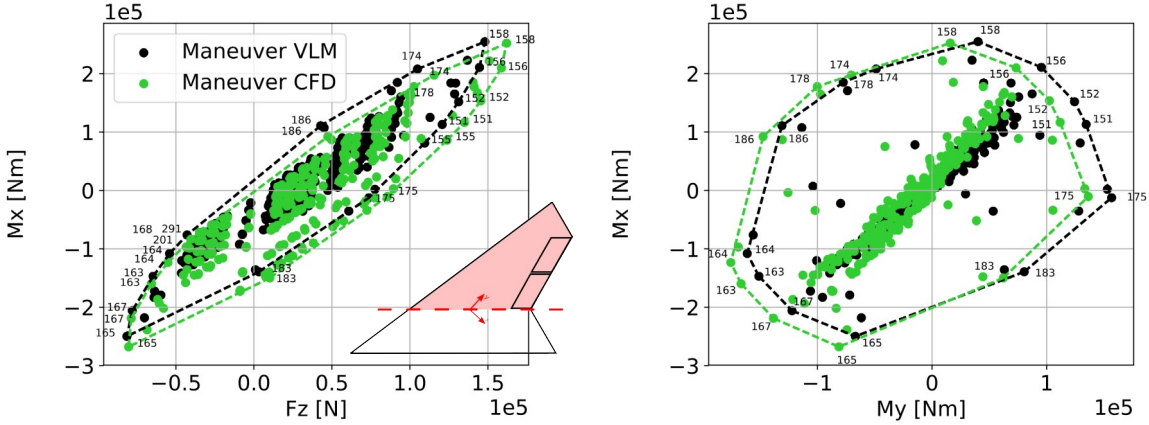

Figure 6.11: Loads envelope of shear force F_z, bending moment M_x and torsion moment M_y at the right wing root

At the right outer wing, the differences are more pronounced as shown in Figure 6.12. While some parts of the envelopes look very similar with a moderate offset, there are some regions, as marked in the plot with grey color, which are completely different. These load cases extend the envelope significantly, especially in terms of bending moment M_x, but the total value is still very low because of the short lever arms.

As expected from the previous studies of the high speed horizontal level flight in Section 6.3, the control surfaces experience a different loading using CFD. The CFD maneuver load envelopes shown in Figure 6.13 are different from the VLM envelopes in both size and shape. While there is a similarity between the inner and outer control surface for the VLM based envelopes, the CFD envelopes show no such similarity. At the inner control surface, a high hinge moment M_y corresponds to a high negative shear force F_z. This is not the case for the outer control surface. Although the deflections of inner and outer control surface are of the

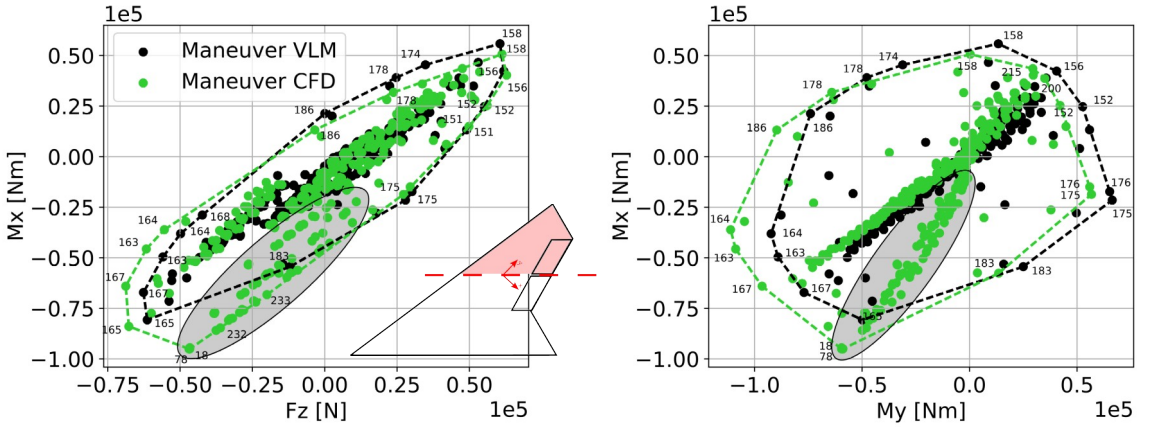

Figure 6.12: Loads envelope of shear force F_z, bending moment M_x and torsion moment M_y at the right outer wing

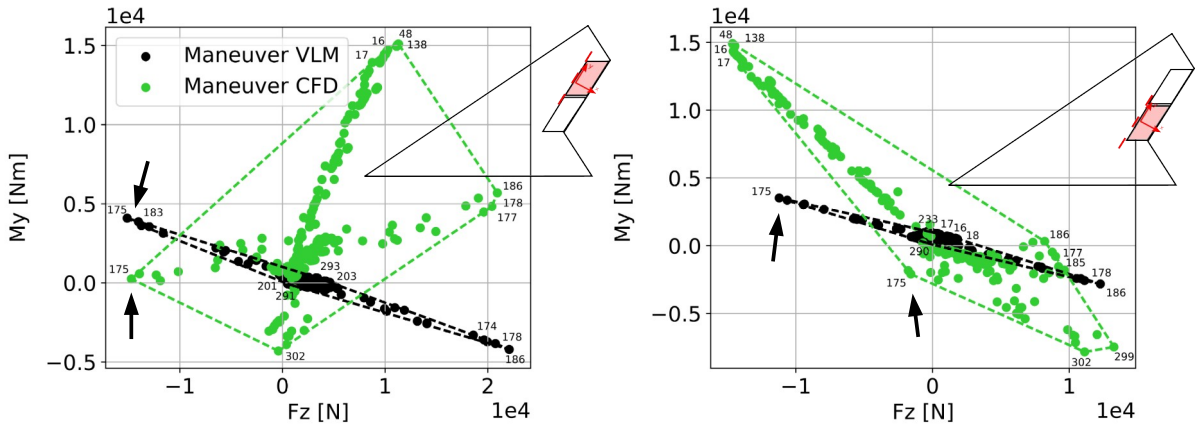

Figure 6.13: Envelope of control surface attachment loads

same magnitude, the resulting shear forces F_z are generally higher at the outer control surface. Looking at the example of maneuver load case number 175, marked with arrows in the plots, one can see that it produces the highest shear force F_z at the outer control surface while the shear force F_z is close to zero at the inner control surface. This might be the reason for the differences observed at the right outer wing in Figure 6.12.

Note that all the differences in section loads shown in Figures 6.11, 6.12 and 6.13 are due to the spatial distribution of the aerodynamic forces only, compare Figures 6.4 and 6.7. This is because the maneuver cases, and thus the overall forces and moments of the aircraft, are the same. Also keep in mind that solely the aerodynamic method is exchanged while the structural, mass and coupling models and even the loads analysis software are identical.

6.5 Influence in Terms of Structural Weight and Loading

In Figures 6.15 and 6.16, the resulting material thickness distribution is shown. The material thickness distribution of the CFD-based maneuver loads loop shows similarities to the VLM-based maneuver loads loop, for example along at the front spar. Significant differences are visible along the rear spar, where the CFD-based maneuver loads cause a significant increase in material thickness. Also, the rear parts of lower skin show a material thickness of approximately 6 to 7mm while the minimum material thickness of 2.5mm was sufficient for the VLM-based maneuver loads loop. The changes in the rear region are likely to be caused by the transonic aerodynamics and the compression shocks observed in Section 6.3. With 1735.9kg, the resulting structural net mass is approximately 200kg heavier than the reference.

The convergence behavior is again very good as can be seen from the development of the structural net mass shown in Figure 6.14 and Table 6.3.

Note that the difference in structural mass has an influence on the location of the center of gravity CG, which has an influence on the trim condition and on loads. For mass configuration M12 (basic flight design mass) for example, the difference in x-direction is less than 1% compared to the VLM based optimization. If the travel of CG becomes larger, it could be considered to adjust payload and/or fuel masses for compensation.

In this context, the aero-structural coupling needs to be considered. Because aerodynamic panel methods calculate the pressure difference $\mathbf{\Delta c_p}$ between upper and lower surface, the engineer is forced to choose one side only for coupling. In this case, all ribs and spars on the lower side were selected. The same strategy is deliberately used for the CFD based maneuver loads to allow for a meaningful comparison where the aerodynamics are changed exclusively. With a three dimensional CFD solution available, that restriction could be removed and the aerodynamic forces could be distributed more evenly on both the upper and lower surface. Presumably, this will have and impact on the prominent material thickness increases on the lower side observed in Figure 6.16. However, that is not the scope of this work and would require far-reaching changes in the loads simulation procedure.

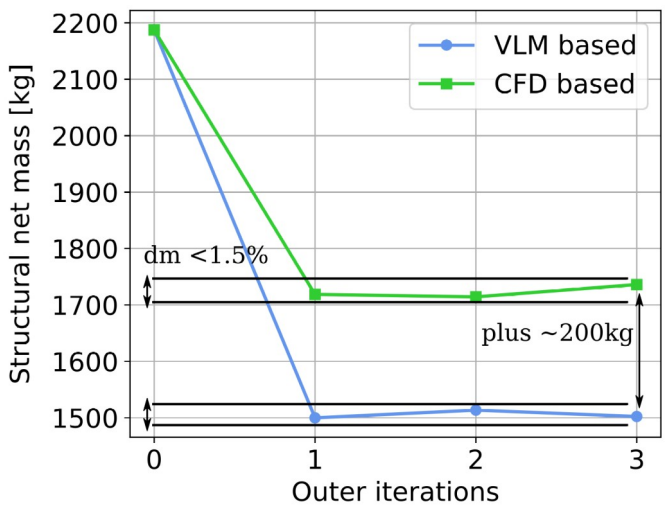

Figure 6.14: Convergence history of structural net mass

Mass after outer iteration	Initial	1	2	3
VLM-based maneuver loads loop	2187.4 kg	1499.6 kg	1513.3 kg	1502.0 kg
CFD-based maneuver loads loop	2187.4 kg	1718.5 kg	1714.1 kg	1735.9 kg

Table 6.3: Convergence history of structural net mass

Summary: The observed change and increase in section loads of the CFD based maneuver loads is reflected in the structural optimization. The new structural mass is approximately 200kg heavier compared to the reference VLM-based maneuver loads loop.

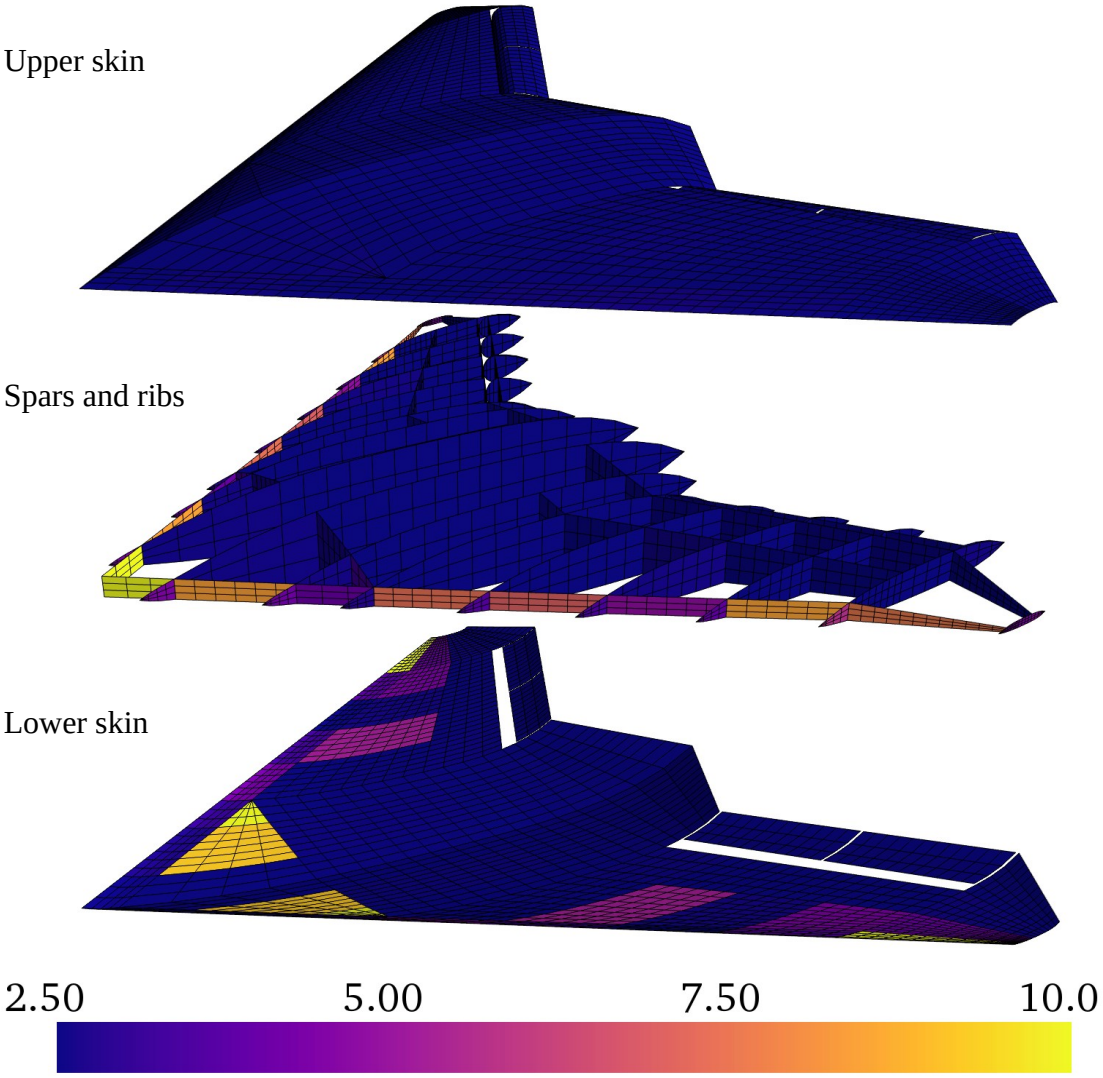

Figure 6.15: VLM-based maneuver loads loop: material thickness distribution of skin, spars and ribs in [mm]

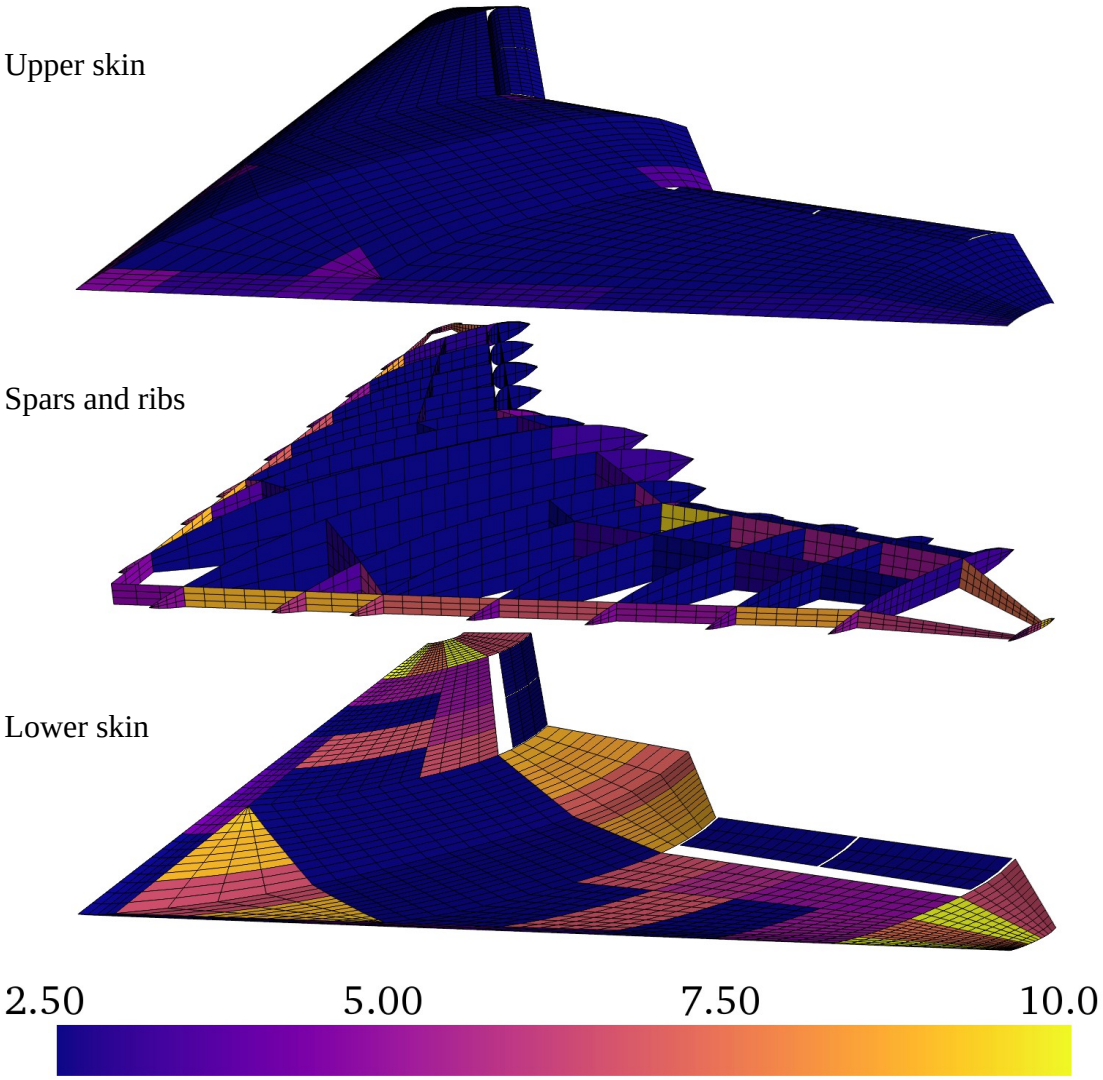

Figure 6.16: CFD-based maneuver loads loop: material thickness distribution of skin, spars and ribs in [mm]

7 Conclusion and Outlook

In this work, the influence of flight loads on the structural design of flying wings is investigated. The focus is on the gust encounter and on improved fidelity of maneuver loads within a preliminary design process.

7.1 Summary of Findings

The **open loop gust encounter** is studied at the example of two flying wing configurations. The MULDICON and the ACFA configurations differ in size, mass and shape but both show a pronounced tendency of pitch up when encountering a positive gust. This has an increasing effect on section loads and should be included in every gust analysis. It is shown that the use of the Pratt formula for quasi-steady gust loads is unsuitable. Both aircraft show a strong penetration effect when entering a gust field. This is especially true for the MULDICON due to its compact, non-slender and highly swept geometry. The unsteady aerodynamic influence is observed to behave differently than with classical wing-fuselage-empennage configurations. At the wing root for example, the peaks of the section loads are reduced but occur earlier in time, compared to quasi-steady aerodynamics.

The **closed loop gust encounter** includes a controller for the pitching motion and significantly reduces the minimum and maximum pitch angles during a gust encounter. It was found the performance of the controller is limited by the maximal control surface rate, especially for short gust gradients. The performance for short gusts can only be improved with higher rates, or by adding prior knowledge of the gust, e.g. obtained from a sensor at the aircraft nose or using LIDAR techniques to measure the flow field in front of the aircraft. Additional limits might be introduced by the maximal allowed attachment loads and unsteady aerodynamic effects on the control surfaces in case of very fast deflections of high frequency.

Considering section load, two effects need to be considered. Because the controller reduces the pitch up tendency, section loads are decreased. Then, from the deflection of the control surfaces, loads along the trailing edge are added. These two effects were found to balance out with respect to the shear force and the bending moment at the wing root but the torsional moment was increased. Obviously, actuation of the control surfaces causes much higher hinge moments and attachment loads.

The operation range of the aircraft is extended to unstable conditions by allowing mass configurations where the payload is positioned further rearwards. The rigid body motion is increased compared to the naturally stable closed loop configuration. An increase in section load is observed for most monitoring stations as well. The attachment loads of the control surfaces are barely affected as they are limited by the maximal allowable control surface rate.

Optimization loops for minimum weight resulted in a final structural weight of approximately 1500kg of all three cases (open loop, closed loop and unstable), which puts the stress engineer in a very preferable situation. Reasons for this are the extremely high stiffness of the structure and high strength capacities.

In general, it can be concluded that compact flying wing configurations of low aspect ratio are sized mainly by local, nodal loads and local peaks. This is contrary to the experience with high aspect ratio wing-fuselage-empennage configurations, where the structural sizing is dominated for example by large bending moments at the wing root.

CFD maneuver loads are studied in a three step approach, first at the example of a low speed horizontal level flight, then for higher speeds and finally for all maneuver cases. Good convergence could be demonstrated for the numerical CFD solutions. For a horizontal level flight at low speed, CFD and VLM converge and deliver similar results in terms of trim conditions with small difference in pressure distribution. This is as it should be and serves as a baseline for the following investigations. For higher speeds, strong transonic effects are visible. They can change the pitching moment significantly, leading to different trim conditions. In addition, a compression shock just in front of / on the control surfaces substantially reduces the control efficiency. A pronounced flow in span-wise direction observed on both the upper and lower side of the wing is also not captured by VLM.

Considering all maneuver load cases requires a failure tolerant process, because not all trim cases can be expected to converge using CFD. Especially unmindfully defined flight points might turn out to be nonphysical. Comparison of the CFD to the VLM based maneuver loads shows load envelopes at the wing root that are similar in size and shape but have an offset. At the outer wing and at the control surfaces, the envelopes take different shapes and new dimensioning load cases are identified. Those changes are reflected in the structural optimization as well. The new structural mass is approximately 200kg heavier than the reference.

These findings and the applied methodologies present a significant progress within a comprehensive loads analysis and structural sizing process during preliminary design of flying wings. Next to the two major topics of this thesis, **several minor topics** have been touched compare Section 1.3 and Figure 1.7. The inclusion of flight mechanical characteristics results in a fully dynamic, unsteady time simulation of gust encounters. This enables the physical profound study of the gust encounter. During the structural design of the MULDICON, a new model reduction strategy based on sub section corner points is developed to reflect the characteristics of compact, planar configurations with wings of low aspect ratio. A generic landing gear module is developed to enable the fast analysis of landing loads during the preliminary design. This contributes to the goal of a thorough design. Finally, the Loads Kernel software is developed. It allows for greater flexibility in loads analysis and deviation from standard procedures offered in commercial products and is inseparably connected to this thesis. In addition, both the user and developer gain a much deeper insight into the loads process and detailed, custom analyses are possible.

7.2 Improvements of Work

Three potential areas of improvement could be considered. The Euler solution is identified to capture all principal effects that are important from a maneuver loads perspective, as discussed in Section 6.1. To quantify the actual influence of viscosity, RANS calculations could be performed. However, that would require a corresponding mesh to be constructed on the very same geometry and with a similar surface discretization. Experience has shown the set-up of a good quality RANS mesh requires some skill and is a manual, time consuming process. Presumably, computational resources won't be the limiting factor for the application

of high fidelity simulations in the future, but the availability and set-up of appropriate simulation models.

As mentioned in Section 6.5, the aero-structural coupling could be improved towards a three dimensional approach as the reason for the restriction to a two dimensional coupling ceased to exist with the use of CFD. The assumption is that the structural loading would benefit a lot from a more physical distribution of the aerodynamic forces. The upper and lower skin would be loaded more evenly. Presumably, this would result in an upper and lower skin of similar material thickness. The author expects that the splining will have a bigger influence on structural weight than the difference between Euler and RANS.

The underlying aeroelastic models presented in Section 3 could be further refined. For example, the structural model could by enhanced by application of lamination parameters for the modeling of the laminate setup and cutouts in the outer skin could be included.

7.3 Next Steps

With the CFD maneuver loads process ready for flying wings, future projects could apply the process to classical wing-fuselage-empennage configurations. Especially the fuselage would benefit from an aerodynamic method that captures its large, volumetric body adequately. Different trim conditions are expected, which have an influence on loads. Transonic effects are found at most wing-fuselage-empennage configurations as well. The mesh generation could be a challenge due to the more complex layout. Areas of transition between two components might not be sufficiently defined at an early stage of the design process, which could lead to undesired flow separations when attempting a high fidelity aerodynamic solution. Examples are the belly fairing or the engine pylon and its attachment to the wing. Maybe this is the reason for so many clamped-wing and wing-empennage configurations studied in literature?

Looking at the visual representation of the fields of advancement shown at the beginning of this thesis (Figure 1.7), a large gap opened up between maneuver and gust loads. Considering **CFD gust encounters** in the preliminary design process would bridge that gap as indicated in Figure 7.1.

Summing up, there is still enough work to do in the future!

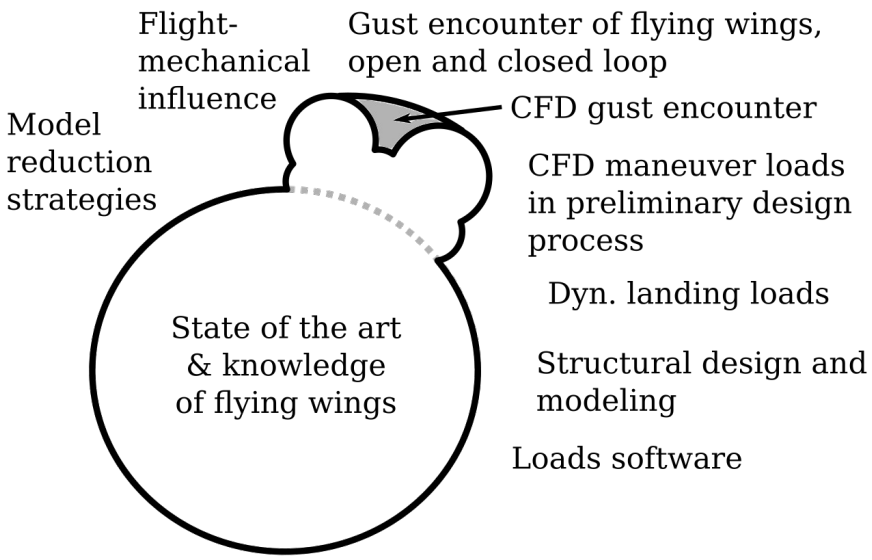

Figure 7.1: Further research to close the gap between maneuver and gust loads

A Appendix

A.1 Overview of Aircraft Parameters

The following key aircraft parameters were assumed for the design of the MULDICON.

Spanwidth (tip to tip): 15.38 m

Area: 77.0 m

Leading edge sweep = 52°

Trailing edge sweep = ±30°

Design mass: ~15.0 t

Payload: 2 x 1.0 t

Fuel: ~4.7 t (see Section 3.3)

Design thrust: 60 kN

Design range: 3000 km

Design cruise altitude: 11 km

Design Mach number: 0.8

Material: carbon fiber reinforced plastic (CFRP, see Section 3.2)

Control: inner and outer control surfaces along trailing edge (see Section 3.4)

Design stability margin: 0.0 - 3.0 % MAC (see Section 3.3)

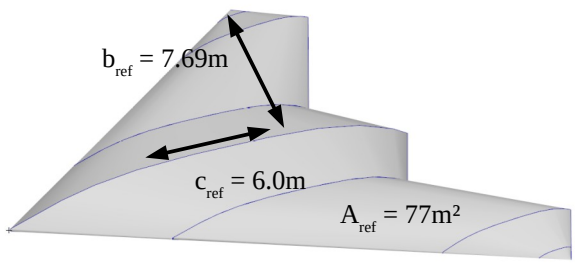

Figure A.1: Geometry of the MULDICON

A.2 Loads Kernel Feature List

From a user's perspective:

- Direct integration in DLR-AE loads process
  - Fewer manual steps
- Simple inputs (dictionaries and lists), always SI units
  - Less mistakes
- Human readable python code
  - Good control and knowledge about of what is happening
  - Better physical understanding
  - Easy to modify, deviate from standard procedure
- Export of data in Python, Matlab, CPACS and Nastran format
  - Special analyses in the user's favorite environment
- Model Viewer
  - Quick visualization of simulation model
  - Identification of model shortcomings → quality control
- Loads Compare
  - Comparison of different sets of loads → quality control

From a technical perspective:

- VLM and DLM Code, translated to python
  - Linear and nonlinear version, induced drag
- Maneuver: VLM
- Gust: VLM + DLM with rational function approximation (RFA) in time domain
- Structural flexibility
  - Modal approach
  - Eigenvalue/-vector analysis of mass and stiffness matrices
  - Matrices (Mgg, Kgg) exported from MSC.Nastran or CoFE
  - Guyan condensation (optional)
- Aero-structural coupling
  - Rigid body spline (with nearest neighbor search)
  - Surface and volume spline (radial basis functions)
- Trim conditions for different types of maneuver
  - Pitch-, roll-, yaw-maneuver, landing at constant sink rate, gliding with loss of altitude at constant speed, ...
  - EFCS for control surface scheduling
- Direct solution with non-linear trim algorithm
- Iterative solution scheme for CFD
- CFD (DLR Tau Code) for maneuver loads
  - Structural flexibility and control surfaces via mesh deformation
  - CFD surface mesh deformation by LK → volume deformation by Tau
  - Directly comparable to VLM-based solution: same trim conditions, matrices, ...
  - Benefits form LK's integration in our loads process

- Linear and non-linear equation for rigid body motion
  - Free flying, flexible aircraft in time domain
  - Flight mechanics included → good for comparisons with flight test
  - Rigid body motion captured correctly (aperiodic motion difficult in frequency domain)
  - Non-linear control possible (not possible in frequency domain)
  - Non-linear external forces, e.g. from landing gear

Bibliography

[1] Abel, I., “An Analytical Technique for Predicting the Characteristics of a Flexible Wing Equipped With as Active Flutter-Suppression System and Comparison With Wind-Tunnel Data,” Langley Research Center, Hampton, Virginia, Technical Paper NASA Technical Paper 1367, Feb. 1979.

[2] Albano, E., and Rodden, W. P., “A Doublet Lattice Method For Calculating Lift Distributions on Oscillation Surfaces in Subsonic Flows,” in *AIAA 6th Aerospace Sciences Meeting*, New York, 1968.

[3] Allemang, R. J., “The Modal Assurance Criterion – Twenty Years of Use and Abuse,” *Sound and Vibration*, pp. 14–21, Aug. 2003.

[4] Arendsen, P., “Final Report of the Garteur action group (SM)AG-21 on ‘Multi disciplinary wing optimization,’” NLR Nationaal Lucht- en Ruimtevaartlaboratorium, Technical Report NLR-TR-2001-557, Nov. 2001.

[5] Azzi, V. D., and Tsai, S. W., “Anisotropic strength of composites,” *Experimental Mechanics*, vol. 5, no. 9, pp. 283–288, Sep. 1965, https://doi.org/10.1007/BF02326292.

[6] Baier, H., Hornung, M., Mohr, B., Paulus, D., Petersson, Ö., Rößler, C., Stroscher, F., and Salmon, T., “Conceptual Design,” in *Modeling and Control for a Blended Wing Body Aircraft*, M. Kozek and A. Schirrer, Eds. Cham: Springer International Publishing, 2015, pp. 29–45.

[7] Becker, R.-G., Reitenbach, S., Klein, C., Otten, T., Nauroz, M., and Siggel, M., “An Integrated Method for Propulsion System Conceptual Design,” in *ASME Gas Turbine Technical Congress and Exposition*, Montréal, Canada, 2015, https://doi.org/10.1115/GT2015-43251.

[8] Beckert, A., and Wendland, H., “Multivariate interpolation for fluid-structure-interaction problems using radial basis functions,” *Aerospace Science and Technology*, vol. 5, no. 2, pp. 125–134, Feb. 2001, https://doi.org/10.1016/S1270-9638(00)01087-7.

[9] Bianchi, J. P., Balmes, E., Des Roches, G. V., and Bobillot, A., “Using modal damping for full model transient analysis. Application to pantograph/catenary vibration,” presented at the ISMA, 2010, https://hal.archives-ouvertes.fr/hal-00589953/.

[10] Bisplinghoff, R. L., and Ashley, H., *Principles of Aeroelasticity*. Dover Publications, 2002, https://books.google.de/books?id=yVa8AQAAQBAJ.

[11] Blair, M., "A Compilation of the Mathematics Leading to The Doublet Lattice Method," Airforce Wright Laboratory, Ohio, Technical Report WL-TR-92-3028, 1992.

[12] Bohn, M., "Aviation Photo #1829344: Airbus A320-233 - LAN Airlines," *Airliners.net*, 09-Jun-2010. [Online]. Available: http://www.airliners.net/photo/LAN-Airlines/Airbus-A320-233/1829344. [Accessed: 03-Mar-2017].

[13] Bramsiepe, K., "Parametrische Aeroelastische Modellierung einer Nurflüglerkonfiguration," DLR Institute of Aeroelasticity, Göttingen, Germany, Internal Report DLR-IB-AE-GO-2016-241, Nov. 2016.

[14] Bramsiepe, K., Handojo, V., Meddaikar, Y. M., Schulze, M., and Klimmek, T., "Loads and Structural Optimisation Process for Composite Long Range Transport Aircraft Configuration," presented at the AIAA Aviation and Aeronautics Forum and Exposition, Atlanta, Georgia, 2018.

[15] Bramsiepe, K., Voß, A., and Klimmek, T., "Design and Sizing of an Aeroelastic Composite Model for a UCAV Configuration with Maneuver, Gust and Landing Loads," presented at the Deutscher Luft- und Raumfahrtkongress, München, 2017, https://elib.dlr.de/114919/.

[16] Brink-Spalink, J., and Bruns, J., "Correction of unsteady aerodynamic influence coefficients using experimental or CFD data," in *AIAA/ASME/ASCE/ASC Structures, Structural Dynamics, and Materials Conference and Exhibit*, Atlanta, Georgia, 2000, https://doi.org/10.2514/6.2000-1489.

[17] Britt, R. T., Jacobson, S. B., and Arthurs, T. D., "Aeroservoelastic Analysis of the B-2 Bomber," *Journal of Aircraft*, vol. 37, no. 5, pp. 745–752, Sep. 2000, https://doi.org/10.2514/2.2674.

[18] Britt, R., Volk, J. A., Dreim, D. R., and Applewhite, K. A., "Aeroservoelastic Characteristics of the B-2 Bomber and Implications for Future Large Aircraft," presented at the RTO AVT Specialists' Meeting on "Structural Aspects of Flexible Aircraft Control," Ottawa, Canada, 1999.

[19] Brockhaus, R., Alles, W., and Luckner, R., *Flugregelung*. Berlin: Springer Berlin, 2010, http://dx.doi.org/10.1007/978-3-642-01443-7.

[20] Brown, P. N., Byrne, G. D., and Hindmarsh, A. C., "VODE: A Variable-Coefficient ODE Solver," *SIAM Journal on Scientific and Statistical Computing*, vol. 10, no. 5, pp. 1038–1051, Sep. 1989, https://doi.org/10.1137/0910062.

[21] Buttrill, C., Zeiler, T., and Arbuckle, P., "Nonlinear simulation of a flexible aircraft in maneuvering flight," in *Flight Simulation Technologies Conference, Guidance, Navigation, and Control and Co-located Conferences*, 1987, https://doi.org/10.2514/6.1987-2501.

[22] Castrichini, A., Cooper, J. E., Benoit, T., and Lemmens, Y., "Gust and Ground Loads Integration for Aircraft Landing Loads Prediction," presented at the 58th AIAA/ASCE/AHS/ASC Structures, Structural Dynamics, and Materials Conference, Grapevine, Texas, 2017, http://arc.aiaa.org/doi/abs/10.2514/6.2017-0636.

[23] Cavagna, L., Ricci, S., and Riccobene, L., “Structural Sizing, Aeroelastic Analysis, and Optimization in Aircraft Conceptual Design,” *Journal of Aircraft*, vol. 48, no. 6, pp. 1840–1855, Nov. 2011, https://doi.org/10.2514/1.C031072.

[24] Chandrasekhara, M., and McLain, B. K., “Aerodynamic studies over a maneuvering UCAV 1303 configuration,” presented at the 2010 RAeS Aerodynamics Conference, Bristol, 2010.

[25] Chandrasekhara, Sosebee, and Medford, “Water Tunnel Force and Moment Studies of a Maneuvering UCAV 1303 and their Control,” presented at the 28th Congress of the International Council of the Aeronautical Sciences ICAS, Brisbane, Australia, 2012.

[26] Chudy, P., “Response of a Light Aircraft Under Gust Loads,” *Acta Polytechnica*, vol. 44, no. 2, Jan. 2004, https://doi.org/10.14311/556.

[27] Cook, M. V., *Flight Dynamics Principles*, Second Edition. Amsterdam; Boston: Elsevier Ltd, 2007, http://search.ebscohost.com/login.aspx?direct=true&scope=site&db=nlebk&db=nlabk&AN=203095.

[28] Crimaldi, J. P., Britt, R. T., and Rodden, W., “Response of B-2 aircraft to nonuniform spanwise turbulence,” *Journal of Aircraft*, vol. 30, no. 5, pp. 652–659, Sep. 1993, https://doi.org/10.2514/3.46394.

[29] Cummings, R. M., Liersch, C., and Schuette, A., “Multi-Disciplinary Design and Performance Assessment of Effective, Agile NATO Air Vehicles,” in *2018 Applied Aerodynamics Conference*, Atlanta, Georgia, 2018, https://doi.org/10.2514/6.2018-2838.

[30] Cummings, R. M., and Schuette, A., “The NATO STO Task Group AVT-201 on ‘Extended Assessment of Stability and Control Prediction Methods for NATO Air Vehicles,’” presented at the AIAA Aviation, Atlanta, GA, 2014, https://doi.org/10.2514/6.2014-2000.

[31] Cumnuantip, S., “Landing gear positioning and structural mass optimization for a large blended wing body aircraft,” Dissertation, TU München, Köln, 2014.

[32] De La Garza, McCulley, Johnson, Hunten, Action, Skillen, and Zink, “Recent Advances in Rapid Airframe Modeling at Lockheed Martin Aeronautics Company,” in *RTO-MP-AVT-173 Workshop*, Bulgaria, 2011.

[33] Deck, U., and Schwochow, J., “Aeroelastische Voruntersuchung des Nurfluegelsegelflugzeugs AK-X,” in *Deutscher Luft- und Raumfahrtkongress 2015*, Rostock, 2015.

[34] Deutsches Zentrum für Luft- und Raumfahrt e. V. (DLR), “CPACS A Common Language for Aircraft Design.” [Online]. Available: http://www.cpacs.de/. [Accessed: 08-Jun-2017].

[35] Deutsches Zentrum für Luft- und Raumfahrt e. V. (DLR), “RCE.” [Online]. Available: http://rcenvironment.de/. [Accessed: 08-Jun-2017].

[36] Dillinger, J. K. S., “Static aeroelastic optimization of composite wings with variable stiffness laminates,” Dissertation, TU Delft, 2014.

[37] Dillinger, J. K. S., Klimmek, T., Abdalla, M. M., and Gürdal, Z., "Stiffness Optimization of Composite Wings with Aeroelastic Constraints," *Journal of Aircraft*, vol. 50, no. 4, pp. 1159–1168, Jul. 2013, https://doi.org/10.2514/1.C032084.

[38] Dimitrov, D., and Thormann, R., "DLM-CORRECTION METHOD FOR AERODYNAMIC GUST RESPONSE PREDICTION," presented at the International Forum on Aeroelasticity and Structural Dynamics, Bristol, 2013.

[39] Dong Guo, Xu, M., and Shilu Chen, "Nonlinear Gust Response Analysis of Free Flexible Aircraft," *International Journal of Intelligent Systems and Applications*, vol. 5, no. 2, pp. 1–15, Jan. 2013, https://doi.org/10.5815/ijisa.2013.02.01.

[40] Dorbath, F., "A flexible wing modeling and physical mass estimation system for early aircraft design stages," Dissertation, TU Hamburg-Harburg, Hamburg, 2014, https://doi.org/10.15480/882.1159.

[41] Dormand, J. R., and Prince, P. J., "A family of embedded Runge-Kutta formulae," *Journal of Computational and Applied Mathematics*, vol. 6, no. 1, pp. 19–26, Mar. 1980, https://doi.org/10.1016/0771-050X(80)90013-3.

[42] Drela, M., "ASWING 5.99 Technical Description - Steady Formulation," Technical Description, Mar. 2015.

[43] Drela, M., "ASWING 5.99 Technical Description - Unsteady Extension," Technical Description, Mar. 2015.

[44] Drela, M., "Integrated simulation model for preliminary aerodynamic, structural, and control-law design of aircraft," presented at the 40th Structures, Structural Dynamics, and Materials Conference and Exhibit, Structures, Structural Dynamics, and Materials, 1999, https://doi.org/10.2514/6.1999-1394.

[45] D'Vari, R., and Baker, M., "Aeroelastic Loads and Sensitivity Analysis for Structural Loads Optimization," *Journal of Aircraft*, vol. 36, no. 1, pp. 156–166, 1999, https://doi.org/10.2514/2.2421.

[46] European Aviation Safety Agency, ed., *Certification Specifications for Large Aeroplanes CS-25*, Amendment 16. 2015.

[47] European Aviation Safety Agency, ed., *Certification Specifications for Normal, Utility, Aerobatic, and Commuter Category Aeroplanes CS-23*, Amendment 3. 2012.

[48] Galante, N., *The Helios Prototype flying wing is shown over the Pacific Ocean during its first test flight on solar power from the U.S. Navy's Pacific Missile Range Facility in Hawaii.* 2001, https://www.dfrc.nasa.gov/Gallery/Photo/Helios/HTML/ED01-0209-3.html.

[49] Ganzert, W., and Dirmeier, S., "Einsatz von Aerodynamischen Korrektur-Matrizen bei der Berechnung von Flügellasten mit MSC NASTRAN," presented at the Deutscher Luft- und Raumfahrt Kongress, 2002.

[50] Garbow, B. S., Hillstrom, K. E., and More, J. J., "minpack/hybrd.html," *Documentation for MINPACK subroutine HYBRD*, 1980. [Online]. Available: https://www.math.utah.edu/software/minpack/minpack/hybrd.html. [Accessed: 20-Apr-2017].

[51] Gibbs, Y., “NASA Armstrong Fact Sheet: Helios Prototype,” *NASA*, 13-Aug-2015. [Online]. Available: http://www.nasa.gov/centers/armstrong/news/FactSheets/FS-068-DFRC.html. [Accessed: 24-Mar-2017].

[52] Giesing, Kalman, and Rodden, W., “Correction Factor Techniques for Improving Aerodynamic Prediction Methods,” Technical Report NASA CR-144967, May 1976.

[53] Goggin, P., “A general gust and maneuver load analysis method to account for the effects of active control saturation and nonlinear aerodynamics,” 1992, https://doi.org/10.2514/6.1992-2126.

[54] Gupta, K. K., “STARS: An Integrated, Multidisciplinary, Finite-Element, Structural, Fluids, Aeroelastic, and Aeroservoelastic Analysis Computer Program,” National Aeronautics and Space Administration, Dryden Flight Research Center, Edwards, California, Technical Memorandum NASA TM 4795, May 1997, http://ntrs.nasa.gov/search.jsp?R=19970023059.

[55] Gupta, K. K., Brenner, M. J., and Voelker, L. S., “Developement of an Integrated Aeroservoelastic Analysis Program and Correlation With Test Data,” Dryden Flight Research Facility, Edwards, California, Technical Paper NASA Technical Paper 3120, 1991.

[56] Guyan, R., “Reduction of Stiffness and Mass Matrices,” *AIAA Journal*, vol. 3, no. 2, p. 280, 1964.

[57] Handojo, V., and Klimmek, T., “Böenlastanalyse der vorwärts gepfeilten ALLEGRA-Konfiguration,” in *Deutscher Luft- und Raumfahrtkongress*, Rostock, 2015.

[58] Hansen, L. U., *Optimierung von Strukturbauweisen im Gesamtentwurf von Blended Wing Body Flugzeugen*. Shaker :, 2009.

[59] Hansen, L. U., Heinze, W., and Horst, P., “Blended wing body structures in multidisciplinary pre-design,” *Structural and Multidisciplinary Optimization*, vol. 36, no. 1, pp. 93–106, Jul. 2008, https://doi.org/10.1007/s00158-007-0161-z.

[60] Hansen, L. U., Heinze, W., and Horst, P., “Representation of Structural Solutions in Blended Wing Body Preliminary Design,” presented at the 25th Congress of International Council of the Aeronautical Sciences, Hamburg, Germany, 2006.

[61] Harder, R. L., and Desmarais, R. N., “Interpolation using surface splines.,” *Journal of Aircraft*, vol. 9, no. 2, pp. 189–191, Feb. 1972, https://doi.org/10.2514/3.44330.

[62] Haryanto, I., Baier, H., and Laschka, B., “Aeroelastische Optimierung von Tragfluegelstrukturen mit semi-analytischen Finite-Element-Modellen,” Universitätsbibliothek der TU München, München, 2015, http://nbn-resolving.de/urn:nbn:de:bvb:91-diss-20151015-1223270-0-1.

[63] Hasselbrink, J., and Jenaro, G., “Use of Linearized CFD for Unsteady Aerodynamics for Gust Loads,” presented at the International Forum on Aeroelasticity and Structural Dynamics, Bristol, 2013.

[64] Hedman, S. G., “Vortex Lattice Method for Calculation of Quasi Steady State Loadings on Thin Elastic Wings in Subsonic Flow,” FFA Flygtekniska Försöksanstalten, Stockholm, Sweden, FFA Report 105, 1966.

[65] Heinze, W., Österheld, C. M., and Horst, P., “Multidisziplinaeres Flugzeugentwurfsverfahren PrADO-Programmentwurf und Anwendung im Rahmen von Flugzeug-Konzeptstudien,” presented at the Deutscher Luft- und Raumfahrtkongress, Hamburg, Germany, 2001.

[66] Hoblit, F. M., *Gust Loads on Aircraft: Concepts and Applications*. Washington DC: American Institute of Aeronautics and Astronautics, 1988, http://arc.aiaa.org/doi/book/10.2514/4.861888.

[67] Huber, K., Schütte, A., and Rein, M., “Numerical Investigation of the Aerodynamic Properties of a Flying Wing Configuration,” in *32nd AIAA Applied Aerodynamics Conference*, New Orleans, Louisiana, 2012.

[68] Hürlimann, F., “Mass estimation of transport aircraft wingbox structures with a CAD/CAE-based multidisciplinary process,” ETH, Zürich, 2010.

[69] Hürlimann, F., Kelm, R., Dugas, M., and Kress, G., “Investigation of local load introduction methods in aircraft pre-design,” *Aerospace Science and Technology*, vol. 21, no. 1, pp. 31–40, Sep. 2012, https://doi.org/10.1016/j.ast.2011.04.008.

[70] Hürlimann, F., Kelm, R., Dugas, M., Oltmann, K., and Kress, G., “Mass estimation of transport aircraft wingbox structures with a CAD/CAE-based multidisciplinary process,” *Aerospace Science and Technology*, vol. 15, no. 4, pp. 323–333, 2011.

[71] IJsselmuiden, S. T., “Optimal design of variable stiffness composite structures using lamination parameters,” Dissertation, TU Delft, 2011, https://repository.tudelft.nl/islandora/object/uuid:973a564b-5734-42c4-a67c-1044f1e25f1c?collection=research.

[72] Jacques, V., and Garrigues, E., “Ground Dynamic Loads Calculations Strategies for Civilian and Military Aircrafts,” presented at the International Forum for Aeroelasticity and Structural Dynamics, Bristol, 2013.

[73] Jirasek, A., Cummings, R. M., Schütte, A., and Huber, K. C., “Extended Assessment of Stability and Control Prediction Methods for NATO Air Vehicles,” NATO STO, Technical Report RDP STO-TR-AVT-201, Nov. 2016, https://www.sto.nato.int/publications/STO%20Technical%20Reports/STO-TR-AVT-201/$$TR-AVT-201-ALL.pdf.

[74] Kaiser, C., Thormann, R., Dimitrov, D., and Nitsche, J., “Time-Linearized Analysis of Motion-Induced and Gust-Induced Airloads with the DLR Tau-Code,” presented at the Deutscher Luft- und Raumfahrtkongress 2015, Rostock, Germany, 2015.

[75] Kaminski-Morrow, D., “Airbus exploits A320 load-alleviation to offer higher MTOW,” *Flight Global*, 20-Nov-2008. [Online]. Available: https://www.flightglobal.com/news/articles/airbus-exploits-a320-load-alleviation-tooffer-higher-mtow-319049/. [Accessed: 29-May-2019].

[76] Karpel, M., and Strul, E., “Minimum-state unsteady aerodynamic approximations with flexible constraints,” *Journal of Aircraft*, vol. 33, no. 6, pp. 1190–1196, Nov. 1996, https://doi.org/10.2514/3.47074.

[77] Katz, J., and Plotkin, A., *Low-speed aerodynamics: from wing theory to panel methods*. New York: McGraw-Hill, 1991.

[78] Kelm, Läpple, and Grabietz, “Wing primary structure weight estimation of transport aircrafts in the pre-development phase,” in *54th Annual Conference of Society of Allied Weight Engineers, Inc.*, Huntsville, Alabama, 1995.

[79] Kier, T., and Hofstee, J., “VarLoads - Eine Simulationsumgebung zur Lastenberechnung eines voll flexiblen, freifliegenden Flugzeugs,” in *Deutscher Luft- und Raumfahrtkongress*, Dresden, 2004.

[80] Kier, T., and Looye, G., “Unifying Manoeuver and Gust Loads Analysis Models,” in *International Forum for Aeroelasticity and Structural Dynamics*, 2009.

[81] Kier, T., Looye, G., Scharpenberg, M., and Reijerkerk, M., “Process, Methods and Tools for Flexible Aircraft Flight Dynamics Model Integration,” in *International Forum on Aeroelasticity and Structural Dynamics*, Stockholm, Sweden, 2007, http://elib.dlr.de/55663/.

[82] Kier, T., Verveld, M. J., and Burkett, C. W., “Integrated Flexible Dynamic Loads Models Based on Aerodynamic Influence Coefficients of a 3D Panel Method,” in *International Forum on Aeroelasticity and Structural Dynamics*, St. Petersburg, Russische Föderation, 2015, http://elib.dlr.de/97804/.

[83] Klimmek, T., “Parameterization of topology and geometry for the multidisciplinary optimization of wing structures,” in *CEAS 2009 - European Air and Space Conference*, Manchester, United Kingdom, 2009.

[84] Klimmek, T., “Parametric Set-Up of a Structural Model for FERMAT Configuration for Aeroelastic and Loads Analysis,” *Journal of Aeroelasticity and Structural Dynamics*, no. 2, pp. 31–49, May 2014, https://doi.org/10.3293/asdj.2014.27.

[85] Klimmek, T., “Statische aeroelastische Anforderungen beim multidisziplinaeren Strukturentwurf von Verkehrsflugzeugflügeln,” Dissertation, Technischen Universität Carolo-Wilhelmina zu Braunschweig, Göttingen, Germany, 2016.

[86] Klimmek, T., and Schulze, M., “cpacs-MONA – An Independent and in High-Fidelity Based MDO Tasks Integrated Process for the Structural and Aeroelastic Design of Aircraft Configurations,” presented at the IFASD 2019 - 18th International Forum on Aeroelasticity and Structural Dynamics, Savannah, Georgia, 2019.

[87] Koehler, A., *Rooster Weather Vane*. 2005, https://commons.wikimedia.org/wiki/File:Rooster_Weather_Vane.jpg.

[88] Kotikalpudi, A., “Body Freedom Flutter (BFF) Doublet Lattice Method (DLM),” *University of Minnesota Digital Conservancy*, 09-Sep-2014. [Online]. Available: http://hdl.handle.net/11299/165566. [Accessed: 12-Feb-2016].

[89] Kotikalpudi, A., Pfifer, H., and Balas, G. J., “Unsteady Aerodynamics Modeling for a Flexible Unmanned Air Vehicle,” in *AIAA Atmospheric Flight Mechanics Conference*, Dallas, Texas, 2015, https://doi.org/10.2514/6.2015-2854.

[90] Kozek, M., and Schirrer, A., eds., *Modeling and Control for a Blended Wing Body Aircraft*. Cham: Springer International Publishing, 2015, https://doi.org/10.1007/978-3-319-10792-9.

[91] Krüger, W., Klimmek, T., Liepelt, R., Schmidt, H., Waitz, S., and Cumnuantip, S., "Design and aeroelastic assessment of a forward-swept wing aircraft," *CEAS Aeronautical Journal*, vol. 5, no. 4, pp. 419–433, 2014, https://doi.org/10.1007/s13272-014-0117-0.

[92] Krüger, W. R., "A multi-body approach for modelling manoeuvring aeroelastic aircraft during preliminary design," *Proceedings of the Institution of Mechanical Engineers, Part G: Journal of Aerospace Engineering*, vol. 222, no. 6, pp. 887–894, Jun. 2008, https://doi.org/10.1243/09544100JAERO264.

[93] Krüger, W. R., "Integrated design process for the development of semi-active landing gears for transport aircraft," Dissertation, Universität Stuttgart, Stuttgart, Deutschland, 2000, http://elib.uni-stuttgart.de/handle/11682/3675.

[94] Krüger, W. R., Besselink, I., Cowling, D., Doan, D. B., Kortüm, W., and Krabacher, W., "Aircraft Landing Gear Dynamics: Simulation and Control," *Vehicle System Dynamics*, vol. 28, no. 2–3, pp. 119–158, Aug. 1997, https://doi.org/10.1080/00423119708969352.

[95] Krüger, W. R., Cumnuantip, S., and Liersch, C. M., "Multidisciplinary Conceptual Design of a UCAV Configuration," in *Proceedings AVT-MP-173*, Sofia, Bulgaria, 2011.

[96] Krumbein, A., "Transition Modeling Activities at AS-$C^2A^2S^2E$ (DLR)," presented at the CFD Transition Modeling Discussion Group Meeting, 36th Applied Aerodynamics Conference, Denver, Colorado, 2017, https://elib.dlr.de/113935/.

[97] Küssner, H. G., "Allgemeine Tragflächentheorie," *Luftfahrtforschung*, vol. 17, no. 11/12, pp. 370–78, Dec. 1940.

[98] Küssner, H. G., "General Airfoil Theory," National Advisory Committee for Aeronautics, Washington, Technical Memorandum NACA-TM-979, Jun. 1941, http://ntrs.nasa.gov/search.jsp?R=19930094437.

[99] Kuzmina, S. I., Chedrik, V. V., and Ishmuratov, F. Z., "Strength and Aeroelastic Structural Optimization of Aircraft Lifting Surfaces using Two-Level Approach," presented at the 6th World Congress of Structural and Multidisciplinary Optimization, Rio de Janeiro, Brazil, 2005.

[100] Lecheler, S., *Numerische Stroemungsberechnung: schneller Einstieg durch anschauliche Beispiele*, 2. aktualisierte und erw. Auflage. Wiesbaden: Vieweg + Teubner, 2011.

[101] Lehoucq, R., Maschoff, K., Sorensen, D., and Yang, C., "ARPACK - Arnoldi Package," *ARPACK SOFTWARE*. [Online]. Available: http://www.caam.rice.edu/software/ARPACK/. [Accessed: 21-Aug-2017].

[102] Leitner, M., Knoblach, A., Kier, T. M., Moreno, C. P., Kotikalpudi, A., Pfifer, H., and Balas, G. J., "Flight Dynamics Modeling of a Body Freedom Flutter Vehicle for Multidisciplinary Analyses," 2015, https://doi.org/10.2514/6.2015-0905.

[103] Lemmens, Y., Verhoogen, J., Naets, F., Olbrechts, T., Vandepitte, D., and Desmet, W., "Modelling of Aerodynamic Loads on Flexible Bodies for Ground Loads Analysis," presented at the International Forum for Aeroelasticity and Structural Dynamics, Bristol, 2013.

[104] Liebeck, R., “Design of the Blended-Wing-Body subsonic transport,” 2002, https://doi.org/10.2514/6.2002-2.

[105] Liebeck, R. H., “Design of the Blended Wing Body Subsonic Transport,” *Journal of Aircraft*, vol. 41, no. 1, pp. 10–25, Jan. 2004, https://doi.org/10.2514/1.9084.

[106] Liepelt, R., Handojo, V., and Klimmek, T., “Aeroelastic Analysis Modelling Process to Predict The Critical Loads in an MDO Environement,” presented at the International Forum on Aeroelasticity and Structural Dynamics, Saint Petersburg, Russia, 2015.

[107] Liersch, C. M., “Excel Sheet MULDICON_V2.2a.xlsx,” DLR Project Mephisto, Internal Conceptual Design Sheet Version 2.2a, Dec. 2016.

[108] Liersch, C. M., and Huber, K. C., “Conceptual Design and Aerodynamic Analyses of a Generic UCAV Configuration,” in *32nd AIAA Applied Aerodynamics Conference*, Atlanta, GA, 2014, https://doi.org/10.2514/6.2014-2001.

[109] Liersch, C. M., Huber, K. C., Schütte, A., Zimper, D., and Siggel, M., “Multidisciplinary design and aerodynamic assessment of an agile and highly swept aircraft configuration,” *CEAS Aeronautical Journal*, vol. 7, no. 4, pp. 677–694, Dec. 2016, https://doi.org/10.1007/s13272-016-0213-4.

[110] Liersch, C. M., and Immisch, T., “DLR-Projekt Mephisto Meilenstein M-4100-1 Lastenhefte für die ausgewaehlten Konfigurationen,” DLR Project Mephisto, Internal Design Specifications Sheet Version 1.3, Nov. 2016.

[111] Liersch, C. M., Schütte, A., Siggel, M., and Dornwald, J., “Design Studies and Multi-Disciplinary Assessment of Agile and Highly Swept Flying Wing Configurations,” in *Deutscher Luft- und Raumfahrtkongress 2018*, Friedrichshafen, Deutschland, 2018, https://elib.dlr.de/126539/.

[112] Loeser, T., Vicroy, D., and Schuette, A., “SACCON Static Wind Tunnel Tests at DNW-NWB and 14x22 NASA LaRC,” 2010, https://doi.org/10.2514/6.2010-4393.

[113] Lutz, H., and Wendt, W., *Taschenbuch der Regelungstechnik: mit MATLAB und Simulink*, 10., ergänzte Aufl. Haan-Gruiten: Verl. Europa-Lehrmittel, Nourney, Vollmer, 2014.

[114] Maierl, R., Petersson, Ö., and Daoud, F., “Automated Creation of Aeroelastic Optimization Models From a Parameterized Geometry,” presented at the IFASD 2013, Bristol, 2013.

[115] Maierl, R., Petersson, Ö., Daoud, F., and Bletzinger, K.-U., “Automatic Generation of Aeroelastic Simulation Models Combined with a Knowledge Based Mass Prediction,” presented at the CEAS 2015, 2015.

[116] Maierl, Reinhold, Petersson, Ö., Daoud, F., and Bletzinger, K.-U., “Automatically Generated Aeroelastic Analysis Models including Physics Based Control Surface Representation,” presented at the 4TH AIRCRAFT STRUCTURAL DESIGN CONFERENCE, Belfast, 2014.

[117] Marquard, M., “Erweiterte Prozesskette zur Erstellung integraler Modelle und Aeroelastikregelung flexibler Transportflugzeuge im transsonischen Machzahlbereich,” Dissertation, Universität Stuttgart, Stuttgart, Deutschland, 2009, https://doi.org/10.18419/opus-3792.

[118] Mauermann, T., “Flexible Aircraft Modelling for Flight Loads Analysis of Wake Vortex Encounters,” Dissertation, Technischen Universität Carolo-Wilhelmina zu Braunschweig, Braunschweig, 2001.

[119] Meddaikar, Y. M., Dillinger, J. K. S., and Govers, Y., “Optimization & Testing of Aeroelastically-Tailored Forward Swept Wings,” presented at the IFASD 2017 - 17th International Forum on Aeroelasticity and Structural Dynamics, Como, Italy, 2017.

[120] Nangia, R., and Palmer, M., “A Comparative Study of UCAV Type Wing Planforms - Aero Performance & Stability Considerations,” in *23rd AIAA Applied Aerodynamics Conference*, Toronto, Ontario, Canada, 2005, https://doi.org/10.2514/6.2005-5078.

[121] NASA, “Helios Mishap Photo Previews,” *NASA News*. [Online]. Available: https://www.nasa.gov/centers/dryden/news/ResearchUpdate/Helios/Previews/index.html. [Accessed: 05-Mar-2018].

[122] NASA, “NASA Releases Helios Prototype Aircraft Mishap Report,” *NASA News*, 27-Nov-2004. [Online]. Available: http://www.nasa.gov/centers/dryden/news/NewsReleases/2004/04-42.html. [Accessed: 05-Mar-2018].

[123] Naser, A. S., Pototzky, A. S., and Spain, C. V., “Response of the Alliance 1 Proof-of-Concept Airplane Under Gust Loads,” Lockheed Martin Engineering and Sciences Company, Hampton, Virginia, Technical Report NASA CR-2001-210649, Mar. 2001, http://ntrs.nasa.gov/search.jsp?R=20010038652.

[124] National Aeronautics and Space Administration, *The Nastran Programmer’s Manual*, NASA SP-223(01). Washington, D.C.: COSMIC, 1972.

[125] Nauroz, M., “Antriebskonzept einer agilen hoch gepfeilten Flugzeugkonfiguration,” in *Deutscher Luft- und Raumfahrtkongress*, Rostock, 2015, http://elib.dlr.de/98597/.

[126] Neill, D. J., Johnson, E. H., and Canfield, R., “ASTROS - A multidisciplinary automated structural design tool,” *Journal of Aircraft*, vol. 27, no. 12, pp. 1021–1027, Dec. 1990, https://doi.org/10.2514/3.45976.

[127] Neumann, J., “Identifikation radialer Basisfunktionen zur räumlichen Strömungs-Struktur-Kopplung unter Berücksichtigung des Interpolations- und des Lasttransformationsfehlers,” Institute of Aeroelasticity, Göttingen, Germany, Internal Report DLR IB 232-2008 J 01, 2008.

[128] Neumann, J., and Krüger, W. R., “Coupling Strategies for Large Industrial Models,” in *Computational Flight Testing*, vol. 123, N. Kroll, R. Radespiel, J. W. Burg, and K. Sørensen, Eds. Berlin, Heidelberg: Springer Berlin Heidelberg, 2013, pp. 207–222.

[129] Neumann, J., and Mai, H., “Gust response: Simulation of an aeroelastic experiment by a fluid–structure interaction method,” *Journal of Fluids and Structures*, vol. 38, pp. 290–302, Apr. 2013, https://doi.org/10.1016/j.jfluidstructs.2012.12.007.

[130] Nickel, K., and Wohlfahrt, M., *Schwanzlose Flugzeuge: Ihre Auslegung und ihre Eigenschaften*. Basel: Birkhäuser, 1990.

[131] Oesterheld, C. M., *Physikalisch begründete Analyseverfahren im integrierten multidisziplinären Flugzeugvorentwurf*. Aachen: Shaker, 2004.

[132] Oesterheld, C. M., Heinze, W., and Horst, P., "Influence of Aeroelastic Effects on Preliminary Aircraft Design," presented at the 22nd INTERNATIONAL CONGRESS OF AERONAUTICAL SCIENCES, Harrogate, UK, 2000.

[133] Oesterheld, C. M., Heinze, W., and Horst, P., "Preliminary Design of a Blended Wing Body Configuration using the Design Tool PrADO," presented at the CEAS Conference on Multidisciplinary Aircraft Design and Optimization, Köln, German, 2001, http://citeseerx.ist.psu.edu/viewdoc/download?doi=10.1.1.69.7786&rep=rep1&type=pdf.

[134] Ouellette, J., "Aeroservoelastic Modeling of Body Freedom Flutter for Control System Design," presented at the 58th AIAA/ASCE/AHS/ASC Structures, Structural Dynamics, and Materials Conference, Grapevine, Texas, 2017.

[135] Palacios, R., Climent, H., Karlsson, A., and Winzell, B., "Assessment of Strategies for Correcting Linear Unsteady Aerodynamics Using CFD or Test Results," in *International Forum on Aeroelasticity and Structural Dynamics*, 2001.

[136] Patil, M., Hodges, D., and Cesnik, C., "Nonlinear aeroelasticity and flight dynamics of High-Altitude Long-Endurance aircraft," in *40th Structures, Structural Dynamics, and Materials Conference and Exhibit*, 1999, http://arc.aiaa.org/doi/abs/10.2514/6.1999-1470.

[137] Patil, M. J., and Hodges, D. H., "On the importance of aerodynamic and structural geometrical nonlinearities in aeroelastic behavior of high-aspect-ratio wings," *Journal of Fluids and Structures*, vol. 19, no. 7, pp. 905–915, Aug. 2004, https://doi.org/10.1016/j.jfluidstructs.2004.04.012.

[138] Patil, M. J., Hodges, D. H., and Cesnik, C. E. S., "Nonlinear Aeroelasticity and Flight Dynamics of High-Altitude Long-Endurance Aircraft," *Journal of Aircraft*, vol. 38, no. 1, pp. 88–94, 2001, https://doi.org/10.2514/2.2738.

[139] Patil, M., and Taylor, D., "Gust Response of Highly Flexible Aircraft," presented at the 47th AIAA/ASME/ASCE/AHS/ASC Structures, Structural Dynamics, and Materials Conference, Newport, Rhode Island, 2006, http://arc.aiaa.org/doi/abs/10.2514/6.2006-1638.

[140] Pinho Chiozzotto, G., "A modular implementation of aircraft simplified loads methods for conceptual design and variable fidelity processes," presented at the Deutscher Luft- und Raumfahrtkongress, Stuttgart, Deutschland, 2013, http://elib.dlr.de/84431/.

[141] Pinho Chiozzotto, G., "Conceptual design method for the wing weight estimation of strut-braced wing aircraft," in *5th CEAS Air & Space Conference*, Delft, The Netherlands, 2015, http://elib.dlr.de/98248/.

[142] Pinho Chiozzotto, G., "Kriterien fuer die Erstellung eines Lastenkatalogs," Institute of Aeroelasticity, iLOADs MS1.2, Feb. 2014.

[143] Pinho Chiozzotto, G., “Wing weight estimation in conceptual design: a method for strut-braced wings considering static aeroelastic effects,” *CEAS Aeronautical Journal*, vol. 7, no. 3, pp. 499–519, Sep. 2016, https://doi.org/10.1007/s13272-016-0204-5.

[144] Powell, M. J., “A hybrid method for nonlinear equations,” *Numerical methods for nonlinear algebraic equations*, vol. 7, pp. 87–114, 1970.

[145] Prandtl, L., “Beitrag zur Theorie der tragenden Fläche,” *ZAMM - Journal of Applied Mathematics and Mechanics / Zeitschrift für Angewandte Mathematik und Mechanik*, vol. 16, no. 6, pp. 360–361, 1936, https://doi.org/10.1002/zamm.19360160613.

[146] Pratt, K. G., “A revised formula for the calculation of gust loads,” National Advisory Committee for Aeronautics. Langley Aeronautical Lab., Langley Field, VA, Technical Note TN 2964, Jun. 1953, http://ntrs.nasa.gov/search.jsp?R=19930084025.

[147] Pratt, K. G., and Walker, W. G., “A Revised Gust-Load Formula and a Re-evaluation of V-G Data Taken on Civil Transport Airplanes From 1933 to 1950,” National Advisory Committee for Aeronautics. Langley Aeronautical Lab., Langley Field, VA, Technical Report NACA-TR-1206, 1953.

[148] QinetiQ Group plc, “QinetiQ’s Zephyr UAV exceeds official world record for longest duration unmanned flight,” *QinetiQ*, 10-Sep-2007. [Online]. Available: https://www.qinetiq.com/media/news/releases/Pages/qinetiqs-zephyr-exceeds-world-record.aspx. [Accessed: 24-Mar-2017].

[149] Quero Martin, D., “An Aeroelastic Reduced Order Model for Dynamic Response Prediction to Gust Encounters,” Dissertation, TU Berlin, Berlin, 2016.

[150] Raghavan, B., and Patil, M., “Flight Dynamics of High Aspect-Ratio Flying Wings,” in *AIAA Atmospheric Flight Mechanics Conference and Exhibit*, American Institute of Aeronautics and Astronautics.

[151] Rampurawala, A. M., “Aeroelastic analysis of aircraft with control surfaces using CFD,” PhD, University of Glasgow, 2005, http://encore.lib.gla.ac.uk/iii/encore/record/C__Rb2463271.

[152] Raymer, D. P., *Aircraft design: a conceptual approach*, 5th ed. Reston, VA: American Institute of Aeronautics and Astronautics, 2012.

[153] Reimer, L., Ritter, M., Heinrich, R., and Krüger, W. R., “CFD-based Gust Load Analysis for a Free-flying Flexible Passenger Aircraft in Comparison to a DLM-based Approach,” in *AIAA Aviation*, 2015, https://doi.org/10.2514/6.2015-2455.

[154] Reschke, “Integrated Flight Loads Modelling and Analysis for Flexible Transport Aircraft,” Dissertation, Universität Stuttgart, Oberpfaffenhofen, Germany, 2006.

[155] Ricciardi, A., “Utility of Quasi-Static Gust Loads Certification Methods for Novel Configurations,” Master Thesis, Virginia Polytechnic Institute and State University, Blacksburg, Virginia, 2011.

[156] Ricciardi, A. P., Patil, M. J., Canfield, R. A., and Lindsley, N., “Evaluation of Quasi-Static Gust Loads Certification Methods for High-Altitude Long-Endurance Aircraft,” *Journal of Aircraft*, vol. 50, no. 2, pp. 457–468, Mar. 2013, https://doi.org/10.2514/1.C031872.

[157] Ricciardi, A., Patil, M., Canfield, R., and Lindsley, N., "Utility of Quasi-Static Gust Loads Certification Methods for Novel Configurations," presented at the 52nd AIAA/ASME/ASCE/AHS/ASC Structures, Structural Dynamics and Materials Conference, Denver, Colorado, 2011, http://arc.aiaa.org/doi/abs/10.2514/6.2011-2043.

[158] Ritter, M., and Dillinger, J., "Nonlinear numerical flight dynamics for the prediction of maneuver loads," in *International Forum on Aeroelasticity and Structural Dynamics*, Paris, France, 2011.

[159] Rodden, W., Harder, R., and Bellinger, D., "Aeroelastic Addition to NASTRAN," NASA Langley Research Center, Los Angeles, California, Contractor Report NASA Contractor Report 3094, Mar. 1979.

[160] Rodden, W., MacNeal, Harder, R., McLean, and Bellinger, D., *MSC.Nastran Version 68 Aeroelastic Analysis User's Guide*. MSC.Software Corporation, 2010.

[161] Rodden, W. P., Giesing, J. P., and Kálmán, T. P., "New Developments and Application of the Subsonic Doublet-Lattice Method for Nonplanar Configurations," *AGARD-CP-80-PT-2 - Symposium on Unsteady Aerodynamics for Aeroelastic Analyses of Interfering Surfaces*, no. Part 2, Jan. 1971.

[162] Rodden, W., Taylor, P., and McIntosh, S., "Further Refinements of the Subsonic Doublet-Lattice Method," *Journal of Aircraft*, vol. 35, no. 5, pp. 720–727, Oct. 1998.

[163] Roger, K. L., "Airplane Math Modeling Methods For Active Control Design," in *AGARD-CP-228*, 1977.

[164] Ross, J., "X-45 Air Vehicle #1 Flight," 19-Dec-2002. [Online]. Available: http://archive.darpa.mil/j-ucas/X-45/gallery.htm. [Accessed: 01-Mar-2018].

[165] Schäfer, D., Vidy, C., Mack, C., and Arnold, J., "Assessment of Body-Freedom Flutter for an Unmanned Aerial Vehicle," in *Deutscher Luft- und Raumfahrtkongress*, Braunschweig, 2016.

[166] Scharpenberg, M., "Uncertainty quantification for nonlinear differential equations with application to aircraft mechanics," Dissertation, TU Hamburg-Harburg, Hamburg, 2012.

[167] Scharpenberg, M., Kier, T., and Taules, L., "Considerations on an Integral Flight Physics Model with Application to Loads Analysis," in *SAE International*, 2011, https://doi.org/10.4271/2011-01-2767.

[168] Scharpenberg, M., and Voß, A., "Application of Nonlinear Geometrical Effects to the Analysis of Structural Loads using Fast Evaluation Methods," presented at the International Forum for Aeroelasticity and Structural Dynamics, Bristol, United Kingdom, 2013.

[169] Schlichting, H., and Truckenbrodt, E., *Aerodynamik des Flugzeuges: Aerodynamik des Tragflügels (Teil 2), des Rumpfes, der Flügel-Rumpf-Anordnung und Leitwerke*, Zweite neubearbeitete Auflage. Springer-Verlag, 1969.

[170] Schreiber, P., Vidy, C., Voß, A., Arnold, J., and Mack, C., "Dynamic Aeroelastic Stability Analyses of Parameterized Flying Wing Configurations," presented at the Deutscher Luft- und Raumfahrtkongress, Friedrichshafen, 2018, https://elib.dlr.de/124855/.

[171] Schuhmacher, G., Murra, I., Wang, L., Laxander, A., O'Leary, O., and Herold, M., "Multidisciplinary Design Optimization of a Regional Aircraft Wing Box," in *9th AIAA/ISSMO Symposium on Multidisciplinary Analysis and Optimization*, Atlanta, Georgia, 2002, http://arc.aiaa.org/doi/abs/10.2514/6.2002-5406.

[172] Schuhmacher, G., Stettner, M., Zotemantel, R., O'Leary, O., and Wagner, M., "Optimization Assisted Structural Design of a New Military Transport Aircraft," presented at the 10th AIAA/ISSMO Multidisciplinary Analysis and Optimization Conference, Albany, New York, 2004, https://doi.org/10.2514/6.2004-4641.

[173] Schürmann, H., *Konstruieren mit Faser-Kunststoff-Verbunden*. Berlin; Heidelberg; New York: Springer, 2007.

[174] Schütte, A., "Numerical Investigations of Vortical Flow on Swept Wings with Round Leading Edges," *Journal of Aircraft*, vol. 54, no. 2, pp. 572–601, Mar. 2017, https://doi.org/10.2514/1.C034057.

[175] Schütte, A., Huber, K. C., and Zimper, D., "Numerische aerodynamische Analyse und Bewertung einer agilen und hoch gepfeilten Flugzeugkonfiguration," presented at the Deutscher Luft- und Raumfahrtkongress, Rostock, 2015, https://elib.dlr.de/98366/.

[176] Schwamborn, D., Gerhold, T., and Heinrich, R., "The DLR Tau-Code: Recent Applications in Research and Industry," in *European Conference on Computational Fluid Dynamics*, 2006.

[177] Schweiger, J., Sensburg, O., and Berns, H. J., "Aeroelastic Problems and Structural Design of a Tailless CFC-Sailplane," in *Second International Symposium on Aeroelasticity and Structural Dynamics*, Aachen, 1985.

[178] Siggel, M., and Schreiber, A., *tixi: Fast and simple XML interface library*. DLR Simulation and Software Technology, 2017, https://github.com/DLR-SC/tixi.

[179] Silvestre, F. J., "Methodology for Modelling the Dynamics of Flexible, High-aspect-ratio Aircraft in the Time Domain for Aeroservoelastic Investigations," Dissertation, TU Berlin, Berlin, 2012.

[180] Solar Impulse SA, "Solar Impulse - Around the world to promote clean technologies," *Solar Impulse*. [Online]. Available: http://www.solarimpulse.com/. [Accessed: 24-Mar-2017].

[181] Stauffer, W. A., Lewolt, J. G., and Hoblit, F. M., "Application of Advanced Methods to Design Loads Determination for the L-1011 Transport," *Journal of Aircraft*, vol. 10, no. 8, pp. 449–458, 1973, https://doi.org/10.2514/3.60248.

[182] Stauffer, W., Lewolt, J., and Hoblit, F., "Application of advanced methods to the determination of design loads of the Lockheed L-1011 TriStar," 1972, https://doi.org/10.2514/6.1972-775.

[183] Stenfelt, G., and Ringertz, U., "Lateral Stability and Control of a Tailless Aircraft Configuration," *Journal of Aircraft*, vol. 46, no. 6, pp. 2161–2164, Nov. 2009, https://doi.org/10.2514/1.41092.

[184] Stenfelt, G., and Ringertz, U., "Yaw Control of a Tailless Aircraft Configuration," *Journal of Aircraft*, vol. 47, no. 5, pp. 1807–1811, Sep. 2010, https://doi.org/10.2514/1.C031017.

[185] Stroscher, F., Schirrer, A., Valášek, M., Šika, Z., Vampola, T., Paluch, B., Joly, D., Breitsamter, C., Meyer, M., Paulus, D., Klimmek, T., and Baier, H., "Numerical Simulation Model," in *Modeling and Control for a Blended Wing Body Aircraft*, M. Kozek and A. Schirrer, Eds. Cham: Springer International Publishing, 2015, pp. 47–104.

[186] Su, W., and Cesnik, C., "Dynamic Response of Highly Flexible Flying Wings," presented at the 47th AIAA/ASME/ASCE/AHS/ASC Structures, Structural Dynamics, and Materials Confere, Newport, Rhode Island, 2006, https://doi.org/10.2514/6.2006-1636.

[187] Su, W., and Cesnik, C., "Nonlinear Aeroelasticity of a Very Flexible Blended-Wing-Body Aircraft," presented at the 50th AIAA/ASME/ASCE/AHS/ASC Structures, Structural Dynamics, and Materials Conference, Palm Springs, California, 2009, https://doi.org/10.2514/6.2009-2402.

[188] Teufel, P., "Boeenmodellierung und Lastabminderung fuer ein flexibles Flugzeug," Universität Stuttgart, Stuttgart, Deutschland, 2003, http://elib.uni-stuttgart.de/opus/volltexte/2003/1400.

[189] The Scipy community, "scipy.integrate.ode," *SciPy v0.18.0 Reference Guide*. [Online]. Available: http://docs.scipy.org/doc/scipy/reference/generated/scipy.integrate.ode.html#scipy.integrate.ode. [Accessed: 08-Aug-2016].

[190] The Scipy community, "scipy.optimize.fsolve," *SciPy v0.17.0 Reference Guide*. [Online]. Available: http://docs.scipy.org/doc/scipy/reference/generated/scipy.optimize.fsolve.html. [Accessed: 24-Feb-2016].

[191] The Scipy community, "scipy.sparse.linalg.eigs," *SciPy v0.19.1 Reference Guide*. [Online]. Available: https://docs.scipy.org/doc/scipy-0.19.1/reference/generated/scipy.sparse.linalg.eigs.html. [Accessed: 21-Aug-2017].

[192] Thormann, R., and Dimitrov, D., "Correction of aerodynamic influence matrices for transonic flow," *CEAS Aeronautical Journal*, vol. 5, no. 4, pp. 435–446, 2014, https://doi.org/10.1007/s13272-014-0114-3.

[193] Tianyuan, H., and Xiongqing, Y., "Aerodynamic/Stealthy/Structural Multidisciplinary Design Optimization of Unmanned Combat Air Vehicle," *Chinese Journal of Aeronautics*, vol. 22, no. 4, pp. 380–386, Aug. 2009, https://doi.org/10.1016/S1000-9361(08)60114-4.

[194] Tijdeman, H., "Investigations of the Transonic Flow Around Oscillation Airfoils," Dissertation, TU Delft, 1977.

[195] Tinoco, E. N., Bogue, D. R., Kao, T.-J., Yu, N. J., Li, P., and Ball, D. N., "Progress toward CFD for full flight envelope," *The Aeronautical Journal*, vol. 109, no. 1100, pp. 451–460, Oct. 2005, https://doi.org/10.1017/S0001924000000865.

[196] Torenbeek, E., *Synthesis of subsonic airplane design: An introduction to the preliminary design, of subsonic general aviation and transport aircraft, with emphasis on layout, aerodynamic design, propulsion, and performance*. Delft : The Hague : Hingham, MA: Delft University Press ; Nijhoff ; Sold and distributed in the U.S. and Canada by Kluwer Boston, 1976.

[197] Vanderplaats, G. N., "ADS - A FORTRAN program for automated design synthesis - Version 1.10," University of California, Santa Barbara, CA, United States, Technical Report NASA-CR-177985, Sep. 1985, https://ntrs.nasa.gov/search.jsp?R=19860002427.

[198] VDI-Fachbereich Kunststofftechnik, "Entwicklung von Bauteilen aus Faser-Kunststoff-Verbund - Berechnungen," Verein Deutscher Ingenieure, Richtlinie VDI 2014 Blatt 3, Sep. 2006.

[199] Vepa, R., "Finite State Modelling of Aeroelastic Systems," Stanford University, California, Ph.D. Dissertation NASA CR-2779, Feb. 1977.

[200] Vidy, C., Katzenmeier, L., Winter, M., and Breitsamer, C., "Verification of the use of small-disturbance CFD aerodynamics in flutter and gust analyses for simple to highly complex configurations," presented at the International Forum for Aeroelasticity and Structural Dynamics, Saint Petersburg, Russia, 2015.

[201] Voß, A., "Comparing VLM and CFD Maneuver Loads Calculations for a Flying Wing Configuration," presented at the 18th International Forum on Aeroelasticity and Structural Dynamics, Savannah, Georgia, 2019, https://elib.dlr.de/127750.

[202] Voß, A., "Comparison between VLM and CFD Maneuver Loads Calculation at the Example of a Flying Wing Configuration," *Journal of Aeroelasticity and Structural Dynamics*, vol. 7, no. 1, pp. 19–37, Dec. 2019, https://doi.org/10.3293/asdj.2019.52.

[203] Voß, A., "Gust Loads Calculation for a Flying Wing Configuration," presented at the AIAA AVIATION Forum, Atlanta, Georgia, 2018, https://doi.org/10.2514/6.2018-3326.

[204] Voß, A., "Open and closed loop gust loads analyses for a flying wing configuration with variable longitudinal stability," *Aerospace Science and Technology*, vol. 89, pp. 1–10, Apr. 2019, https://doi.org/10.1016/j.ast.2019.03.049.

[205] Voß, A., and Klimmek, T., "Design and sizing of a parametric structural model for a UCAV configuration for loads and aeroelastic analysis," *CEAS Aeronautical Journal*, vol. 8, no. 1, pp. 67–77, Mar. 2017, https://doi.org/10.1007/s13272-016-0223-2.

[206] Voß, A., and Klimmek, T., "Maneuver Loads Calculation with Enhanced Aerodynamics for a UCAV Configuration," in *AIAA AVIATION Forum*, Washington, D.C., 2016, https://doi.org/10.2514/6.2016-3838.

[207] Voß, A., and Ohme, P., "Dynamic maneuver loads calculations for a sailplane and comparison with flight test," *CEAS Aeronautical Journal*, vol. 9, no. 3, pp. 445–460, Apr. 2018, https://doi.org/10.1007/s13272-018-0300-9.

[208] Voß, A., Pinho Chiozzotto, G., and Ohme, P., "Dynamic Maneuver Loads Calculation for a Sailplane and Comparison with Flight Test," presented at the IFASD 2017 - 17th International Forum on Aeroelasticity and Structural Dynamics, Como, Italy, 2017, https://elib.dlr.de/113152/.

[209] Voss, G., Cumnuantip, S., and Neumann, J., "A Steady Aeroelastic Analysis of an Unmanned Combat Aircraft Vehicle Conceptual Design," presented at the 29th AIAA Applied Aerodynamcics Conference, Honolulu, Hawaii, USA, 2011, https://doi.org/10.2514/6.2011-3020.

[210] Voss, R., "The Legacy of Camillo Possio to Unsteady Aerodynamics," in *System Modeling and Optimization*, 2005, pp. 1–14, https://doi.org/10.1007/0-387-33006-2_1.

[211] Wang, Lui, Chen, and Mook, "Tightly-Coupled Nonlinear Aerodynamics/Nonlinear Structure Interaction: A HALE Wing Aeroelastic Case Studied," presented at the International Forum for Aeroelasticity and Structural Dynamics, Stockholm, Sweden, 2007.

[212] Wang, Y., Da Ronch, A., and Ghandchi Tehrani, M., "Adaptive Feedforward Control for Gust-Induced Aeroelastic Vibrations," *Aerospace*, vol. 5, no. 3, p. 86, Sep. 2018, https://doi.org/10.3390/aerospace5030086.

[213] Wang, Z., and Chen, P. C., "Accurate Rational Function Approximation for Time- Domain Gust Analysis," presented at the 58th AIAA/ASCE/AHS/ASC Structures, Structural Dynamics, and Materials Conference, Grapevine, Texas, 2017.

[214] Waszak, M., Buttrill, C., and Schmidt, D., "Modeling and Model Simplification of Aeroelastic Vehicles: An Overview," NASA Langley Research Center, NASA Technical Memorandum 107691, Sep. 1992.

[215] Waszak, M. R., and Schmidt, D. K., "Flight dynamics of aeroelastic vehicles," *Journal of Aircraft*, vol. 25, no. 6, pp. 563–571, Jun. 1988, https://doi.org/10.2514/3.45623.

[216] Weisshaar, T., and Ashley, H., "Static aeroelasticity and the flying wing," presented at the 14th Structures, Structural Dynamics, and Materials Conference, Williamsburg, Virginia, 1973, http://arc.aiaa.org/doi/abs/10.2514/6.1973-397.

[217] Weisshaar, T., and Ashley, H., "Static aeroelasticity and the flying wing, revisited," *Journal of Aircraft*, vol. 11, no. 11, pp. 718–720, 1974, https://doi.org/10.2514/3.44409.

[218] Wellmer, G., "A modular method for the direct coupled aeroelastic simulation of free flying aircraft," RWTH Aachen, Aachen, 2014, http://publications.rwth-aachen.de/record/459451.

[219] Wildschek, A., Haniš, T., and Stroscher, F., "L∞-Optimal feedforward gust load alleviation design for a large blended wing body airliner," *Progress in Flight Dynamics, Guidance, Navigation, Control, Fault Detection, and Avionics*, no. 6, pp. 707–728, 2013.

[220] Wildschek, A., Stroscher, F., Klimmek, T., Šika, Z., Vampola, T., Valášek, M., Gangsaas, D., Aversa, N., Berard, A., Raumfahrt, L., and others, "Gust load alleviation on a large blended wing body airliner," presented at the ICAS2012 - 27th International Congress of the Aeronautial Sciences, Nice, France, 2010.

[221] Winther, B. A., Hagemeyer, D. A., Britt, R. T., and Rodden, W. P., "Aeroelastic Effects on the B-2 Maneuver Response," *Journal of Aircraft*, vol. 32, no. 4, pp. 862–867, Jul. 1995, https://doi.org/10.2514/3.46802.

[222] Woolvin, S., "A Conceptual Design Studies of the 1303 UCAV Configuration," in *24th Applied Aerodynamics Conference*, San Francisco, California, 2006, https://doi.org/10.2514/6.2006-2991.

[223] Woolvin, S., “UCAV Configuration & Performance Trade-Offs,” 2006, https://doi.org/10.2514/6.2006-1264.

[224] Wright, J. R., and Cooper, J. E., *Introduction to aircraft aeroelasticity and loads*. Chichester, England ; Hoboken, NJ: John Wiley, 2007.

[225] ZONA Technology Inc., *ZAERO Theoretical Manual*, vol. Version 9.0. Scottsdale, Arizona, 2014.

[226] ZONA Technology Inc., *ZAERO User’s Manual*, vol. Version 9.0. Scottsdale, Arizona, 2013.

[227] *Getting Started with MSC Nastran User’s Guide*. MSC Software Corporation, 2004.

[228] *MSC.Nastran 2005 Quick Reference Guide*. MSC Software Corporation, 2004.

[229] *MSC.Nastran 2014 Design Sensitivity and Optimization User’s Guide*, 5th ed. MSC Software Corporation, 2014.

[230] “US. Standard Atmosphere 1976,” National Aeronautics and Space Administration, Washington, D.C., Technical Report NASA-TM-X-74335, NOAA-S/T-76-1562, Oct. 1976.

[231] “X-48B BWB Team Completes Phase 1 Test Flights,” *NASA*, 05-Jun-2013. [Online]. Available: http://www.nasa.gov/centers/dryden/news/NewsReleases/2010/10-12.html. [Accessed: 25-Aug-2015].

ISSN 1434-8454

ISRN DLR-FB-2020-20